



**HAL**  
open science

# Impact of wing loading on the properties and dynamics of trailing vortices, a water towing tank analysis

Rolando Cruz Marquez

► **To cite this version:**

Rolando Cruz Marquez. Impact of wing loading on the properties and dynamics of trailing vortices, a water towing tank analysis. Fluids mechanics [physics.class-ph]. Centrale Lille Institut, 2023. English. NNT : 2023CLIL0037 . tel-04593746

**HAL Id: tel-04593746**

**<https://theses.hal.science/tel-04593746v1>**

Submitted on 30 May 2024

**HAL** is a multi-disciplinary open access archive for the deposit and dissemination of scientific research documents, whether they are published or not. The documents may come from teaching and research institutions in France or abroad, or from public or private research centers.

L'archive ouverte pluridisciplinaire **HAL**, est destinée au dépôt et à la diffusion de documents scientifiques de niveau recherche, publiés ou non, émanant des établissements d'enseignement et de recherche français ou étrangers, des laboratoires publics ou privés.



CENTRALE LILLE

THESE

*Présentée en vue d'obtenir le grade de*

**DOCTEUR**

*En*

**Spécialité : MÉCANIQUE DES MILIEUX FLUIDES**

*Par*

**ROLANDO CRUZ MARQUEZ**

Doctorat délivré par CENTRALE LILLE

*Titre de la thèse :*

---

**Impact du chargement alaire sur les propriétés et la  
dynamique des tourbillons de sillage, une analyse en bassin  
hydrodynamique**

**Impact of wing loading on the properties and dynamics of trailing vortices, a  
water towing tank analysis**

---

*Soutenue le 21 décembre 2023 devant le jury d'examen :*

PRÉSIDENTE DU JURY	Henda DJERIDI	Professeure	LEGI
RAPPORTEUR	Ivan DELBENDE	Professeur	LIMSI
RAPPORTEUR	Thomas LEWEKE	Directeur de recherche	IRPHE
DIRECTEUR DE THÈSE	Patrick DUPONT	Professeur	LMFL
JURY	Jean-Philippe LAVAL	Directeur de recherche	LMFL
JURY / ENCADRANTE	Marie COULIOU	Ingénieure de recherche	ONERA
ENCADRANT	Vincent BRION	Ingénieur de recherche	ONERA
ENCADRANT	Geoffrey TANGUY	Ingénieur de recherche	ONERA

*Thèse préparée dans le laboratoire :*

Laboratoire de Mécanique des Fluides de Lille - Kampé de Fériet  
ONERA - ELV  
Ecole Doctorale ENGSYS-632

CENTRALE LILLE

*Résumé*ONERA - ELV  
Ecole Doctorale ENGSYS 632

Docteur en mécanique des milieux fluides

**Impact du chargement alaire sur les propriétés et la dynamique des tourbillons de sillage, une analyse en bassin hydrodynamique**

by Rolando CRUZ MARQUEZ

L'impact de la charge alaire sur les propriétés et la dynamique des tourbillons marginaux est étudié dans des expériences en bassin hydrodynamique. Dans le cadre de la théorie de la ligne portante, la circulation locale  $\Gamma_y$  (avec  $y$  la coordonnée en envergure) dépend de la corde locale, de l'incidence effective et du coefficient de portance. Pour un avion commercial, la géométrie de l'aile varie en fonction de la phase du vol (par exemple, déploiement des dispositifs hyper-sustentateurs pour le décollage/l'atterrissage), modifiant ainsi  $\Gamma_y$ . Cela affecte les propriétés du sillage tourbillonnaire, issu de l'enroulement de la nappe tourbillonnaire initiale caractérisée par une intensité  $-d\Gamma_y/dy$ . Les grandes échelles de longueur impliquées dans le développement du sillage sont difficiles à traiter par un seul et même outil. Dans le présent travail, nous utilisons une expérience en bassin hydrodynamique pour explorer ce sujet sur une bonne portion du domaine d'intérêt.

Cette recherche est motivée par la préoccupation de longue date concernant le danger des tourbillons de sillage, un problème encore largement ouvert d'un point de vue technique et qui suscite une pression croissante dans l'industrie aéronautique, particulièrement aux abords des aéroports, du fait des contraintes induites par les règles de séparation et les difficultés à créer de nouvelles pistes ou de nouveaux aéroports. Cette pression résulte de l'augmentation continue du trafic aérien, malgré la préoccupation grandissante du rôle de l'aviation dans les problèmes sociétaux actuels (propagation des épidémies, impact climatique) qui auraient pu un temps laisser croire à une réduction de l'utilisation du transport aérien. La question centrale du point de vue de la mécanique des fluides est de savoir s'il est possible de réduire le danger des tourbillons par une conception intelligente de l'aile ou par des perturbations de forme passive qui modifient le sillage tourbillonnaire, réduisant ainsi les risques pour un avion suiveur.

Le travail présent considère initialement le cas de référence d'une aile rectangulaire, représentative du vol de croisière, puis varie la charge alaire avec des cas sélectionnés. Le premier cas consiste en une configuration où le bord de fuite a une forme ondulée. Cette modification géométrique est inspirée des résultats d'analyses de stabilité qui suggèrent que certaines perturbations qui sont périodiques dans le sens de l'envergure peuvent perturber le sillage et réduire la circulation du tourbillon. Le deuxième cas consiste en une configuration où une incidence géométrique supplémentaire est appliquée au volet central de l'aile afin d'obtenir une distribution de charge hyper-sustentée, similaire à celle adoptée par les avions commerciaux lors de l'atterrissage et le décollage. Le troisième et le quatrième cas consistent en des configurations qui génèrent une paire de tourbillons de chaque côté du sillage.

Dans le troisième cas, les tourbillons d'un même côté du sillage sont co-rotatifs alors que dans le quatrième ils sont contra-rotatifs. Ces configurations sont spécialement conçues pour une interaction accélérée des tourbillons.

Le développement du sillage est étudié depuis le stade d'enroulement jusqu'à 300 envergures en aval, ce qui correspond à deux fois l'échelle de temps  $t_b$  basée sur l'induction mutuelle des tourbillons. Ici,  $t_b = 2\pi b^2/\Gamma$  où  $b$  est la distance entre les tourbillons et  $\Gamma$  une mesure de leur circulation. Dans ces expériences, le nombre de Reynolds moyen, basé sur la corde, de  $Re_c = 10^5$  et le nombre de Reynolds moyen basé sur la circulation est de  $10^4 < Re_\Gamma < 10^5$ . Des mesures Stéreo-PIV sont effectuées dans des sections du sillage généré par les ailes tractées afin d'évaluer les caractéristiques du tourbillon dans une large gamme de vitesses de traction ( $[1,5]m/s$ ) et angles d'incidence ( $[-3^\circ, 20^\circ]$ ). Le plan SPIV est fixe et le modèle se déplace dans le référentiel du laboratoire. Cela pose des difficultés pour suivre les tourbillons du sillage sur une longue période de leur évolution ainsi que pour décomposer l'écoulement en ses composants moyen et perturbateur. Un ensemble complet de procédures de post-traitement pour l'analyse des données SPIV et une stratégie spécifique pour la moyenne des données sont mises en oeuvre.

Les résultats mettent en évidence la structure globale du sillage et le nombre de tourbillons marginaux par rapport à la charge alaire. Les propriétés essentielles des tourbillons (profil, rayon, circulation, écoulement axial et évolution temporelle associée) sont présentées et analysées pour en extraire un sens physique. Il est confirmé que le rayon du tourbillon croît en accord avec les prédictions obtenues à partir d'un modèle visqueux. De plus, une décroissance de la circulation est observée. Nous attribuons ce phénomène aux effets induits par les frontières du canal et, à un niveau moins important, aux imprécisions de la mesure PIV. Dans certains cas, le développement de perturbations sur le tourbillon marginal formé dans le sillage lointain est mis en évidence. En effet, des composantes périodiques dans la trajectoire des tourbillons suggèrent la présence d'ondes de Kelvin de type retrogrades. Cependant, ce phénomène n'est pas observé de façon consistante sur l'ensemble des expériences réalisées et donc les conditions nécessaires pour son apparition restent inconnues. Dans les cas où les trajectoires ne présentent pas de composantes périodiques, une analyse POD révèle que les modes de vorticité les plus énergétiques ont une structure qui ressemble à celle d'une superposition de dipôles, ce qui potentiellement explique le déplacement erratique du centre du tourbillon. Additionnellement, l'évolution temporelle de l'écoulement axial est étudié et deux mécanismes sont mis en évidence. Initialement, une croissance de la magnitude de l'écoulement axial est observée. Cette croissance est probablement liée à l'évolution temporelle de l'écoulement azimuthal à travers l'équilibre cyclostrophique. Ensuite, une réduction de la magnitude de l'écoulement axial est observée quand elle approche celle de l'écoulement azimuthal. Il est hypothétisé que ceci est dû à des mécanismes de stabilisation opérant au niveau du coeur du tourbillon. L'analyse des trajectoires et des propriétés du tourbillon suggèrent que l'instabilité de Crow ne se développe pas de façon significative avant que les tourbillons sortent de la fenêtre de mesure PIV, c'est-à-dire, avant  $t = 2t_b$ .

L'impact d'une ondulation de la forme du bord de fuite de l'aile est analysé. Cette modification est basée sur des résultats théoriques récents où le sillage tourbillonnaire est perturbé en agissant dans une région proche du bord de fuite. L'analyse montre que, quand l'amplitude de l'ondulation du bord de fuite croît, le tourbillon marginal est élargi par rapport au cas de référence, tout en conservant la même circulation. Cet élargissement du tourbillon réduit le risque pour un avion suiveur.

Pour une portance identique, les configurations hyper-sustentées qui génèrent des paires de tourbillons co-rotatifs dans le sillage proche présentent d'abord une fusion des tourbillons de même signe, puis un effet diffusif sur le noyau du tourbillon fusionné par rapport à la configuration de base. Cet effet diffusif se caractérise par des vitesses azimuthales réduites et un rayon plus large dans le cas hypersustenté par rapport au cas de référence. De plus, une augmentation de la circulation normalisée, jusqu'à 20%, est observée en raison de la proximité plus grande des tourbillons.

Le phénomène de fusion est étudiée en analysant l'évolution temporelle des propriétés des tourbillons de la paire. Ici, les variables qui gouvernent la dynamique du système de tourbillons sont le ratio de circulations ( $\gamma$ ) et celui des distances ( $\beta$ ) entre les tourbillons générés par le bout d'aile (principaux) et ceux générés par le volet central (secondaires). Les trajectoires des tourbillons principaux et secondaires montrent un mouvement orbital autour du barycentre de vorticité. La fusion commence avec un rapprochement des tourbillons qui a pour conséquence l'accélération de leur vitesse d'orbitation. La circulation du tourbillon de volet est transférée au tourbillon de bout d'aile. La fusion conclut lorsque les tourbillons du dipôle deviennent indiscernables, typiquement dans une période correspondant à une orbite complète du dipôle.

En revanche, les configurations qui présentent des tourbillons contra-rotatifs de chaque côté du sillage montrent un processus de diffusion visqueuse qui entraîne une réduction de la circulation du tourbillon de bout d'aile. Dans ces configurations, les systèmes de tourbillons exhibent des trajectoires de type périodique, stationnaire ou divergentes, en fonction des caractéristiques initiales du dipôle ( $\gamma_0$  et  $\beta_0$ ). Pour  $\gamma_0$  et  $\beta_0$  donnés, un modèle de tourbillons ponctuels prédit avec précision les trajectoires des tourbillons de l'expérience durant les phases initiales du développement du sillage. Au-delà des phases initiales de développement, les phénomènes tels que la diffusion des tourbillons induisent une dépendance temporelle de  $\gamma$  et de  $\beta$  non reproduite par le modèle. Dans les cas où les trajectoires des tourbillons sont de type stationnaire ou périodique, le processus diffusif s'étend sur une échelle de temps entre  $20b_0/U_0$  et  $80b_0/U_0$ . le tourbillon de volet finit par être complètement diffusé, alors que le tourbillon de bout d'aile persiste avec une circulation qui est réduite de 30 à 80% par rapport à sa magnitude initiale. De plus, la diffusion des tourbillons dans ces configurations semble être liée à des phénomènes dits de "cancellation visqueuse", ce qui suggère que des instabilités coopératives ne se développent pas de manière significative pendant l'échelle de temps observée.

Dans l'ensemble, le présent travail montre que la charge alaire a un impact important sur la position spécifique, la force et la taille des tourbillons dans le sillage.

CENTRALE LILLE

*Abstract*ONERA - ELV  
Ecole Doctorale ENGSYS-632

Doctor in fluid mechanics

**Impact of wing loading on the properties and dynamics of trailing vortices, a water towing tank analysis**

by Rolando CRUZ MARQUEZ

The impact of wing loading on the properties and dynamics of trailing vortices is investigated in a water towing tank facility. In the framework of the lifting line theory, the local circulation  $\Gamma_y$  (with  $y$  the span-wise coordinate) depends on the local chord, effective incidence and lift coefficient. For a commercial aircraft, the wing geometry varies depending on the phase of flight (eg. deployment of high-lift devices for take-off/landing) which modifies  $\Gamma_y$ . This impacts the properties of the vortex wake, which originates from the roll-up of the initial vortex sheet characterized by strength  $-d\Gamma_y/dy$ . Given the substantial length-scales involved in modelling wake development to capture dynamically relevant timescales, numerical simulations remain a very costly solution to capture the dynamics of trailing vortices. Therefore in the present work we use a towing tank experiment to explore this topic.

This research is motivated by the longstanding concern of wake vortex hazard, an issue that remains unresolved and that is the cause of increasing pressure in the aviation industry and at airports. This pressure continues to mount due to the continuous rise in air traffic, despite the rising concern of the role of aviation in societal problems (disease outbreaks, climate impact) which spell the idea of a reduced use of air travel. The central question from a fluid mechanics perspective is whether it is possible to reduce wake hazard through intelligent wing design or through passive shape perturbations that alter the vortex wake, consequently reducing the risks for a following aircraft. The present work initially considers a baseline case of a rectangular wing, which represents cruise-like flight, and then varies the wing-loading with selected cases: a high-lift loading configuration, a loading with trailing edge disturbances and loadings featuring multiple vortices, specifically designed for accelerated vortex interaction. The development of the vortex wake is investigated from the roll-up stage up to 300 spans downstream at a chord-based Reynolds number of  $Re_c = 10^5$ . SPIV measurements are made in sections of the wake generated by the towed wings in order to assess the vortex characteristics in each situation. The SPIV plane is fixed and the model is moving in the laboratory frame. This poses difficulties for tracking the wake vortices over a long period of their evolution as well as for decomposing the flow into its mean and disturbance components. A complete set of post-processing procedures for analyzing the SPIV and a specific strategy for averaging the data is implemented.

The results highlight the overall wake structure and the number of trailing vortices relative to the wing loading. The essential properties of the vortices (profile, radius, circulation, axial flow and the associated temporal evolution) are presented and analyzed to provide physical meaning. In some cases, we are able to expose the development of perturbations upon the trailing vortex formed in the far wake.

The impact of an undulation of the shape of the trailing edge of the wing is analyzed. This modification is based on recent theoretical results where the perturbation of the vortex wake is achieved by acting in the trailing edge region. The analysis shows that the trailing vortex is enlarged compared to the baseline case, while keeping the same circulation.

Given identical lift, high-lift wing-load configurations that generate pairs of co-rotating vortices in the near wake exhibit first a fusion of the same-signed vortices and then a diffusive effect on the fused vortex core compared to the baseline configuration. Additionally, an increase in circulation, up to 20%, is observed due to the closer proximity of the vortices. On the other hand, wing-load configurations that feature counter-rotating vortices on each side of the wake exhibit a process of viscous diffusion that leads to a reduction of the circulation of the wing-tip vortex.

Overall, the present work shows that wing loading has an important impact on the specific position, strength and size of vortices in the wake.

## *Acknowledgements*

Je remercie la Région Hauts-de-France et l'ONERA qui ont financé ce projet de thèse. Le personnel du Laboratoire de Mécanique des Fluides de Lille, en particulier des unités ELV et AMES de l'ONERA, a chaleureusement soutenu mon travail. Leur aide dévouée, notamment de Jean Claude Monnier, Christophe Verbeke, Alberto Baretter, et Guillaume Delannoy, a rendu les expériences au canal hydrodynamique possibles, merci! Mes remerciements vont également à Yves Le-Sant et Christophe Cuvier pour leur disponibilité lors de mes questions sur la PIV, ainsi qu'au professeur Louis Cattafesta pour sa contribution aux premières études menées au canal.

Je tiens à exprimer ma profonde gratitude envers l'équipe d'encadrement, en commençant par Patrick Dupont, mon directeur de thèse, sans qui ce projet n'aurait pas vu le jour. Pour sa disponibilité et son soutien à que cette thèse se déroule au mieux, je lui suis reconnaissant. Mes remerciements s'adressent également à Vincent Brion, Marie Couliou et Geoffrey Tanguy pour leur dévouement et leur encadrement exceptionnels. Leur partage généreux d'expertise scientifique s'est toujours accompagné d'une attitude proactive, positive, respectueuse et patiente. Ils ont accueilli mes idées avec enthousiasme et ont soutenu activement mes projets, ceux relatifs à la recherche comme mes projets artistiques et d'enseignement. Grace à votre soutien, ces quatre années ont été pour moi formatrices et enrichissantes. Merci infiniment !

A ce sujet, je souhaite remercier les personnes qui ont soutenu mes projets artistiques et de médiation scientifique depuis la direction du centre de l'ONERA Lille et de l'unité ELV, notamment Bruno Mialon, Quentin Gallas, Eric Garnier, Geoffrey Tanguy, Eric Deletombe et Jacky Miette. La participation d'autres acteurs, tels qu'Eric Prigent du Fresnoy et Bruno Delannoy et Gaelle Wisniewski du collège de Divion, a été essentielle pour certains projets. Je suis convaincu que votre soutien de ces initiatives a inspiré de nombreux jeunes à s'intéresser à l'héritage scientifique de l'ONERA Lille. Au nom de ces personnes, je vous adresse mes sincères remerciements !

Ensuite, je souhaite remercier Ivan Delbende et Thomas Leweke pour avoir accepté d'être rapporteurs de ce manuscrit. Je les remercie eux ainsi que Henda Djeridi et Jean-Philippe Laval pour avoir lu attentivement ce document et surtout pour avoir partagé leur retours en tant que jurys lors de ma soutenance de thèse.

Le pouvoir de l'amitié a joué un rôle clé dans cette aventure professionnelle. Étant loin de ma famille pendant cette thèse, je ne minimise point l'importance des ami.e.s et collègues. Je tiens à remercier Thomas Huret, Elvina Derhille, Franco Chavarria, Bérénice Bieuville, Anaïs Delacuisine et Thibault, qui m'ont apporté une aide essentielle lors de la soutenance. Merci également à Nicolas Vauchel, Lauriane Lefevre, Baptiste Isnard, Pierre Louis Spychalla, Baptiste Caro et à Léo Claus pour avoir partagé ces années de thèse avec moi, ainsi que pour leur patience et leur ouverture. Je suis reconnaissant envers d'autres personnes qui m'ont soutenu pendant les périodes de travail intense, notamment Libertad, Jules, Charlotte, Camille, Diana, Sabine et Léo.

Y finalmente, agradezco a mis padres, Nadia Marquez y Javier Cruz, quienes dieron durante muchos años (muchos mas que los de una tesis!) un esfuerzo de trabajo, de amor y de respeto hacia mi y hacia mi hermano. La complecion de este doctorado es un logro de los cuatro.



# Contents

<b>Contents</b>	<b>ix</b>
<b>1 Introduction</b>	<b>1</b>
1.1 Background . . . . .	1
1.2 Aims and objectives . . . . .	5
<b>2 Literature Review</b>	<b>7</b>
2.1 The wake vortex hazard . . . . .	7
2.2 From the formation to the natural demise of a trailing vortex . . . . .	9
2.2.1 The formation of vortex wakes . . . . .	11
2.2.1.1 Fundamental properties of vorticity . . . . .	11
2.2.1.2 The generation of vortex sheets around a body . . . . .	14
2.2.1.3 The generation of trailing vorticity in the near wake of a wing . . . . .	15
2.2.1.4 The roll-up of trailing vorticity in the near wake of a wing . . . . .	19
2.2.1.5 Summary . . . . .	21
2.2.2 The physics of an isolated vortex . . . . .	21
2.2.2.1 Vortex characteristics . . . . .	21
2.2.2.2 Mechanisms of vortex decay . . . . .	24
2.2.2.3 Tri-dimensional effects . . . . .	26
2.2.3 The physics of a pair of trailing vortices . . . . .	30
2.2.3.1 Time-scales of wake evolution . . . . .	30
2.2.3.2 Cooperative instabilities on a vortex pair . . . . .	32
2.2.4 Summary . . . . .	34
2.3 Multipolar vortex wakes . . . . .	35
2.3.1 A model of a multipolar vortex wake . . . . .	36
2.3.1.1 The roll-up of the trailing vorticity into multiple vortices . . . . .	36
2.3.1.2 The physics of four vortex wakes . . . . .	37
2.3.2 Co-rotating 4-vortex systems . . . . .	40
2.3.3 Counter-rotating 4-vortex systems . . . . .	46
2.3.4 Higher order instabilities . . . . .	47
2.3.5 Summary . . . . .	48
<b>3 Experimental installation</b>	<b>49</b>
3.1 Towing tank facility . . . . .	49
3.1.1 Baseline wing model . . . . .	50
3.1.2 Towing device . . . . .	51
3.1.3 Operating conditions . . . . .	51
3.2 Measurement setup . . . . .	53
3.2.1 Aerodynamic force measurements . . . . .	53
3.2.2 Velocity field measurements . . . . .	55

3.2.2.1	PIV installation . . . . .	56
3.2.2.2	PIV software . . . . .	59
3.2.2.3	Analysis of the measurement resolution . . . . .	59
3.2.2.4	Analysis of the measurement accuracy . . . . .	61
3.3	Intermediate conclusion . . . . .	63
<b>4</b>	<b>Characterization of the baseline and undulated trailing edge cases : configurations with two vortices</b>	<b>65</b>
4.1	The ONERA Lille towing tank : a facility for wake studies . . . . .	65
4.1.1	Lifting line theory predictions of the flow evolution . . . . .	65
4.1.2	Analysis of the steadiness, repetability and symmetry of the flow	70
4.1.2.1	Verification of the steadiness of the aerodynamic efforts around the generating wing . . . . .	71
4.1.2.2	Verification of the repeatability of the aerodynamic forces generated by the wing under the same towing configuration . . . . .	72
4.1.2.3	Validation of the aerodynamic characterization of the reference wing (NACA 4412) . . . . .	73
4.1.2.4	Analysis of vortex trajectories in order to assess the symmetry of the wake . . . . .	75
4.1.2.5	Intermediate summary . . . . .	78
4.2	Extraction of vortex characteristics from PIV measurements . . . . .	78
4.2.1	Identification of the vortex center . . . . .	78
4.2.2	Extraction of the 2D vortex velocity field . . . . .	81
4.2.3	Extraction of the 1D velocity profile . . . . .	82
4.2.4	Estimation of vortex characteristics . . . . .	85
4.2.4.1	Measurement of vortex size . . . . .	85
4.2.4.2	Measurement of vortex strength . . . . .	87
4.2.4.3	Vortex trajectories . . . . .	90
4.3	Analysis of physical phenomena causing the evolution of vortex characteristics . . . . .	91
4.3.1	Physical mechanisms driving vortex decay . . . . .	91
4.3.1.1	Laminar diffusion of the vortex core . . . . .	91
4.3.1.2	Analysis of the circulation decrease . . . . .	92
4.3.2	Evolution of the peak vortex velocities and of the swirl number	94
4.3.3	Random and periodic components in the trajectories of the trailing vortices . . . . .	96
4.3.4	Intermediate summary . . . . .	100
4.4	Analysis of the impact of a modification of the wing geometry on the characteristics of its vortex wake . . . . .	101
4.4.1	Modification of the wing geometry in order to introduce a spanwise perturbation on the flow . . . . .	101
4.4.2	Results . . . . .	101
4.5	Intermediate conclusion . . . . .	104
<b>5</b>	<b>Analysis of vortex interaction in a co-rotating trailing vortex system</b>	<b>105</b>
5.1	Generation of a co-rotating pair of vortices . . . . .	105
5.2	Wake of the CoR wing . . . . .	107
5.2.1	Estimation of the wake behavior from a numerical model . . . . .	107
5.2.2	Analysis of experimental results . . . . .	109
5.3	Wake of the HL wing . . . . .	110

5.3.1	Analysis of experimental results . . . . .	110
5.3.2	High-lift wake before vortex fusion ( $t < t_f$ ): characterization of the fusion mechanism . . . . .	113
5.3.2.1	Characterization of the vortices . . . . .	113
5.3.2.2	Evolution of the properties of the co-rotating pair . . . . .	115
5.3.3	High-lift wake after vortex fusion ( $t > t_f$ ): Comparison of the far wake evolution of the fused vortex characteristics with that of the baseline vortex in order to estimate the impact of a high-lift configuration on the vortex wake hazard . . . . .	119
5.4	Intermediate conclusion . . . . .	120
<b>6</b>	<b>Analysis of vortex interaction in a counter-rotating trailing vortex system and properties in the far wake</b>	<b>123</b>
6.1	Modification of the wing geometry in order to generate a counter- rotating vortex system . . . . .	123
6.2	Analysis of vortex trajectory and circulation in a counter-rotating system	126
6.2.1	Identification of the vortices . . . . .	126
6.2.2	Assessment of the flap and tip vortices circulation in order to characterize the counter-rotating system . . . . .	132
6.2.3	Analysis of vortex trajectories in order to identify the system regime . . . . .	135
6.2.3.1	Periodic motion . . . . .	135
6.2.3.2	Divergent motion . . . . .	137
6.2.3.3	Steady motion . . . . .	139
6.2.3.4	Analysis of the three regimes . . . . .	142
6.3	The effect of flap vortex diffusion on the evolution of the vortex system	142
6.3.1	$t < t_\Delta$ : Analysis of the diffusion of the flap vortex through viscous cancellation . . . . .	143
6.3.2	$t > t_\Delta$ : Analysis of the wing-tip vortex after the complete diffusion of the flap vortex . . . . .	145
6.4	Intermediate conclusion . . . . .	147
<b>7</b>	<b>General conclusion and perspectives</b>	<b>149</b>
7.1	Conclusion . . . . .	149
7.2	Discussion of results and perspectives . . . . .	152
<b>A</b>	<b>Description of the database</b>	<b>157</b>
<b>B</b>	<b>Calibration procedure on the experimental installation</b>	<b>161</b>
B.1	Calibration of the wing angle of attack . . . . .	161
B.2	Verification of the calibration of force measurements . . . . .	164
B.3	Calibration of velocity field measurements . . . . .	167
B.4	Time-synchronisation of the measurements . . . . .	170
<b>C</b>	<b>Analysis of the uncertainty of the PIV measurement</b>	<b>173</b>
<b>D</b>	<b>Method for computing the average and standard deviation of combined sub-populations</b>	<b>183</b>
	<b>Bibliography</b>	<b>185</b>



# List of Abbreviations

## Acronyms :

TE	wing trailing edge
PIV	particle image velocimetry
S-PIV	stereo-PIV
FFT	fast Fourier transform
POD	Proper orthogonal decomposition
LO	acronym to denote the Lamb-Oseen vortex model
Q	acronym to denote the $q$ -vortex model
G1	vortex detection criteria from Graftieaux <i>et. al</i> [36]
LL	refers to results obtained using the lifting line model
PV	refers to results obtained using a point vortex model
<i>Exp</i>	refers to results obtained directly from measurements
<i>th</i>	refers to results that are an analytical prediction
ICAO	International Civil Aviation Organization
MTOM	aircraft maximum take-off mass
DNS	direct numerical simulations
RANS	Reynolds-averaged Navier-Stokes equations

## Software, Hardware and materials :

XFOIL	software for the prediction of aerodynamic efforts
XLFR5	software for the prediction of aerodynamic efforts
AMTI-MC3A	force probe model
PHI-70	force probe model
ND:YAG	a category of laser that uses a specific crystal as a medium
PMMA	synthetic polymer used on the fabrication of the towing tank windows
LAVISION sCMOS	camera model for PIV
AFFIX 2	software for image treatment for PIV
FOLKI	software for PIV post-processing ( <i>Flot Optique Lucas Kanade Itératif</i> )
20a,23a	denotes the main PIV camera framing configurations
b,c,d,	denotes secondary PIV camera framing configurations used to track specific vortex trajectories
e	denotes the PIV camera frame located below the others, used to track the vortex at large downstream stations
S20	Denotes a structure that is used to attach the wing model to the chariot
S23	Denotes a structure that is used to attach the wing model to the chariot



# List of Symbols

Bold symbols are vectorial quantities.

## Conditions in the water tank :

$N$	PIV seeding density	$[m^{-2}]$
$\odot$	PIV particle diameter	$[m]$
$\rho_p$	PIV particle density	$[kg/m^3]$
$T^\circ$	water temperature	$[K]$

## Variables of the flow :

$\rho$	density	$[kg/m^3]$
$\nu$	kinematic viscosity	$[m^2/s]$
$p$	pressure field	$[Pa]$
$p_\infty$	pressure in the far field	$[Pa]$
$\mathbf{u}$	velocity field	$[m/s]$
$U_\infty$	velocity in the far field	$[m/s]$
$\boldsymbol{\omega}$	vorticity field	$[s^{-1}]$
$\mathbf{f}$	body forces	$[N]$
$\Omega_{ij}$	rotation-rate tensor	$[s^{-1}]$
$e_{ij}$	strain-rate tensor	$[s^{-1}]$
$s^\pm$	induced strain field	
$\lambda$	eigen-value	
$\Omega$	rate of rotation	$[s^{-1}]$
$I_1$	first moment of vorticity	$[s^{-1}]$
$I_2$	second moment of vorticity	$[m^2/s]$

## Wing model geometry :

$Ref$	Reference wing configuration	
$HL$	High-lift wing configuration	
$CoR$	wing configuration for co-rotating vortices	
$CnR$	wing configuration for counter-rotating vortices	
$U_0$	wing velocity (constant velocity during towing)	$[m/s]$
$\alpha$	wing geometric angle of attack	
$\alpha_s$	stall angle of attack	
$\alpha_i$	induced angle of attack	
$\alpha_{corr}$	correction in the angle of attack yielded by calibration	
$C_i$	towing configuration = ( $wing, U_0, \alpha$ ), see appendix A	
$\Theta$	wing geometric twist	
$S$	wing surface	$[m^2]$

$AR$	wing aspect ratio	
$c_0$	wing chord	[m]
$b_0$	wing span	[m]
$b_f$	wing span of a follower aircraft	[m]
$A$	amplitude of undulation of the wing trailing edge	[m]

### Reference frame attached to the towing tank :

$L, W_C, H_C$	respectively usable length, width and height of the towing tank	[m]
$X, Y, Z$	respectively stream-wise, span-wise and vertical directions	[m]
$O_C$	position of the origin for the towing motion	
$\mathcal{R}_C$	reference frame attached to the towing tank = $(O_C, X, Y, Z)$	
$X_{PIV}$	longitudinal position of the measurement installation	[m]
$X_m$	longitudinal position of the wing model trailing edge	[m]
$u_m$	instantaneous velocity of the wing model trailing edge	[m/s]

### Aerodynamic characterization of the wing :

$f_{acq}$	sampling frequency of the force probe measurement	[Hz]
$\ell_y$	local lift in a section of the wing	[N/m]
$F_z, F_x, F_y$	respectively aerodynamic lift, drag and side forces	[N]
$M_z, M_x, M_y$	respectively aerodynamic rolling, pitching and yawing moments	[N.m]
$\mathbf{F}_i$	= $(F_z, F_x, F_y)$ aerodynamic forces	[N]
$\mathbf{M}_i$	= $(M_z, M_x, M_y)$ aerodynamic moments	[N.m]
$C_x$	= $F_x / (0.5\rho U_0^2 c_0 b_0)$ drag coefficient	
$C_y$	= $F_y / (0.5\rho U_0^2 c_0 b_0)$ side force coefficient	
$C_z$	= $F_z / (0.5\rho U_0^2 c_0 b_0)$ lift coefficient	
$C_{z\alpha}$	gradient of lift coefficient with $\alpha$	
$C_R$	induced rolling moment coefficient	
$A_n$	Fourier coefficients of the wing bound circulation in the lifting line model	[m <sup>2</sup> /s]

### Reference frame in the measurement plane :

$x, y, z$	respectively stream-wise, span-wise and vertical directions	[m]
$O_M$	position of the mid-plane at the trailing edge of the wing	
$\mathcal{R}_M$	= $(O_M, x, y, z)$ reference frame attached to the wing model	
$\mathbf{x}_\perp$	a position in the measurement plane = $(U_0 t, y, z)$ following the passage of the wing	[m]
$h$	water surface vertical position in $\mathcal{R}_M$	[m]
$H_g$	ground vertical position in $\mathcal{R}_M$	[m]
$u, v, w$	respectively stream-wise, span-wise and vertical velocities	[m/s]
$\mathbf{v}$	= $(u, v, w)$ velocity field in the PIV measurement plane	[m/s]
$\mathbf{v}_\perp$	= $(0, v, w)$ in-plane velocity field	[m/s]
$\mathbf{v}_x$	= $(u, 0, 0)$ out-of-plane velocity field	[m/s]
$\omega_x$	axial vorticity	[s <sup>-1</sup> ]
$\omega_n$	distribution of $\bar{\omega}_x(r \geq R_1)$ about its mean value	[s <sup>-1</sup> ]
$\sigma_\omega$	standard deviation of $\omega_n$	[s <sup>-1</sup> ]
$X_r$	length scale of vortex roll-up	[m]
$K_r$	measure of the degree of roll-up	

**Position of vortices in the measurement plane :**

$x_m$	position of the extremum of axial vorticity	[m]
$\Omega_m$	a circular region of integration estimated to contain all of the flow vorticity	
$x_\omega$	position of the barycenter of vorticity	[m]
$x_c$	position of the vortex center	[m]
$x_r$	position of the portside vortex	[m]
$x_l$	position of the starboardside vortex	[m]
$b$	= $ x_r - x_l $ separation between vortices	[m]
$s$	= $b/b_0$ wing load factor	
$x_{LL}$	position of the vortex predicted through a model of lifting line theory of image vorticity effects of the tank frontiers	[m]
$x_i$	position of the vortex in an ideal unperturbed trajectory	[m]
$x_\delta$	offset between the vortex real position and its ideal trajectory, in the traverse plane	[m]
$r_i, \omega_i, \phi_i$	respectively the amplitude, pulsation and phase of the motion of $x_\delta$	[m, s <sup>-1</sup> , -]

**In a co- or counter- rotating vortex pair :**

1	subscript for the wing-tip vortex	
2	subscript for the flap-tip vortex	
$x_1$	position of the wing-tip vortex	
$x_2$	position of the flap-tip vortex	
$x_{1+2}$	position of the pair's barycenter of vorticity	
$x_s$	position of the stagnation point	
$\Omega_i$	a circular region of integration centered on $x_{\omega,i}$ (where $i = 1, 2$ )	
$\Lambda_i$	an octogonal region of integration centered on $x_i$ (where $i = 1, 2$ )	
$\Lambda_{Tot}$	a rectangular region of integration extending over most of the measurement plane	
$\gamma$	= $\Gamma_2/\Gamma_1$ circulation ratio between the main and the secondary vorticity	
$\gamma_s$	circulation ratio characteristic of the steady motion regime	
$\beta$	= $b_2/b_1$ separation ratio between the main and the secondary vortices on each side of the plane	
$\beta_0, \gamma_0$	characteristic ratios of separation and circulation for a given towing configuration	
$d$	distance between the main and the secondary vorticity	[m]
$d_0$	characteristic distance for a given towing configuration, estimated to be the distance between the flap and wing tips	[m]
$\phi$	orbit angle of the vortex pair	
$\Omega_{orb}$	= $(\Gamma_1 + \Gamma_2)/(2\pi d^2)$ angular velocity of rotation of the pair	
$J$	angular momentum of the pair	[m/s]
$\Delta_\Gamma$	a quantification of the average loss in circulation endured by the wingtip vortex	

**Scales of velocity :**

$V_s$	horizontal velocity induced by the image effects of the water surface	[m/s]
$V_g$	horizontal velocity induced by the image effects of the tank ground	[m/s]

$V_v$	$= dy_\omega(t)/dt$ measured horizontal velocity of the vortex dipole	[m/s]
$W_g$	vertical velocity induced by the image effects of the tank ground	[m/s]
$W_w$	vertical velocity induced by the image effects of the tank lateral walls	[m/s]
$W_v$	$= dz_\omega(t)/dt$ measured vertical velocity of the vortex dipole	[m/s]
$W_d$	$= \Gamma/(2\pi b)$ predicted descent velocity of the vortex dipole	[m/s]
$w_i$	vertical velocity induced by the vorticity sheet in the near wake	[m/s]
$\Theta$	descent angle of the vortex dipole	
$\Omega$	rate of rotation of the flow around the vortex centroid	[s <sup>-1</sup> ]
$\Delta U$	maximum axial flow in the vortex, it is the differential between the far field ( $r \rightarrow \infty$ ) and the vortex core ( $r \rightarrow 0$ )	[m/s]

### Vortex characteristics :

$R_\omega$	radius where axial vorticity is contained	[m]
$R_a$	vortex core radius	[m]
$R_d$	vortex dispersion radius	[m]
$R_1$	an empirical estimation of the radial distance beyond which measurement noise is dominant over vorticity computation	[m]
$\Gamma_r$	vortex circulation as a function of the radial distance	[m <sup>2</sup> /s]
$\Gamma$	vortex total circulation	[m <sup>2</sup> /s]
$\Gamma_0$	vortex root circulation	[m <sup>2</sup> /s]
$\Gamma_{Tot}$	total circulation on the flow	[m <sup>2</sup> /s]
$\Gamma_y$	local circulation on the wing	[m <sup>2</sup> /s]
$\gamma_\omega$	$= \frac{d\Gamma_y}{dy}$ intensity of the vorticity sheet shed at the trailing edge	[m/s]
$Re_{b_0}$	$= U_0 b_0 / \nu$ span based Reynolds number	
$Re_c$	$= U_0 c / \nu$ chord based Reynolds number	
$Re_\Gamma$	$= \Gamma_0 / \nu$ vortex Reynolds number	
$q$	$= \Omega R_d / \Delta U$ swirl number	
$v'$	$= (v'_x, v'_r, v'_\theta)$ and $p'$ , perturbation flow field	[m/s, Pa]
$\omega$	temporal characteristic of a perturbation mode	
$k, m$	respectively axial and azimuthal wavenumber of a perturbation	
$\tilde{y}, \tilde{z}$	amplitude of a perturbation	[m]
$\lambda$	axial wavelength of a perturbation	[m]
$\sigma$	growth rate of a perturbation mode	[s <sup>-1</sup> ]
$\delta$	cut-off parameter	[m]
$\omega$	self induction function	[s <sup>-1</sup> ]
$l$	rotation direction of a wave	
$\omega_i$	self induced rotation rate	[s <sup>-1</sup> ]
$f_i$	temporal frequency of mode $i$	[Hz]

### Measurements of time :

$t_C$	elapsed time from the beginning of the towing motion	[s]
$t_1$	end time for the phase of towing acceleration	[s]
$t_2$	time at which the phase of towing deceleration begins	[s]
$t_{C,PIV}$	time at which the wing model crosses the PIV plane	
	$X_m(t_{C,PIV}) = X_{PIV}$	[s]
$t$	elapsed time from the crossing of the PIV plane by the wing	[s]
$t_0$	time of the first PIV measurement available during an experiment	[s]
$N_5$	number of measurements available for $tU_0/b_0 \leq 5$	

$t_f$	time from the shedding of a co-rotative vortex pair to its fusion	
$t_{max}$	time of the last PIV measurement available during an experiment	[s]
$t_\Delta$	time at which the flap vortex circulation reaches 0	[s]
$t_d$	$= b_0/U_0$ time scale of the incoming flow	[s]
$t_b$	$= 2\pi b^2/\Gamma$ time scale of vortex mutual induction	[s]
$t_v$	$= \pi R_d^2/\nu$ time scale of vortex viscous diffusion	[s]
$t_{orb}$	$= (2\pi d)^2/\Gamma$ time scale of the orbital velocity of a vortex pair	[s]

### Mathematical operators :

$max(X)$	operator to denote the maximum value of population $X$
$\langle X \rangle$	operator to denote a time-average on the population $X$
$\tau$	length of the time window on a time average operation on the vortex field
$\langle X \rangle_\tau$	operator to denote the time average of population $X$ over a time-frame $[t - \tau/2, t + \tau/2]$ .
$\langle X \rangle_{\tau,\theta}$	operator to denote an azimuthal average over $[0, 2\pi]$ on top of the time average over a time-frame $[t - \tau/2, t + \tau/2]$ .
$\bar{X}$	operator to denote and average between different realizations of an experiment for the population $X$
$s_X$	standard deviation operator on the population $X$
$\Delta X/\Delta T$	linear rate of time-evolution for $X$
$P(f)$	power spectrum operation over a signal $f$
$Re(X) Im(X),$	real and imaginary parts of variable $X \in \mathbb{C}$
$\dot{x}$	time derivative operator for variable $x(t)$
$\delta()$	Dirac function
$\mathbf{n}$	elemental vector normal to a given volume $V$ or surface $S$

### Characteristics of PIV :

$I$	for computation : field of intensity recorded by the camera	
$X$	for computation : field of particle positions	
$\mathbf{k}$	for computation : matrix of grid point indices	
$\mathbf{X}_k$	for computation : a grid point in the plane	
$\mathcal{W}_k$	for computation : interrogation window centered around $\mathbf{X}_k$	
$F$	for computation : transformation to correct perspective deformations	
$d$	for measurement : Particle displacement	[px]
$d_{opt}$	for measurement : optimal particle displacement	[px]
$dt_{opt}$	for measurement : optimal inter-frame time $= d_{opt}/v_\theta$	[px]
$dt$	for measurement : inter-frame time	[s]
$f_{PIV}$	for measurement : sampling frequency	[Hz]
$\Delta t$	for measurement : time resolution	[s]
$\Delta x$	for measurement : spatial resolution (grid step)	[m]
$M$	for measurement : denotes the image calibration procedure	
$U_i$	for measurement : uncertainty in the measurement of variable $i$	



## Chapter 1

# Introduction

### 1.1 Background

Wake vortices trailing behind commercial airplanes pose a threat to air traffic. During a wake encounter, a rolling moment or a down-wash force can be induced upon the following aircraft. The degree of hazard is a function of the vortex strength and size, which are a bi-product of the lift generated by the leading aircraft [6, 18]. One way to tackle this issue is to develop vortex alleviation techniques.

Motivated by the above problem, groundwork on the stability of a vortex pair was early provided by Crow [22], as he carried out a stability analysis of a pair of vortex filaments. This established the foundations of vortex alleviation efforts where the usual approach is to play on the intrinsic dynamics of systems of multiple vortices to hasten their decay. Crow characterized the sinusoidal growing mode of perturbation that results from the interaction between the self-induced waves of a deformed vortex and the induced strain field caused by the opposite vortex, also known as the Crow instability. The wavelength is typically about eight times the spacing of the vortices. In the far wake, these deformations lead to the linking of the vortices of the pair, with the tilting of the axial vorticity in the direction perpendicular to the initial line of vortices. Using a setting of flapping plates in a water tank Roy *et. al* [89] and then Leweke & Williamson [58] could characterize the growth rates and wavelengths of these long-wave instabilities, in good agreement with Crow's theory.

The mechanisms behind these instabilities are related to the tri-dimensional deformation that occurs in a vortex column. The fundamental understanding of how a 3D perturbation propagate along a vortex comes from the work of Lord Kelvin [97]. The propagation of a perturbation is ensured by an axial pressure gradient that is generated when the cyclostropic equilibrium in the vortex core is disturbed. These so-called Kelvin waves provide a decomposition base for any arbitrary perturbation in an inviscid vortex [3]. The study of Kelvin waves was extended to models of viscous vortices by Fabre *et.al.* [33, 29]. This allowed for a categorization of the modes present in the viscous vortex into families that share an underlying physical mechanism. Almost all modes are dampended to some degree by viscosity. A particular family of waves, called *displacement waves*, have a net effect of displacing the whole vortex core. These displacement waves are those which participate in the development of the cooperative Crow instability that ultimately leads to vortex linking.

Although linking does not constitute the final stage of the vortex dynamics, it is usually considered as a mark of the vortex lifespan in its original structure. However, the natural time-scale for the development of the Crow instability is too large to be usefully applied in the context of commercial flight. This motivated research efforts aimed at actively triggering instability in the wake. Along these lines Brion

*et. al.* [10] characterized the zone of sensitivity for the excitation of the Crow instability in a vortex dipole. The results of Navrose *et. al.* [70] on the transient growth in the near wake show that, on the wing, the zone of sensitivity for the optimal perturbation of the vortex wake is located far from the zone where the vortex is shed. The outcome is potentially a much better efficiency of the control, yet with difficulties when transposing theoretical results to experimental practice. In the search for a flow that displays suitable characteristics to promote vortex decay, a part of the research turned towards more complex wake configurations and the necessary conditions to generate them in-flight.

Betz [7] and later Rossow [86] developed an analytical method to relate the topology of the wake and the vortices in it to the span-wise distribution of lift of the generating wing. Based on lifting line theory, where  $\ell_y$  the local lift at a span-wise station  $y$  is related to the bound circulation  $\Gamma_y$ , Betz method derives the distribution of circulation in a Trefft plane of the wake far downstream. This allows to approximate the number, position and strength of the vortices in the wake, taking as input the wing geometry. For instance, a multipolar vortex wake can be formed from the wing/tail vortices but also shed by the discontinuities in the geometry of an aircraft wing alone. The discontinuous nature of the resulting span-load profile generates peaks in the trailing vorticity sheet around which the sheet rolls-up, generating additional vortices besides the one at the wing-tip. This model could not describe the vortex dynamics during its formation stage nor its interactions in the far wake. However, it is at these stages where the dynamics that are essential for the design of control strategies occur.

For example, the set of vortices in the near-wake are known to merge and form a single trailing vortex between 0 and 10 wingspans downstream from the wing [8]. On a commercial aircraft, this phenomenon can be induced by the wing ailerons and flaps, but also by the engine nacelle or the empennage. Additional vorticity can be co-rotating or counter-rotating with the wing-tip vortex. The typical setup of a system of 4 vortices is sketched in Fig. 2.16. Work by Crouch [20], Fabre & Jacquin [30] [32] and later Bristol *et al.* [11] turned towards the analysis of cooperative instabilities on systems of multiple wake vortices. Towing tank experiments led by Ortega [73] focused on the far wake characterization of co-rotating and counter-rotating vortex pairs shed by rectangular wing models. These research efforts allowed to prove the existence of unstable modes which, compared with the Crow mode, exhibited greater growth rates and smaller characteristic times. Furthermore, essential parameters for the development of this phenomenon were found to be vortex spacing and the circulation ratio between vortex pairs (respectively  $\beta$  and  $\gamma$  in the figure). On a commercial wing configuration, however, the necessary conditions for the development of unstable vortex pairs in the wake are seldom met. Namely, the flow configuration that showed promise with respect to wake hazard reduction was found to be a pair of counter-rotating vortices ( $\gamma < 0$ ), whereas commercial wing configurations often produce a co-rotating pair ( $\gamma > 0$ ).

The dynamics of co-rotating vortex systems of equal strength was studied in experiments by Meunier & Leweke [62] and in DNS calculations of Laporte & Leweke [52]. Their work allowed for the characterization of the merging mechanism occurring between co-rotating vortices, also called vortex fusion. At low Reynolds number, merging follows a 2D, laminar process in which vortices initially orbit around each other because of their induced velocities. The vortices size (here denoted by  $R_d$ ) increase under the action of viscous diffusion [90] until a critical value, relative to the co-rotating vortices distance  $d$ , is reached. A *fusion* phase follows in which the

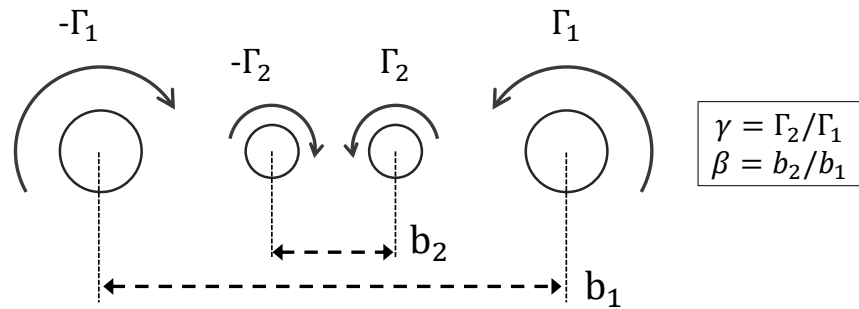


FIGURE 1.1: Diagram of a system of four vortices

distance between the vortices drops significantly and the vorticity from both vortices is merged. During fusion, vortices can be split into filaments some of which are advected outwards from the pair while the rest are fed into the dominant vortex. Filamentation occurs more prominently in configurations where there is a significant difference in strength between the vortices as it was observed in the experiments of Chen [17]. The *fused* vortex is rendered nearly axisymmetric by viscous diffusion. Experimental results and full scale observations display however fusion times shorter than the ones predicted by the 2D model.

To study the reason why fusion occurs earlier than expected, the stability of co-rotating vortex systems were studied in the experiments of Chen [17], Bristol *et.al* [12], Meunier & Leweke [62], Roy *et.al* [89] and Breitsamter *et. al* [8] among others. They identified the development of elliptic instabilities that participate to the fusion process. At high Reynolds numbers vortices undergo a short-wave, three-dimensional instability which translates into a sinusoidal perturbation of their trajectory. Analog to the analysis of Crow [22] and Widnall [101], if the self-induced rotation rate acts in a co-grade sense with the orbit-induced rotation rate their respective action may partially cancel [11]. In this scenario, elliptical streamlines in the flowfield result from the interaction between the weaker vortex with the strain field induced by its counterpart. Linear stability analysis and numerical simulations of Bristol *et.al* [11] showed that this elliptic instability plays a major role in the fusion process, allowing vorticity to be transferred at a faster rate from the weaker to the stronger vortex. Instability growth rates measured in the experiments of Meunier [61] were in good agreement with theoretical predictions. Fusion was completed within one orbit period. In the experiments of Chen [17] accelerated fusion times, relative to the predictions of inviscid theory were attributed to the action of the elliptic instabilities. These interesting results, where the vortices studied were generated from simplified wings or even parallel plates, remained to be transferred to the scenario where the wake is generated by a far more complex geometry which includes the fuselage, wing and nacelle.

Breitsamter *et. al* [8] performed wind tunnel experiments on a scaled 4-engine transport aircraft wing in high lift configuration and observed that the flap and nacelle vortices (both co-rotating with the wingtip vortex) quickly fuse and formed a dominant vortex that eventually absorbs the wingtip vortex. It was shown that co-operative instabilities, namely the Crow instability, is present in this remaining vortex system but the effective lifespan of the vortices could not be characterized within the wing tunnel length. It was observed that counter-rotating flow is generated by the horizontal tailplane and by the fuselage, but these structures did not trigger any early dissipation of vorticity.

Multiple wing/tail vortices combinations were explored in a towing tank by

Crouch [21] and numerically by Stumpf [96] to determine promising configurations in terms of induced rolling-moment hazard reduction. Stumpf [96] designed wing configurations taking into account the tail vortices, which are counter-rotating with respect to the wing-tip vortices. This led to a passive reduction of 44 – 52% for the maximum rolling-moment. Introducing active control in the form of ailerons oscillating motion, Crouch proved that an early vortex linking can be achieved with a level of forcing viable for commercial configurations. At this stage of research, however, this methodology leaves out crucial aircraft design objectives like lift coefficient which interferes with its applicability.

Besides the main modes present in the vortex wake, the action of modes of higher order may also provide a pathway to vortex instabilities. Recent work by Edstrand [28] developed a linear stability analysis of the wake of a nominal wing geometry. They analyzed the downstream development of stability modes in the wake and dressed numerical simulations of the wake evolution under the action of each mode. This work permitted to show that the 5th wake mode, although initially stable, can lead to an unstable flow configuration downstream in the wake. The growth rates of this instability are greater than Crow's. The numerical simulations revealed that the shape function of the 5th mode becomes counter rotating with the main tip vortices downstream which causes instability. Their analysis provided the shape function of this mode which is distributed in the span-wise direction at the surface of the wing. A similar investigation conducted by Navrose [71, 70] also led to the conclusion that the optimal perturbation is located in a region covering the entire span of the wing. However, the authors could not provide an effective control strategy to produce this specific perturbation, leaving the existence of these modes yet to be proven experimentally.

The dynamics of the wake is also impacted by the presence of axial flow in the core of vortices, which is neglected by most wake models. Trailing vortices with axial flow were described early-on by Batchelor [5] and Moore & Saffman [67]. Wake-type axial flow is related to azimuthal velocity through the cyclostropic equilibrium. The velocity deficit in the wing boundary layer and pressure perturbations traveling in a columnar vortex have also been shown to cause the development of strong axial flow [61, 65, 67]. The dynamics of the Batchelor vortex are piloted mainly by the swirl number  $q$ , the ratio of azimuthal to axial velocities in the vortex. Analytical groundwork allowed for the identification of another family of unstable modes besides those of cooperative-instabilities. Indeed the vortex becomes unstable at low values of swirl, as was first shown analytically by Lessen *et.al* [56] and by Mayer & Powell [60]. The considered instability is called "helical" relating to the structure of the corresponding modes along the vortex axis (see [45, 65] for a DNS visualization). Numerical studies like those of Delbende *et.al* [24] and Olendraru *et.al* [72] corroborated that the application of axial flow is an efficient means of promoting amplification of linearly unstable helical modes in wake type vortices. The development of the helical instability under these conditions was also observed through DNS and LES by Moet [65]. Beyond moderate swirl values ( $q > 0.7$ ) Jacquin & Pantano [45] observed the development of an annular *stable buffer layer* preventing the transport of perturbations in the vortex until  $q \approx 1.5$ , where all helical modes fully dampen. Little experimental validation exists to corroborate these analytical and numerical results.

## 1.2 Aims and objectives

To summarize, research efforts around wake vortices have brought forward models for the prediction of unstable wake configurations. These include multipolar vortex wakes, which are a case often observed in landing/take-off wing configurations of commercial aircraft. In conjunction with numerical simulations, experimental work has proven the existence of instability mechanisms such as long wave, short wave, elliptic and multipolar cooperative instabilities. Stability analysis has provided zones of sensitivity on the wing surface for the excitation of unstable modes, often leading to an action along the wingspan. With the addition of active and passive methods, such as ground effect, flow control strategies for wake demise have been proposed.

However, on most cases the resulting growth rates do not meet a substantial reduction of the time scales to dissipation. On one hand, the strategies of control proposed are insufficient to excite unstable modes at short times under the constraints of end-product applicability. Unstable modes excited by active control actuating over the wingspan have not been observed experimentally. The vortex base-flow employed during control design studies (experimental and numerical) is often representative of vortices during cruise flight : this approach neglects how vortices are affected by the lift distributions which varies particularly during landing and take-off. On the other hand, analytical predictions of the near-wake behavior of trailing vortices has been validated by experiments in wind-tunnels or with parallel plates in a water tank, but special installations such as a towing tank are required to study the far wake dynamics of trailing vortices. Because of this most experimental installations rely on early hints of instability development in the near wake, as they cannot observe the dynamics of the wake at a sufficiently large downstream station where the fully developed instability takes place.

This work is motivated by the need to understand the behavior of the physical properties of trailing vortices when subjected to physical mechanisms that lead to a reduction in vorticity. This includes identifying the presence of cooperative instabilities or other phenomena that have been mentioned earlier. To achieve this, we conduct a series of experiments using wing models with varying span-wise lift distributions in the ONERA towing tank. In doing so, we aim to address some unresolved questions regarding how the load profile affects the dynamics of vortex wakes.

In the initial set of experiments, we studied the wake of a plain rectangular wing, modeling an aircraft in cruise flight configuration. A second set of experiments involved studying the impact of shape modifications inspired by recent stability analysis results. In the third set of experiments we modified the span-wise evolution of the geometric twist to create configurations resembling landing/take-off scenarios. The fourth set of experiments allowed us to investigate the physical interaction between co-rotating and counter-rotating vortices. These findings not only contribute to our understanding of vortex behavior but also provide experimental data to validate numerical models designed to develop control strategies. In this way we contribute to the objective of wake hazard alleviation.

This work is structured in seven chapters. We present a summary of the knowledge that is pertinent to our study of trailing vortices dynamics in Chapter 2. In Chapter 3, we describe the materials and methodologies that were employed to conduct our experiments.

Chapter 4 focuses on characterizing the wake physics under nominal conditions at significant downstream distances, providing insight into the full-scale flow in the laboratory frame. In section 4.1, we validate the representativeness of the towing tank experiment by characterizing the aerodynamic response of the wing model. In section 4.2, we develop a methodology for computing the vortex characteristics since they are indicators of physical phenomena occurring in the flow. To do this, we identify the vortex field center and derive a mean 1D vortex profile from the 2D velocity field. The objective in section 4.3 is to identify physical phenomena within the vortices of the experiment. Lastly, in section 4.4, we explore the impact of a modification in the wing's trailing edge which is inspired by stability analysis results and seeks to accelerate the decay of trailing vortices.

Chapter 5 investigates the wake of a wing modified to mimic a flaps-down configuration. This geometry is of interest because of its direct application to commercial aircraft wing configurations during landing/take-off. This introduces co-rotating vortices in the wake. Therefore, we focus first into characterizing the co-rotating pair properties from their generation until their fusion in section 5.3.2.2. Then we assess how the wing geometry modification impacts the trailing vortices. In section 5.3.3 the properties of a fused vortex are compared with those obtained previously for the reference wing configuration.

We know that rather than co-rotating vortex pairs, the most effective mechanism for vorticity diffusion in the wake results from the interaction between wing-tip vortices and counter-rotating flow. This is why Chapter 6 explores the wake of a wing modified to introduce counter-rotating vortices. First, in section 6.1 we model the behavior of the pair via point-vortex simulations, in order to adapt our experimental installation to this particular flow. Subsequently, in section 6.2, we relate the experimental observations to the vortex pair properties, comparing them to analytical predictions. Finally, in section 6.3, we analyze the temporal evolution of both the flap and the wing-tip vortices to assess the impact of the counter-rotating configuration on vorticity diffusion. We present concluding remarks and a discussion of our results in Chapter 7.1.

## Chapter 2

# Literature Review

*More work is needed on [...] the development of guidelines for the design of aircraft so that they shed benign wakes. Admittedly, a satisfactory solution has not yet been found, but the research to date indicates that a solution is possible.*  
- V. Rossow [87]

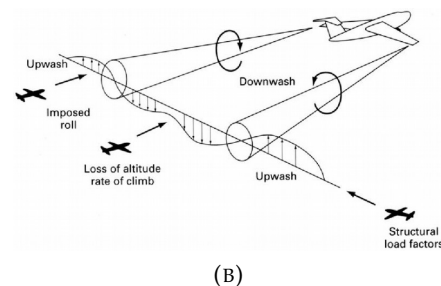
### 2.1 The wake vortex hazard

On the domain of safety in commercial aviation, one of the main challenges consists on the hazard that wake vortices of leading aircraft represent for a following aircraft. The problem is that wake vortices dissipate on a long time scale. As a consequence, air traffic is slowed down by safety regulations.

The terms "trailing vortices" or "vortex wake" refer to the rotating air masses that form, as an indirect consequence of lift, behind any lifting surface. Behind every aircraft, the far wake takes the form of two counter rotating vortex columns (Fig. 2.1a) for which the strength is indirectly proportional to the weight of the generating plane : the wings of a heavy aircraft need to generate strong lift forces and consequently generates strong vortices. As such, this wake is particularly dangerous when an aircraft encounters the wake of a large and wide-bodied civil jet. As illustrated on Fig. 2.1b, downwash forces or a rolling moment can be induced on an aircraft that encounters trailing vortices. These forces can compromise the pilot's control over the aircraft, and lead sometimes to fatal accidents. The risk of wake encounter therefore regulates air traffic in-flight and close to airports.



(A)



(B)

FIGURE 2.1: Trailing vortices : a) Contrail visualization behind an aircraft in the 'HEAVY' category and b) effects of a wake encounter on a following aircraft (from Rossow [87]).

The need for safety regulations arose in the late 1960s with the commercialization of "jumbo jets" which shared the airspace with lighter aircraft. The vortices generated by an aircraft close to a runway creates a zone of danger in parallel runways less than 760 m apart or crossing runways less than 300 m below (see Fig. 2.2 for an illustration). To prevent wake encounters, rules on safety distances between a leading and a following aircraft were established since 1970 by the International Civil Aviation Organization (ICAO). A *safe separation minimum*, as defined by EUROCONTROL [84] "implies to consider wake vortex generated by an aircraft but also the wake encounter impact and resistance of the following aircraft on departure or final approach". These rules were originally based on the aircraft maximum take-off mass (MTOM). After classifying aircraft into different MTOM categories, the ICAO issued minimum separation distances for each combination of weight category.

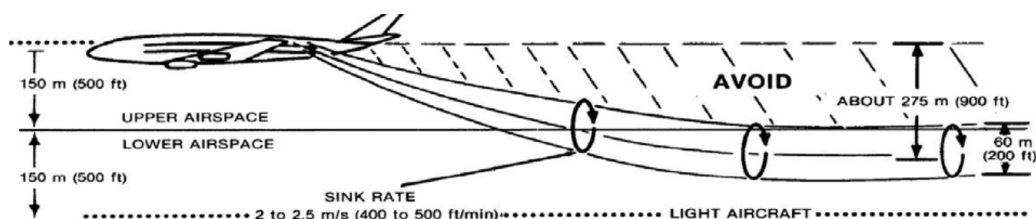


FIGURE 2.2: Dangerous zones for a wake encounter as presented by the ICAO [42]

Due to a saturation in commercial air traffic and airport capacity, the design trend of the aviation industry is to fabricate civil aircraft models with greater passenger capacity. The first set of separation rules, designed 50 years ago, became outdated when civil aircraft of even larger MTOM were commercialized [84] (eg. the A380 model). On one hand, the danger represented by a wake encounter is increased giving that the MTOMs of some models are larger and the flight paths are more frequently occupied. But on the other hand, ICAO rules led to over-conservative safety measures when the encountering airplane was on the upper limit of its weight category. It is now known [38, 69] that besides weight, other parameters play a role when defining the strength of the vortices and the encountering plane response. The hazard caused by a vortex on a following aircraft may be estimated by "hazard models" that take these parameters into consideration [14]. The generating aircraft swept, wingspan and spanloading have an impact on the number of vortices, their orientation, sense of rotation etc. [87, 93]. For the aircraft that encounters the wake, its wingspan and weight but also the pilot reaction time are taken into account in the hazard model [14]. As aircraft models and our understanding of trailing vortices evolve, separation rules are revisited and updated. For example, a re-assessment of aircraft weight categories leading to new separation times were proposed for European airports under the RECAT-EU [84] program in 2015, showing that the strategies of wake hazard prediction and alleviation are as relevant now as when they were first studied in the late 60's. With the popularization of flow control strategies, contemporary research now turns towards ways of hastening the decay of trailing vortices, effectively reducing the danger they pose, in the hope of establishing new, less constrained flight path regulations [34].

As described by Rossow [87], research efforts around wake hazard focus on three main questions : 1. Quantifying the hazard represented by the lift-generated wake shed by a given aircraft, 2. modifying the wake to make it non-hazardous while

still retaining the efficiency of the generating aircraft and 3. effectively and efficiently avoiding vortex wakes. Relative to 1., at the present time, for a given lift, it is possible to predict the strength of vortex wakes generated by simple wing configurations [1, 87]. The downwash or rolling moments induced on a given aircraft by the trailing vortices are also well estimated [88]. However, there is still not enough knowledge to propose a universal model that predicts (under given conditions of Reynolds number, wing configuration, ground proximity, vortex interactions..) the decay of wingtip vortices over time. This dulls the estimation of the hazard represented by the far-field wake which is necessary to propose optimal separation times. The knowledge necessary to address subject 2. relates to the impact of the wing configuration on the structure and stability of the wake. A promising approach consists in playing on the dynamics intrinsic to systems of two or more co- or counter-rotating vortices. To study this problem requires to reliably predict the number and strength of vortices that can be expected to form in the near wake of the wing. For wings of complex configurations (like those of commercial aircraft), there is still no agreement on an analytical model that serves this purpose, so the the problem can only be approached through numerical simulations (e.g. RANS). Although cooperative instabilities have been well studied over the last decades, there is still not an efficient control strategy that could be applied on the wing surface to excite these mechanisms further downstream. Finally, regarding subject 3., the challenge is to estimate the trajectory of hazardous vortices in the wake. This is easily addressed by simple approaches like the Biot & Savart model as it will be seen further down. There is also extensive documentation on the possible ways a vortex can behave when subjected to external phenomena like ground proximity, crosswind and atmospheric stratification or turbulence. Here again predicting the decay characteristics of the vortices is essential to apply these models to the far wake. Nevertheless current models are in agreement over the region of higher danger for wake encounters : At one wingspan above the ground, the descent of the vortex pair stalls, aggravating the chances of an encounter [38]. If an aircraft encounters the wake of another aircraft at low altitude, it will have little speed, altitude and reaction time to recover from the downwash force or the rolling moment imposed by the vortex wake [42]. This is why the characteristics of the wake of a wing in landing/take-off configuration is of interest for our purposes.

## 2.2 From the formation to the natural demise of a trailing vortex

As opposed to a simple wake (which is when viscous flow attaches to a body and generates drag), the *vortex wake* is a product of the flow around a lifting body (and therefore linked to induced drag). This is why when considering the flow around an aircraft, the origin of the vortex wake can be traced to the flow shed by its lifting surfaces : mainly the wing, the horizontal stabilizer and, to a lesser amount, the fuselage. The engine exhaust gases also impact the vortices velocity and thermodynamic characteristics, but this effect is neglected for the purposes of this work.

Four basic phases for the lifespan of the vortex wake are distinguished. These phases are illustrated in Fig.2.3 and are detailed on the following sections. First, there is a *zone of formation* where the vorticity shed from the lifting body concentrates into discrete groups which constitute the vortices in the near wake. Secondly, there is a *stable zone* where the numerous vortices in the wake may fuse to form a main dipole of counter-rotative vortices. As it is detailed further down, vortices in this

zone have the form of coherent vortex tubes and at first order their dynamics can be estimated from those of a 2D dipole of point vortices. An *unstable zone* ensues where the vortex tubes deform under the action of tridimensionnal effects and/or physical instabilities. To predict the behavior of such mechanisms requires the introduction of models of 3D vortex tubes with a finite core. The magnitude of the deformations of the vortices usually increases until vorticity can be exchanged between each side of the wake. This exchange is referred to as "vortex linking" and marks the end of the unstable zone. Finally, during the *vortex breakdown zone*, vortex rings develop from the linked vortices. Rings eventually disperse through mechanisms like bursting. Although vorticity is still present in this zone, the beginning of linking is often considered to mark the end of the lifespan of the vortex wake.

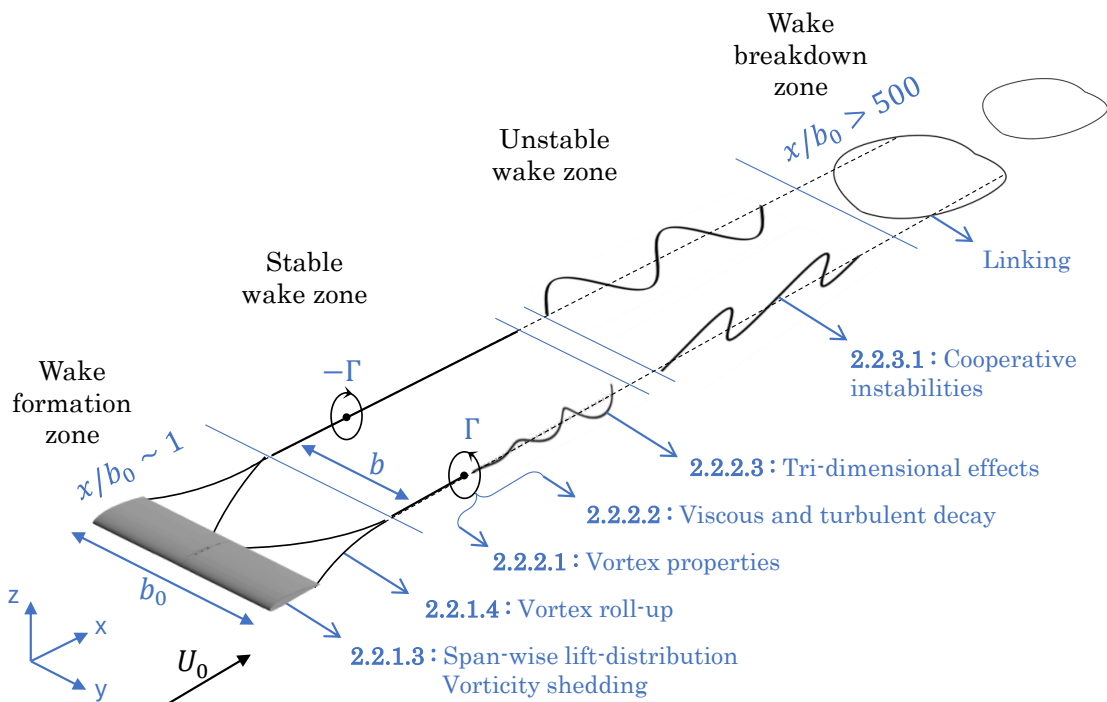


FIGURE 2.3: Schematics of the evolution phases of an aircraft vortex wake. Various phenomena occurring in the wake are schematized. The paragraphs in this text corresponding to each phenomena are indicated.

In the upcoming sections, challenges essential to understanding vortex dynamics are broken down. These challenges are defined following guidelines of previous work, like that of Donaldson and Bilanin [26]. The insights provided by the study of physical phenomena related to each of these topics form the heart of our study on vortex hazards. In section 2.2.1, the first challenge is tackled : predicting how vortex sheets roll up in the "formation zone". The focus is on understanding the behavior of vorticity shed at the wing trailing edge through an analytical approach. Moving on, we explore the second issue: the interactions between these vortices in the "stable zone". To do this the physics of a single vortex are studied in section 2.2.2. The characteristics of a vortex right after formation are first defined and then its evolution over time is studied. This includes studying how viscous and turbulent transport mechanisms affect the diffusion of the vortex core, and what impact 3D

deformations have on a single vortex tube.

Lastly, section 2.2.3 focuses on the fundamentals of how a pair of trailing vortices interact. This includes addressing the field of rolling moment and downwash they might induce on a following aircraft, which constitutes the essence of the wake hazard. Understanding the interaction between the two trailing vortices allows to address the "unstable zone" of the wake where physical instabilities develop. In short, the upcoming sections provide a comprehensive exploration of the core physics of a vortex wake composed of two trailing vortices.

## 2.2.1 The formation of vortex wakes

### 2.2.1.1 Fundamental properties of vorticity

In this section, we describe the fundamental concepts necessary for the study of vortical flows. A concrete definition of vorticity and a basic vortex model are provided. The extent of the description for the concepts listed here is purposely limited to what is strictly useful for the argumentation of the following sections. The reader who wishes further details is referred to [90].

Consider the velocity field  $\mathbf{u}$  written  $(u, v, w)$ . The *vorticity*  $\boldsymbol{\omega}$  is the gradient of the velocity profile along a perpendicular direction, that is

$$\boldsymbol{\omega} = \nabla \times \mathbf{u} \quad (2.1)$$

The rate of change of  $\boldsymbol{\omega}$  can be obtained by applying the same operator to the Navier-Stokes equations

$$\frac{D\boldsymbol{\omega}}{Dt} = (\boldsymbol{\omega} \cdot \nabla)\mathbf{u} + \nu\Delta\boldsymbol{\omega} + \frac{\nabla \times \mathbf{f}}{\rho} \quad (2.2)$$

Which is known as the Helmholtz equation [39]. Here,  $\frac{D}{Dt} = \frac{\partial}{\partial t} + (\mathbf{u} \cdot \nabla)$ ,  $\nu$  is the fluid kinematic viscosity and  $\rho$  its density. The term  $(\boldsymbol{\omega} \cdot \nabla)\mathbf{u}$  is a source term that accounts for tridimensional effects like the stretching or tilting of vorticity. The second term,  $\nu\Delta\boldsymbol{\omega}$  translates the diffusion of vorticity under the action of viscosity, and the last term,  $\frac{\nabla \times \mathbf{f}}{\rho}$  translates the action of non-conservative body forces. The Helmholtz equation shows that pressure and conservative body forces have no incidence on the evolution of vorticity. Furthermore, in the absence of non-conservative body forces the third term vanishes. In 2D flow the source term also vanishes which leads to the key conclusion that, in this specific scenario, vorticity only decays through viscous effects.

For a velocity field located in the 2D plane defined by cartesian coordinates  $(y, z)$ , it follows from eq. 2.1 that the vorticity perpendicular to this plane is written

$$\omega_x = \partial_y w - \partial_z v \quad (2.3)$$

Consider now two nearby material points  $A$  and  $B$ . Their difference in velocity and position is  $\delta\mathbf{u} = \mathbf{u}_B - \mathbf{u}_A$  and  $\delta\mathbf{x} = \mathbf{x}_B - \mathbf{x}_A$ , therefore

$$\delta u_i = \mathbf{u}_B - \mathbf{u}_A|_i = \sum_{j=1}^3 \frac{\delta u_i}{\delta x_j} \delta x_j = \delta_j u_i \delta x_j \quad (2.4)$$

where the term on the right is  $\delta u_i$  expressed in einstein's notation. Equation 2.4 can be written as

$$\delta u_i = \frac{1}{2} (\delta_i u_i + \delta_i u_j) \delta x_j + \frac{1}{2} (\delta_i u_i - \delta_i u_j) \delta x_j \quad (2.5)$$

$$\delta u_i = e_{ij} \delta x_j + \Omega_{ij} \delta x_j \quad (2.6)$$

Here,  $e_{ij}$  is denoted the *rate of strain tensor* and  $\Omega_{ij}$  the *rotation tensor*. The strain tensor is symmetric and diagonalizable and expresses a deformation. If one denotes its eigenvalues as  $\lambda_i$ , then  $\lambda_i > 0$  can be classified as a stretch and  $\lambda_i < 0$  as a compression. As its name indicates, the tensor  $\Omega_{ij}$  expresses a rotation in  $\mathbf{u}$ . It is characterized by the scalar  $\Omega$  which is the rate of rotation. In other words, under straining motion, line elements are extended or contracted and spheres are deformed into polygons with the principal axes along those of the tensor  $e_{ij}$ . Under solid body rotation motion, line elements stay of constant length, spheres remain spheres while rotating with angular velocity  $\Omega r$ .

Having defined the vorticity, the strain and the rotation, we can now describe two fundamental flows denoted as solid body rotation and potential flow. Consider the velocity field  $\mathbf{u}$  written in polar coordinates as  $\mathbf{u} = (v_r, v_\theta, v_x)$ . On one hand, solid body rotation is a rotational flow that does not entail a deformation. This can be exemplified by a field such that

$$\mathbf{u}(\mathbf{x}) = \begin{cases} v_r & = & 0 \\ v_\theta & = & \Omega r \\ v_x & = & 0 \end{cases} \quad (2.7)$$

$$\boldsymbol{\omega}(\mathbf{x}) = \frac{1}{r} \frac{\partial}{\partial r} (r v_\theta) = 2\Omega \mathbf{e}_x \quad (2.8)$$

On the other hand, an example of potential flow is a field such that

$$\mathbf{u}(\mathbf{x}) = \begin{cases} v_r & = & 0 \\ v_\theta & = & \frac{\Gamma}{2\pi r} \\ v_x & = & 0 \end{cases} \quad (2.9)$$

Here,  $\Gamma$  is the circulation of  $\mathbf{u}$  around a closed circle  $\mathcal{C}$  of radius  $R$ . It is defined in general terms as the line integral of the velocity field around any closed curve  $\mathcal{C}$ . Invoking Stoke's theorem, we can in turn link  $\Gamma$  to the flux of vorticity through the disc  $\mathcal{D}$  bounded by  $\mathcal{C}_{(r)}$ , we get :

$$\Gamma = \oint_{\mathcal{C}_{(r)}} \mathbf{u} \cdot d\boldsymbol{\ell} = \iint_{\mathcal{D}_{(r)}} \boldsymbol{\omega} \cdot n dS \quad (2.10)$$

Note that, considering  $\mathbf{u}$  defined in 2.9, we have

$$\oint_{\mathcal{C}_{(r)}} \mathbf{u} \cdot d\boldsymbol{\ell} = \int_0^{2\pi} \frac{\Gamma}{2\pi r} \mathbf{e}_\theta \cdot r d\theta \mathbf{e}_\theta = \Gamma \quad (2.11)$$

It follows that in this example of a potential flow, vorticity is focused at  $\mathbf{x}_\omega = (0, 0, 0)$  and defined by :

$$\boldsymbol{\omega}(\mathbf{x}) = \frac{1}{r} \frac{\partial (r v_\theta)}{\partial r} \mathbf{e}_x = \frac{1}{r} \frac{\partial (\Gamma/2\pi)}{\partial r} \mathbf{e}_x \quad (2.12)$$

which is 0 at every point except at  $\mathbf{x}_\omega$ , where  $\omega_x(\mathbf{x}_\omega) = \Gamma \delta(y) \delta(z)$  and  $\delta(\cdot)$  is the Dirac function. The regions of the fluid where  $\boldsymbol{\omega}(\mathbf{x}) = 0$  are said to be in irrotational

motion. Computing the strain tensor for  $\mathbf{u}$  results in a strain rate of  $|e_{r\theta}| = \left|\frac{\Gamma}{2\pi r^2}\right|$ , which defines a stretching direction and a compression direction which are both located in  $(r, \theta)$  and are orthogonal to each other.

We dispose now of sufficient concepts to define a fundamental vortex model, named Rankine vortex. Here, the flow field  $\mathbf{u} = (0, v_\theta, 0)$  is discontinuous around a region defined by  $r = R_a$ .

$$\omega_x(r) = \begin{cases} \Omega & r \leq R_a \\ 0 & r > R_a \end{cases} \quad (2.13)$$

Substituting  $\Omega = \frac{\Gamma}{2\pi R_a^2}$ , we obtain

$$\mathbf{u}(\mathbf{x}) = \begin{cases} v_r = 0 \\ v_\theta(r) = \begin{cases} \frac{\Gamma}{2\pi R_a^2} r & r \leq R_a \\ \frac{\Gamma}{2\pi r} & r > R_a \end{cases} \\ v_x = 0 \end{cases} \quad (2.14)$$

This vortex model is characterized by two regions delimited by  $R_a$ , also called the vortex core size. A solid body rotation flow occurs in the inner region while a potential flow occurs in the outer region. Note that this model is inviscid and shows no axial velocity. Azimuthal velocity  $v_\theta$  is continuous at  $r = R_a$ , but axial vorticity is not as  $\omega_x(r)$  is finite and uniform inside of the vortex core and null outside. Although this discontinuous nature is not physical, the Rankine model is widely used because of its simplicity and allows for the analytical study of multiple physical properties of natural vortices. Indeed, the Rankine model is sufficient for the purposes that are developed in the following sections, and more complex vortex models are introduced further down as the need for them arises.

Consider a region of fluid where vorticity is not null everywhere. A curve parallel to the vorticity vector  $\boldsymbol{\omega}(x, t)$  in each of its points is called a vortex line. A set of vortex lines which intersect a path is denoted as a vorticity surface or vorticity sheet. If this path is closed then the surface defines a vorticity column. By construction vorticity is everywhere parallel to the surface of the column i.e.  $\boldsymbol{\omega} \cdot \mathbf{n} = 0$ . From this, it can be shown that the flux of vorticity through any cross-section of the column is constant [90].

$$\int_{S_1} \boldsymbol{\omega} \cdot \mathbf{n} dS - \int_{S_2} \boldsymbol{\omega} \cdot \mathbf{n} dS = \int_V \text{div}(\boldsymbol{\omega}) dV = 0 \quad (2.15)$$

where  $V$  is a volume delimited by the two cross sections of the column  $S_1$  and  $S_2$ . The strength of the column is defined by the circulation computed along a closed curve on the column. This is equal to the flux of vorticity along the column. From these results we deduce that **the circulation is uniform along the column**. On most cases, this in turn implies that vortex columns must be closed or begin and end on boundaries [90]. A vortex filament is defined by a column surrounded by irrotational fluid. For practical purposes in this work, we shall extend this definition to any vortex column of infinitesimal thickness as it has been done before [Helmoltz1858]. It should be noted that **viscosity diffuses vorticity**, which at first approach contradicts the assumption of surrounding irrotational fluid, however the definition of vortex filament is still useful in real fluids of small viscosity [90], i.e.

$$Re_\Gamma = \frac{\Gamma}{\nu} \gg 1 \quad (2.16)$$

Where  $\nu$  is the kinematic viscosity and  $Re_\Gamma$  is the circulation based Reynolds number

which is further defined below. Finally, it should be said that in the analytical studies that are described in the following sections, most referrences of vortices imply a vortex filament in 3D space.

At this stage we have provided a concrete definition of vorticity  $\omega$  and of circulation  $\Gamma$  and we have provided a fundamental vortex model, named the Rankine vortex, where two separate regions are characterized by a different type of flow. In the inner region of the Rankine vortex ( $r \leq R_a$ ) the flow is of type solid body rotation. This means that the rotation rate is finite and the strain rate null. The vorticity is uniform of value  $\omega(x) = 2\Omega e_x$ . In the outer region ( $r \geq R_a$ ) we have a potential flow, also called irrotational flow. This means that the rotation rate is null and the strain rate is finite. Orthognal directions of stretching and compression are embedded in the plane of the vortex. The vorticity is null at every point of this region i.e.  $\omega(x) = 0$ . Then, we defined a vortex filament which is a particular distribution of vorticity. The strength of a filament is defined by the circulation around a closed path surrounding it. Finaly, we showed that the strength of the filament is uniform at any of its stations, albeit in real cases one must also account for the diffusive action of viscosity. In the following section, we use these concepts to show how an immersed body may generate trailing vorticity.

### 2.2.1.2 The generation of vortex sheets around a body

Consider a vorticity sheet in which vorticity is infinite. From the point of view of velocity, this is a surface in which the tangent component of velocity is discontinuous. This constitutes a fundamental block to understand the generation and roll-up of vortices in the near wake of a lifting wing.

Let  $\mathbf{u} = (0, v, 0)$  be a mixing layer flow perpendicular to  $e_x$ :

$$\mathbf{u}(x) = \begin{cases} v_1 e_y & z > 0 \\ v_2 e_y & z < 0 \end{cases} \quad (2.17)$$

The flow is discontinuous along direction  $e_y$  if  $v_1 \neq v_2$  and this discontinuity layer implies that vorticity is infinite at  $z = 0$ . The plane  $(x, y, z = 0)$  defines a vorticity sheet where :

$$\omega(z = 0) = \delta(z) \gamma_\omega \quad (2.18)$$

Here,  $\gamma_\omega = |\gamma_\omega|$  is finite and it is the sheet intensity. Furthermore  $\gamma_\omega \cdot \mathbf{n} = 0$  where  $\mathbf{n} = e_z$ . By considering the computation of circulation round an infinitesimal contour that traverses the vorticity sheet, one can show that

$$\mathbf{u}(z < 0) - \mathbf{u}(z > 0) = \gamma_\omega \times \mathbf{n} \quad (2.19)$$

which implies that the flow is discontinuous in the tangent direction, but continuous in the normal direction. The conitnuity in the normal direction can also be seen as a consequence of the conservation of mass [90].

We choose now to replace the fluid plane  $(x, y, z = 0)$  by a solid plane. The hypothesis of tangent discontinuity and normal continuity in this model still hold in this situation which reveals its utility when studying the generation of vortex sheets. Consider then a 2D material plate normal to  $e_z$  and extending from  $y = -a$  to  $y = +a$  and from  $x = -\infty$ , to  $x = +\infty$ . The plate is in motion in the normal direction  $e_z$  and therefore a velocity field  $\mathbf{u}$  is generated around it. This problem can be solved, as done by Batchelor [4] or Saffman [90], to determine the strength of the

vortex sheet that the represented by the discontinuity that the plate introduces :

$$\gamma_\omega = \frac{2U_y}{\sqrt{a^2 - y^2}} \quad (2.20)$$

where  $U_y$  is the boundary condition of velocity at  $z = 0$  and  $|y| < a$ . This goes to show that the vorticity is maximum (infinite) at the extremities of the plate. The shape of the sheet is however maintained as the plate is infinite in the  $e_x$  direction. Arguments brought by Klein [49] stated that if the plate were to be removed, then the vorticity sheet would remain. The vorticity sheet, which behaves as a material line, is then free to evolve under its own induced velocity. We can then model the evolution of such a material line through a 2D spiral sheet model proposed by Kaden [47].

Through this model, one can show that the shape of the vorticity sheet evolves from a straight line into a spiral, entraining more of itself and becoming nearly axisymmetric. The sheet stretches during this process, so that fluid particles that were close to each other on the straight sheet become separated by an angle of  $2\pi$ . In other words, each section of the sheet tends to form concentric circles around the spiral's tip, with the sheet's strength being highest at the center and decreasing with increasing radius  $r_p$ . The gap between neighboring circles is proportional to  $r_p/t$ , and thus tends to close-in over time. In the absence of viscosity, the sheet becomes infinitely thin, but in real flows viscosity smoothens the velocity differences between closely spaced circles. This leads to the sheet transitioning from a spiral shape to a compact region of vorticity with decreasing strength inversely proportional to radius, and where velocity evolution is continuous.

### 2.2.1.3 The generation of trailing vorticity in the near wake of a wing

In the previous section it was shown that each side of an unbound vorticity sheet of finite length stretches and spirals around its neighbouring tip of the sheet. It was also shown that this situation can be analytically modeled by an discontinuous velocity field generated around an infinite plate in motion. In this section, we relate this model to a more representative model of the flow field generated around a lifting body. Specifically, the flow around a rectangular wing is analyzed in order to show that a vorticity sheet is shed at its trailing edge and that subsequently the sheet evolves into two counter rotating trailing vortices. Also, a link is established between the load distribution over the wing and the velocity distribution of the trailing vortex generated.

We provide here an illustration of the formation of vorticity sheets at the trailing edge of a wing starting from the distribution of pressure around a lifting surface. This is a common reasoning found in the literature, here we follow the guidelines of Prandtl [78] and Glauert [35]. For a classical wing where the distribution of lift is maximum at the mid-span, it follows that above and below its spanwise center there is, respectively, a large decrease and a large increase of pressure. At the tip of the wing, where the local lift vanishes, the pressure differences is also null, resulting in a monotonic decrease of pressure difference from the mid-span to the wingtip. Following this pressure distribution, streamlines passing above the wing tend to flow inwards towards the center while those passing below have a tendency to flow outwards. This scenario is illustrated on Fig. 2.4. At the trailing edge, where the streamlines meet, a discontinuity of direction forms between the streamlines coming from the pressure side and those coming from the suction side of the wing. The

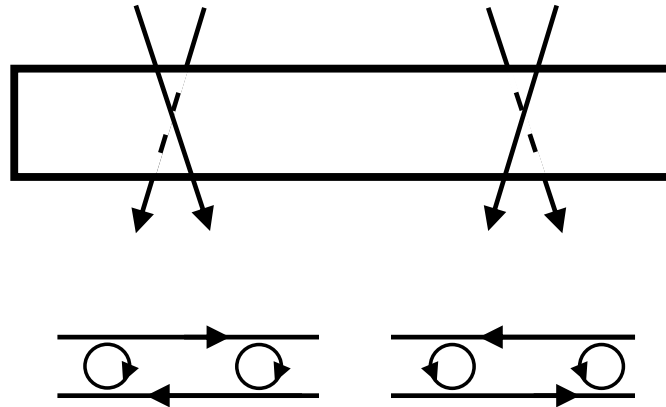


FIGURE 2.4: From [35] : surface of streamline direction discontinuity at the trailing edge of a wing.

surface of discontinuity thus formed generates a vorticity sheet shed by the lifting surface. This sheet can further be modeled as a series of adjacent axial vortex lines of different strength that reside on the sheet plane. An illustration of this is provided further down in Fig. 2.6b. Note that the relative velocities inward and outward of the flow at the trailing edge are perpendicular to the mean velocity. Indeed, from Bernoulli equation it can be shown that the numerical values of velocities in the two layers must be equal in the absence of a pressure difference between them [78]. Thus the relative velocity is greater with a greater spanwise pressure gradient, i.e. the greater the spanwise change of lift.

Having established the relationship between the strength of the shed vortex line and the spanwise change of lift over the airfoil, we now address the spanwise distribution of lift along the wing. In other words, we wish to determine the spanwise distribution of lift along the span of a wing moving in a quiet fluid at a velocity  $U_0$  and at a geometric angle of attack  $\alpha$ . To do this, Prandtl's lifting line theory is applied. Our description of lifting line theory follows guidelines of Prandtl [78] and of Anderson [2].

The fundamentals of this theory is that the phenomena of lift implies the existence of a descending flow in the neighborhood of the wing and this induces an effective angle of attack and an additional component of drag, called induced drag. Indeed, the flow around the wing is modified by the vorticity close to its trailing edge. This modification of the flow is then a function of the span-wise station but also of the chord-wise station. However, in the simplest model, the cordwise dependency is neglected. This results in the so-called lifting-line model. We model a wing of finite span as a line of bound vorticity (see Fig. 2.5 for an illustration). This line exerts on the fluid the same forces as a lifting wing. In practice, Prandtl argued that on a real wing of high aspect ratio, the lift is concentrated on a narrow region close to the leading edge, further supporting the line approximation.

The lifting line theory is now described. This theory focuses on the vortex filaments shed from finite wings. Particularly near the trailing edge, the filaments can be considered to be straight, since vorticity that is further downstream has a negligible effect on the flow around the wing (see Fig. 2.6b for an illustration). A model of an infinitely long wing can be drawn analogous to the finite lifting line. The infinitely long wing, however, generates rectilinear flow without shedding downstream vorticity. The vortices shed from the lifting line induce a downwash current,

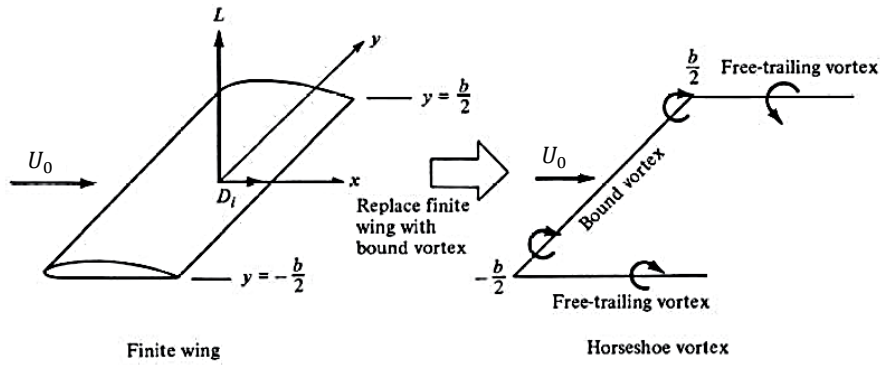


FIGURE 2.5: From [2] : Replacing a rectangular finite wing with a line of bound vorticity.

necessitating an increased angle of attack to maintain lift (see Fig. 2.6a). This effective angle thus obtained is the same as that of the infinite wing. This phenomenon is quantified by the normal velocity,  $w_i$  induced by the bound vorticity line, leading to an induced angle of attack  $\alpha_i$  :

$$\alpha_i(y) = w_i(y)/U_0 \tag{2.21}$$

Flow angles at the spanwise section  $y$  are therefore defined by the section twist  $\Theta$ , the free-stream direction  $\alpha$  and by  $\alpha_i(y)$ . The resulting 2D incidence seen by the wing section is

$$\alpha_{2D}(y) = \alpha - \alpha_i(y) + \Theta(y) \tag{2.22}$$

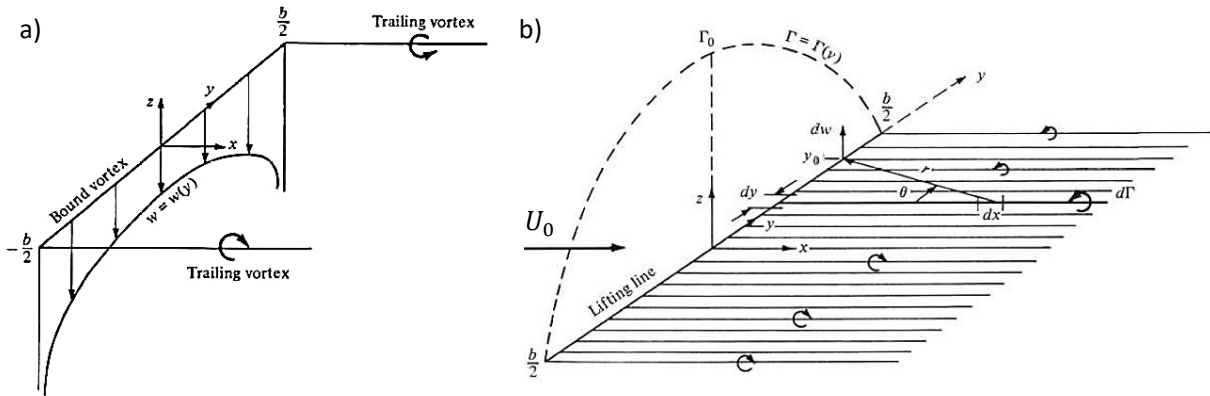


FIGURE 2.6: From [2] : Schematics of the lifting line model, **a)** Downwash distribution along the span-wise axis for a horseshoe vortex and **b)** superposition of an infinite number of horseshoe vortices along the lifting line.

Following the Kutta-Jukowski result, the bound circulation  $\Gamma(y)$  can then be related to the 2D lift coefficient of the wing section and in turn to the flow incidence.

$$C_z^{2D}(y) = C_{z,\alpha}(\alpha_{2D}(y) - \alpha_0) = \frac{2\Gamma(y)}{U_0 c} \tag{2.23}$$

where  $C_{z,\alpha}$  and  $\alpha_0$  are aerodynamic characteristics of this airfoil profile.  $C_{z,\alpha}$  is the lift slope and  $\alpha_0$  is the airfoil section zero lift angle of attack. This equation leads to

$$\Gamma(y) = \frac{1}{2}U_0cC_{z,\alpha}(\alpha - \alpha_i(y) + \Theta(y) - \alpha_0) \quad (2.24)$$

Following this, the aerodynamic force is tilted from the same angle and its projection on the direction of the flight is now an induced drag. Therefore with greater lift and with vortices closer to the middle of the wing, the downwash is greater and so is the induced drag.

Regarding the strength  $\gamma_\omega(y)$  of the vortex filament shed at a given spanwise station, it was also previously shown that it is related to the bound vorticity (the lifting line of local strength  $\Gamma(y)$ ) as variations on  $\Gamma(y)$  :

$$\gamma_\omega(y) = -\frac{d\Gamma(y)}{dy} \quad (2.25)$$

Considering the relation 2.25 when integrating equation 2.24 over the wingspan, one can obtain the fundamental equation of the lifting line theory [77].

$$\frac{2\Gamma(y)}{U_0c(y)} + \frac{C_{z,\alpha}}{4\pi U_0} \int_{-b/2}^{b/2} \frac{1}{y-\zeta} \left(\frac{d\Gamma}{dy}\right)_{y=\zeta} d\zeta = C_{z,\alpha}[\alpha - \alpha_0 + \Theta] \quad (2.26)$$

The only unknown in this equation is the section circulation distribution  $\Gamma(y)$ . This equation can be solved if the distribution is written as a Fourier series. Let  $s$  be the semi-span and  $y$  the span-wise distance from the wing root, the position is mapped by the angle  $\theta \in [0, \pi/2]$ . Using the change of variables  $y = s\cos(\theta)$  one obtains :

$$\Gamma(\theta) = 4sU_0 \sum_{n=1}^{\infty} A_n \sin(n\theta) \quad (2.27)$$

where  $\theta = \cos^{-1}(-2y/b)$ . In eq. 2.27 we define  $n$  distribution coefficients  $A_n$  that can be computed from the surface flow boundary condition of null normal flow.

Methods to solve this computation were published as early as 1926 [35]. In summary, one can compute the bound vorticity strength from eq. 2.27 to obtain *in fine* an expression for the induced downwash velocity as Fourier series. By truncating the result to the  $N$  first coefficients of the series (assuming that subsequent coefficients are negligible) and applying it to  $N$  different wing span positions, one can compute the  $A_n$  ( $n \in [1 : N]$ ) coefficients with a set of  $N$  linear equations. The resulting equation contains all the information on the section geometry and flow characteristics, and can therefore be used to evaluate the loading profile of any given wing geometry, provided the wing aspect ratio is large enough. The theory allows to account for the effect of flaps.

From the coefficients obtained the  $C_z$  and  $C_x$  can be computed. The total lift is computed from the first coefficient  $A_1$ , and the induced drag is dependent of higher order coefficients. Therefore, the lifting line theory can be applied to deduce a geometry that minimises induced drag. We illustrate this procedure following guidelines from Saffman [90]. A "light loading" approximation is employed so that the trailing

vortex filaments are assumed to be parallel to the undisturbed flow. From the Biot-Savart formula, the downwards induced velocity is

$$w_i(y) = \frac{1}{4\pi} \int_{-b/2}^{+b/2} \frac{d\Gamma(y')}{dy'} \frac{dy'}{y - y'} \quad (2.28)$$

for  $y \in [-b/2; +b/2]$ . Furthermore, by using the Kutta formula the induced drag can be computed

$$F_{x,i} = \int_{-b/2}^{+b/2} w_i(y) \Gamma(y) dy \quad (2.29)$$

It can be then shown that the induced drag, for a given lift, is minimum for

$$\Gamma(y) = \Gamma_0 \left(1 - \frac{4y^2}{b_0^2}\right)^{1/2} \quad (2.30)$$

which is known as the elliptic loading law.

The elliptic loading is a subject that is well understood and one possible wing geometry to achieve it is known to be also of elliptic planform. However, for the purposes of this work it is worth mentioning that the lift distribution of a wing of rectangular planform and moderate aspect ratio does not deviate greatly from the elliptic loading type. This is a result first found by Prandtl [78]. The theoretical drag for usual aspect ratios is at most 5% greater than the elliptic type.

In summary, in this section we have established that the span-wise lift distribution on the wing relates the wing geometry to the downwash that the wing introduces in the flow downstream. In the following section the models and real life observations made on the roll up of such vortex sheets are analyzed as these precede the formation of the trailing vortices and their evolution in the stable wake zone.

#### 2.2.1.4 The roll-up of trailing vorticity in the near wake of a wing

As shown above, the distribution of vorticity trailing behind a wing is related to the flow around the wing, in particular to the wing spanwise distribution of lift. Furthermore, the analytical model of the Kaden's spiral (briefly described in sec. 2.2.1.2) proves that a free semi-infinite vortical shear layer has a natural tendency to roll up into two concentrated vortices. In this section these two points are connected to characterize the roll up of vorticity trailing behind a wing through analytical arguments and experimental observations. The models discussed here differ from that of Kaden's spiral in that they include more of the physics specific to classical wings.

Here, the overall objective is to model the wake formation zone in a way that is applicable to the real life scenario of the vortex wakes of aircraft and to those we will encounter in our experiments. Specifically, we wish to determine the spacial distribution of the vorticity during the wake formation zone : This refers to the downstream distance from the wing trailing edge to a station that could be characterized as the "end" of roll-up and also refers to the span-wise distance between the two vortices formed.

The first attempt consists in estimating the distance downstream at which the vortex sheet can be considered to be *essentially* rolled-up. This is done through a dimensional analysis following guidelines described by Donaldson & Bilanin [26] and also by Spreiter & Sacks [94].

Consider a wing of span  $b_0$  and root circulation  $\Gamma_0$ . The distance at which roll-up is complete may be equated to the distance required to redistribute trailing vorticity

over a length scale  $\propto b_0$ . The downwash induced in the wake is  $w_i \propto \Gamma_0/b_0$  and serves as the velocity scale for this analysis. Note that in the framework of lifting line theory and elliptic loading, one obtains  $w_i = \Gamma/2b_0$ . The time scale associated with this process is then  $\propto b_0^2/\Gamma_0$  which is  $\propto U_0 b_0^2/\Gamma_0$  in terms of downstream distance. When expressed in terms relative to the wing, a length scale for roll-up  $X_{r,1}$  is obtained

$$X_{r,1}/b_0 \propto AR/C_z \quad (2.31)$$

where  $AR = \frac{b_0^2}{S}$  is the wing aspect ratio and the lift coefficient is obtained from  $C_z = \frac{\Gamma_0 b \pi}{2U_0 S}$ . This shows that the roll-up distance is dependent on the lift (higher lift, faster roll-up) but also on geometry (higher AR, slower roll-up). However the notion of "essential roll-up" is yet to be defined.

Relation 2.31 was also obtained by Spreiter & Sacks [94] [83] but starting from the assumption that the "degree of roll-up" is the evolution of downwash velocity at the midplane (generated solely by the vortices) non-dimensionalized by the free stream velocity  $w_i(x)/U_0$ . The authors here define a constant  $K_r$  to measure the degree of roll-up such that

$$X_{r,2}/b_0 = K_r * (AR/C_z) \quad (2.32)$$

And determined  $K_r = 0.28$  by employing the results of Kaden theoretical analysis [47]. Consider, for the sake of the cases developed further down, rectangular wings for which  $AR = 5.7$  and  $C_z = 0.45$ , eq. 2.32 reads :

$$X_{r,2} = 3.55b_0 \quad (2.33)$$

which reveals a very short roll-up process when compared to the lifespan of trailing vortices.

Further study of the roll-up distance has been attempted numerically by a 2D method in which the trailing vorticity sheet is replaced by  $n$  point vortices. These types of models assume a finite span, zero thickness wake formed by a given initial distribution of vorticity (say, an elliptically loaded wing). The choice to replace a continuous vorticity sheet with a row of discrete line vortices is suitable for slow roll-up processes, as its the case on high AR wings. Early work of Westwater [100] showed that by mutual induced velocities, the line vortices would adopt helical trajectories in accordance with Kaden's analysis. Further development was provided by studies like that of Moore [66] who studied the numerical limitations of such a model and the one of Rossow [86] who studied the effect of loading distribution in the model. The effect of numerical precision and of the vortex induced velocity model was also explored by studies like that of Dalton & Xuegeng [23]. However, as pointed by Donaldson & Bilanin [26], they fail to represent the neverending stretching of the sections of the sheet that is predicted by the Kaden spiral model. Numerical strategies can be employed to overcome this problem, as demonstrated by Krasny [50]. Stable solutions of roll-up can be achieved this way albeit at a high computational cost. This example shows that establishing an analytical model that fully describes the vortex roll-up process is a challenging task. For this reason, in this work we approximate the duration of the roll-up phase based on eq. 2.32.

Now, we aim to determine the spanwise distance between the vortices after the completion of their roll-up. Let  $b$  be the spanwise distance between the centroids around which vorticity will concentrate during roll-up.  $b$  is obtained by integrating

the bound circulation across the span of the wing,

$$b = 2 \int_0^{b_0/2} \frac{\Gamma_y(y)}{\Gamma_0} dy \quad (2.34)$$

The ratio  $s = \frac{b}{b_0}$  is called the load factor. The value of  $s$  for wings of arbitrary geometry is commonly approximated by  $\pi/4$ , which is the exact result in the case of the elliptic loading.

### 2.2.1.5 Summary

In summary, some of the basic knowledge to characterize the wake formation zone is provided in this section. We start by defining the fundamental properties of vorticity. From there, we explain how a lifting body generates trailing vorticity in its wake. Then this knowledge is applied to the case of lifting wings of finite span. We present and employ lifting line theory in order to show that the distribution of vorticity in the wake of a wing is directly related to the wing geometry. Finally, we provide some basic characteristics of the wake formation zone, namely an approximation of its length downstream and of the spanwise distance that exists between the vortex pair by the end of roll-up. In the next section, we focus on the physical characteristics of the wake in its stable zone. Specifically, we characterize the two trailing vortices present in the wake and describe basic aspects of their interaction.

## 2.2.2 The physics of an isolated vortex

In this section we describe some of the fundamental characteristics of the stable zone of the wake. Concretely, this refers to the downstream region that spans from the end of vortex roll-up to the beginning of the development of the cooperative instabilities. In paragraph 2.2.2.1 we define the characteristics of a vortex like its strength and core size. This allows us to define the characteristic time scales that are useful during our experimental study. In paragraph 2.2.2.2 we comment on the time evolution of the trailing vortices. Thirdly, in paragraph 2.2.2.3, we introduce some of the tridimensional effects that typically occur in a columnar vortex.

### 2.2.2.1 Vortex characteristics

In this section some physical quantities that characterize a vortex flow are described. We give a particular focus to the quantities that can be measured through stereo-PIV as this is the framework of our study. We do this through a description of fundamental vortex models which are also employed in our work. To illustrate our purposes, we compare in Fig. 2.7 the velocity and vorticity distributions of the vortex models that are discussed now.

The vortex key attributes are its circulation  $\Gamma$  and size. Notably, circulation is an invariant of the flow for a barotropic and ideal fluid in the absence of non-conservative forces [90]. This is known as the Kelvin theorem. To do this one could consider the rate of change  $\frac{d\Gamma}{dt}$  by developing eq. 2.10.

From  $\omega(\mathbf{x})$ , one can define the first moment of vorticity, referred to as hydrodynamic impulse,

$$I_1 = \frac{1}{2} \int \mathbf{x} \omega(\mathbf{x}) dx \quad (2.35)$$

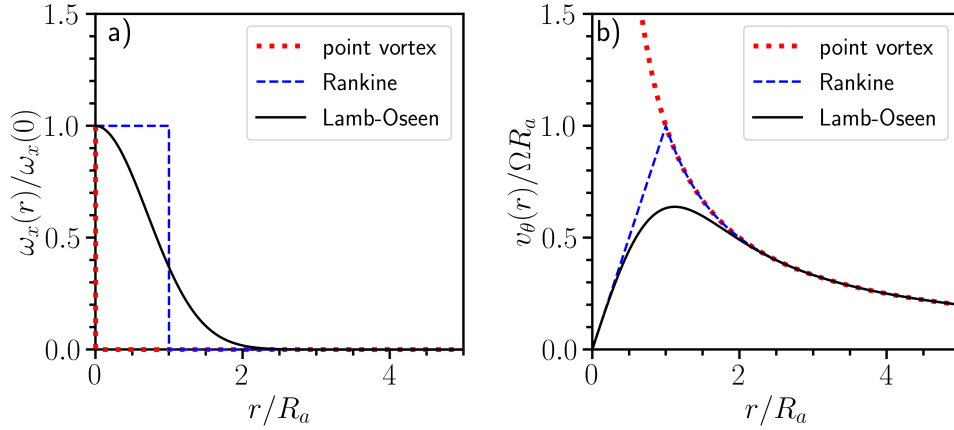


FIGURE 2.7: **a)** scaled axial vorticity and **b)** scaled azimuthal velocity for a Lamb-Oseen, Rankine and point vortex model.

The rate of change of  $I_1$  is related only to the action of non-conservative body forces, rendering it an invariant of motion even in unsteady flow, provided non-conservative forces are absent.

In our examination of vorticity (section 2.2.1.1), we establish a baseline distribution of vorticity which is that of the point vortex, plotted as a solid line in Fig. 2.7. Here, the vorticity is limited to a single point in space, which is called the centroid of vorticity and can be defined using  $I_1$  :

$$\mathbf{x}_\omega = \frac{\int_S \mathbf{x}\omega(\mathbf{x})dS}{\int_S \omega(\mathbf{x})dS} \quad (2.36)$$

In flows with multiple vorticity sources  $\mathbf{x}_\omega$  defines a general barycenter of vorticity in space. Note that in cases where vortices have opposing signs, this centroid position is such that  $|\mathbf{x}_\omega| \rightarrow \infty$ .

Real flows have non-singular vorticity distributions. The second moment of vorticity  $I_2$  (eq. 2.37), provides the vortex size.  $I_2$  is defined by [51, 90],

$$I_2 = \int_S (\mathbf{x} - \mathbf{x}_\omega)^2 \omega dS \quad (2.37)$$

$I_2$  also serves as an invariant of the motion in unbound flow [90]. This leads to a characteristic length, denoted the dispersion radius  $R_d$ , which measures the vorticity's spread in a 2D plane.

$$R_d^2 = \frac{\int_S (\mathbf{x} - \mathbf{x}_\omega)^2 \omega dS}{\int_S \omega(\mathbf{x})dS} \quad (2.38)$$

Additionally, the radius at which azimuthal velocity reaches its maximum, denoted  $R_a$ , offers another measure of the vortex core size. From  $\Gamma$  and  $R_d$  one can define the rate of rotation :

$$\Omega = \frac{\Gamma}{2\pi R_d^2} \quad (2.39)$$

Using these principles, we introduced the Rankine vortex model in section 2.2.1.1, eq. 2.14. This model combines solid body rotation within a radius  $R_a$  and potential flow outside. This model exhibits a discontinuous vorticity distribution, with finite vorticity inside the core and none outside.

Next we define the Lamb-Oseen vortex model (also called Gaussian distribution),

$$\omega_x(r) = \frac{\Gamma}{4\pi\nu t} e^{-r^2/4\nu t} \quad (2.40)$$

This solution describes the gradual evolution of a vortex due to viscosity. Notably,  $I_2$  ceases to be an invariant in such conditions, instead undergoing a rate of change that signifies angular momentum diffusion. In 2D flow, an expression of this diffusion is provided by Dirlshel [27, 90],

$$\frac{dI_2}{dt} = 8\nu\Gamma \quad (2.41)$$

Consequently, the vortex core size grows due to viscous diffusion :

$$R_d(t)^2 = R_d(0)^2 + 4\nu t \quad (2.42)$$

In practical scenarios [93, 34], the determination of the core radius is often complemented by characterizing the vortex outer boundary, which is  $R_2$ . The region extending up to  $R_2$  contains the entire vorticity associated to the vortex and the flow beyond  $R_2$  is irrotational. The total circulation can be attained using a contour of radius  $r \geq R_2$  [34, 43].

Using the concepts above the velocity field that the trailing vortices of a leader aircraft induce on a following aircraft can be analyzed. This is composed of an induced rolling moment  $C_R$  and induced lateral, up and down-wash forces. Let the subscript  $f$  refer to the following aircraft and, for practical considerations, let  $b_f = b_0/2$  and  $U_f = U_0$  be its wing span and flight speed.

In the framework of thin airfoil theory, the resulting  $C_R$  is a function of the section lift  $l$  induced at every span-wise station of the wing, expressed in terms of induced vertical velocity  $W_i$  [18], yielding :

$$C_R = \frac{2\pi}{U_0 b_f^2} \int_{y_f - \frac{b_f}{2}}^{y_f + \frac{b_f}{2}} (y - y_f) (W_{i,1}(y, z_f) + W_{i,2}(y, z_f)) dy \quad (2.43)$$

$C_R$  is maximum when the aircraft is aligned with the vortex axis. This yields for Lamb-Oseen vortices :

$$C_R = \frac{\Gamma}{b_f U_0} \left( 1 - \frac{\sqrt{2\pi} R_d}{2.24 b_f} \right) \quad (2.44)$$

Relation 2.44 shows that for a follower aircraft of fixed span, the induced rolling moment can be reduced either by a lower vortex circulation or by enlarging the upstream vortex core. For a classical flight configuration where  $b_f = \frac{1}{2}b_0$ , doubling the vortex core size brings about a reduction of 5% in  $C_R$ .

Finally, we consider the addition of finite axial flow into the vortex model, as done by Batchelor [5] :

$$\mathbf{u}(\mathbf{x}) = \begin{cases} v_r(r) & = & 0 \\ v_\theta(r) & = & \frac{\Omega R_d}{r/R_d} \left( 1 - e^{-(r/R_d)^2} \right) \\ v_x(r) & = & U_\infty + \Delta U e^{-\left(\frac{r}{R_d}\right)^2} \end{cases} \quad (2.45)$$

Expression 2.45 is called a  $q$ -vortex. Here, azimuthal and axial flows are linked through the swirl parameter  $q$ .

$$q = \frac{\Omega R_d}{\Delta U} \quad (2.46)$$

Where  $\Delta U$  is the difference between the far-field velocity ( $r \rightarrow \infty$ ) and the maximum axial flow in the core of the vortex

$$\Delta U = \max(v_x) - U_\infty \quad (2.47)$$

This model, governed by  $q$  and the axial flow ratio  $U_\infty/\Delta U$ , encompasses cases with "wake-like" or "jet-like" flows [72]. It is worth noting that in the context of our experiments, where the wing is in motion amidst a quiescent surrounding flow,  $\Delta U = \max(v_x)$  or  $\max(v_x)$  if axial flow is wake or jet-like, respectively.

### 2.2.2.2 Mechanisms of vortex decay

*[...] the gradual rise of the circulation from  $r = 0$  to  $r = R_2$  has a damping effect on centrifugal instabilities. Turbulence is therefore unlikely, unless sustained by axial flow*

- P. Spalart [93]

As shown above, under classical arguments, the core of trailing vortices grows in time under the action of viscous diffusion, but most critically their strength remains constant at all times, suggesting that the hazard they represent should decay through slow viscous diffusion of the radius. Non-symmetry of the wake can also contribute [26] to vortex deformation, but this aspect is out of the scope of our study.

Based on the Navier-Stokes equations, Saffman [90] explored a way to relate the downstream decay of the axial flux of a vortex flow to viscosity. In this analysis, the equations of motion are treated using a boundary layer-type approximation called the viscous light loading approximation, which simplifies the downstream derivatives and vortex velocities relative to the aircraft velocity. The equation thus obtained (see chap. 13 of ref. [90] for details) translates a transfer of induced drag into the deficit of axial momentum flux :

$$U_0 \frac{d}{dx} \int_0^\infty v_x r dr = \frac{1}{2} \frac{d}{dx} \int_0^\infty r v_\theta^2 dr < 0 \quad (2.48)$$

Where induced drag is expressed by the kinetic energy of transverse motion. Then, these equations are solved to sign the rate of change of the axial flux along the downstream axis :

$$\frac{d}{dx} \int_0^\infty r v_\theta^2 dr < 0 \quad (2.49)$$

$$\frac{d}{dx} \int_0^\infty r v_x dr < 0 \quad (2.50)$$

Showing that the axial flux, and consequently maximum velocities, do decrease downstream under the action of viscosity. Although one can argue that at small downstream distances the viscous growth of the region containing the vorticity represents an alleviation of wake hazard (since it causes an outwards redistribution of angular momentum and a decrease of the maximum velocities) this in itself is ineffective to produce a decay of total circulation in the vortex. In other words, under classical arguments the peak vorticity inside the core is affected by viscosity. Regarding this matter, Rom [83] stated that, at the Reynolds numbers of flight, under the action of viscous diffusion alone, trailing vortices with high tangential velocities would persists for ranges that reach thousands of wingspans.

One way to show this is to consider a cross section ( $y, z$ ) of a vortex wake symmetrical about its midplane ( $y = 0$ ), and to derive the result that the only decay in

circulation would stem from the diffusion of vorticity across the midplane, which would cause countersign vorticity in the wake to cancel out. This result was obtained by Yates [26], who generalized equations of the moments of vorticity (derived by Betz) to the viscous case. It should be noted that this reasoning is equivalent to studying the effect of viscous friction of vorticity near a solid wall.

Following Helmholtz laws with the hypothesis of a flow in barotropic fluid and in the absence of external forces, the rate of change of circulation is :

$$\frac{d\Gamma}{dt} = \int_S \frac{d\omega_x}{dt} dS = \int_S \nu \Delta \omega_x dS \quad (2.51)$$

Since

$$\nu \int_S \Delta \omega_x dS = \nu \int_{\partial S} (\mathbf{n} \cdot \nabla) \omega_x ds \quad (2.52)$$

The circulation then evolves following

$$\frac{d\Gamma}{dt} = -\nu \int_{-\infty}^{\infty} \left. \frac{\partial \omega_x}{\partial y} \right|_{y=0} dz \quad (2.53)$$

where the boundary term, for the right vortex, is that occurring at the symmetry plane of the wake whose normal is  $\mathbf{n} = -\mathbf{e}_y$ . In the case of a real aircraft wake, however vortices are located too far appart for this transfer to occur even at large downstream stations [93].

Nevertheless observations of the real case like those realized by Hallock [37] or in experiments like those of Ortega [73] result in characteristic times to dissipation shorter than those associated with viscosity effects. If 3D effects are present then the decay of vortex strength might occur through breakdown, which is a sudden loss of coherence of the vortex, most commonly preceded by instability mechanisms. If the decay is not related to breakdown then it can stem from effects of the environnement, namely atmospheric turbulence, wind shear, or stratification, in addition to viscosity. We derive two conclusions from this observation, the first one being that when studying the decay caused by viscosity or turbulence we can consider the vortices in the pair to evolve like isolated vortices (we do so in this paragraph). The second conclusion is that in order to study cooperative instabilities we must first study the effects that cause isolated vortices to deform, initiating tridimensional effects. This is done in sections 2.2.2.3 and 2.2.3.2.

The authors of [37] explained the decay of vortex circulation, measured in the wake of a jet transport aircraft, through two types of physical mechanisms : On one hand, countersign vorticity can interact with the trailing vortices and lead to an effective cancelation of their outer vorticity. Counter-signed vorticity can stem from buoyancy forces, windshear gradient effects or, for the specific measurements realized at ground proximity, by the detachment of boundary layers over the ground or other surfaces. The elements of the list above are typical of the environnement in which trailing vortices develop. On the other hand, turbulence outside the vortex core can also contribute to the diffusion of the vorticity located in the vortex outer region. Also, right after roll-up the vortex core may contain turbulence, which either comes from the generating wing, from atmospheric turbulence that rolled-up during the vortex formation [9]. However, turbulence does not sustain itself closer to the vortex centroid due to the stabilizing effect of rotation. This is of particular interest, since the inhibition of turbulent fluctuations inside the vortex leads to the laminarization of the vortex core [38]. Furthermore, during the laminarization process, perturbations from turbulence may be dispersed into inertial vortex waves [9,

45]. Through this process, angular momentum is maintained.

### 2.2.2.3 Tri-dimensional effects

In this section, we look into the available analytical investigations of the stability properties of a vortex column and of a vortex filament. Throughout the discussion, we use the terms "vortex" to refer to either columns or filaments, providing necessary distinctions when relevant.

Consider a vortex aligned along the  $e_x$  axis, isolated from any other sources of vorticity. The vortex may experience displacement from its original axis due to perturbations. These perturbations can either dampen over time, leading to stable dynamics, or grow exponentially, resulting in unstable behavior. For instance, as curvature is introduced on the vortex with a 3D-deformation, sections of the vortex induce a rotation and a strain field on each other. This is called self-induction and it is a key mechanism for the development of cooperative instabilities (this is shown in section 2.2.3.2). Even if the position of the vortex is not initially displaced, the interaction between axial and azimuthal velocity fields might also lead to unstable scenarios. This is why, in the following we first characterize perturbations in our base flow which take the form of bending waves. Next, we analyze the impact of axial flow on the dynamics of the vortex. Finally, we define the self induction of the vortex spuring from these perturbations. To analyze this problem, we mainly follow the work of Ortega [73], Fabre [29], and Mille [63].

**2.2.2.3.1 Kelvin waves in a columnar vortex** Our study on the stability of a columnar vortex begins by formulating the problem of linear stability in a manner similar to that presented in [29]. The velocity  $(V_x, V_r, V_\theta)$  and pressure  $(P - P_0)$  fields are decomposed into a base flow  $(v_x, v_r = 0, v_\theta, p)$  and a perturbation flow  $(v'_x, v'_r, v'_\theta, p')$ , as follows:

$$V_x = v_x(r) + v'_x(x, r, \theta, t) \quad (2.54)$$

$$V_r = v'_r(x, r, \theta, t) \quad (2.55)$$

$$V_\theta = v_\theta(r) + v'_\theta(x, r, \theta, t) \quad (2.56)$$

$$(P - P_0)/\rho = p(r) + p'(x, r, \theta, t) \quad (2.57)$$

The base flow is assumed to be invariant along the axial and azimuthal directions. Exploiting these symmetries, perturbations can be decomposed into eigenmodes of axial wavenumber  $k$ , azimuthal wavenumber  $m$  and frequency  $\omega$  :

$$(v'_x, v'_r, v'_\theta, p') = \text{Re}(\mathbf{A}(r)) \exp(ikx + im\theta - i\omega t) \quad (2.58)$$

Here,  $\mathbf{A}(r)$  is a complex vector containing the unknown amplitudes of each perturbation function. The question of the flow stability revolves around whether the perturbation modes grow exponentially or decay over time. The modes are characterized by  $\omega = \text{Re}(\omega) + i \text{Im}(\omega)$  and  $\text{Im}(\omega)$  represents its frequency. Our focus lies on the axial wave number  $k$  and the azimuthal wave number  $m$ . The parameter  $k$  is related to the axial wavelength of the perturbation through  $\lambda = 2\pi/k$ . The value of  $m$  determines the azimuthal geometry of a particular mode. Figure 2.8 provides schematics illustrating the geometry of specific wave families for three different values of  $m$ . We look into the definition of these waves in what follows. For now, it is

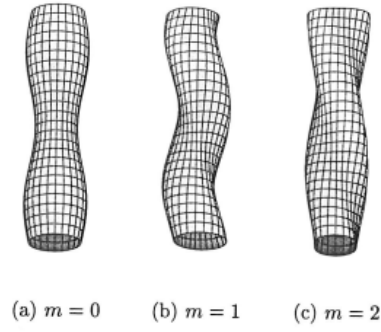


FIGURE 2.8: From [29] : Schematics of the shape of Kelvin waves : a) axisymmetric waves  $m = 0$ , b) helical waves  $m = 1$  and c) double helix waves  $m = 2$

sufficient to note that an axisymmetric mode corresponds to  $m = 0$ , helical modes correspond to  $m = \pm 1$ , and a double helix is characterized by  $m = \pm 2$ .

By inputting  $(V_x, V_r, V_\theta, P)$  in the Navier-Stokes equations, one obtains a linear differential system of equations. Classical stability analysis (e.g. [22, 11, 73, 29]) employs an eigenvalue problem approach to determine the eigen modes of the flow. For a vortex, the eigen modes are found to have real frequencies, indicating oscillatory behavior and stability. These oscillatory modes, known as Kelvin waves, were first studied by Kelvin [97] for the Rankine vortices. Kelvin waves provide a complete decomposition base for arbitrary perturbations [3]. Physically these waves represent the propagation of perturbations within the vortex column. However, the behavior of Kelvin waves differs in vortices where the vorticity extends beyond the core and viscosity affects the flow, such as in a Lamb-Oseen vortex. Based on numerical analysis by Fabre [29], it was observed that in this case only axisymmetric perturbations ( $m = 0$ ) and specific helical perturbations ( $m = \pm 1$ ) can propagate as non damped waves along the columnar vortex. Perturbations for which  $m > 2$  rapidly dissipate.

**2.2.2.3.2 The effect of vortex axial flow on helical perturbations** The presence of strong axial flow within the vortex core can trigger the development of helical instabilities. Notably, the Batchelor model exhibits instability with respect to perturbations when  $m < 0$  and when the swirl number is such that  $q < \sqrt{2}$  (approximately 1.5), as demonstrated by Lessen *et.al* [56] and by Mayer & Powell [60]. This was further confirmed in numerical studies by Delbende [24] and by Olendraru [72].

However, analytical and numerical studies of Jacquin & Pantano [45], showed that when  $q$  is low, a secondary mechanism occurs. The authors of [45] conducted a local stability analysis for different values of swirl  $q$  and obtained the radial distribution of growth rate  $\sigma^2(r)$ , as depicted in Fig. 2.9. It can be seen that as  $q$  decreases, an area with  $\sigma^2 > 0$  emerges within the vortex core. The development of helical instabilities is promoted in this way. For  $q = 0.7$ , the unstable region occupies almost the entire flow domain. The authors of [45] postulated that the region in which  $\sigma^2 < 0$  for  $0.7 < q \leq 1.5$  may act as a *dispersion buffer*. Energy from the core is transported into this buffer, leading to weakened axial velocity while maintaining angular momentum. In the buffer, perturbations are dispersed with no amplification. An added consequence is the increase in swirl parameter  $q$ , which further reduces turbulence production. In other words, this region would be the reason why the vortex does not sustain turbulence in its core.

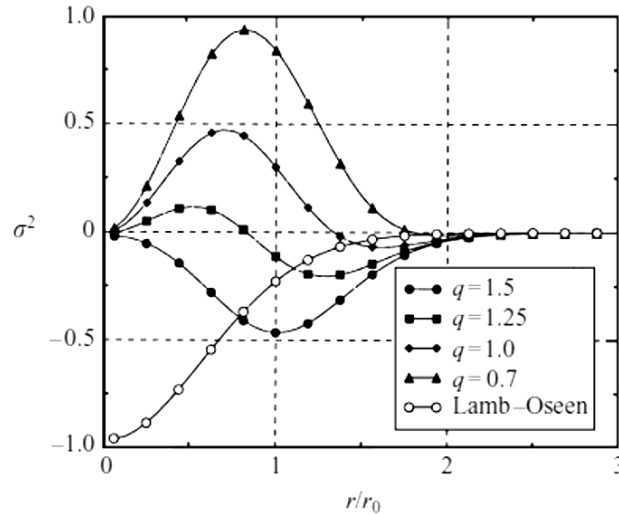


FIGURE 2.9: From [45]: Amplification rate  $\sigma^2(r)$  of short wave instabilities in a Batchelor vortex for  $q = 1.5, 1.25, 1, 0.7$  and for a Lamb-Oseen vortex ( $q = \infty$ ).  $\sigma^2(r)$  is non-dimensionalized with  $v_\theta(t = 0)$  and with the initial radius. Values are divided by 10 for the Lamb-Oseen case.

**2.2.2.3.3 Displacement waves on a vortex filament** A specific family of Kelvin waves, known as helical waves with  $m = \pm 1$ , play a significant role in the analysis that is done in this work. These waves are characterized by their angular velocity relative to that of the vortex core. Cograde waves have an angular velocity greater than that of the vortex, while retrograde waves have a lower angular velocity. Counter-rotating waves, on the other hand, possess an angular velocity opposite to that of the vortex. Within this family, Fabre [29] identified a distinct type of counter-rotating wave that induces a displacement of the vortex away from the axis. These are known as *displacement waves* and possess some noteworthy properties. They affect the velocity field of the vortex outside of the core region while other helical waves are primarily confined to the internal region of the core. In a 2D scenario with  $k = 0$ , displacement waves become stationary (null angular velocity). The resulting 2D mode can be interpreted as a simple displacement of the vortex centroid relative to the unperturbed axis of the vortex tube. Fabre [29] associated displacement waves with the phenomenon of vortex meandering, drawing comparisons with experimental data. Notably, these waves exhibit minimal dependence upon viscosity and the specific vortex model employed. Moreover, the onset of cooperative instabilities can be attributed to the displacement waves as they were found to be destabilized under the strain field of an opposite vortex. In order to investigate the influence of axial flow on the behavior of Kelvin waves, Fabre [29] conducted a comparative analysis between a  $q$ -vortex, characterized by a maximum axial velocity magnitude of  $0.4 \max(v_\theta)$ , and a Lamb-Oseen vortex where axial velocity is null. Overall, the effect of an axial flow on wave propagation exhibits a mostly intuitive behavior. An axisymmetric wave ( $m = 0$ ) propagates symmetrically in both directions along the axis of a Lamb-Oseen column, and the presence of axial flow leads to asymmetric propagation. The axial component of the flow promotes the propagation of axisymmetric waves in the positive direction while slowing down waves traveling in the opposite direction. For perturbation waves with  $m = 1$  and  $m = 2$ , which exhibit a helical structure, the presence of axial flow enhances the propagation of the waves

that turn in the same direction as the base flow.

The effect of the deformed vortex filament upon itself is studied now. Each section of the filament behaves like a point vortex inducing rotation and strain fields. The perturbed filament is defined by combining the baseflow ( $x\mathbf{e}_x$ ) with displacements along the perpendicular directions. The perturbation is therefore defined by amplitudes  $\tilde{y}$ ,  $\tilde{z}$  and wavenumbers  $k$  and  $m$ . The spatial shape of the vortex is determined by the real part of the perturbed filament :

$$\mathbf{x}(x, t) = x\mathbf{e}_x + (y(t) + \tilde{y}(t)e^{ikx})\mathbf{e}_y + (z(t) + \tilde{z}(t)e^{ikx})\mathbf{e}_z \quad (2.59)$$

Where  $y(t), z(t)$  are the mean positions of the vortices, here  $y(t) = z(t) = 0$ . The *self induction* of the vortex occurs due to the curvature introduced by the perturbation. Indeed, when they are displaced, the sections of the filament induce a velocity field on the rest. This can be computed in the form of a self induction function  $\omega$ , which is dependent on the spatial characteristics of the perturbation  $k, m$ . From  $\omega$  and the strain rate  $\Gamma/2\pi$  one can derive an expression for the self induced rotation rate  $\omega_i$ . This represents the angular velocity rate of rotation of the bending modes around the unperturbed axis of the vortex caused by self induction effects.

Several techniques have been used to derive the expression of the self induction function  $\omega$ . Crow [22] employed a Biot-Savart law combined with a cut-off method. This had limitations for large perturbation wavenumbers. Kelvin [97] derived an expression for  $\omega$  which avoided the use of cut-off for a Rankine vortex, while Krishnamoorthy [Krishnamoorthy] extended it to include a uniform axial velocity. Widnall [102] derived an expression of  $\omega$  suitable for arbitrary velocity distributions, but with limitations regarding the initial perturbation amplitudes and prohibiting a viscous core that grows in time. Moore & Saffman [68] extended upon models by balancing various parameters, considering the lift force, momentum flux, and vortex line tension and obtained an expression that takes into account arbitrary initial perturbations and the variation of the core size under the effects of viscosity and curvature.

The methodology employed to compute  $\omega$  in this study follows the guidelines of Ortega [73] and Bristol *et al.* [11]. It combines the results for a Rankine vortex with no axial flow [97, 90] and extends them to a Lamb-Oseen vortex.

From Saffman's stability study, a dispersion relationship (eq. 6 p.232 of [90]) is obtained as a function of the wavenumbers  $k$  and  $m$ , as well as the core size  $R_a$ . The dispersion relationship is solved to find the roots  $\kappa_n$ . The self induction function  $\omega$  is derived using the dispersion relationship and gives the following equation:

$$\omega = \frac{2lk}{\sqrt{k^2 + \kappa_n^2}} - m \quad (2.60)$$

Here,  $l$  indicates the rotation direction of the wave relative to the swirling flow of the vortex. For the computation of the self induced rotation rate  $\omega_i$ , the retrograde helical displacement waves with  $l = 1$  and  $m = 1$  are considered [73, 29]. The self induced rotation rate  $\omega_i$  is the frequency of the Kelvin wave  $\omega(k, l = 1, m = 1)$ , normalized by the swirl velocity of the vortex core.

$$\omega_i = \frac{\Gamma}{2\pi R_a^2} \omega(k, l = 1, m = 1) \quad (2.61)$$

Positive values of  $\omega_i$  indicate retrograde rotation. This equation illustrates the relationship between  $\omega_i$  and the shape of the perturbation and also shows that the

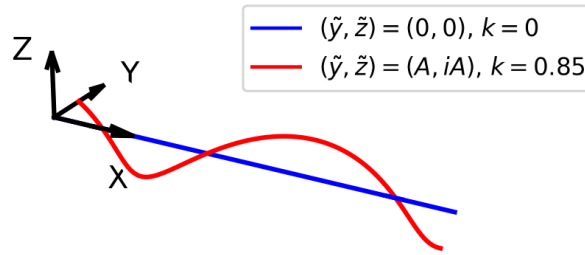


FIGURE 2.10: Schematics of a vortex filament perturbed by a helical wave following equation 2.62

rotation rate is influenced by the vortex strength and size. A stronger strain field  $\Gamma/2\pi$  leads to an increased rotation, while a larger core size decelerates the rotation rate.

Following this, the perturbation of the vortex can be expressed as Fourier modes. Considering the perturbed vortex described in Equation 2.59, specifically for a  $\omega(k, l = 1, m = 1)$  wave with amplitude  $A$ , the expressions for  $\tilde{y}$  and  $\tilde{z}$  can be written as:

$$x(x) = x\mathbf{e}_x + Ae^{i(kx+\omega_i t)}\mathbf{e}_y + iAe^{i(kx+\omega_i t)}\mathbf{e}_z \quad (2.62)$$

The resulting perturbation (with  $A > 0$  and  $k = 0.85$ ) is schematized in Fig. 2.10. The choice of  $k$  is related to the properties of the Crow instability that we discuss in section 2.2.3.2. The perturbed filament exhibits a helical shape due to the amplitudes  $(\tilde{y}, \tilde{z}) = (A, iA)$ , and the rotation rate of the perturbation is determined by  $\omega_i$ .

**2.2.2.3.4 Summary** In this section, we have introduced a framework to study the linear stability of the flow in vortex columns. The analysis involves decomposing the velocity and pressure fields into a base flow and a perturbation flow, characterized by eigen-modes with axial and azimuthal wave numbers. Of particular significance are the Kelvin waves, which represent oscillatory modes that propagate along the column, introducing deformation. To understand the effects of deformation on the vortex, a vortex filament model is employed. This model captures the self induction phenomenon, where each section of the filament induces a velocity field on the rest. By considering the self induction function, the self induced rotation rate is computed. This velocity represents the angular velocity rate of rotation of bending modes caused by self induction effects. The relationship between the rotation rate and the shape of the perturbation is established, emphasizing the influence of vortex strength and size on the rotation rate. At this stage, we have defined the basic properties of a single vortex column. Building upon this understanding, in the next section we shift our focus to the analysis of systems consisting of two counter rotating vortices, which form the fundamental model of a vortex wake.

## 2.2.3 The physics of a pair of trailing vortices

### 2.2.3.1 Time-scales of wake evolution

In this section, we analyze a two-vortex system as the most basic representation of an aircraft vortex wake. Vortices induce both strain and rotational fields in their vicinity. Here the focus is put on the interactions between induced and self-induced velocity fields of each vortex of the pair to explore how the flow evolves in such systems. To do this, the different time-scales that define the evolution of the simple

wake model are first discussed. Then, some specific scenarios where the interaction between two counter-rotating vortices can trigger a cooperative instability are analyzed.

Let  $\Gamma_1$  and  $\Gamma_2$  be the circulations of a pair of line vortices composing a vortex wake and let  $b$  be the distance separating them. The ratio of circulation between the pair is

$$\gamma = \Gamma_2/\Gamma_1 \quad (2.63)$$

$\gamma = -1$  translates, therefore, a counter-rotating pair where both vortices have equal strength, i.e.  $\Gamma_1 = -\Gamma_2 = \Gamma$ .

The temporal evolution of this system results from physical phenomena that presented here along with their characteristic time-scales. Consider a wing (or any lifting body) traversing a quiescent fluid at velocity  $U_0$  in the  $x$ -wise direction. We remind the reader that the wing geometrical characteristics are the span  $b_0$ , the chord  $c_0$  and surface  $S$ . Aspect ratio is defined as  $b_0^2/S$ . The time-scales discussed below are compared for a rectangular wing ( $AR = 5.7$ ) in Fig. 2.11. Stations  $X$  alongside the  $x$  direction are considered and time is denoted  $t$ . Time, in seconds, is elapsed from the moment where the wing passed by station  $X$ .

$X$  is then a measure of the downstream distance from the trailing edge of the wing,

$$X = \frac{tU_0}{b_0} = \frac{t}{t_d} \quad (2.64)$$

Where we use  $t_d = b_0/U_0$ , the characteristic time scale of the incoming flow.

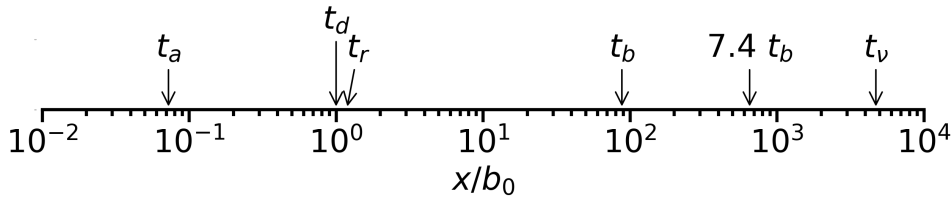


FIGURE 2.11: Characteristic time scales of the dynamics of a vortex wake generated by a rectangular wing. Data is scaled as a distance downstream on the wake of the wing, counted in wingspans

The time-scale associated to the roll-up of the shed vorticity into axisymmetric vortices is derived from eq. 2.32 yielding

$$t_r = K_r \frac{AR^2 S}{C_z U_0} \quad (2.65)$$

This time-scale is useful to estimate the moment at which the flow can be compared to a simple system of two counter-rotating vortices (or more in the case of multiple-pairs systems). The vortices thus formed are characterized by their circulation and radius  $R_d$ .

A particle on the rolled-up vortex would do one rotation about the vortex centroid in a time-scale estimated by

$$t_a = \frac{2\pi R_d^2}{\Gamma} \quad (2.66)$$

And this time scale is related to the intraction of turbulent diffusion within the vortex [45]. Also, it is useful to estimate a time-scale  $t_v$  for the viscous diffusion of the vortex.

$$t_v = \frac{2\pi R_d^2}{\nu} \quad (2.67)$$

In 2D flow the trajectories of the vortices describe a circular motion around the center of vorticity  $\mathbf{x}_\omega$  (see eq. 2.36). The angular velocity of rotation in the pair is

$$\Omega_{orb} = \frac{\Gamma_1 + \Gamma_2}{2\pi b^2} \quad (2.68)$$

The characteristic time-scale of the rotating system is then the period of orbit of the vortex trajectories, given by

$$t_{orb} = \frac{2\pi}{\Omega_{orb}} = \frac{(2\pi b)^2}{\Gamma_1 + \Gamma_2} \quad (2.69)$$

In the case of two counter-rotating vortices of equal strength, the mutual induction provokes the vortex pair to displace vertically at a downwash velocity noted  $W_d$ .

$$W_d = \frac{\Gamma}{2\pi b} \quad (2.70)$$

We define a time-scale  $t_b$  as the time needed for the vortices to traverse a vertical distance of  $b$ .

$$t_b = \frac{b}{W_d} = \frac{2\pi b^2}{\Gamma} \quad (2.71)$$

The quantities considered here can be expressed as a function of the geometrical and load aspects of the wing,

$$W_d = \frac{c_0}{4\pi s^2 b_0} U_0 C_Z \quad (2.72)$$

The time scale  $t_b$  provides a good estimation of the time required for a deformation of the vortices to grow by one order of magnitude under the action of a cooperative instability [22]. In practice, the exponential growth of the amplitude of the vortex oscillations leads to a disruption of the flow after about 5 to 6 characteristic times [9].

### 2.2.3.2 Cooperative instabilities on a vortex pair

*[...] rotation of planar perturbations must be overcome for the strain field to cause instability.*

- R. Bristol [11]

When contrail formations or other phenomena make the trailing vortices visible, a symmetric and sinusoidal instability between the vortices can be seen in the wake of some airplanes. This phenomenon is illustrated with laboratory experiments and simulations from the litterature in Fig. 2.12. In Fig. 2.12a, one can see that the deformations in the vortices grow in amplitude until they provoke a reconnection of the vortices. After about 8 characteristic time scales, the wake has the form of a series of vortex rings. However, this can translate to hundreds of wingspans in real life (see, for instance, Fig. 2.11). In Fig. 2.12b it can be seen that, prior to reconnection, the deformations are inclined with respect to the spanwise direction by an angle  $\theta$ . In 1970, Crow [22] used classic stability theory of a pair of Rankine vortex filaments in order

to describe this deformation. As a result, the stability of the system was found to be dependent of the vortex radius and separation distance  $b$ , a cutoff parameter  $\delta$ , and of the perturbation wavenumber  $k$ .  $\delta$  intervenes when considering self-induction at distances comparable to  $R_a$ . For a rectangular wing of elliptical loading, the ratio  $\delta/b = 0.063$  was used [22]. The use of the cut-off method generates spurious unstable configurations and has since been replaced by more efficient approaches [11, 29, 73]. One of these approaches involves the computation of the self-induction term  $\omega$  which we described in section 2.2.2.3.3. The results are close to those of Crow : the most unstable mode has a wavelength in the order of  $8b$  and the perturbation plane is inclined of about  $\theta \sim 45^\circ$ . This instability is sometimes termed *long-wavelength instability*.

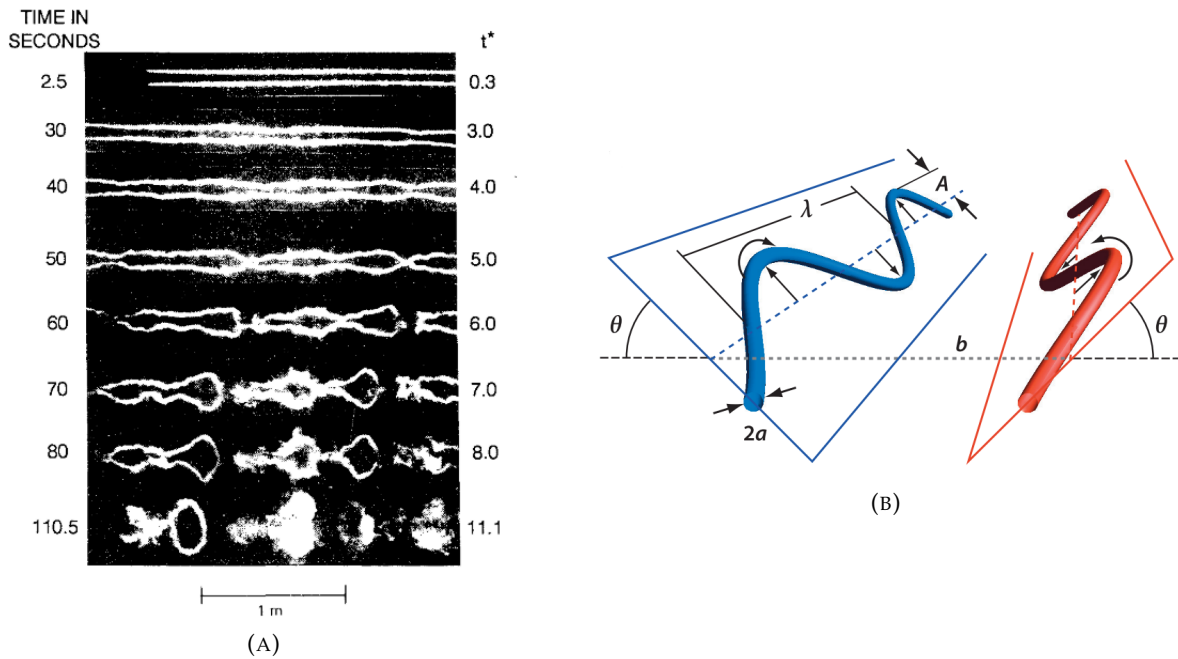


FIGURE 2.12: Illustration on the development of long-wave instability **a)** From [59] : development of a linking instability in a quiescent, neutrally stable water tow tank experiment. In the figure,  $t^* = t/t_b$ . **b)** From [57] : Schematics of symmetric displacement mode associated to the Crow instability. In the figure,  $a$  is the vortex core.

A second type of instability, called Widnall instability, develops in the pair but with a *short wavelength*, comparable in length to the core radius. This phenomenon was first characterized by Tsai & Widnall [98] on a Rankine vortex. This characteristics of this instability in a Lamb-Oseen vortex were studied by Sipp & Jacquin [92] among others. Often, the pair of vortices is affected simultaneously by both the Crow and Widnall instability, as shown in the experiments of Laporte & Leweke [52]. However, to this date a practical application of the Widnall instability in order to alleviate the vortex wake hazard has not been found. Moving forward we focus our attention on the Crow instability.

We wish to briefly describe the classical framework used to study the stability of a vortex wake. Consider a system of two parallel vortex filaments of opposite strength. The positions of each vortex at the downstream station  $x$  are given by  $\mathbf{x}_n(x, t)$  with  $n = 1$  or  $2$ .  $\mathbf{x}_n$  is broken down in a straight filament baseflow and a displacement perturbation in a manner analog to eq. (2.59). At the station  $x$ , one can

derive the effect of the velocity fields induced on vortex  $n$  by the vorticity of vortex 1 and 2 by applying the Biot-Savart law:

$$\frac{\partial \mathbf{x}_n}{\partial t} = \sum_{m=1}^2 \frac{\Gamma_m}{4\pi} \int_{-\infty}^{\infty} \frac{(\mathbf{x}'_m - \mathbf{x}_n)}{\|\mathbf{x}'_m - \mathbf{x}_n\|^3} \times \frac{\partial \mathbf{x}'_m}{\partial x'_m} dx'_m \quad (2.73)$$

Condition (2.73) shows that the vortex deformation evolves under the action of both mutual induction (when  $m \neq n$ ), and of self-induction (when  $m = n$ ). Primes are used to differentiate the terms when  $n = m$ .

A physical interpretation of the action of both mutual induction and self-induction is provided now. In a reference frame descending with the pair, the strain field induced by the base flow of vortex 2 on vortex 1 results in a stagnation point flow field with a main stretching direction. The motion that arises from the combined perturbation of the two vortices also induces rotation and stretching on the perturbation plane. Self-induction results only in an induced rotational motion of the perturbation plane. In a stable case, the perturbation rotates on the  $(y, z)$  plane, interacting periodically with the stretching and compression directions of the strain field [73]. This is why the perturbation amplitude exhibits a periodic evolution. Instability at, say, vortex 1 occurs when the different rotations induced at  $\mathbf{x}_1$  cancel each other out, leaving only stretching action along a fixed direction  $\theta$ . In this scenario, the perturbation diverges in amplitude along the stretching direction.

A detailed mathematical framework to solve this problem is provided in [73]. We summarize here key results of this analysis : Two eigenmodes can be found on this system that represent a symmetric and antisymmetric mode on the perturbation of the vortex pair with respect to the  $(x, z)$  plane. The growth rate of the modes is denoted  $\alpha$ . The development of the system is known to be dominated by the most unstable wavenumber for which  $\alpha$  is maximum. In the range of parameters that concern aircraft wakes, only the symmetric mode shows a region of instability [22]. The symmetric mode in the case of wake vortices, ( $\gamma = -1$ ,  $\Omega_{orb} = 0$  and  $\omega_1 = \omega_2 = \omega$ ) is schematized in Fig. 2.12b.

The evolution of the amplification rate  $\alpha$  as a function of the normalized wavenumber  $kb$  as obtained by Ortega [73] is shown in Fig. 2.13. Here, the results are compared between the cut-off model (plotted with dotted lines) and those obtained using  $\omega$  of eq. 2.60 (solid line). The values of  $R_q/b$  and of  $\delta/b$  have been chosen appropriately in order to compare the two methods. The second band of instability located around  $kb = 5.3$  is spurious. The maximum growth rate is achieved at  $kb = 0.85$ , resulting in a mode of wavelength  $\sim 7.4b$  oriented at  $\theta = 48^\circ$ .

As explained above, when  $\gamma \neq -1$ , the pair does not descend vertically but rotates with angular velocity  $\Omega_{orb}$  (see eq. 2.68) around  $\mathbf{x}_\omega$ . Then, the rotation components need not cancel but add up to  $\Omega_{orb}$  for the perturbation to diverge. It has been shown that this is never the case for co-rotating vortex pairs [46, 73] while all counter-rotating vortex pairs are unstable with respect to long-wave cooperative instabilities [32, 49]. The stability of vortex pairs when  $\gamma \neq -1$  is of relevance for the study of wakes with multiple vortices, and this subject is further developed in section 2.3.

## 2.2.4 Summary

In this section we conduct a comprehensive analysis of the wake generated by a simple geometric lifting body, specifically an elliptic or rectangular wing. Through analytical work, we establish that such wings produce a pair of counter-rotating

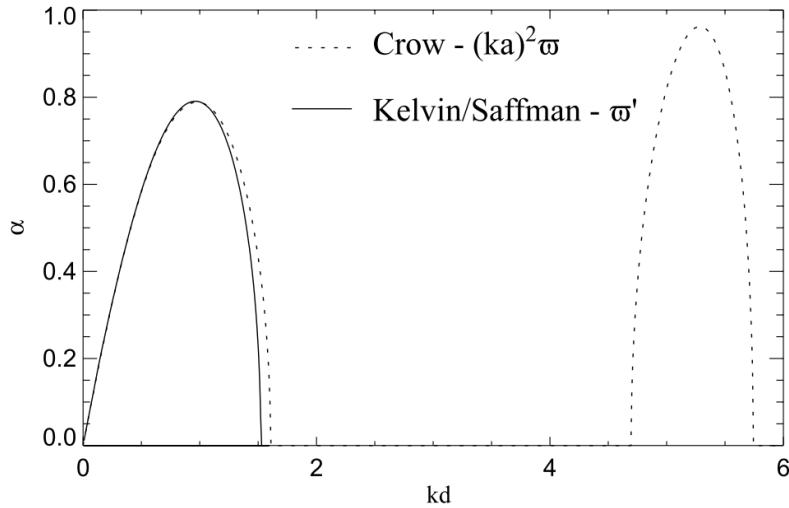


FIGURE 2.13: from [73]: Growth rate curves for  $\gamma = -1$  based upon two different self-induced rotation rate models.  $kd$  in the figure corresponds to  $kb$  in our notations.

vortices at their tips, forming a dynamic system where strain and rotational fields are induced by the vortices of the pair. Extensive experimental and numerical studies have confirmed the validity of these models.

Furthermore, we investigate how vortex interactions can lead to cooperative instabilities within the wake. These cooperative instabilities manifest as a diverging displacement of the vortex positions, facilitating increased vorticity exchange across the midplane and eventual linking of the vortices. Consequently, the strength and lifespan of vorticity in the wake are reduced. The models predicting the emergence and behavior of cooperative instabilities have been validated by both experimental and numerical investigations.

In light of the extended time scales associated with the decay of the vortex dipole, even factoring in the Crow instability, addressing wake hazards in commercial aviation remains a challenge. To accelerate wake dissipation, real-world complexities, not represented in our basic models, are considered. For instance, aircraft wings feature additional components like flaps or engines. It is known that distinct vortices are shed from these components, as it was observed in a wind tunnel survey conducted by Breitsamter [8] on a scaled four-engine large transport aircraft. These multipolar vortex systems have been explored in research, revealing their potential to accelerate wake dissipation more effectively than the Crow instability alone. In the subsequent section, we delve into the modeling of multiple vortex systems, utilizing analytical, experimental, and numerical approaches to investigate their role in mitigating wake hazards.

## 2.3 Multipolar vortex wakes

In this section we explore the dynamics of multipolar wakes, which involve the presence of more than two vortices. The additional vortices are generated by various sources such as the wing flaps. Secondary vorticity coexists and interacts with the dominant vorticity of the wing-tip vortex. Usually, one simplifies this problem by considering the cases where only one secondary group of vortices exists besides the wing-tip vortices, making four total. These secondary vortices exhibit a motion that

can be classified as either co-rotating or counter-rotating with respect to the wing-tip vortices.

During the formation stage, these vortices may either diffuse around the dominant vorticity or fuse with it, usually resulting in the formation of a single trailing vortex in the stable wake zone. However, prior to the disappearance of the secondary vortices, complex dynamic interactions take place among them. We study these interactions as they include mechanisms that have the potential to accelerate the diffusion of the wake.

In section 2.3.1, the model employed to characterize a 4-vortex system is presented. Then, section 2.3.2 focuses on the scenario where the secondary vorticity is co-rotating with the dominant vortex. Here, the fusion mechanism that occurs is analyzed and implications for the evolution of the wake are explored. In section 2.3.3, we shift our attention to the case where the secondary vorticity is counter-rotating with the dominant vortex. This type of flow is less common in real aircraft wakes, however it is interesting for the development of strategies of wake hazard alleviation because the interaction between counter-rotating vortices can lead to instabilities with significant growth rates.

Continuing our exploration, section 2.3.4 investigates the role of higher-order perturbations in the wake of a rectangular wing. Analytical and numerical evidence suggests that these specific perturbations, manifested in the form of counter-rotating flows, may precipitate the diffusion of the main vorticity.

### 2.3.1 A model of a multipolar vortex wake

It is evident from full-scale observations that additional vortices do form in the near-wake of a wing in flaps-down configuration. Experimental evidence [20] shows that these vortices can indeed be counter- or co-rotating with the tip vortices, and that in a flaps down configuration they are generated at the inboard and outboard edges of the flap, respectively. Analytical and numerical models based on the 2D vorticity transport equation effectively described the early dynamics of these vortices. Building upon these findings, this section presents simplified models of 4-vortex systems, considering co- or counter-rotating vortices shed from a wing, to study their behavior using two-dimensional dynamics. Specific parameters that play a significant role in these dynamics are explored. This encompasses the circulation ratio and vortex spacing.

#### 2.3.1.1 The roll-up of the trailing vorticity into multiple vortices

A simple model allows us to link the characteristics of a lifting wing to the number and characteristics of vortices in its wake. This model is an extension of the Betz method, which is described in [87]. Indeed, when a single vortex is shed at each side of the wing, the simplified Betz method effectively links the spanwise evolution of the vorticity shed at the trailing edge to the structure of the wake downstream. In this case of an elliptic loading, the strength of the vortex sheet generated by the wing  $\gamma_w(y)$  is monotonically increasing from the mid-span to the wing tip. However, on civil aircraft wings  $\gamma_w(y)$  does not show a monotonous span-wise evolution. Also, the starting point for the roll-up cannot be assumed to be at the wing tip. Following these discrepancies Rossow [86] extended the Betz method with two additional rules :

1. Vortex roll-up sites are located at maxima of sheet strength and at abrupt changes of sheet strength.

2. Segments of vortex sheet that roll into the same vortex are separated by a vanishment, a change of sign or a minimum of  $\gamma_w(y)$ .

The resulting model is of interest for our study, in that it allows for multiple vortices to roll-up from the trailing vorticity sheet at each side of the wake. Following rule 1, when  $n$  vortices originate from the semi-span, the correct roll-up site  $y_n$  is considered in the model (see eq.43 of [86]). Following rule 2, the vorticity sheet is divided into segments that will each roll-up into a distinct vortex. Consider for example the local circulation distribution in a representative flaps-down configuration as shown in Fig. 2.14. The inboard flap has a larger effective angle of attack, and therefore generates more lift. Because of this, the local circulation is stronger in the inboard region ( $y/b_0 < 0.2$  in the figure). This is translated into a strong spike of  $\gamma_w(y)$  at the flap tips. The strongest spike of vorticity lies at the wing-tip as expected. Following rule 1 of the extended Betz model, both the flap tip and the wing tip are considered to be a roll-up location.

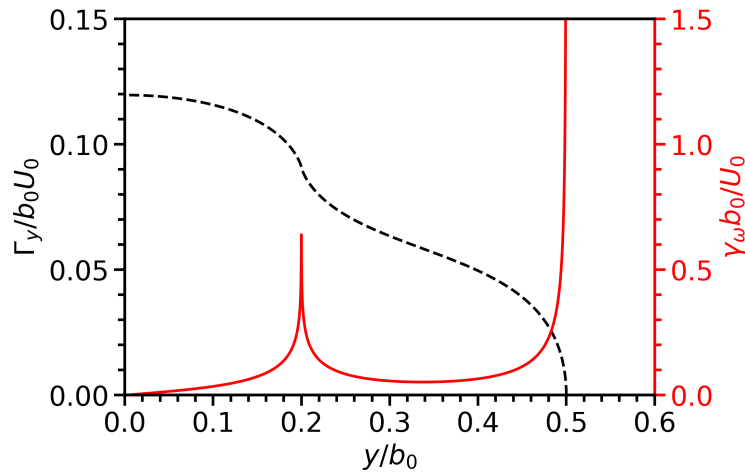


FIGURE 2.14: Span-wise  $\Gamma_y(y)$  (dotted line) and  $\gamma_w(y)$  (solid line) distribution, as predicted by lifting line theory, on a configuration representative of a flaps-down wing. Note that  $\lim_{y/b_0 \rightarrow 0.5} \gamma_w(y) = +\infty$

Figure 2.15 serves as an illustration of the two types of roll-up predicted by the extended Betz method. If the roll-up site is located at the end of the sheet segment, the vorticity will be incorporated as a *single branched* spiral until the form of an axisymmetric vortex is attained. If the roll-up site is located somewhere else along the sheet, the vorticity will roll-up from one side and the other, forming a *double branched* spiral before achieving the axisymmetric form.

In summary, we presented here an efficient method used to relate an arbitrary lift distribution on a wing to the number and position of vortices in its wake. This will be useful during the design stage of our experiments. Moving on, we shall address the expected dynamics of the 4-vortex system generated.

### 2.3.1.2 The physics of four vortex wakes

One can consider the vortices formed to be initially aligned along the wing span direction. However, the resulting system of vortices will not remain static but evolve under the influence of mutual induction. To obtain a reliable prediction of the motion of the vortices in the system is of interest as this affects directly the degree of interaction between the vortices. This is why in this section, we describe a model by

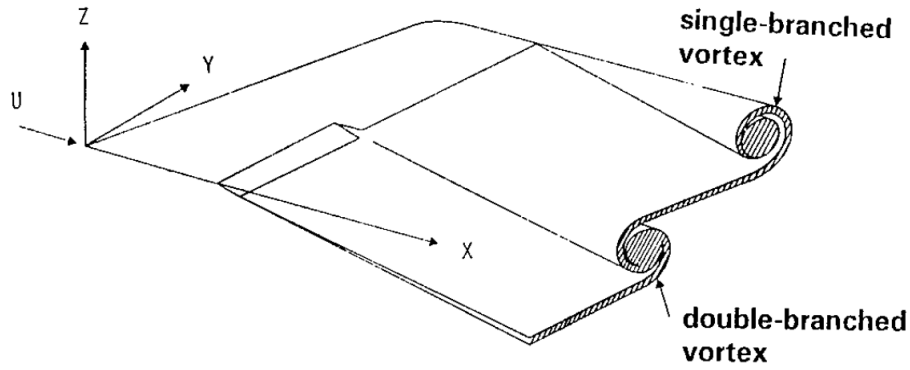


FIGURE 2.15: from [40] : Roll-up of a multipolar vortex wake

which one can predict the downstream evolution of a wake composed of two vortex pairs.

The model here described follows the guidelines shown by Fabre [29], who studied the stability of systems of symmetrical vortex pairs. Here, the vortices are modeled as vortex filaments like in eq. 2.59. If one neglects the perturbations ( $\tilde{y}_n = \tilde{z}_n = 0$ ), the behavior of the system can be described using 2D theory. Figure 2.16 illustrates this configuration. The main vorticity of the system is formed by the wing-tip vortices, with the portside main vortex characterized by circulation  $\Gamma_1$  and radius  $R_{d,1}$ . The port-side secondary vortex, typically the flap vortex, is characterized by circulation  $\Gamma_2$  and radius  $R_{d,2}$ . The system exhibits symmetry with respect to the  $y = 0$  plane, where  $\Gamma_4 = -\Gamma_1$  and  $\Gamma_3 = -\Gamma_2$ . The distances between the wing-tip (main) vortices and the flap (secondary) vortices are denoted as  $b_1$  and  $b_2$ , respectively. Additionally, the system is characterized by non-dimensional parameters  $\gamma = \Gamma_2/\Gamma_1$ ,  $\beta = b_2/b_1$ ,  $R_{d,1}/b_1$ , and  $R_{d,2}/b_2$ .

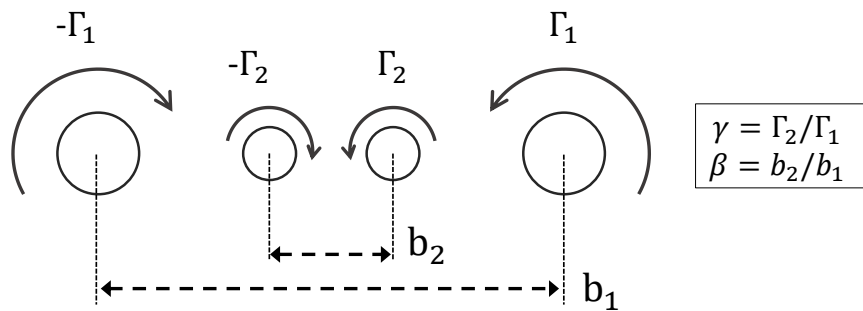


FIGURE 2.16: Diagram of a system of four vortices (figure inspired from [29]).

Since the vortices are considered to behave like vortex filaments, their radii are required to be small with respect to vortex spacing, i.e.

$$R_{d,1}, R_{d,2} \ll b_1, b_2, (b_1 - b_2)/2 \quad (2.74)$$

In this model, co-rotating and counter-rotating cases are respectively defined by  $\gamma > 0$  and  $\gamma < 0$ . Furthermore it is supposed that  $|\gamma| < 1$  in the co-rotating case. We exclude some cases in which the flap vortex may constitute the main vorticity of the system.

In the work of Fabre [29], the stability of a system of  $N$  vortex filaments is studied through the parametric equation of each filament (eq. 2.59). When considering the amplitude of the perturbations to be small with respect to the distances between the filaments, the stability equations can be linearized. The results from the stability study of four-vortex systems is discussed later in sections 2.3.2 and 2.3.3. At order 0, the tridimensional perturbations are neglected and we obtain the trajectories of the filaments as motion equations of point vortices in 2D flow.

$$\frac{dY_n}{dt} = \sum_{m \neq n} -\frac{\Gamma_m}{2\pi} \frac{(Z_n - Z_m)}{(Y_n - Y_m)^2 + (Z_n - Z_m)^2} \quad (2.75)$$

$$\frac{dZ_n}{dt} = \sum_{m \neq n} \frac{\Gamma_m}{2\pi} \frac{(Y_n - Y_m)}{(Y_n - Y_m)^2 + (Z_n - Z_m)^2} \quad (2.76)$$

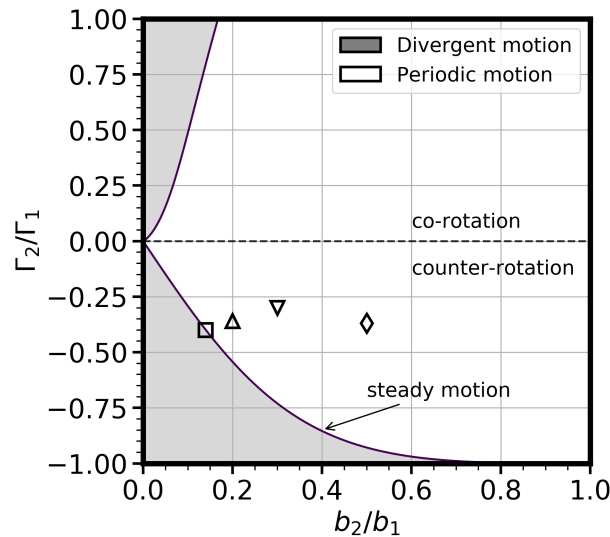


FIGURE 2.17: Diagram of the evolution of a system of four vortices. Configurations studied by other authors are marked by symbols. Numerical simulations : Fabre [29] (□ and ▽), Reinnich & Lele [82] (□). Experiments : Ortega *et al.* [75] (◇) and Jacquin *et al.* [43] (△).

A diagram of the behavior of the system as a function of the parameters  $\gamma$  and  $\beta$  is shown in Fig. 2.17. With respect to these parameters, the trajectories obtained from this system are periodic, steady or divergent. We show an illustration of each of this states in Fig. 2.18. The barycenter of vorticity for the pair  $\mathbf{x}_1$  and  $\mathbf{x}_2$  is  $\mathbf{x}_{1+2}$  and plotted with dotted red lines. In the periodic case, the vortices in each half-plane of the wake orbit around  $\mathbf{x}_{1+2}$ . In the divergent case, the secondary vortices are ejected far from the main ones. This diagram was first proposed by Donaldson & Bilanin [26]. Curves in this diagram are obtained from considerations made upon two invariants of the vortex system, namely the first moment of vorticity and the kinetic energy of the vortices [29].

The curve marking the limit between the divergent and periodic motion for  $\gamma > 0$  is obtained by analyzing the kinetic energy of the vortices, and defining a kind of "escape velocity" of the flap vortices with respect to the field induced by the main vortices. For  $-1 < \gamma < 0$  and  $0 < \beta < 1$ , the curve that marks the boundaries between the periodic and divergent motion is denoted as "steady motion" in Fig. 2.17 and is of particular interest for our work. This curve is obtained by equating the

vertical velocities that the wingtip and flap vortices induce on each other following [26, 29, 82] :

$$(\beta)^3 + 3(\gamma)(\beta)^2 + 3(\beta) + (\gamma) = 0 \quad (2.77)$$

Condition 2.77 represents configurations where the four vortices in the system descend vertically without exhibiting circular motion. The system is effectively steady in a reference frame that descends with the vortices. Note that any slight offset from the conditions of eq. 2.77 results in periodic or divergent motion, rendering this equilibrium unstable with respect to 2D perturbations [29].

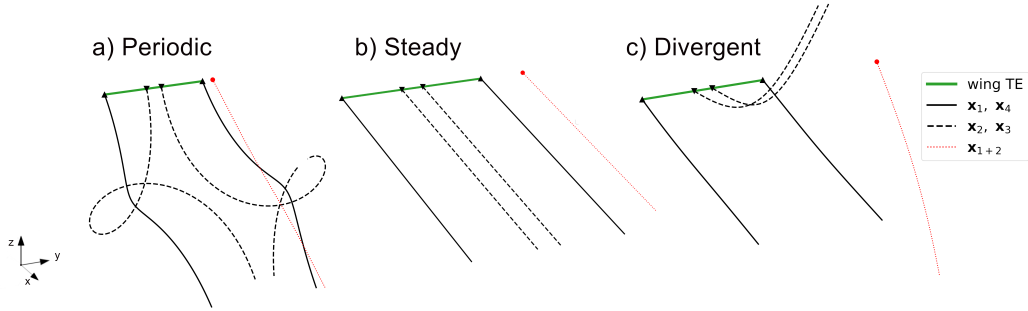


FIGURE 2.18: Illustration of the trajectories of counter-rotating point vortices and the portside barycenter of vorticity in **a)** periodic **b)** steady and **c)** divergent configurations.

Having defined the model of 4-vortex systems used in our study, we now distinguish between the cases where the dipoles in each side of the wake ( $y < 0$  and  $y > 0$ ) are co-rotating or counter-rotating. For each system, their main properties are defined and the expected behavior beyond the wake formation zone is discussed. The focus is on the stability analysis of these flows, drawing upon analytical, numerical, and experimental references [19, 44, 73].

### 2.3.2 Co-rotating 4-vortex systems

Co-rotating vortex systems are characterized by the interaction of vortices with the same rotational direction. Two key aspects of these dynamic systems are the trajectory of the vortices influenced by their mutual velocity induction and the fusion process that occurs in many co-rotating dipoles. Extensive research has explored these phenomena, including the influence of three-dimensional effects. This chapter aims to provide a brief description of co-rotating vortex flows, drawing insights mainly from the works of Meunier & Leweke [61] and of Ortega [73].

Consider two vortices referred to by subscripts 1 and 2. Reynolds number is defined from the mean circulation between both vortices. The degree of interaction between the vortices is most intuitively characterized by the ratio  $R_d/d$ . Configurations where  $R_d/d$  is small behave like two co-rotating point vortices in 2D flow, and their trajectories can be predicted by the system 2.75.

The trajectories of vortices in a co-rotating configuration for two specific cases :  $(\gamma = 1, \beta = 0.5)$  and  $(\gamma = 0.5, \beta = 1.0)$  are illustrated in Fig. 2.19. In this model, the circulation of each vortex is constant over time. Under the influence of the vortices in the opposite side of the wake, the pair descends vertically in the laboratory reference frame as seen in Fig. 2.19a. This is why we plot  $x_1(t)$  and  $x_2(t)$  in a reference frame centered around the barycenter of vorticity  $x_{1+2}(t)$  in Fig. 2.19b. Here, the trajectories exhibit circular patterns. The center of rotation is precisely

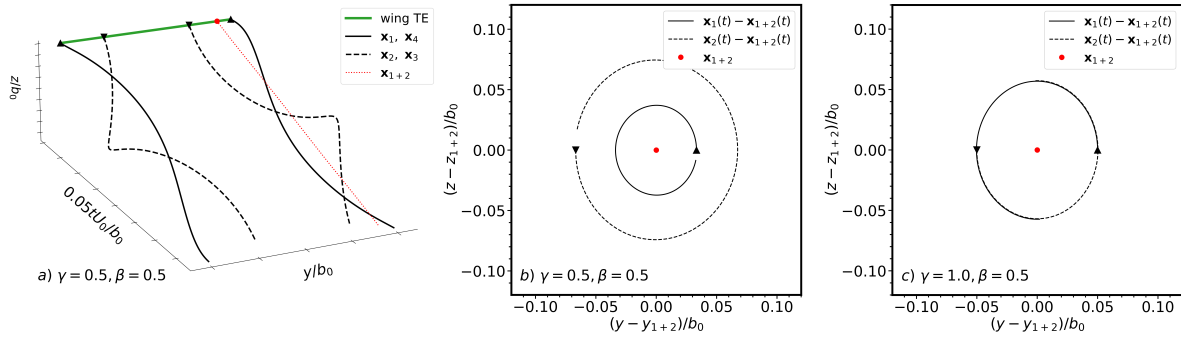


FIGURE 2.19: Trajectories of point-vortices in a co-rotating dipole **a)** in the laboratory frame for configuration  $(\gamma = 0.5, \beta = 0.5)$  and in the reference frame centered around  $x_{1+2}(t)$  for **b)**  $(\gamma = 0.5, \beta = 0.5)$  and for **c)**  $(\gamma = 1.0, \beta = 0.5)$

$x_{1+2}(t)$ . Moreover, the radius of this circular trajectory is determined by the relative strengths of each vortex pair, with the stronger vortex positioned closer to the center of rotation. This is seen by comparing Fig. 2.19b, where  $\gamma = 0.5$  and Fig. 2.19c, where  $\gamma = 1.0$ . The velocity of the pair's orbitation is characterized by  $\Omega_{orb}$ , defined in eq. 2.68. The period of rotation is  $t_{orb}$  (see eq. 2.69).

The orbit motion thus defined is linearly stable [61]. However, in real fluids the vortices radius  $R_d$  grows under the action of viscosity. When  $R_d/d$  reaches a critical value  $(R_d/d)_c$ , the dynamics of the system become more complex as they lead to the fusion of both vortices.

The dynamics of vortex fusion is today a well-studied phenomenon. A key focus of research efforts has been determining the critical value of  $(R_d/d)_c$ . Early studies on this topic include point vortex simulations by Rossow [85]. In more recent work, an analytical framework to study co-rotating systems has been provided by Ortega [73], Crouch[20], and Fabre [29]. DNS studies on vortex merging were carried out by le Dizès and Verga [54] and by Laporte & Leweke [52]. Experimental studies by Meunier and Leweke [61] have involved the generation of equal-strength vortices using parallel plates in a water tank. Ortega[73] and Bristol [12] conducted dye visualizations and PIV measurements of the wake of a wing in a towing tank. Additionally, Breitsamter[8] conducted a wind tunnel study on the wake of a scaled commercial aircraft wing.

When the vortex size is defined by the dispersion radius  $R_d$ , these various studies converge to a critical ratio value close to  $(R_d/d)_c \approx 0.22$  [62]. In what follows, we comment on the characteristics of vortex fusion where  $(R_d/d) > (R_d/d)_c$ . We will analyze the time evolution during merging of the vortex strength and size, of the distance between the vortices  $d$  and of the dipole rotation rate.

At low Reynolds numbers ( $500 \leq Re_\Gamma \leq 2000$ ) the evolution of the dipole is mainly laminar and 2D [8]. During the initial phase of interaction, the vortices are subject to the potential velocity induced by their pair. At first order, the induced field results into a displacement of the vortex centroid and into a deformation. As a result from this displacement, the vortices orbit around each other (as illustrated in Fig. 2.19) With respect to the deformation, there is only strain since the flow is potential. The induced strain field contains a stretching and a compression direction. Thus the vorticity patch deforms into an elliptic shape. This is schematized in Fig. 2.20, here, the magnitude of strain  $s_i$  induced by vortex  $i$  on its pair is a function of their

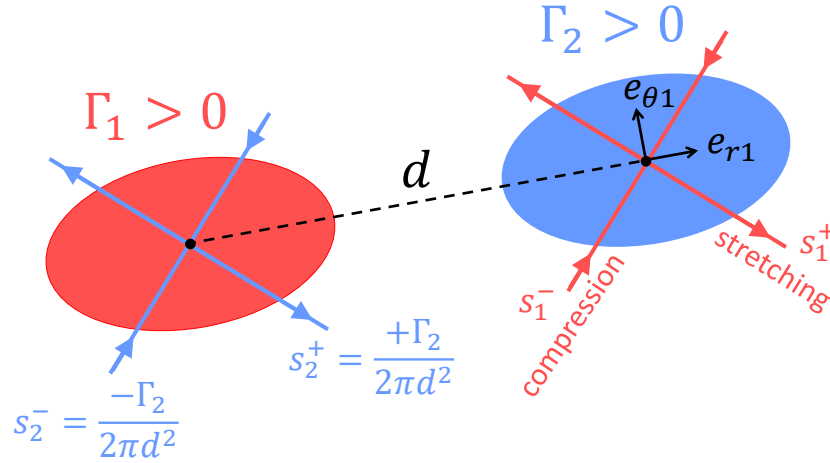


FIGURE 2.20: Schematics of the elliptic deformation entailed by the induced strain fields  $s_i^+$  and  $s_i^-$  in a symmetric co-rotating pair

circulation and distance  $d$  such that

$$s_i^\pm = \pm \frac{\Gamma_i}{2\pi d^2} \quad (2.78)$$

This deformation phenomenon was neglected above under hypothesis 2.74, where we consider vortices to behave like point vortices, but recovers its relevance on the arguments below. Note that the rate at which the vortices orbit, defined in equation 2.68 is now time dependent because of the time dependency of  $d(t)$ . For example, the ellipticity of the vortices brings about a deformation of their orbit trajectory, resulting in a wavering of  $d(t)$  around a mean value as a function of time.

As mentioned above, the vortex radii will grow under the action of viscous diffusion. The moment when  $(R_d/d)_c$  is attained can be considered to be the proper onset of merging, a second stage in the dynamics of the dipole ensues. In the case of  $\gamma = 1$ , each vortex ejects a strong filament of vorticity in a radial direction away from their center of rotation. This ejection creates a significant angular momentum, and this brings the vortices to close-in together because of the conservation of angular momentum. This can be tracked by a sudden drop in  $d(t)$ . Next, the filaments wrap up around the dipole stretching and distributing towards an axisymmetric distribution. This process continues until the two main lobes of vorticity are separated by a distance comparable to the diffusion length. Under the action of viscosity, the final vortex is rendered nearly axisymmetric. The vorticity that was advected away lies around the vortex cores and is smoothed out too during this process, resulting in a final vortex with strong vorticity inside the core surrounded by a low vorticity distribution outside. The profile of azimuthal velocity of such a vortex is non gaussian, but follows a power law  $\propto r^{-n}$  in the region surrounding the core [31]. It is important to note that in general vortices are not of equal strength  $0 \leq \gamma(t) < 1$ . Merger in asymmetric pairs occurs with a well defined transfer of vorticity from the weaker vortex to its stronger counterpart. However in this scenario the onset of filamentation and the role of viscosity remain the main properties of the merging process. Notably, configurations with significant initial strength differences between vortices exhibit more pronounced filamentation, as observed in the experiments of Chen [17]. Some of the filaments coming from the weaker vortex are absorbed by the dominant vortex instead of being advected away, which translates in a decrease

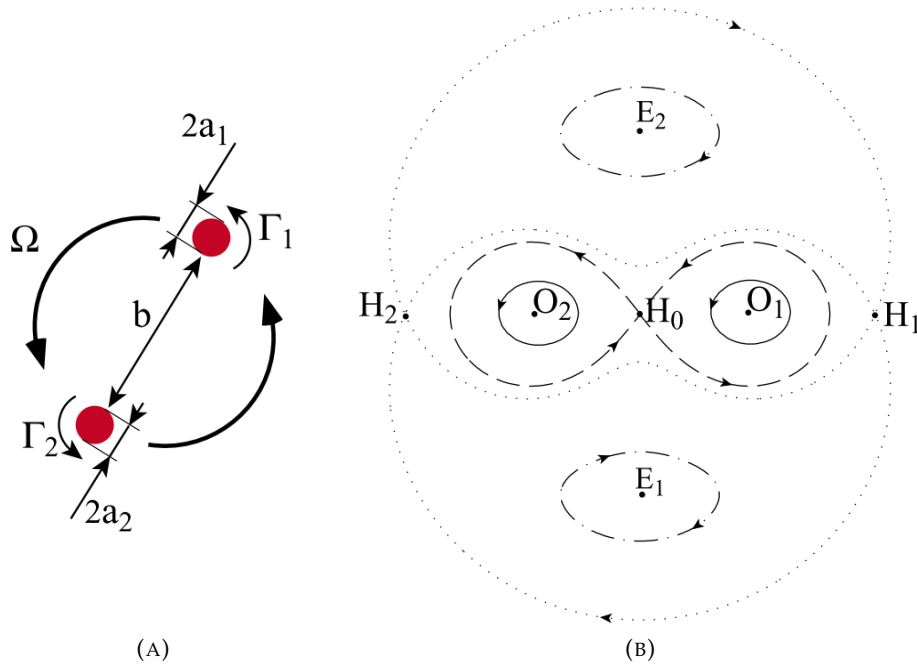


FIGURE 2.21: From [61] : a) System of co-rotating vortices of size  $a_1$  and  $a_2$ , separated by a distance denoted as  $b$  and of circulations  $\Gamma_1$  and  $\Gamma_2$ . b) Streamlines of the flow for two point vortices, in the reference frame rotating with the dipole : vortex positions are denoted as  $O_{1,2}$ , hyperbolic points in the flow as  $H_{1,2}$ , fixed points are denoted as  $E_{1,2}$

of  $\gamma(t)$  over time.

We have seen that at low  $Re_\Gamma$  the onset of merging is characterized by the ejection of vorticity filaments by the vortices in the dipole. Analytical work by Meunier *et al.* [62] provides insight as to why this ejection of vorticity occurs. A diagram of the pair observed in a reference frame turning at rate  $\Omega_{orb}$ , as drawn by Meunier [61] is showcased in Figure 2.21. In this reference frame, the streamlines present characteristic stationary points [61]. For instance, around the position of the vortices, streamlines are elliptic. Most notably, in this reference frame two hyperbolic points  $H_1$  and  $H_2$  appear outside the dipole field. It is found that as the size of the vortex increases, vorticity that reaches the outer hyperbolic point is advected outside of the pair. Vortex filaments are created this way.

Monitoring the distance  $d(t)$  separating the vortices reveals a temporal evolution which depends on the stage of the fusion process. As mentioned above, the temporal evolution of  $d(t)$  results in a temporal evolution of  $\Omega_{orb}(t)$  which can be analyzed through the angle  $\phi(t) = \phi_0 + \int_0^t \Omega_{orb}(t) dt$  formed between vortices and the horizontal direction. The temporal evolutions of  $d(t)$  and of  $\phi(t)$  are plotted in Figure 2.22 and commented below. The wavering of  $d(t)$  has been observed in experiments by Bristol [12] and by Meunier [61] (see the later's results in Figure 2.22a). Note that, in Figure 2.22a,  $d(t)$  seems to decrease abruptly at initial time. This is a consequence of the experimental setting considered in this reference (two parallel plates in a water tank) and should not be considered as a dynamic proper to co-rotating vortices. When fusion is triggered, a sudden and monotone drop of  $d$  is observed as vortices close in together. This can be seen in Figure 2.22a for  $1.0 < t/t_{orb} < 1.5$  for the data obtained at  $Re_\Gamma = 2258$ . Most notably, the evolution of  $d(t)$  during this stage can

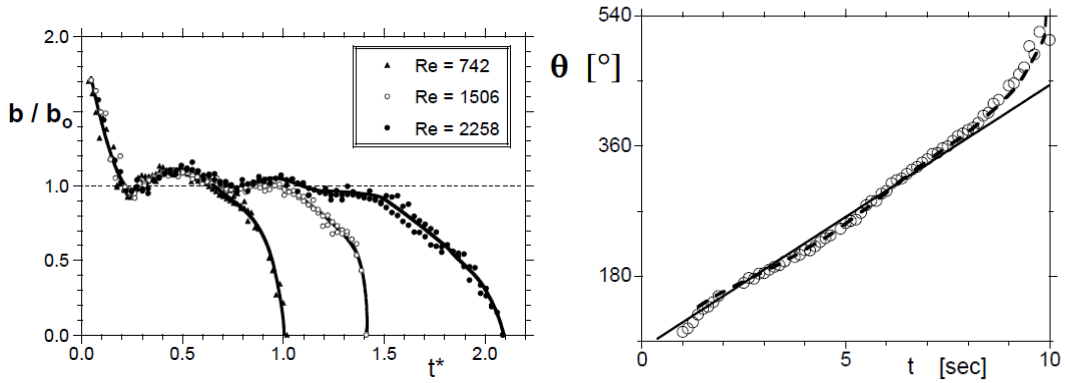


FIGURE 2.22: From Meunier [61] : Temporal evolution during merging of **a**) the separation distance  $b$  ( $d$  in our notations) scaled by the initial separation and of **b**) the orbit angle  $\phi$ , the solid line corresponds to a model for which the pair characteristics is constant and the dotted line takes the temporal evolution of  $d(t)$  into account.

be predicted with precision by modeling the angular momentum of the pair [27, 61], which shows that the behavior of  $d$  is mainly piloted by this invariant of the flow. The temporal evolution of  $\phi(t)$  (white circles in 2.22b) follows the one predicted by the constant angular velocity  $\Omega_{orb}$  from the 2D model (a solid line in the figure) until a critical time here observed at  $t \approx 8s$ . Indeed, when accounting for the impact of the temporal evolution of distance in  $\Omega_{orb}(t)$  (a dashed line in the figure), the prediction is excellent.

To continue describing the physics of vortex fusion, we turn now our attention to the temporal evolution of the core radius distance  $R_d(t)$ . Indeed, we have seen that the viscous growth of  $R_d(t)$  is the main driver that allows the conditions to trigger vortex fusion. Viscous growth of the core can be modeled by that of a Lamb-Oseen vortex following eq. 2.42. This rate of growth can in turn be expressed with respect to the time scale of orbit :

$$\left(\frac{R_d(t)}{d(t)}\right)^2 \propto k_{orb} \frac{\pi^2}{Re_\Gamma} \frac{t}{t_{orb}} \quad (2.79)$$

With  $k_{orb} = 8$  in reference [62]. One can make use of these time scales when appropriate to define an origin of time such that  $\left(\frac{R_d}{d}\right)^2(t = t_o) = 0$ . Finally, one can track the time evolution of  $\frac{R_d}{d}$  to discern stages of the merging process, most notably the proper time at which merging is considered complete. The evolution of  $\left(\frac{R_d}{d}\right)^2$  over the viscous time scale in the experiments and calculations of Meunier *et al.* [62] are shown in Fig. 2.23. We focus first on the case "without instability" (black circles) which occurs at  $Re = 1506$ . The scaled vortex radius is seen to grow abruptly during merging. A similar trend was observed by Breitsamter [8] in a wind tunnel experiment of a co-rotating pair of vortices shed from a scaled commercial wing.

As shown in Fig. 2.23, instabilities may develop at higher  $Re_\Gamma$  and accelerate the time of merging. Indeed, experimental results and full scale observations display fusion times shorter than the ones predicted by the 2D model. In the experiments of Chen *et al.* [17], the author observed that moments of vorticity measured on the plane (orthogonal to the unperturbed vortex axis) were not conserved, which was attributed to tridimensional effects. The three-dimensional dynamics of co-rotating

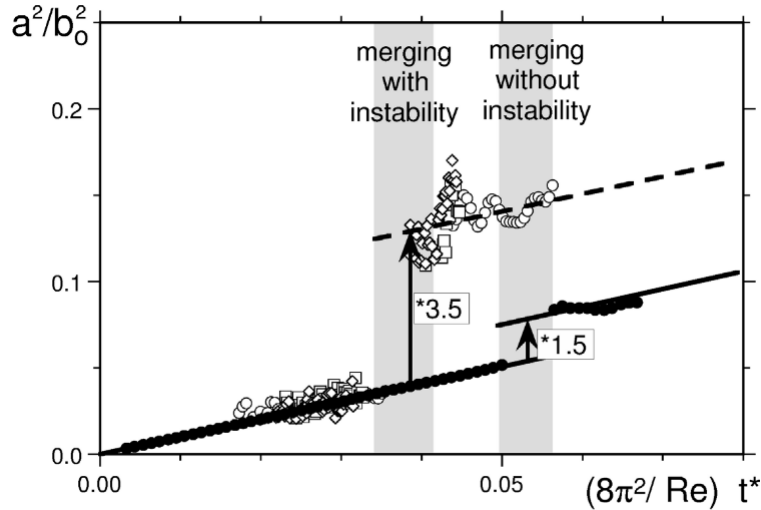


FIGURE 2.23: From Meunier *et al.* [62] : Time evolution of  $\left(\frac{R_d}{d}\right)^2$  for experiments at  $Re = 1506$  ( $\bullet$ );  $Re = 3350$  ( $\circ$ );  $Re = 5000$  ( $\square, \diamond$ ) and for two-dimensional numerical results (solid lines and dashed lines at different Reynolds)

vortex systems have been explored in experiments [8, 11, 17, 61, 89] and instabilities that contribute to the fusion process are consistently identified. Nice visualizations of sinuous deformations, which are a manifestation of these instabilities, occurring in co-rotating vortices of similar strength can be observed in the towing tank experiments of Bristol *et al.* [11]. It has been shown that the addition of axial flow in the vortices does not inhibit the development of these instabilities [89]. In general, the interaction between one of the vortices and the strain field induced by its counterpart leads to the development of elliptical streamlines in the flowfield. As a consequence, the process by which perturbations develop is related to the elliptical instability of Kelvin modes and manifests as a sinusoidal undulation of the vortex core. More specifically, Roy, Leweke & Thompson [89] performed a POD analysis on co-rotating pairs generated during a water channel experiment and found that the unstable mode poses a spatial structure resulting from the interaction of two Kelvin modes which are periodic in the axial direction. Upon characterizing these modes, they found a good match with those characteristic from elliptic instabilities in vortex pairs. Furthermore, linear stability analysis and numerical simulations have demonstrated the role of these instabilities in facilitating faster vorticity transfer from the weaker to the stronger vortex [11]. Experimental measurements of instability growth rates have aligned well with theoretical predictions [11, 61], and so, the accelerated fusion times that have been observed in experiments are usually attributed to the action of elliptic instabilities [17]. It is thought that an elliptic instability will promote fusion because when it grows in at least one of the vortices, vorticity from the vortex whose position is perturbed will more easily reach the other vortex, creating a bridge by which vorticity can be exchanged between the two. This bridge is in turn strained and intensified in the  $(\theta, r)$  plane [11], accelerating the transfer of vorticity from the weaker vortex to the dominant one.

Outside of these observations, the phenomenology of fusion is most similar to the 2D case described before. The separation distance  $d(t)$  decreases rapidly at the

onset of merging suggesting that filamentation occurs and impacts the angular momentum of the pair.  $\left(\frac{R_d}{d}\right)^2$  increases in size but at a faster time and by a larger proportion than in the case without instability (see Fig. 2.23), showing again the role of the instabilities in the acceleration of fusion. The velocity profile of the resulting vortex does display a region  $\propto r^{-n}$  outside of its viscous core, which shows that vorticity was advected outside of the pair during the merging.

### 2.3.3 Counter-rotating 4-vortex systems

Systems of counter-rotating vortex pairs exhibit a strong potential for physical mechanisms that can lead to a significant decay of vorticity in the wake. The study of cooperative instabilities inherent to these systems has received attention with numerical [20, 32, 82] and experimental [74, 96] work. In this section we will describe key results from the litterature in order to show why this type of flow shows promise when developing control strategies to reduce aircraft wake hazard.

We focus our attention on periodic and steady cases, where the vortices stay in close vicinity during large downstream distances. Indeed, in the divergent case, the secondary vortices are expelled far from the main ones, rendering their interaction minimal (see Fig. 2.18c). In periodic cases, the secondary vortices orbit around the main ones, as illustrated in Fig. 2.18a. Cooperative instabilities can develop in these cases as we will show below. In the case of counter-rotating pairs in periodic motion, the distance between the pair is kept small (in the order of the distance between the flap and wing tips) which promotes their interaction. Cooperative instabilities can develop in the manner described previously in section 2.2.3.2.

While this system has the potential to develop instabilities, they do not always result in the formation of vortex rings. Typically, deformation is more significant on the weaker vortex than on the stronger one. This deformation grows until the weaker vortex breaks-up while the stronger vortex is altered but keeps its coherence. Experiments and numerical simulations have explored the altered states that the stronger vortex may exhibit after the weaker one breaks-up. These alterations can involve a net loss of circulation, an enlarged core, or even a streamwise sinusoidal displacement, creating periodic distortions in the vortex cores. This sinusoidal displacement of the main vortices may enable the forcing of specific wavelengths of perturbation, promoting the linking of the main vortices.

Considering this, the scenario where the system of vortices evolves in a steady motion is of particular interest. This case is described by eq. 2.77 and the resulting trajectories of the vortices are illustrated in Fig. 2.18b. Numerical simulations by Reinnich & Lele [82] showed that this specific configuration allows a rapid growth of the long-wavelength perturbations. Indeed, the presence of the inboard vortices enhances the development of the Crow instability between the outboard vortices. As shown by Fabre & Jacquin [30], the growth rate of this mechanism is larger, by an order of magnitude, than that of Crow instability with no inboard vortices present. This renders this wake configuration attractive for control strategies. However, the long-wavelength instabilities are not the most amplified instability in this situation. This implies that this long-wave instability might not develop passively and must be the subject of active forcing. Furthermore, the most amplified instability is a short-wave one, and it provokes the decay of the secondary vortices leading to what could be seen as an unperturbed state for the main ones. Finally, from a practical standpoint, steady motion is an unstable equilibrium point with respect to

2D perturbations, which means that the conditions to generate them are difficult to attain in practice.

We go back to the general case where the conditions for steady motion are not met and the trajectories of the vortices are periodic. It has been observed in experiments that short wave cooperative instabilities would still develop between the inboard and outboard vortices, causing the former to wrap around the later and creating vortex "hoops". Upon dissipation of the weaker vortices the perturbation remaining on the outboard vortices would exhibit a wavelength often too short to excite the Crow instability [32, 75]. Furthermore, when  $\gamma$  is small, the stronger vortices are mostly unperturbed.

It appears that a forcing strategy is necessary if the mechanisms inherent to two counter-rotating pairs are to bring about an acceleration of the linking stage of the main vorticity. An active control strategy exploiting these mechanisms was proposed by Crouch [19].

Although the physical mechanisms that develop in counter-rotating vortex systems make them attractive for wake hazard control purposes, it is important to note that their generation may come with a great cost from the point of view of aerodynamic efficiency. This is easily understood from the conclusions derived from the extended Betz model in section 2.3.1.1. Indeed, to generate opposed signed vorticity close to the wing tip vortex, the span-wise circulation distribution should show a positive derivative in the inboard region. This may be achieved with an inboard flaps-up configuration, but represents a net loss of generated lift for the aircraft. As pointed by Crouch [19], strategies to compensate for this lift loss often result in either a net increase of tip vortex strength or in though constraints for the efficiency or manoeuvrability of the aircraft, rendering the problem of designing a control strategy that exploits counter-rotating vortices unresolved.

### 2.3.4 Higher order instabilities

Recent work on linear parabolized stability analysis provided new insight of the stability of the wake generated by a rectangular NACA 0012 wing. Observing the progression of various unstable modes in the wake, Edstrand *et al.* [28] found that the growth rate of the dominant mode decreased monotonically downstream whereas the fifth mode growth rate became increasingly unstable. As pointed out by Edstrand [28], this behavior relates to the structure of the perturbation generated by each mode downstream. An illustration of the shape of each mode is given in Fig. 2.24. With downstream progression, the fifth mode energy distribution evolves from undulating structures over the wingspan into vorticity streaks counter-rotating with the main trailing vortices with a destabilizing effect. On the other hand, the principal mode, although being most unstable in the near wake, evolves from a perturbation located near the tip of the wing into a vortex region that co-rotates with the main vortex. As stated in previous chapters (see, for example, section 2.2.3.2), a co-rotating flow does not lead to the development of instabilities in the vortex dipole.

Therefore, the location on the wing surface for the optimal perturbation of the wake seems to be distributed over the wing-span instead of focused at the wing-tips. This conclusion was also found by Navrose *et al.* [71, 70], who studied transient growth in the near wake of a wing. In his work, the optimal perturbation is located close to the wing surface and takes the shape of chord-wise periodic structures, with an initial perturbation that decreases from the wing root to the wing tip. Navrose carried out direct numerical simulations (DNS) of the perturbation with finite amplitude, and observed that the perturbation evolves downstream into a wave

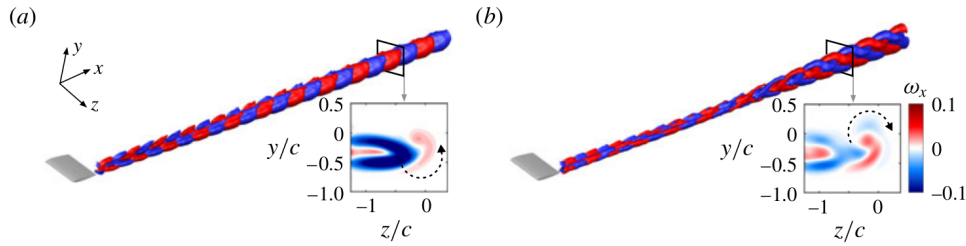


FIGURE 2.24: From Edstrand *et. al* [28] : Isosurfaces and cross-sectional cut of streamwise vorticity  $\omega_x$  for the **a)** principal and. **b)** fifth wake mode in the tip vortex region. Broken arrows indicate the rotation direction of the modes. The main wingtip vortex rotates in the trigonometric direction

packet that migrates to the vortex upon sufficient initial amplitude. The roll-up of the vorticity sheet transports the wave packet into the proximity of the trailing vortex allowing for the interaction between the vortex and the perturbation.

The authors of [28] suggested that the excitation by the higher order modes in the wake of a wing would promote the decay of the circulation and the decrease of the stream-wise vorticity of the trailing vortices hence becoming a more effective wake alleviation method. However, due to the initially weak growth rate of these modes, the wake must be interrogated at a sufficiently far downstream location for the perturbations to evolve into perceivable instabilities. In his work numerical simulations at a Reynolds number of  $10^3$  were used to validate the conclusions found through the stability analysis. These simulations yielded prominent high order mode instabilities after 8 wing-chords downstream in the wake of the wing. Edstrand's work is used as a guide for the experimental study presented in section 4.4.

### 2.3.5 Summary

In this section, we characterize the dynamics of systems of 4 vortices in configurations where pairs in each side of the wing wake are co- or counter-rotating. Instabilities may develop between each vortex in the pair for both situations. The mechanism behind these phenomena is similar to the one obtained from the linear stability analyses of Crow [22] and Widnall *et al.* [101], in that it consists in an annihilation of the stabilizing action of rotation on planar perturbations which are then free to grow under the action of the strain field and cause instability.

Under these constraints, co-rotating pairs are stable to long-wavelength perturbations but can develop short-wavelength elliptic instabilities. Nevertheless, the fate of a co-rotating pair is in general a fusion stage after which a unique vortex still persists in the wake. Instabilities in this scenario do affect the merging phenomenon but do not lead to a significant reduction of the overall vorticity in that side of the wake nor to an accelerated time-to-linking between the vortices in each side of the wake.

Counter-rotating pairs may be destabilized by long-wavelength displacement perturbations. The interaction between the weaker vortex and the dominant one leads to the formation of loops and eventually rings of vorticity in each side of the wake. These rings are oriented in such a way that they self-induce towards the mid-plane and facilitate the exchange of vorticity between each side of the wake. This mechanism is most promising for applications to reduce the wake vortex hazard.

## Chapter 3

# Experimental installation

In this study, a rectangular wing is towed across a water tank. Force probe and stereo-particle image velocimetry (S-PIV) measurements are then used to study the vortex wake which develops downstream from the towed wing. This chapter provides a comprehensive description of the experimental facility (paragraph 3.1), of towing configurations (paragraph 3.1) and of the measurement (paragraph 3.2). During the period of time of this research, different experimental campaigns were conducted. In the following paragraphs the changes that were introduced between the different campaigns (e.g. better equipment) are specified when relevant.

### 3.1 Towing tank facility

The experiment is carried out in the water towing tank of the ONERA Lille research center in Hauts-de-France region, France (Fig. 3.1). The tank features a length of  $L_C = 22\text{ m}$ , a width of  $W_C = 1.5\text{ m}$  and a depth of  $H_C = 1.3\text{ m}$ . The facility permits to tow a rectangular wing model over  $L = 18\text{ m}$  to investigate the development of the wing vortex wake. Near the middle length of the canal ( $X_{PIV} = 11\text{ m}$ ), the velocity field is measured using particule image velocimetry. Also, a 6 component force probe is used to measure the aerodynamic forces and moments generated by the wing during the experiment. The span of the wing model used in this study ( $b_0$ ) is used as the reference length scale. The reference velocity scale is  $U_0$ , which is the constant towing velocity achieved during an experiment, detailed further down.

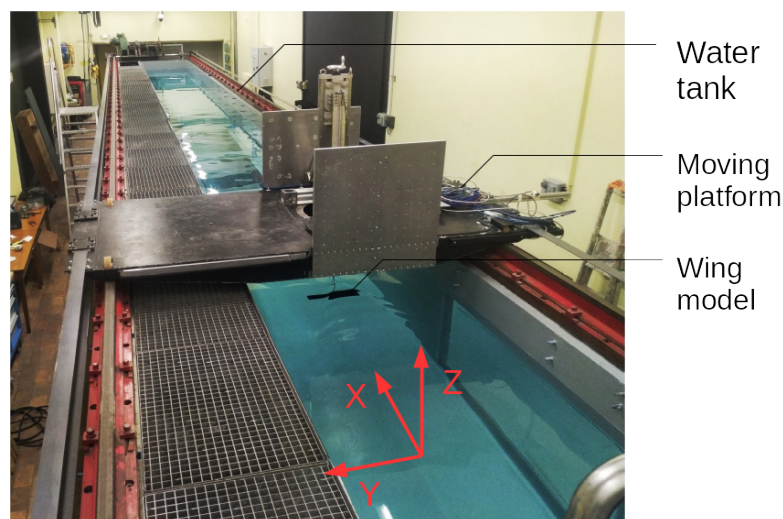


FIGURE 3.1: Towing tank installation

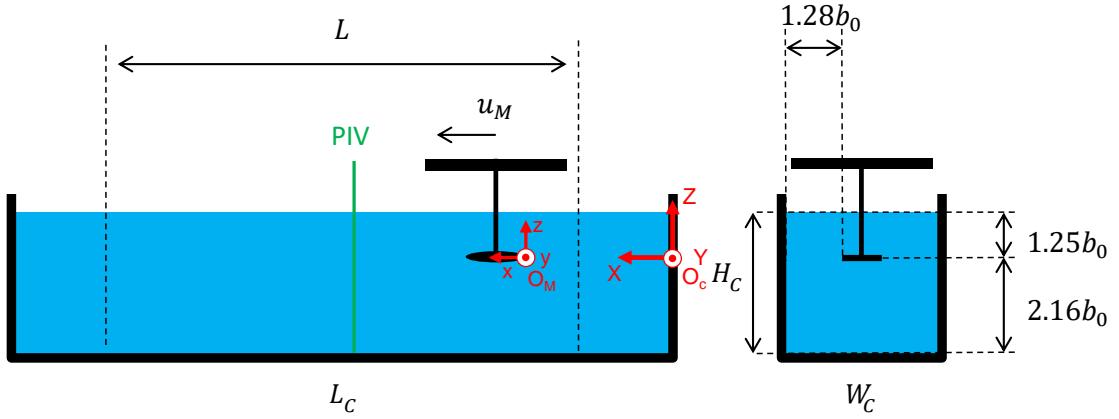


FIGURE 3.2: Towing tank experiment. (left) Side and (right) front views.

A schematic of the experimental facility and setup is given in Fig. 3.2. Two reference frames are used to describe the experiment. The first one is attached to the water tank and is denoted  $\mathcal{R}_C = (O_C, X, Y, Z)$  with  $X$  the towing direction,  $Y$  the transverse horizontal direction and  $Z$  the vertical upward direction. The origin  $O_C$  at  $X = 0$  is located at the right side of the tank. The velocity field is denoted  $\mathbf{v} = (u, v, w)$ . The second reference frame is attached to the model and is denoted  $\mathcal{R}_M = (O_M, x, y, z)$ . The origin  $O_M$  is set at the trailing edge of the model and the mid section of the wing. The force sensor measurements are attached to  $\mathcal{R}_M$  while PIV is achieved in  $\mathcal{R}_C$  at the position  $X = X_{PIV}$ . During a towing experiment the instantaneous position of the model in  $\mathcal{R}_C$  is given by

$$X_m(t_c) = X_m(0) + \int_0^{t_c} u_M(\xi) d\xi \quad (3.1)$$

where  $u_M$  is the instantaneous velocity of the model and  $X_m(0)$  is the initial location of the model close to  $X = 0$ . The time  $t_c$  is the time elapsed from the start of the towing motion. Time  $t$  is defined as the time elapsed from the crossing of the PIV plane by the trailing edge of the wing which occurs at  $t_{c,PIV}$  and  $X_m(t_{c,PIV}) = X_{PIV}$ , such that  $t = t_c - t_{c,PIV}$ . The value of  $t_{c,PIV}$  is repeatable between experiments with the same towing velocity. This is achieved thanks to a synchronization procedure which is detailed in appendix B.4.

### 3.1.1 Baseline wing model

In this work, the wing models consist on a reference configuration, plus configurations that are variations about this reference. The baseline wing geometry and its variations were designed by Moens [64]. The characteristics of the baseline wing model are here described. The main baseline geometry is, then, a wing of rectangular planform of span  $b_0 = 0.4 \text{ m}$  and chord  $c_0 = 0.07 \text{ m}$ , with a NACA 4412 profile. The wing aspect ratio is 5.7. For a given chord-wise station, the span-wise evolution of wing thickness is constant, therefore the wing-tips are not rounded, but sharp-edged. Unless specified, the wings are fabricated with stainless steel and have an impermeable coating. This plain configuration is referred to as *Ref* a photo of which is shown in Fig. 3.3. For most wings of this work, the variations about this reference

are obtained by modifying the spanwise evolution of geometric twist. Each wing model design is detailed in their corresponding chapter.

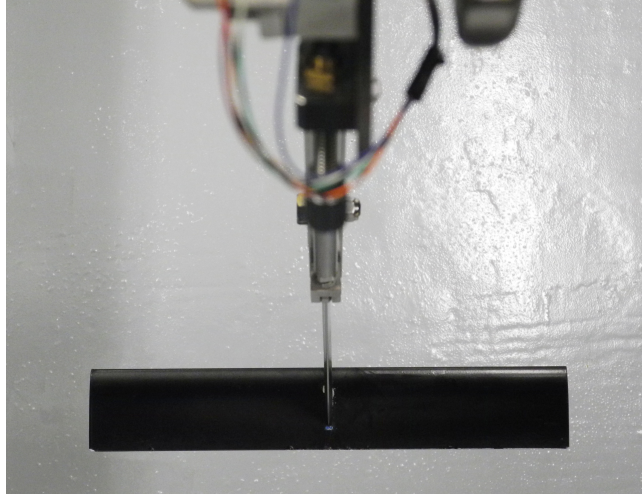


FIGURE 3.3: Top view of the reference (*Ref*) wing design when mounted on the canal.

### 3.1.2 Towing device

During an experiment, the wing model is towed at constant depth  $h$ , constant angle of attack  $\alpha$  and reaches a nominal towing velocity denoted  $U_0$ . Before each run, these parameters are set using the towing device shown in Fig. 3.4. A chariot, sliding over rails over the water tank, ensures the towing motion. A structure fixed on the chariot supports the rest of the devices which are the force probe, a strut and the wing model. The support ensures that the model is positioned symmetrically about the mid-plane ( $O_C XZ$ ) of the water tank. The depth of the model below the free surface of the water is controlled using an endless screw system on the support. Unless specified, this depth is set to  $h = 0.5$  m, representing  $1.25b_0$ . The force probe is then mounted on the support. A profiled strut of length 0.53 m, chord  $0.1b_0$  and faired leading and trailing edges is connected through a pivot to the force probe. The wing model is then attached at the end of the strut so that only the model and part of the strut are underwater. The angle of attack  $\alpha$  is set by pivoting the entire strut. This means that the depth  $h$  of the wing and its axial position vary slightly with the angle of attack of the wing but this variation of  $h$  has a negligible effect on the wake downstream. The angle of attack is set with a precision of  $\pm 0.25^\circ$  thanks to a calibration campaign. More details on the structure and on the calibration campaign are provided in appendix B.1.

### 3.1.3 Operating conditions

The main controllable parameters of an experiment are the wing model geometry, its incidence  $\alpha$  and the constant velocity set for towing  $U_0$ . A *towing configuration*, denoted as  $(wing, U_0, \alpha)$ , is thus defined to characterize each experiment in this study. The towing configurations for the baseline wing model, referred to as *Ref*, are shown in Fig. 3.5. The range of angles of attack ( $\alpha \in [-4^\circ, +24^\circ]$ ) and towing velocities ( $U_0 \in [1, 5]$ ) explored correspond to what is achievable in the experimental facility. The complete set of experiments with the other wing models are enumerated in appendix A.

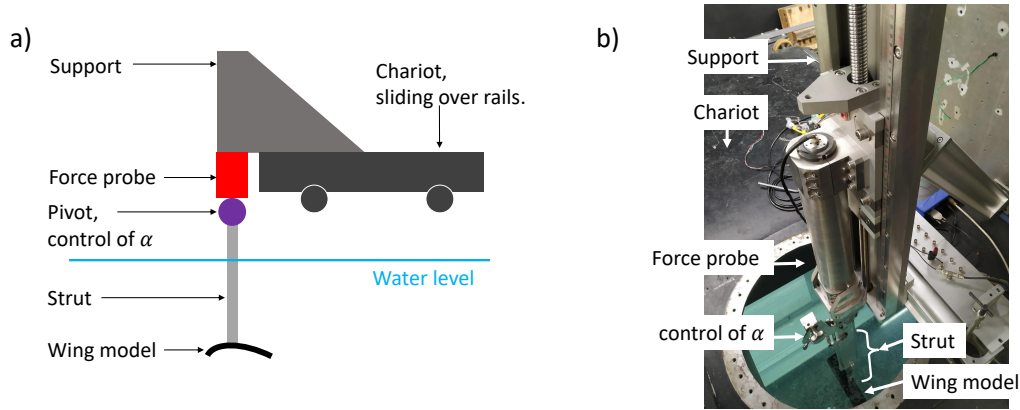


FIGURE 3.4: Structure used to attach the strut and wing ensemble to the chariot. **a)** schematics of the structure **b)** photographs of the structure (S23) as seen from above (left photo) and from below (right photo).

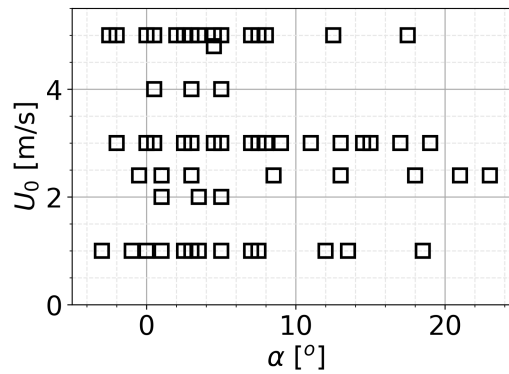


FIGURE 3.5: Experiment database on the baseline wing configuration ( $Ref, U_0, \alpha$ )

The towing of the wing is now described. Towing motion can be divided in three phases : the acceleration phase, the constant velocity phase and the deceleration phase. A typical towing sequence is shown in Fig. 3.6a, with the evolution of  $u_M$  along  $X$ . The towing sequence is adjusted to maximize the useful phase where  $u_M(t) = U_0$ , under the constraints of the towing system and absence of model vibrations. During the acceleration phase, the wing passes a sensor that triggers the acquisition of data. In the experiment shown in Fig. 3.6a, the phase of constant speed  $U_0$  is maintained over approximately  $16m$ . It is worth noting that the towing length  $L$  and the duration of acceleration phases dictate the temporal duration of the vortex wake experiment in the measurement plane. Specifically the abrupt start and stop of the wing generates vortex waves in the trailing vortices that disturb the experiment when these waves reach the measurement plane. These waves are known to travel at approximately the maximum tangential velocity in the vortices, an estimation of which yields  $v_\theta/U_0 \simeq 0.175$  for a towing motion at  $\alpha = 5^\circ$  and the velocity conditions represented in Fig.3.6a. With the half length of the tank being about  $25b_0$ , the effect of the vortex waves is estimated to reach the measurement plane at about  $t \frac{U_0}{b_0} = 140$ .

The velocity measurements during the constant velocity phase are now analyzed. The platform that tows the wing sees a maximum acceleration and deceleration of

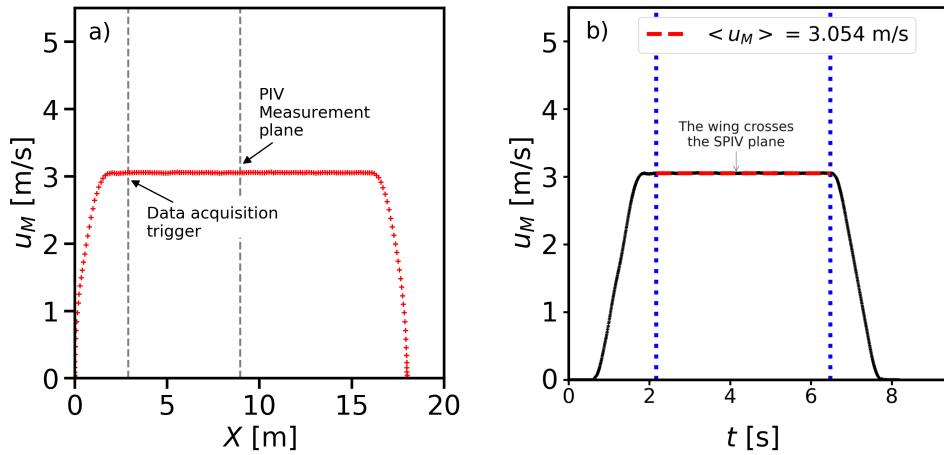


FIGURE 3.6: Platform velocity for an experiment where the reference wing is towed at  $U_0 = 3\text{ m/s}$  and  $\alpha = 0.5^\circ$ . **a)** Evolution of  $u_M$  along station  $X$  during the experiment and **b)** Time evolution of  $u_M$ . The duration of the constant velocity phase is shown by blue dotted lines and the mean value recorded during this period is shown by a red dashed line.

$3.125\text{ m/s}^2$  at the beginning and end of its course. Let  $t_1$  mark the end of the acceleration phase and  $t_2$  mark the beginning of the deceleration phase.  $t = 0$  is the instant when the platform begins its movement. A closed-loop control system is equipped on the platform commands. This causes the platform velocity  $u_M(t)$  to oscillate around its real nominal velocity  $U_0$  from  $t = t_1$  to  $t = t_2$ . The real nominal velocity  $U_0$  may differ from the target velocity by up to 1.8% which is due to the precision of the installation equipment. However, velocity measurements during this phase have a dispersion of 0.001% of  $U_0$ , thus we denote the period  $t_1$  to  $t_2$  to be the constant velocity phase. The platform velocity recorded during an experiment where the target velocity is  $U_0 = 3\text{ m/s}$  is shown in Fig. 3.6b. In this example, the constant velocity phase lasts from  $t_1 = 2.4\text{ s}$  to  $t_2 = 6.7\text{ s}$  and it is indicated by vertical blue dotted lines in the figure. The real nominal velocity is  $U_0 = 3.054 \pm 0.003\text{ m/s}$ .

## 3.2 Measurement setup

### 3.2.1 Aerodynamic force measurements

The aerodynamic forces ( $F_x, F_y, F_z$ ) and moments ( $M_x, M_y, M_z$ ) generated by the water on the wing are measured using a 6-components force probe. Schematics of the directions of forces and moments are provided in Fig. 3.7. An AMTI-MC3A force probe model is used during the first and second campaigns and for the third campaign a PHI-70 force probe is used. The different aspects regarding calibration of the probes are detailed in appendix B.2. A summary of this calibration process is provided here : Before the experimental campaign, the force probe signal is calibrated in laboratory conditions using well calibrated weights and accounting for the coupling factors between the sensor channels. Then, measurements of the forces applied by the air and water on the isolated strut (with the wing removed) are performed. In particular, this allows for the identification of the drag and pitching moment generated by the strut as a function of towing velocity. During an experiment, the towed chariot translates on rails, which ensures a smooth ride and negligible vibrations.

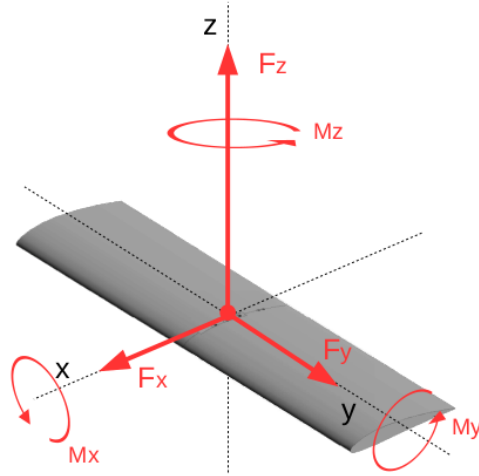


FIGURE 3.7: Schematics of the directions of aerodynamic forces and moments.

The data acquired by the force probe is then post-processed : Random drift of the probe is corrected using data recorded before the beginning of the chariot movement. The drag and pitching moment generated by the wing is then obtained after subtraction of the forces due to the strut, neglecting interference effects between the strut and the wing. Aerodynamic force coefficients are obtained as follows :

$$C_x = (F_x - F_{strut}) [0.5\rho U_0^2 S]^{-1} \quad (3.2)$$

$$C_y = F_y [0.5\rho U_0^2 S]^{-1} \quad (3.3)$$

$$C_z = F_z [0.5\rho U_0^2 S]^{-1} \quad (3.4)$$

With  $S = b_0 c_0$  and  $\rho$  the water density. Water density is affected by the variations on water temperature [41]. The water temperature recorded in the canal during a given time frame of the experimental campaign is shown in Fig. 3.8. The temperature fluctuates during the campaign within the range  $C^\circ \in [15^\circ, 21^\circ]$ , the resulting variation in density ( $\rho \in [1000, 998] \text{kg/m}^3$ ) is negligible for our study. Therefore, a constant value  $\rho = 1000 \text{kg.m}^{-3}$  is set for consistency.

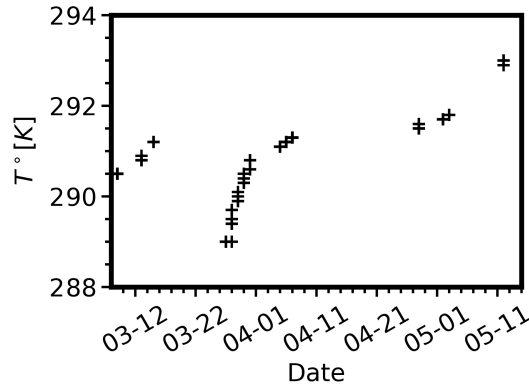


FIGURE 3.8: Water temperature recorded in the canal during a time-frame of year 2023.

The measurement uncertainty of the force probes is determined based on the

maximum nominal load of each load cell. This information must be obtained through a calibration campaign in which precisely controlled loads are applied into the measurement channels of the probe. The results of this calibration are provided by the probe manufacturer. Furthermore, we perform our own calibration campaign in order to verify the good functioning of the probe. This is further detailed in appendix B.2. The corresponding maximum loads and uncertainty for each component are provided in table 3.1. The measurement voltage amplitude is  $\pm 5 V$  on the *AMTI-MC3A* model and  $\pm 4 V$  on the *PHI-70* model. The appropriate gain is then applied to obtain the force measurement. Since the magnitude of forces measured during the experiments varies significantly across different towing configurations, the accuracy of the aerodynamic coefficients also differs. For an experiment realized at  $U_0 = 3 m/s$ , the uncertainty on  $Z [N]$  translates to an uncertainty of  $\Delta C_z = \pm 0.017$  for the *AMTI-MC3A* probe and of  $\Delta C_z = \pm 0.024$  for the *PHI-70* probe, which is satisfactory for our purposes.

Probe	Acquisition Frequency		Uncertainty						
	$U_0 [m/s]$	$f_{acq} [Hz]$	$err [\%]$	$X [N]$	$Y [N]$	$Z [N]$	$M_x [N.m]$	$M_y [N.m]$	$M_z [N.m]$
AMTI-MC3A	1	5000	0.2%	$\pm 1.1$	$\pm 1.1$	$\pm 2.2$	$\pm 0.06$	$\pm 0.06$	$\pm 0.03$
	3	5000							
	5	5000							
PHI-70	1	1000	0.01%	$\pm 1.0$	$\pm 1.2$	$\pm 3$	0.01	0.02	0.01
	3	3000							
	5	5000							

TABLE 3.1: Characteristics of force probes

Force measurements during an experiment are realized at a high acquisition frequency (between 1000 and 5000  $Hz$ ). The sampling rates of force signals are provided in table 3.1. Analyzing the brute signals is necessary to quantify the variability of aerodynamic efforts and moments during the constant velocity phase. An example of brute measurements of  $F_z$  is shown in Fig. 3.9. To exclude the noise associated to the force probe from the measurements, a running mean procedure is applied. This acts as a low-pass filter over the brute signals. On the convolved signals, the standard deviation of the lift force measurements during towing is on the order of 1% of the averaged value, thus validating the conditions during the towing motion.

### 3.2.2 Velocity field measurements

The wake of the towed wing is characterized by the three components of the velocity field in the transverse plane ( $O_C YZ$ ), which we measure using Particle Image Velocimetry. PIV software reconstructs the velocity field  $\mathbf{v} = (u, v, w)$  by analyzing consecutive images taken with a short time interval  $dt$ . The displacement of particles between successive images is estimated to calculate the velocity. This methodology is thoroughly explained in reference [80]. In summary, by comparing images taken at time  $t$  and  $t + dt$  within an interrogation window, the displacement (denoted as  $d$ ) is computed using a correlation function, and the velocity is derived from it. In our work, a stereoscopic PIV setup is used with two cameras placed on either side of the measurement plane, allowing for measurement of the axial component ( $u$ ) in addition to the in-plane velocities ( $v$  and  $w$ ). This is denoted 2D-3C measurement.

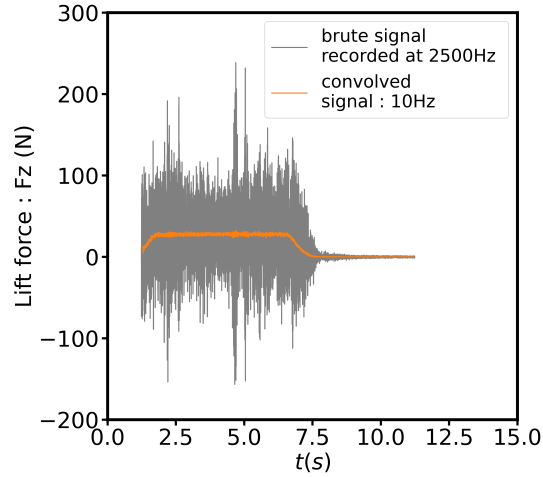


FIGURE 3.9: Brute and filtered signal of  $F_z(t)$  measured by the force probe for an experiment where the reference wing is towed at  $U_0 = 3\text{ m/s}$  and  $\alpha = 0.5^\circ$ .

The elements of the PIV installation and the software employed are described in paragraphs 3.2.2.1 and 3.2.2.2, respectively. The measurement resolution is compared to the physical scales of the flow in sec. 3.2.2.3. Additionally, the PIV uncertainty is assessed in appendix C.

### 3.2.2.1 PIV installation

PIV requires that the water tank is seeded. The tank is filled with water previously filtered to remove unwanted particles. The water is then seeded with polyamid particles of diameter  $\varnothing = 20\ \mu\text{m}$  and density  $\rho_p = 1.03\ \text{g/cm}^3$ . This seeding configuration is based on the setup of a similar experiment [13]. Furthermore, a numerical study is used to investigate the effect of  $\varnothing$  on the PIV uncertainty (see appendix C), confirming that this particle diameter is adequate for our purposes. Between two experiments, a wait time of 20 minutes at minimum is imposed so that the tank water can return to still conditions.

The PIV acquisition is automatically triggered when the trailing edge of the wing pass a gate located 5 m upstream of the measurement plane. This ensures the acquisition of images from the moment the wing reaches  $X_{PIV}$ . Illustrations of the PIV camera setup are provided in Fig. 3.10. This setup consists of two LaVision sCMOS cameras equipped with 35 mm lenses and a 380 mJ Nd:YAG laser. To minimize refraction at the air-water interface, water-filled prisms are placed on the surface of the PMMA window at the sides of the tank. Illustrations of these elements are provided in Figs. 3.10b and 3.10a.

The cameras are equipped with a  $2560 \times 2160$  pixel sensor size and their field of view can be adjusted using specific settings. The viewing angle is primarily determined by the prism angle as the cameras align parallel to the prism plane. Modifying the prism incident angle allows for an extension of the width of the field of view. Furthermore, the lateral or vertical displacement of the field of view can be fine-tuned by adjusting the distance between the cameras and the laser plane or their respective heights.

The images acquired during the experiments suffer from perspective deformations. Therefore a calibration procedure is realized prior to the experiments in order to produce a *dewarp* function that allows for image correction. The calibration

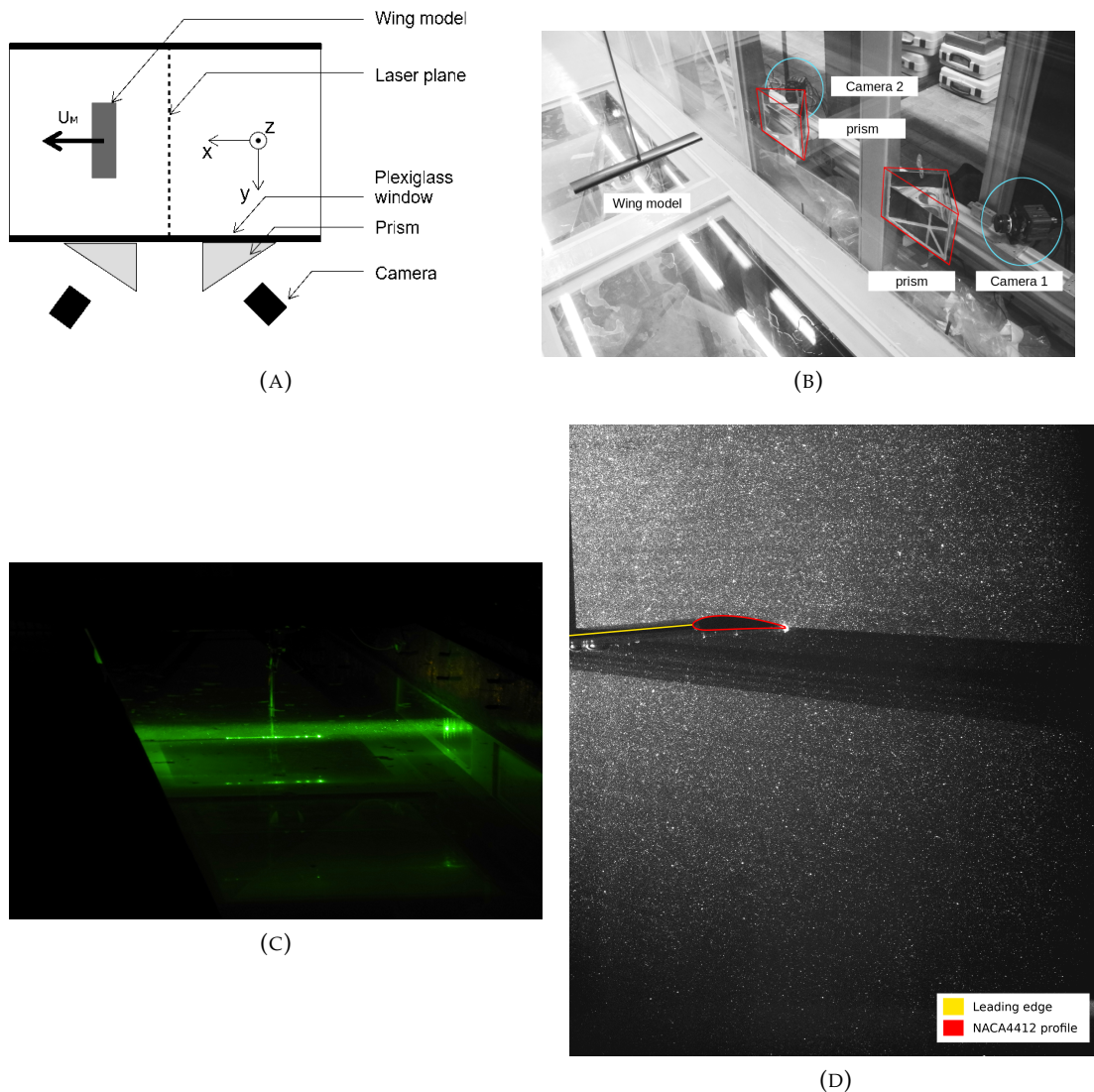


FIGURE 3.10: Image acquisition setup : a) photograph of the camera setup in dry conditions, b) top view schematics of the PIV setup, then views of the wing trailing edge illuminated by the laser plane c) as seen from the laboratory, of the and d) as seen through the PIV camera (frame  $d$ ).

methodology is thoroughly described in appendix B.3. In summary, a calibration target is positioned at the measurement plane, parallel to the wing's trailing edge. Images of this target are captured then analyzed using the AFFIX 2 software in order to determine the *dewarp* function.

Precise alignment of the laser plane with the measurement plane is essential. This alignment is initially achieved by orienting the laser plane with the calibration target. The alignment is then further refined by analyzing images of the plane using the calibration and PIV softwares. The laser plane is therefore parallel to the wing's trailing edge, as depicted in Fig. 3.10c (captured during an alignment test). Figure 3.10d displays a PIV image taken simultaneously. It can be observed that seeding conditions seem optimized, ensuring even particle distribution and minimal particle clumping, with the exception of one adhering to the trailing edge (which has no

impact on PIV results). This is verified quantitatively by the correlation field in quiescent flow (an illustration of this field can be seen in Fig. B.11). Nevertheless, the diffusion of the laser light in the water medium results in an illumination gradient along the  $Y$ -direction. To compensate for this gradient, adjustments to the laser intensity are made to optimize the lighting conditions in regions where vortex evolution is anticipated (this covers particularly the center of the field captured in Fig. 3.10d).

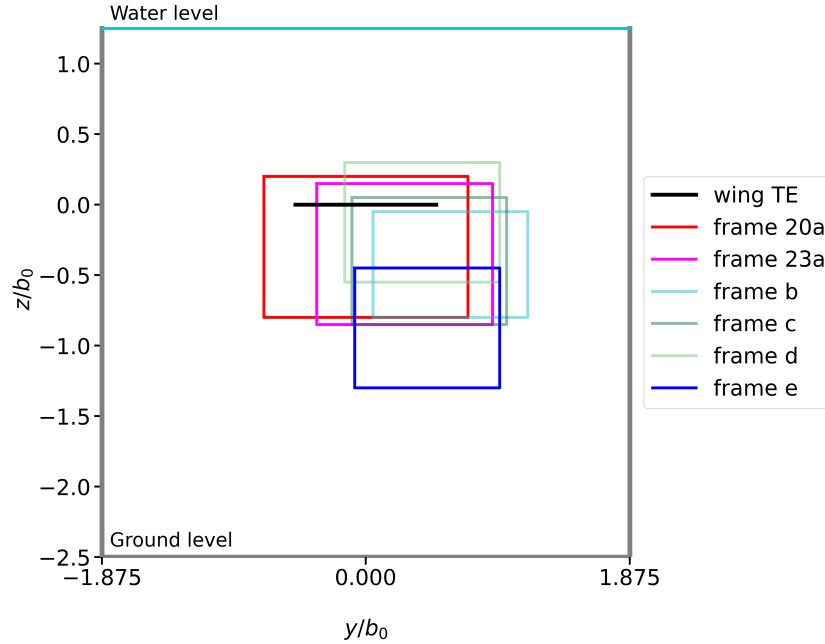


FIGURE 3.11: Dimensions of PIV frames used during the experimental campaign.

During the experimental campaign, different field-of-view settings (referred to as frames) were used, as depicted in Fig. 3.11. Each frame's specific positioning and dimensions were chosen based on the intended observation goals and requirements of the experimental campaign. Here are the key characteristics of each frame:

1. *Frame 20a*: This frame is centered around the tank mid-plane, slightly above the model. This frame is characterized by its width of  $1.45b_0$  which is due to a prism incident angle of  $37^\circ$ . This wide width allows us to capture the entire span of the wake but has an adverse effect on the PIV optical conditions, as will be demonstrated below. The height of the window is  $1b_0$ , allowing for tracking of both tip vortices descent for approximately  $0.8b_0$  until they reach the bottom frontier. Further descent causes the vortices to cross the bottom frontier, ending the measurements. In this frame, the mean pixel resolution is  $\Delta px \sim 2.34 \times 10^{-4} \text{ m/px}$ .
2. *Frames 23a, b, c, and d*: These frames have a prism incident angle of  $45^\circ$ , resulting in better optical conditions for PIV but resulting in a reduced width compared to frame 20a. Frame 23a is therefore centered around the right wing tip and primarily focuses on studying the wake formation zone of the wing models. It also allows for the investigation of the wake stable zone until vortices reach  $z = -0.85b_0$ . The width of the frame is  $1.25b_0$ . Frames *b, c, and d* have similar dimensions but are positioned with offsets, as they were used to

track vortices with strong upward or sideways trajectories. In this frame, the mean pixel resolution is  $\Delta px \sim 2.03 \times 10^{-4} m/px$ .

3. Frame  $e$ : This frame shares the same characteristics as frame 23a but it is located at a distance of  $-0.45b_0$  below the wing model. It enables tracking of the vortex until  $z = -1.3b_0$ .

### 3.2.2.2 PIV software

The ONERA FOLKI software [16, 55] is used to reconstruct the velocity fields. This PIV software uses a modified iterative wrapping scheme analog to the dense Lucas-Kanade algorithm, details about this algorithm are provided in [53]. In summary, FOLKI utilizes GPU processing to evaluate velocity vectors around each pixel in the image, creating a *dense field*. Rather than employing the traditional FFT-based correlation function [80], it calculates a correlation measurement using a non-linear least squares criterion between the field of initial particle positions  $\mathbf{X}$  and the field of displaced particle positions  $\mathbf{X} + \Delta\mathbf{X}$ . Let  $I^i$  be the 2D field of intensity recorded by camera  $i$ .  $I^i$  is a 2D matrix and  $\mathbf{k} = [k, l]^t$  are its grid point indices.  $\mathbf{X}_\mathbf{k}$  is a grid point in this plane, and  $\mathcal{W}_\mathbf{k}$  a squared interrogation window centered around  $\mathbf{X}_\mathbf{k}$ . The 2D plane positions and displacement  $\mathbf{X}_\mathbf{k}$  and  $\Delta\mathbf{X}(\mathbf{k})$  are corrected from perspective deformations (related to the camera view) through a transformation denoted  $F(\cdot)$ . More specifically,  $x_k^i = F^i(\mathbf{X}_\mathbf{k})$  is used where  $F^i(\cdot)$  is the nonlinear projective transformation obtained from the camera stereoscopic calibration. The 3C displacement  $\Delta\mathbf{X}$  that we seek to measure is directly obtained as the minimizer of the criterion :

$$\sum_{i=1}^2 \sum_{k' \in \mathcal{W}(k)} \left( I^i(x_{k'}^i, 0) - I^i(x_{k'}^i - \nabla F^i \Delta\mathbf{X}(\mathbf{k}), dt) \right)^2 \quad (3.5)$$

Note that  $\Delta\mathbf{X}$  refers to the particles contained in  $\mathcal{W}_\mathbf{k}$ . FOLKI implements this algorithm within a multi-resolution pyramid framework, where each level represents a lower-resolution version of the image being processed. This approach significantly reduces computation time. However, not all the calculated vectors (one per pixel) are utilized in the final output grid. Instead, they are decimated, with only one vector selected, for example, every 32 pixels.

### 3.2.2.3 Analysis of the measurement resolution

**Inter-frame time  $dt$  :** To accurately track particle displacements, it is crucial to select an inter-frame time that is consistent with the expected vortex velocity and time scales. This is because particles are expected to displace following the flow velocity field from  $t$  to  $t + dt$ . Therefore,  $dt$  is set so that this displacement covers one-fourth of the interrogation window, ensuring optimal conditions for PIV measurement. Squared windows of size 32x32 pixels are used here to process the PIV images. As a result, the expected optimal displacement of a particle is  $d_{opt} = (8\Delta px) m$ , where  $\Delta px$  is the resolution of the image, in  $m/px$ .

To determine the optimal inter-frame time  $dt_{opt}$ , the velocity at a distance  $r$  from a vortex centroid, denoted as  $v_\theta(r)$ , is estimated. The vortex velocity field scales as  $\Gamma/2\pi r$  outside the vortex core. An illustration of the particle displacement measurements around a *Ref* vortex is provided in Fig. 3.12b. The data used to set  $dt$  is extracted on a region outside the vortex core (point  $p_3$  in Fig. 3.12b). This allows to draw a compromise between the maximum velocities near the core (point  $p_4$ ) and

minimum velocities far from the core (point  $p_1$ ). For the *Ref* vortices, a suitable location that meets these conditions is  $r = 0.05b_0$ .

Thus, the estimated optimal inter-frame time is calculated as  $dt_{opt} = d_{opt}/v_\theta$ . The values of  $dt$  set for the experiments with the *Ref* configuration are shown in Fig. 3.12a. Data is plotted as a function of  $Re_\Gamma$ , which is an indicator of  $v_\theta$ . The process of determining  $dt$  for a specific towing configuration involves trial and error, starting with  $dt_{opt}$  (represented by a red dashed line in Fig. 3.12a) as an initial condition. Experiments where the chosen  $dt$  does not yield satisfactory results (not shown in Fig. 3.12a) are discarded.

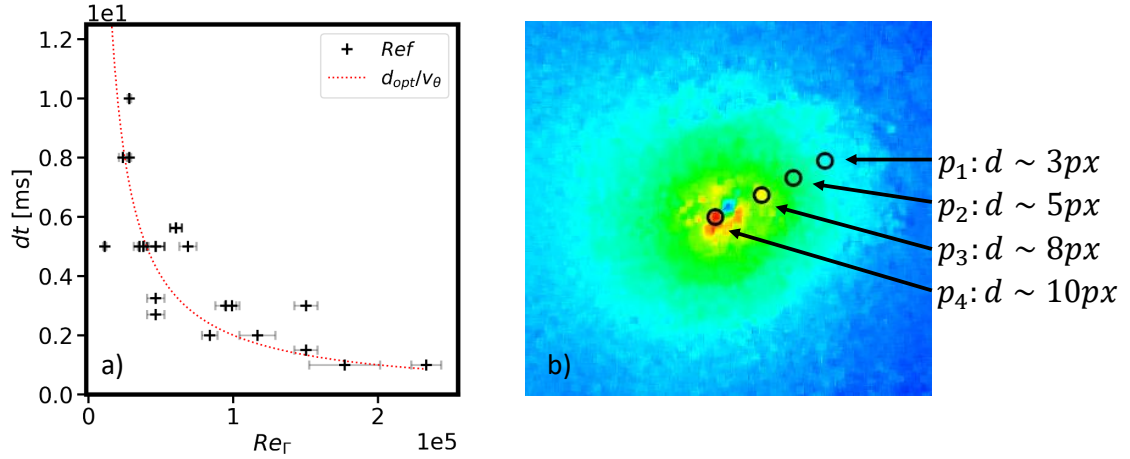


FIGURE 3.12: **a)** Inter-frame separation time  $dt$  for experiments with the baseline wing model as a function of vortex Reynolds number  $Re_\Gamma$ , **b)** measured particles displacement  $d$  on a *Ref* vortex ( $Re_\Gamma = 0.4 \times 10^5$ ,  $dt = 3.25ms$ )

**Spatial resolution  $\Delta x$  :** The spatial resolution of measurements is analyzed based on the characteristic scales of the vortices in this flow. Indeed, data is acquired over a cartesian 2D grid of measurement points, denoted a measurement grid, characterized by  $\Delta x$  which is the step from one point to its neighbour. The average spatial resolution for frames 20a and 23a (shown in Fig. 3.11) is approximately  $\Delta x = 1.29 \times 10^{-3}$  m and  $\Delta x = 1.95 \times 10^{-3}$  m, respectively. The grid resolution is coarser on frame 23a than on frame 20a. This is a deliberate choice made to ensure better correlation conditions. The characteristics of frames b to e are the same as those of frame 23a as described above.

The grid resolution is compared to a length scale of the vortex, which is its core radius  $R_a$ . The vortex exhibits high velocity gradients from the centroid to  $R_a$ , so a high resolution in this region ensures precise localization of the vortex centroid. Within 10 normalized time units after the passage of the wing through the measurement plane (i.e. when the vortex is smaller)  $R_a$  is on the order of  $0.03b_0$ . This results in a resolution of approximately  $R_a/\Delta x_{20a} = 9$  and  $R_a/\Delta x_{23a} = 6$ , which is enough to measure the vortex field as it is shown further down in sec. 4.2.1.

**Sampling rate  $f_{PIV}$  and duration of the experiment  $t_{max}$  :** In this paragraph the time resolution of the measurements is compared to the physical time scales of the flow. The PIV measurements are conducted at a frequency of  $f_{PIV} = 5$  Hz for experiments in frame 20a and 10 Hz for the remaining experiments. In the chosen towing velocity range the snapshot recording frequency of 5 Hz corresponds to a Strouhal

number of  $f_{PIV}b_0/U_0 = 2$  and  $0.4$  respectively for the lowest and highest velocities. When  $f_{PIV} = 10$  Hz,  $f_{PIV}b_0/U_0 = 4$  and  $0.8$  respectively.

Based on this sampling rate and on the measurement grid resolution  $\Delta x$ , the reliability of the measurement of vortex displacement is assessed. Indeed, the vortices descend vertically due to mutual induction at velocity  $W_d$ . In scenarios where the ratio  $\frac{W_d}{f_{PIV}\Delta x}$  is small, the descent of the vortex may not be well captured between two measurements. In these experiments,  $W_d$  ranges between  $W_d = 0.004$  m/s and  $0.060$  m/s (Chapter 4). Consequently, low descent velocities cover a distance of approximately  $\frac{W_d}{f_{PIV}\Delta x} = 0.6$  and  $0.2$  grid points per measurement for frames  $20a$  and  $23a$ , respectively. On the other hand, high descent velocities cover a distance of approximately  $\frac{W_d}{f_{PIV}\Delta x} = 9.3$  and  $3.0$  grid points per measurement for frames  $20a$  and  $23a$ , respectively. The measurement of vortex descent is therefore insufficiently resolved at the lowest descent velocities. However, the computation of  $W_d$  is improved upon by performing measurements over a large time frame and comparing the results to analytical predictions (see, for instance, eq. 2.72).

In some experimental configurations (e.g., *HL* and *CoR* wings), a significant physical event is the fusion of co-rotating vortices. This occurs over a time scale denoted  $t_f$  which is now compared to the PIV sampling rate. The fusion time can be scaled as  $t_f \frac{U_0}{b_0} \sim 6$ . For frame  $20a$ , the physics of the wake can be resolved when  $U_0 = 1$  m/s, providing approximately  $t_f f_{PIV} = 12$  measurements before fusion. However, when  $U_0 = 5$  m/s, there might be only a few more than 2 measurements available before  $t_f$ , resulting in limited data.

### 3.2.2.4 Analysis of the measurement accuracy

**Physical factors that lead to measurement degradation :** The correlation score in PIV measurements is directly affected by the concentration of seeding particles. Previous studies [80, 48] determined the minimum number of particles required in an interrogation window to achieve a valid detection probability of  $\geq 95\%$ . In the context of single exposure/double frame PIV, where there is no loss of particles between one frame and the next, it is found that 5 particles in the interrogation window are sufficient. Increased seeding often leads to improved accuracy. In the present experiments, the particle concentration is approximately 8 within a window of  $32 \times 32$  pixels. The impact of seeding density, denoted as  $N$ , on PIV accuracy in this measurement setup is thoroughly analyzed using numerical simulations, as detailed in appendix C. The key finding is that the PIV error related to seeding density tends to converge for values of  $N \geq 2 \times 10^5$  particles per square meter, which is approximately the observed density in our PIV images.

However, it is important to note that the measurement at the center of a vortex is affected by a lower seeding density compared to the rest of the flow. This phenomenon is often attributed to centrifugal forces, which tend to expel particles away from the vortex centroid. Nevertheless, due to the presence of cyclostrophic equilibrium in the vortex, these centrifugal forces are counteracted by a pressure gradient that draws particles towards the centroid, enabling measurements even at high rotational velocities. Additionally, during our experiments, high axial flow may develop within the vortex core, posing a significant challenge. Axial flow causes particles within the core region to exit the laser plane perpendicularly between consecutive frames, rendering correlation computation impossible. To address this issue, it is necessary to reduce the inter-frame time interval ( $dt$ ). However, reducing  $dt$  can

also impact the correlation computation of in-plane displacements of particles outside the core region. Therefore, a compromise is found by adjusting  $dt$  through trial and error until both axial and azimuthal velocities are accurately resolved. In some extreme cases, it may be impossible to accurately measure the flow due to these limitations, which leads to discarding the measurements.

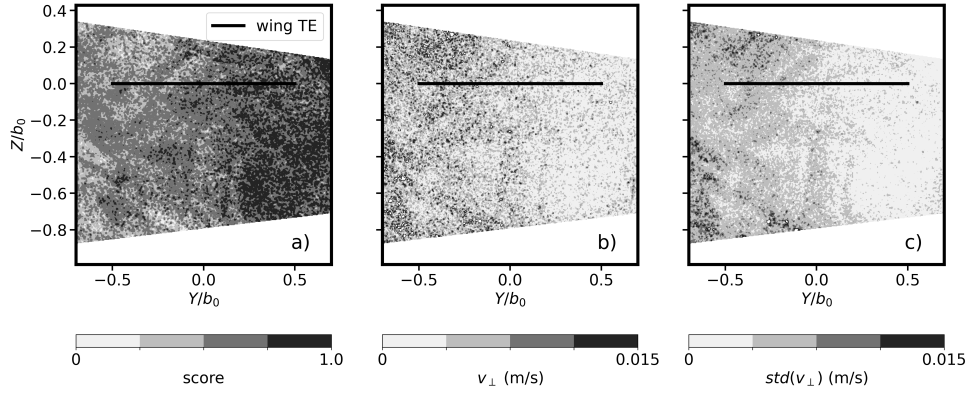


FIGURE 3.13: PIV measurements of quiescent flow ( $t_C = 1s$ ) on frame 20a. **a)** correlation score, **b)** in-plane velocity magnitude and **c)** standard deviation of  $\langle v_{\perp} \rangle$  computed over 1s. The expected position of the wing trailing edge is represented by a thick line.

Another important point is that the measurement uncertainty differs between sides, being larger on the left side ( $Y < 0$ ) compared to the right side ( $Y > 0$ ). This discrepancy is quantified as a degradation of approximately 20% in the correlation field data on the left side in comparison to the right side. An example of the correlation field for frame 20a in quiescent fluid is shown in Fig. 3.13a. The time evolution of the average of correlation score on each side of the field ( $Y > 0$  or  $Y < 0$ ), plotted in Fig. 3.14a reveals that, previous to the passage of the wing, the mean score is about 0.55 for  $Y > 0$  and increases to 0.7 for  $Y < 0$ . This difference can be attributed to two factors. Firstly, the left side is located further from the PIV cameras, which are positioned on the opposite side of the tank. Consequently, the optical path for the left side is more inclined compared to the right side. Secondly, the gradient in lighting along the  $y$  axis contributes to this degradation, with the left side receiving more light than optimal for PIV.

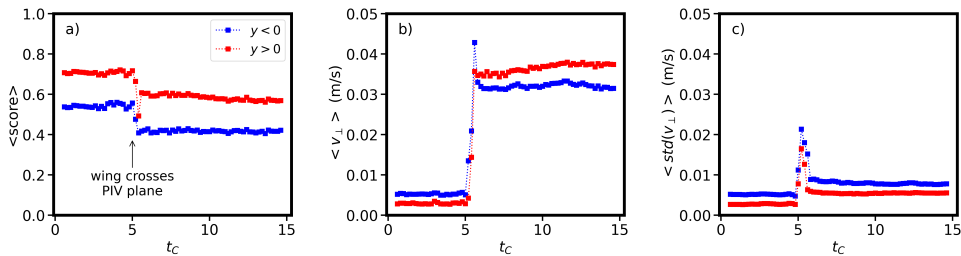


FIGURE 3.14: Temporal evolution of **a)** correlation score, **b)** in-plane velocity and **c)** dispersion over time of velocity measurements, averaged over the right or left sides of the plane. The same experiment as in Fig. 3.13 is represented.

To understand the impact of this loss of correlation, the velocity measurements are examined. The in-plane velocity magnitude  $v_{\perp}$  and the standard deviation  $std(v_{\perp})$  (shown respectively in Figs. 3.13b and c.) over a small time window are analyzed.

Standard deviation is computed as described in appendix D, considering a population  $x$  which is the velocity magnitude obtained on a given grid-point across 5 subsequent measurements (i.e. over one second). This time average operation yields a value of  $v_{\perp}$  and of  $std(v_{\perp})$  on each grid-point in the field. A spatial average of  $v_{\perp}$  and of  $std(v_{\perp})$  is then realized over each side of the measurement plane and yields  $\langle v_{\perp} \rangle$  and  $\langle std(v_{\perp}) \rangle$ , respectively. These quantities are plotted as a function of time in Figs. 3.14b and c, respectively. As expected, a transition is observed when the wing crosses the measurement plane, as vorticity is introduced in the flow. Both  $\langle v_{\perp} \rangle$  and  $\langle std(v_{\perp}) \rangle$  exhibit higher values on the left side ( $Y < 0$ ), with a gradient that is not an inherent property of the flow but a consequence of the measurement degradation. This gradient results in an additional dispersion of approximately  $0.0025 \text{ m/s}$  in velocities on the left side compared to the right side. To overcome this challenge, we frequently prioritize analyzing the right-side vortex data, even when data from the left side is available.

**An assessment of PIV uncertainty :** The correlation score alone does not offer sufficient information of the precision of PIV-obtained velocity measurements. Our aim is to derive an estimation of the measurement uncertainty  $U_v$  associated with each velocity vector  $v$ . To accomplish this, we need to account for errors linked to pixel displacement estimation  $d_{px}$ , inter-frame timing  $dt$ , and image calibration (referred to by  $M$ ), as expressed by the formula:

$$\left(\frac{U_v}{v}\right)^2 = \left(\frac{U_{d_{px}}}{d_{px}}\right)^2 + \left(\frac{U_{dt}}{dt}\right)^2 + \left(\frac{U_M}{M}\right)^2 \quad (3.6)$$

The detailed analysis of each term in eq. 3.6 is presented in appendix C. Summarizing the key elements of this analysis: The term  $\frac{U_{d_{px}}}{d_{px}}$  is determined to be negligible with respect to  $\frac{U_M}{M}$  and  $\frac{U_{d_{px}}}{d_{px}}$ . The evaluation of  $\frac{U_M}{M}$  takes into account uncertainties linked to elements responsible for aligning the measurement plane with the calibration target in the experimental setup.  $\frac{U_{d_{px}}}{d_{px}}$  is influenced by various factors, including particle size, density, and displacement magnitude. To compute this term, numerical simulations are conducted, generating artificial particle images that were then processed by the PIV software. An estimation of  $U_{d_{px}}$  is thus derived through a qualitative comparison between artificial and real images. As a result, a field of uncertainty  $\frac{U_v}{v}(r)$  is derived relative to the vortex velocity field. In regions characterized by both low and moderate velocities within the vortex (e.g., points  $p1$  to  $p4$  in Fig. 3.12b),  $\frac{U_v}{v} = 2.1\%$ . This level of uncertainty is significantly smaller than the velocity measurements and therefore meets our requirements.

### 3.3 Intermediate conclusion

In this section, we have provided a comprehensive overview of the materials and methodologies used to create our experimental database. First, we explained the core concept of our experiment, which involves towing a wing model in a water tank. We defined the towing configuration, denoted as  $(wing, U_0, \alpha)$ , which encompasses the key aspects of each experiment.

Moving on, we described the measurement installation which consists in force measurements with a force probe and of velocity measurements with PIV. We also described some analysis methodologies used to process our data. We showed that

despite some modifications in materials and methodologies that occurred over the duration of this thesis, results from different campaigns can still be compared. We demonstrated that the inter-frame time in our PIV measurements is appropriate to accurately capture vortex velocities. Additionally, we demonstrated the suitability of our chosen spatial and time resolutions for capturing the essential characteristics of the vortices, including their spatial distribution and vertical descent. Furthermore, we briefly addressed one limitation of our experiment, specifically the influence of the camera viewing angle, which resulted in degradation of correlation field data on the left side of the wake.

In the third section, we presented the wing models that were tested during our experiments. We provided detailed information about the baseline wing geometry, featuring a NACA 4412 airfoil with a rectangular planform of span  $0.4m$  and chord  $0.07m$ . We emphasized that the design of these models aligns with three main focuses: exploring the impact of the load law, investigating the influence of secondary vorticity, and examining the effects of an undulated trailing edge on the vortex wake. With the installation and models described, we laid the foundation for studying the baseline flow generated in this setup, which is the primary focus of the next section.

## Chapter 4

# Characterization of the baseline and undulated trailing edge cases : configurations with two vortices

This chapter focuses on the wake of a plain wing, which is taken as the reference configuration.

First, in section 4.1, we closely examine the data from both numerical models and real measurements of this wake with the objective of understanding the capabilities and limitations of our experimental setup. Next, in section 4.2, we dive into a detailed analysis of PIV measurements. We aim to assess the physical characteristics of the trailing vortices generated during an experiment. In section 4.3, we look at the evolution of the vortex properties. Our aim is to identify the underlying physical phenomena. Finally, in section 4.4, we study the wake generated by a wing where the trailing edge geometry has been modified into a sinusoidal shape. Our aim is to analyze the impact of the wing modification on the vortex properties.

### 4.1 The ONERA Lille towing tank : a facility for wake studies

In this section, we will assess the capabilities and limitations of our towing tank experiment with respect to the generation of vortex wakes suitable for our research purposes. First, we will quantify the limitations of the experiment based on theoretical arguments. We are interested in quantifying the maximum vortex ages observable in the experiment and the effects of the tank walls and free surface. Next, we will analyze the raw measurements generated during an experiment to assess the steadiness, repeatability and symmetry of the flow generated.

#### 4.1.1 Lifting line theory predictions of the flow evolution

The maximum measurable time is compared with the time scales of physical phenomena, such as ground effects or instabilities. To do this, we consider a standard towing configuration where the *Ref* wing is towed at  $U_0 = 3 \text{ m/s}$  and  $0.5^\circ$  of incidence. We denote it  $C_{27} = (\text{Ref}, U_0 = 3 \text{ m/s}, \alpha = 0.5^\circ)$  as per indicated in appendix A. In our analysis, we employ lifting line theory to predict the aerodynamic load distribution and, consequently, the characteristics of the vortices. Lifting line theory takes as input the characteristics of the wing at discrete sections and computes the local lift of each element. The contributions are integrated to yield an estimation of the spanwise distribution of bound circulation, which is then related to that of lift. It is important to note that the present analysis neglects the effects of the

three-dimensionality of the vortices, such as those caused by the deformation or displacement of vortex cores.

As mentioned in 3, the wingspan  $b_0$  is the chosen length scale (recall that  $b_0 = 0.4 \text{ m}$ ). We use  $U_0$  as the velocity scale. The resulting Reynolds number writes

$$Re_{b_0} = \frac{U_0 b_0}{\nu} \quad (4.1)$$

where  $\nu \sim 10^{-6} \text{ m}^2/\text{s}$  is the kinematic viscosity of water. Another useful velocity scale is the wake descent speed  $W_d$  which yields a Reynolds number

$$Re_\Gamma = \frac{\Gamma}{2\pi\nu} \quad (4.2)$$

The two Reynolds numbers are related by  $Re_{b_0} = \Theta^{-1} Re_\Gamma$  where  $\Theta$  is the wake descent angle. For towing configuration  $C_{27}$ ,  $Re_{b_0} = 1.20 \times 10^6$  and  $Re_\Gamma = 6.6 \times 10^3$ . Overall, the *Ref* experiments are characterized by  $Re_{b_0}$  in the range  $10^5$  to  $10^6$  and  $Re_\Gamma$  in the range  $10^3$  to  $10^5$ .

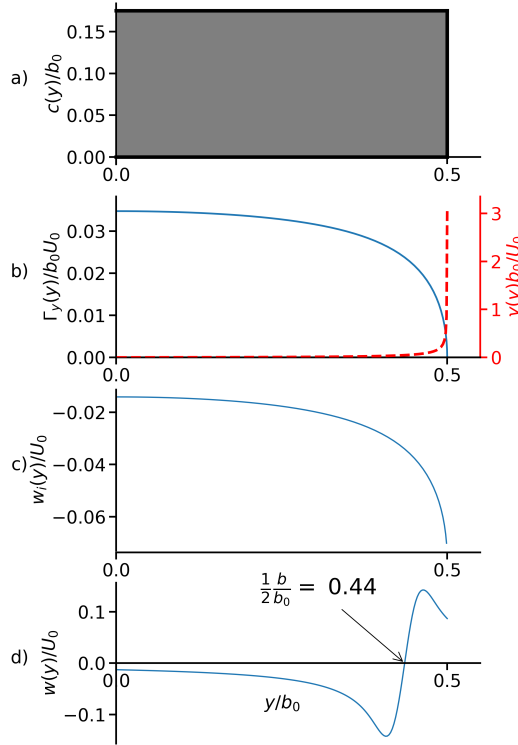


FIGURE 4.1: Lifting line results for the *Ref* wing under towing configuration  $C_{27}$ , **a**) wing geometry, **b**) bound circulation  $\Gamma_y$  and vorticity  $\gamma$  and **c**) vertical velocity profile ( $w$ ) in the near wake.

Lifting line results for the *Ref* wing towed under configuration  $C_{27}$  are shown in Fig. 4.1. The geometry of the wing is rectangular as shown in Fig. 4.1a. The resulting span-wise bound circulation  $\Gamma_y$  is shown in Fig. 4.1b. The rectangular wing load distribution closely approximates the elliptic one. The root-bound circulation is denoted as  $\Gamma_0 = \Gamma_y(y = 0)$ . Fig. 4.1c displays the span-wise evolution of the vorticity sheet strength  $\gamma = \frac{d\Gamma_y}{dy}$  shed at the trailing edge, which concentrates at the

wing-tip and gives rise to a single vortex with circulation

$$\Gamma = \frac{F_z}{b\rho U_0} \quad (4.3)$$

As shown in sec. 2.2.1.4, integrating the bound circulation across the span yields the load factor  $s$  (eq. 2.34), from which we deduce the vortex spanwise distance  $b = sb_0$ . The vortex is modeled using a Lamb-Oseen distribution, as shown in Fig. 4.1d.

It was shown in sec. 2.2.3 that the counter-rotating vortex dipole thus formed descends vertically. The descent speed  $W_d$  is approximated using eq. 2.72. From this it is predicted that vortices of configuration  $C_{27}$  would "reach the ground" at  $t = 52$  s.

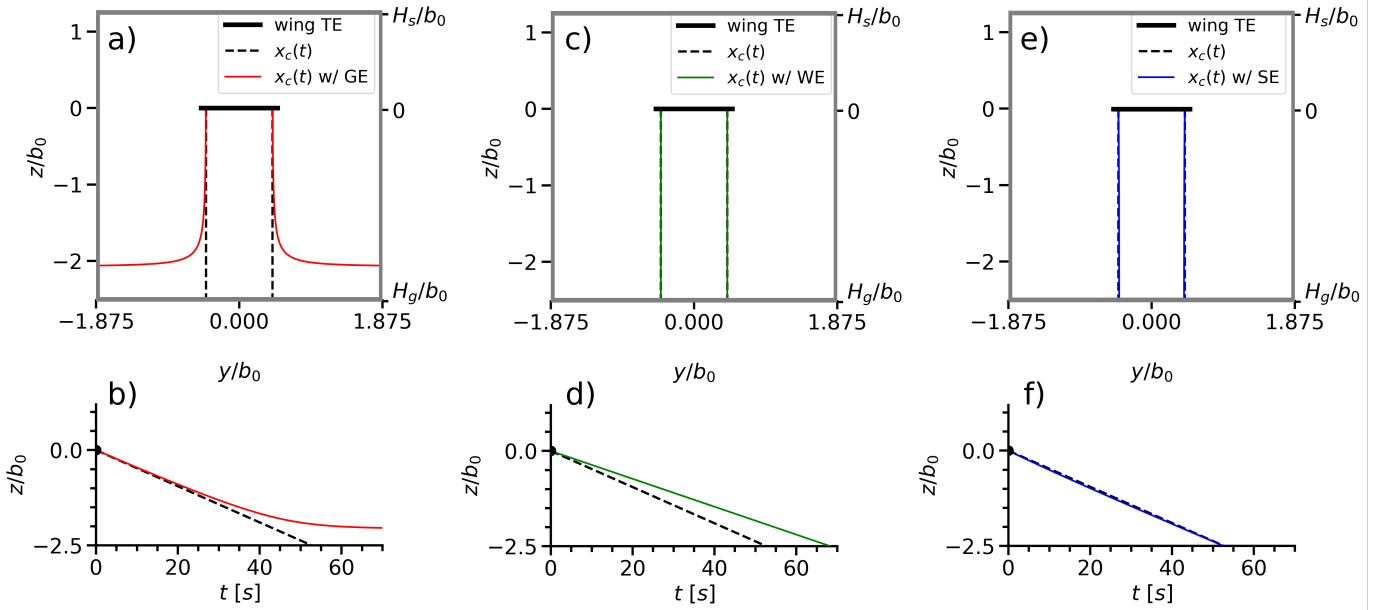


FIGURE 4.2: Vortex trajectories of the  $C_{27}$  configuration in the  $(y, z)$  and  $(x, z)$  planes when 2D effects induced by the tank boundaries are considered. **a)** and **b)** : effect induced by the tank ground, **c)** and **d)** effect induced by the lateral walls and **e)** and **f)** effect induced by the water free surface.

Vortices experience an interaction with the walls of the towing tank. In an inviscid framework, wall effects are modeled by introducing image vorticity, with the tank boundary acting as a symmetry plane. An infinity of images can thus be defined where the distance from each new set of image vorticity to the vortices in the flow is a multiple of the distance that separates the vortices in the flow from the boundaries of the tank. Therefore, the effect of the tank boundaries can be approximated by considering only the first set of image vorticity. A two-dimensional numerical model of this situation has been constructed to evaluate the trajectory of the portside vortex  $\mathbf{x}_r(t) = (y_r(t), z_r(t))$ , following

$$\frac{d\mathbf{x}_r(t)}{dt} = \sum_i^{N_v} \frac{\Gamma_i(t)}{2\pi(\mathbf{x}_i(t) - \mathbf{x}(t))} \quad (4.4)$$

Here, each of the  $N_v$  vortices induces a velocity component  $\frac{\Gamma_i}{2\pi(\mathbf{x}_i - \mathbf{x})}(t)$  on the vortex located at  $\mathbf{x}(t)$ . For instance, the starboardside vortex located at  $\mathbf{x}_i(t) = (-y_r(t), z_r(t))$  induces the vertical velocity  $W_d$  on the portside vortex, yielding, for the unbound

case :

$$\frac{dy_r(t)}{dt} = 0 ; \quad \frac{dz_r(t)}{dt} = \frac{-\Gamma(t)}{2\pi b(t)} \quad (4.5)$$

where

$$b(t) = |\mathbf{x}_l(t) - \mathbf{x}_r(t)| \quad (4.6)$$

The simulation is initialized using the lifting line model, then the model is time marched using an order one explicit time scheme.

The image vorticity introduced by the hard walls is of opposite sign to the vortices in the flow. We first consider the effect induced by the tank ground. Let  $z(t) - H_g$  be the vertical distance between the vortex center and the tank ground, image vorticity is located at a vertical distance of  $2(z(t) - H_g)$ . A simple calculation allows to determine  $V_g$  and  $W_g$ , respectively the net horizontal and vertical velocities induced on the portside vortex by the ground :

$$V_g(t) = \frac{-\Gamma(t)(z(t)-H_g)}{\pi} \left( \frac{1}{4(z(t)-H_g)^2} - \frac{1}{4(z(t)-H_g)^2+b(t)^2} \right) \quad (4.7)$$

$$W_g(t) = \frac{\Gamma(t)}{2\pi} \left( \frac{b(t)}{4(z(t)-H_g)^2+b(t)^2} \right) \quad (4.8)$$

Figs 4.2a and b illustrate the trajectories of the vortices with and without ground effect. The black dashed lines represent unbound vortices, while the red line represents vortices affected by ground effect (GE). The velocity field induced by the image vorticity leads to a reduction of the vertical descent and a lateral outwards motion of the vortices in the tank. This effect becomes significant at a vertical distance of approximately one wingspan from the ground, which corresponds to  $t = 31.6$  s.

A similar effect is induced by the tank lateral walls. A front and side-view of the vortex trajectories when subjected to wall-induced effects are shown in Fig. 4.2c and d respectively. Image vorticity from both vortices in the tank are generated at each wall and induce a velocity field on the trailing vortices. One can see from Fig. 4.2c and d that this amounts to a net vertical velocity induced by the walls which we denote  $W_w$ .  $W_w$  is a function of the vortices lateral position and of the tank width  $W_c$ :

$$W_w(t) = \frac{\Gamma(t)}{\pi} \left( \frac{1}{W_c - b(t)} - \frac{1}{W_c + b(t)} \right) \quad (4.9)$$

Showing that for our experiments  $W_w$  will always be positive i.e. opposed to the vertical descent of the vortices.

To account for the effects of the water free surface above the vortices, we make the first-order approximation of a plane water surface. The surface effect is modeled by image vorticity that counter-rotates with the vortex in the tank, with the water surface acting as a symmetry plane.

As shown in Fig. 4.2e and f, the effects induced by the free surface amount to a slight inward motion  $V_s$  which is present from the early stages of development of the vortex.

$$V_s(t) = \frac{-\Gamma(t)(H_c - z(t))}{\pi} \left( \frac{1}{4(H_c - z(t))^2} - \frac{1}{4(H_c - z(t))^2 + b(t)^2} \right) \quad (4.10)$$

This effect is neglected due to its weak impact on the vortices trajectories. The velocity induced also has a vertical component  $W_s$  which is found to be negligible.

The last effect that we take into account is the temporal evolution of  $\Gamma$ . In unbound flow, the conservation of axial flux of vertical momentum can be derived to

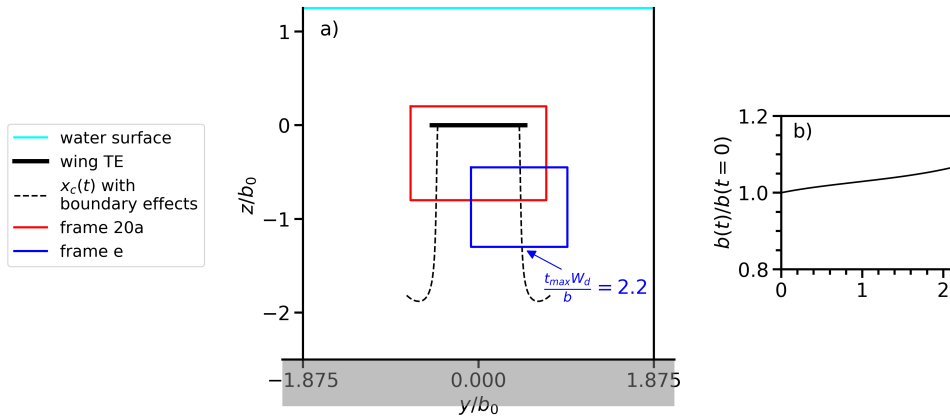


FIGURE 4.3: Evolution of the vortices of the  $C_{27}$  configuration when 2D effects induced by the tank boundaries are considered. **a)** Vortex trajectories in the  $(y, z)$ -plane. The field of view of two PIV frames is represented by colored rectangles. Time evolution of vortex distance  $b(t)$  normalized by its value at  $t = 0$

obtain :

$$\Gamma(t)b(t) = \Gamma(t = 0)b(t = 0) \quad (4.11)$$

In the case of the tank with hard walls, the flow is unbounded and vorticity may decrease by viscous friction occurring at the walls (see eq. 2.53). However the viscous effect of the tank walls is neglected at this stage of the model. This effect is studied during the analysis of experimental data, in sec. 4.3.1.2.

Having defined the effects induced by the tank boundaries, we can now assess the trajectories that we expect to observe during our experiments. The final trajectories of the vortices, accounting for the tank-induced effects, are obtained from :

$$\frac{dy_r(t)}{dt} = V_g(t) \quad (4.12)$$

$$\frac{dz_r(t)}{dt} = W_d(t) + W_g(t) + W_w(t) \quad (4.13)$$

$$(4.14)$$

where the time-dependence of  $\Gamma(t)$  and of  $b(t)$  is taken into account in the terms on the right hand side. The result of the simulation is depicted in Fig. 4.3a. It should be noted that the simulation does not include the roll-up stage during which the vortex forms and reaches its nominal position. However, as seen in sec. 2.2.1.4, this stage is predicted to cover a distance of only  $X_r/b_0 \sim 0.28AR/C_Z = 1.85$  wingspans downstream of the wing trailing edge.

Now we can analyze the consequences that these effects will have on our measurements. In Fig. 4.3, the camera frames 20a and e are represented by the colors red and blue, respectively. With camera frame 20a, the vortices are expected to exit the PIV measurement window at  $tU_0/b_0 = 171$ . With frame e, the vortices are expected to enter at  $tU_0/b_0 = 90$  and exit at  $t_{max}U_0/b_0 = 300$ . When scaled by the induction time scale, the maximum observable time under configuration  $C_{27}$  is  $t_{max} \frac{W_d}{b} = 2.2$ .

The predicted trajectories of the vortices during the experiment allow us to discuss the effects of the tank boundaries.

The canal is not large enough for wall-induced effects to be completely negligible, resulting in slower vertical descent of the vortices compared to an unbound case. Although it is unfortunate that we cannot perfectly reproduce unbound conditions, the side walls do not induce any lateral motion on the vortices. This slower descent provides a larger time window for measurement, which is in some way beneficial for the experiment.

The effects induced by the ground of the tank (an horizontal wall) reduce the vortices descent and also introduce some lateral motion which is detrimental to the experiment. However, these effects are only significant when the vortices are at a distance of less than one wingspan from the ground. In our measurement frame  $e$ , these effects are expected to be observed only in the lower region. After exiting the measurement frame  $e$ , the effects of the side walls and the tank ground lead to a scenario where the vortices displace upwards along the vertical side walls. This is not a concern as the measurements are interrupted once the vortices exit the frame.

The Crow instability evolves on a time scale  $t_b = \frac{b}{W_d}$ . Large deformations of the vortices under the effect of this instability are expected to be observable at  $t \frac{W_d}{b} > 3$  and they may provoke vortex linking around  $t \frac{W_d}{b} \sim 8$  (see for example, the experiments of Liu [59], illustrated in Fig. 2.12). Therefore, most of this phenomenon occurs at times longer than what is achievable in the present tank experiments. However, we may still detect early stages of its development.

The duration of an experiment is also considered with respect to the time scale of viscous effects in order to assess if these can be measured. Even for the shortest experiments (i.e. when vortices exit quickly) where  $t_{max} U_0 / b_0 = 100$ , viscous effects such as significant vortex growth can occur. The length scale of viscous diffusion (within the range of  $U_0 \in [1, 5]$  m/s) is approximately  $(\nu t_{max})^{1/2} \sim 6.3$  mm and 2.8 mm. Therefore our spatial resolution is capable of resolving these scales, allowing us to identify viscous effects when analyzing the entire time range of the experimental data.

The circulation decreases with time under the effect of the tank boundaries. This is the most significant consequence of the boundaries-induced effects vis-a-vis of the purposes of this work. The temporal evolution of  $b(t)$  is shown in Fig. 4.3b. The instantaneous values are scaled by the value at  $t = 0$ . When the vortex exits frame  $e$ , the separation  $b(t_{max})$  is equal to  $1.03b(t = 0)$ . This is caused by the induced effect of the ground. At  $t < t_{max}$  however, the effect of this outward motion is negligible.

It is important to note that real trajectories may differ from these predictions due to effects that we neglected. For instance, the effect of vortex deformations upstream or downstream of the measurement plane may propagate and reach the measurement plane. During the experimental campaign, we analyze the measurements in order to identify these phenomena, if present. This will be discussed further down.

#### 4.1.2 Analysis of the steadiness, repetability and symmetry of the flow

We now assess the robustness of our experimental setup by analysing the raw data obtained during an experiment. We focus on three key aspects of the generated flow : flow steadiness, experiment repeatability, and flow symmetry.

In what follows, we analyze our experiment in  $(O_T, X, Y, Z)$  the reference frame that is attached to the water tank. This reference frame was first introduced in section 3.1, it is sketched in Fig. 4.4.

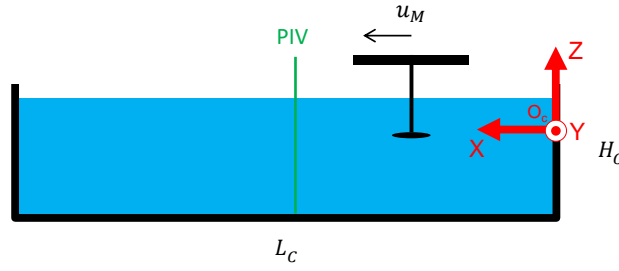


FIGURE 4.4: Diagram of the reference frame attached to the water tank

#### 4.1.2.1 Verification of the steadiness of the aerodynamic efforts around the generating wing

The path of the generating wing must be parallel to the longitudinal axis of the canal and parallel to the ground and water surface. The aerodynamic efforts generated by the wing must be steady when it crosses the measurement plane. Indeed, the time evolution of the aerodynamic forces and moments is an indicator of the steadiness of the flow around the wing.

The aerodynamic forces and moments recorded during an experiment at conf.  $C_{27}$  are shown in figure 4.5. As described in sec. 3.1.3, the towing motion is characterized by a constant velocity phase from  $t = t_1$  to  $t = t_2$ . A single value for the lift generated during this experiment can be obtained from  $F_z(t)$  averaged over the constant velocity phase. The operator  $\langle x \rangle$  is used to translate the time-average of any variable  $x = x(t)$ . In this case :

$$\langle F_z \rangle = \frac{1}{t_2 - t_1} \int_{t_1}^{t_2} F_z(t) dt \quad (4.15)$$

For all the experiments in this work, the variation of  $F_z(t)$  with time amounts to a maximum standard deviation of 1.5% and 0.9% from the mean value respectively for low and high velocity experiments. We conclude that the generated aerodynamic lift is fairly constant during the constant velocity phase. Drag force and pitching moment measurements ( $F_x(t)$  and  $M_y(t)$ ) inside of the constant velocity phase are unaffected by the remnants of the acceleration and deceleration of the platform. As shown in appendix B, to the wing drag we subtract the drag of the strut which was measured in previous experiments where no wing is attached. We observe a low-frequency oscillation on the filtered  $F_x(t)$  data which is due to the oscillation of  $u_M(t)$  caused by the velocity control. The standard deviation of drag measurements ranges between 0.5 and 2N around its respective mean  $F_x$  value over the selected experiments. In some experiments where the towing velocity is low, this dispersion is of the same order of magnitude as  $F_x$ . However, as it will be shown below in sec. 4.1.2.3, the evolution of drag measurements with the towing parameters  $U_0$  and  $\alpha$  is coherent with reference values, which validates the measurements. In spite of these oscillations the mean measured drag does not grow or decrease with time.

The alignment of the wet surface (the wing and the part of the strut below the water level) with the towed direction X is extremely important to guarantee the expected symmetry of the wake. By analyzing the rolling and yawing moments ( $M_x(t)$  and  $M_z(t)$ ) we deduce that a misalignment causes an inclination of the wing around

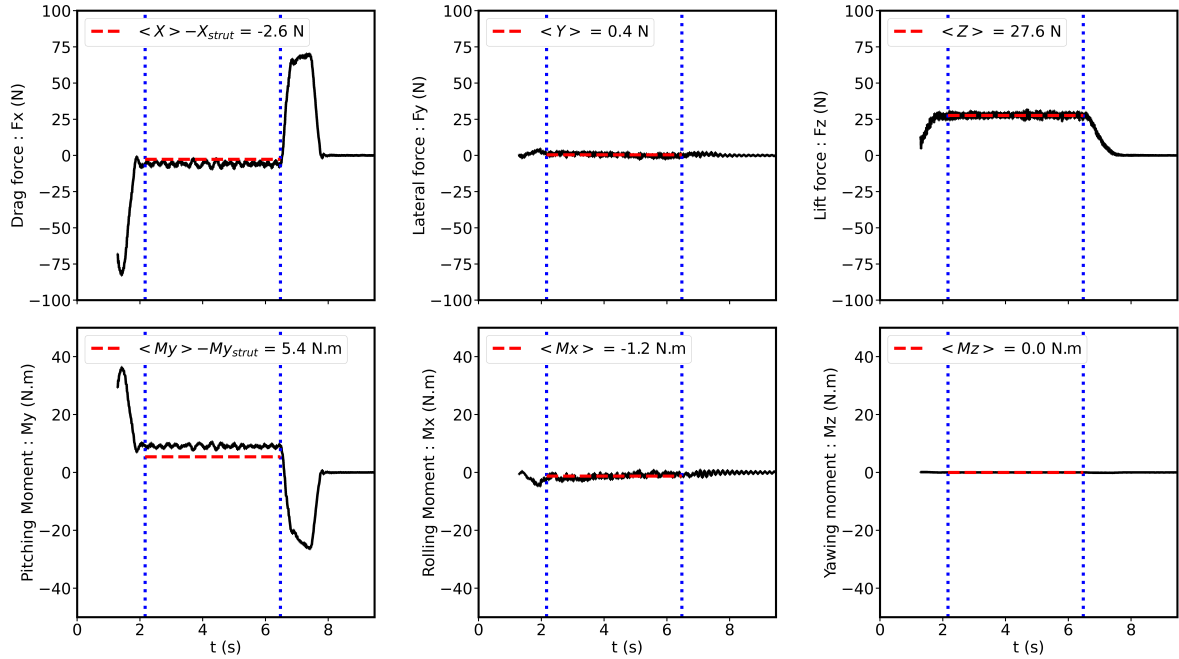


FIGURE 4.5: Aerodynamic efforts and moments measured by the force probe for an experiment where the reference wing is towed at  $U_0 = 3\text{m/s}$  and  $\alpha = 0.5^\circ$ . The duration of the constant velocity phase is shown by blue dotted lines and the mean values recorded during this period are shown by a red dashed line.

the rolling axis instead of a yaw angle during the constant velocity phase. The symmetry of the wake is verified using the PIV measurements (described further down) when  $F_y \neq 0$ . Typically we observe a good symmetry of the flow whenever the mean values of the forces respect  $F_y < 0.1F_z$ .

#### 4.1.2.2 Verification of the repeatability of the aerodynamic forces generated by the wing under the same towing configuration

We perform multiple experiments with the same towing configuration (same wing, towing velocity and angle of attack) in order to discard eventual ambiguities regarding the vortex characteristics obtained for a specific configuration. Indeed, vortex attributes like position, size, and strength must remain constant under identical towing conditions with the same wing model. Therefore, it is necessary to confirm first that  $F_i(t)$  and  $M_i(t)$  generated during an experiment are repeatable and a function of the towing configuration only. To do this, we analyze the dispersion between the time evolution of the force measurements obtained under the same towing configuration.

An example of this procedure is shown in Fig. 4.6. The scales on this figure have been adapted for each force and moment for clarity. Here, two experiments were performed under the configuration  $C_{27} = (Ref, U_0 = 3\text{m/s}, \alpha = 0.5^\circ)$ . Regarding the drag values, the drag of the strut has been subtracted from  $F_x$  and  $M_y$ . The time evolution of  $F_i(t)$  and  $M_i(t)$  between both experiments follow each other closely except on the case of  $F_y(t)$ . This shows that the lateral effect coming from the misalignment in the strut is for most cases not repeatable between the experiments. The mean values corresponding to each experiment differ by  $\max(\Delta \langle F_i \rangle) = 0.89\text{ N}$  and  $\max(\Delta \langle M_i \rangle) = 0.07\text{ N.m}$  which is in the order of magnitude of the force probe

precision (see section 3.2.1). A statistical analysis of the measurements coming from both populations (experiment 1 and experiment 2 in the figure) is performed following the methodology described in appendix D. This yields  $\bar{F}_i$  and  $\bar{M}_i$  which is the value of the forces and moments averaged over the multiple realizations of the same experimental configuration. We also obtain  $s_{F_i}$  and  $s_{M_i}$ , which are the dispersion of measurements about this average. Regarding the lift values, during the constant velocity phase, the measurements have a dispersion of  $s_{F_i} = 1.3 \text{ N}$ , which represents 4.6% of the mean value  $\bar{F}_z$ .

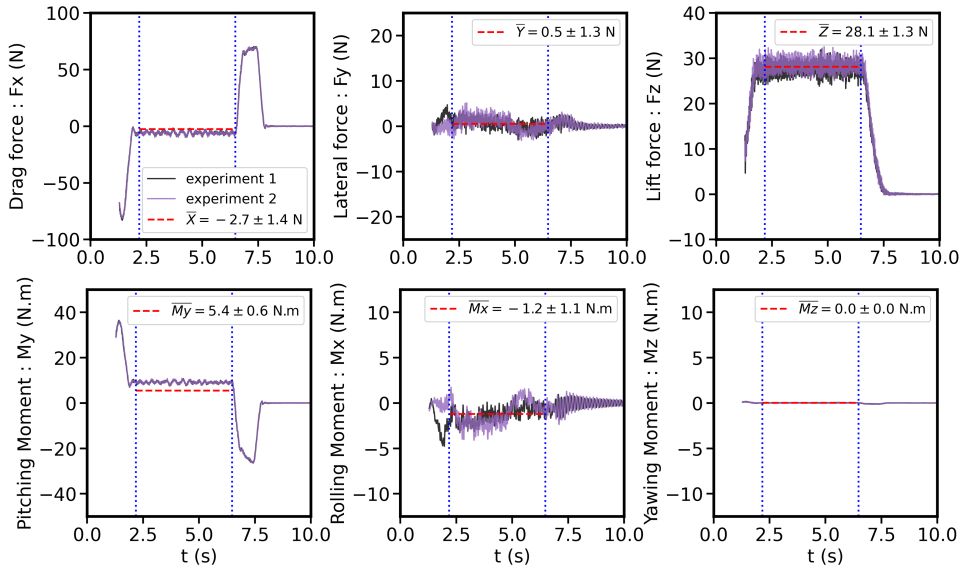


FIGURE 4.6:  $F_i(t)$  and  $M_i(t)$  measured during an experiment where the reference wing is towed at  $U_0 = 3 \text{ m/s}$  and  $\alpha = 0^\circ$ .

The averaged values obtained for  $\bar{F}_i$  and  $\bar{M}_i$  for the configuration ( $Ref, U_0 = 3 \text{ m/s}, \alpha = 0.5^\circ$ ) are reported in Fig. 4.6. Dispersions obtained in these measurements are acceptable for the purposes of this work.

#### 4.1.2.3 Validation of the aerodynamic characterization of the reference wing (NACA 4412)

Following the methodology described above, from the  $N$  experiments realized under each towing configuration ( $Ref, U_0, \alpha$ ) for the reference wing the values of  $\bar{F}_i$  and  $\bar{M}_i$  are obtained.

$\bar{F}_i$  and  $\bar{M}_i$  as a function of  $\alpha$  for different towing velocities  $U_0$  are plotted in Fig. 4.7. The dispersions  $s_{\bar{F}_i}$  and  $s_{\bar{M}_i}$  are shown for every configuration by error bars. The evolution of lift and drag values is linear at moderate  $\alpha$ , as expected.

During the experimental campaign, the lateral forces  $F_y(t)$  are monitored and the orientation of the strut is corrected between experiments to reach a minimum lateral effect. By doing this, we ensure that  $\bar{F}_y < 0.1\bar{F}_z$  for all configurations, which is a condition (empirically set through trial and error) for obtaining symmetrical flows in these experiments.

Finally, the aerodynamic coefficients are computed. The drag and lift coefficients  $C_x, C_z$  are shown in Figs. 4.8a and b respectively. Error bars in the figure express both the precision on  $\alpha$  and the dispersion of results obtained during the repetitions of each experiment. The sanity of the measurements is assessed by comparing the results to those of numerical computations. XFOIL computations performed for a

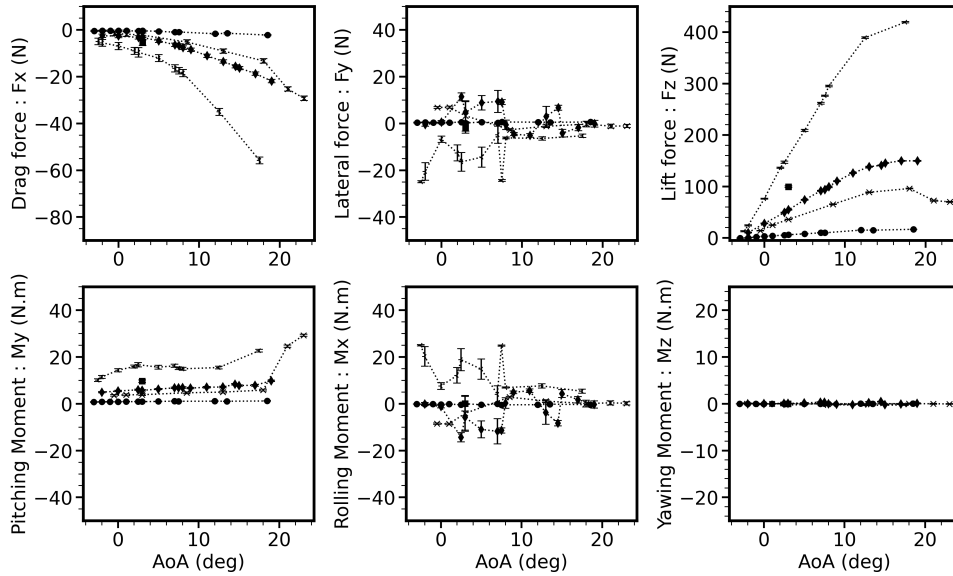


FIGURE 4.7: Evolution of aerodynamic forces and moments generated by the reference wing as a function of the towing configuration. Each curve represents a specific towing velocity  $U_0$ .

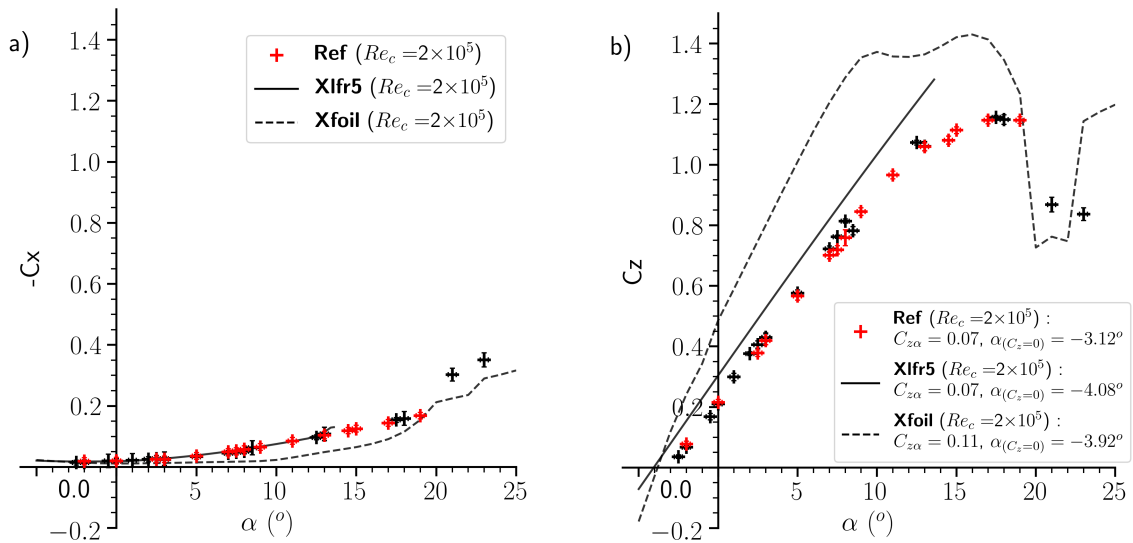


FIGURE 4.8: Evolution of a) drag and b) lift coefficients of the reference wing as a function of the angle of attack.

2D wing with a NACA 4412 profile are shown by a dotted line. Also, XLFR5 computations performed for a 3D wing with a NACA 4412 profile are shown by a solid line.

First, the effect of  $Re_c$  is investigated. The data from experiments where the wing is towed at  $U_0 = 3m/s$  (i.e.  $Re_c \sim 2 \times 10^5$ ) is plotted in red in Fig. 4.8. It is observed that this data evolves similarly to the rest of the measurements which range in  $Re_c \in [9 \times 10^4, 3.5 \times 10^5]$ . The range of chord Reynolds number tested in these experiments is small, and therefore the effect of  $Re_c$  on the evolution of  $C_x$  and  $C_z$  in this dataset is negligible. The stall angle, where a sudden increase of drag and a sudden decrease of lift is observed, is  $19^\circ < \alpha_s^{Ref} < 21^\circ$ . Also, a maximum lift coefficient of  $C_z = 1.12$

is achieved at  $\alpha(C_{z,max}) \sim 17^\circ$ . The value of  $\alpha(C_{z,max})$  and the range of  $\alpha_s^{Ref}$  is slightly greater than the ones observed on the 2D model. The XLFR5 model does not predict flow detachment, which explains its absence in the tested range of  $\alpha$  values.

The lift slope  $C_{z\alpha}$  (in the linear region of the curve) is now considered. It is observed that  $C_{z\alpha}^{Ref}$  (obtained in the experiments) differs by  $C_{z\alpha}^{Ref} - C_{z\alpha}^{2D} = -0.04$  with the 2D model but it is predicted correctly by the 3D calculation  $C_{z\alpha}^{3D}$ . Regarding the angle of zero lift  $\alpha(C_z = 0)$ , one can observe that the 2D and 3D models are in agreement but show a discrepancy of  $\Delta\alpha(C_z = 0) = -0.8^\circ$  with respect to the experimental value. Since both the measurements and the 3D model exhibit the same value for the lift slope ( $C_{z\alpha}^{Ref} = C_{z\alpha}^{3D}$ ), this difference covers the entire range until  $\alpha_s$ . This difference of  $\Delta\alpha(C_z = 0)$  could be explained in part by the presence of the strut at the midplane. Indeed, it is expected that because of this the midplane section of the wing does not generate lift, which would slightly decrease  $C_z$ . Also, drag coefficient measurements are in agreement with the 3D computations, and this is expected since drag measurements are corrected from the drag of the strut (see appendix B). It is worth noting that the numerical tools used in this study are commonly employed in the literature, and the aforementioned results are consistent with expectations.

At this stage, we have validated the robustness and representativeness of our experimental setup regarding the conditions under which vortices are generated. We have done this by analyzing the aerodynamic efforts and moments generated by the wing during towing and showed that they are steady and repeatable. Also, we have verified that our wing model does reproduce the aerodynamic characteristics of a NACA 4412 wing by comparing its lift and drag coefficients to those obtained by simulations.

#### 4.1.2.4 Analysis of vortex trajectories in order to assess the symmetry of the wake

This section focuses on characterizing the geometry of the wake measured on the PIV plane in order to validate the conditions in which the vortex flow is generated. Vortices on the portside and starboardside of the wake must be symmetrical, namely, their position and characteristics must be equal during the experiment. As shown above, this is achieved through conditions where the rolling angle on the towed wing is kept minimal. It is further confirmed that the flow is symmetrical by comparing the trajectories of the portside and starboardside vortices. To do this, the vortex positions are first determined. This mandates that one verifies that the PIV setup ensures a correct correlation when measuring the displacement of particles in the vortex core. We shift to the reference frame that is attached to the wing model and is denoted  $\mathcal{R}_M = (O_M, x, y, z)$ .  $\mathcal{R}_M$  is sketched in Fig. 4.9. In order to identify the vortices, from the PIV measured velocity field  $\mathbf{v} = (u, v, w)$ , the in-plane velocity field  $\mathbf{v}_\perp = (0, v, w)$  is separated from the out-of-plane velocity  $\mathbf{v}_x = (u, 0, 0)$ . Pseudo-streamlines of the flow are obtained from  $\mathbf{v}$ . The fields of out-of-plane vorticity  $\omega_x$  and of out-of-plane velocity  $v_x$  obtained from a PIV image are illustrated in Fig. 4.10.

Examining the  $\omega_x$  field, one can clearly identify the two counter-signed vortices. In the initial images following the wing passage (not shown), vorticity in the wake of the strut is observed but quickly dissipates. The pseudo-streamlines of  $\mathbf{v}_\perp$  are also shown in Fig. 4.10a. Although curvature of the streamlines is not a sufficient argument in itself to identify vortices, based on the vorticity measurements we can see that this curvature is concentrated around the previously identified vortices. Moreover, the streamlines are symmetrically distributed around the  $(O_Mzx)$  plane and mostly symmetrical about the axis between the two vortices.

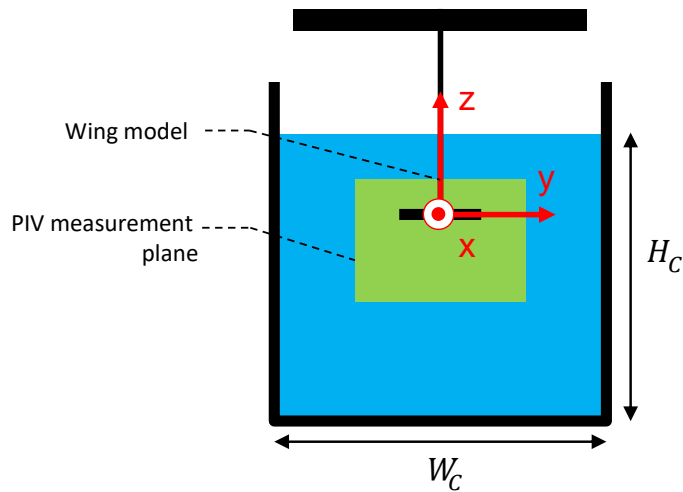


FIGURE 4.9: Diagram of the reference frame attached to the wing  $\mathcal{R}_M$  when the wing model is positioned at station  $X = X_{PIV}$

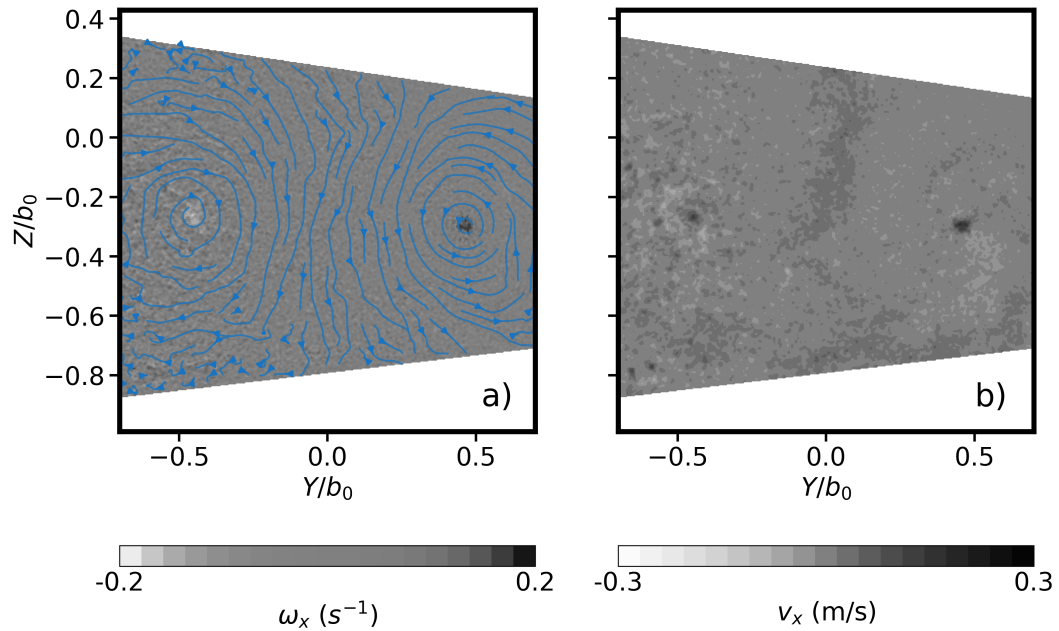


FIGURE 4.10: PIV fields measured 70 wingspans behind the wing towed under configuration ( $Ref, U_0 = 3 \text{ m/s}, \alpha = 0.5^\circ$ ), **a**) axial vorticity field  $\omega_x$  and **b**) axial velocity  $v_x$ .

From the out-of-plane velocity field, shown in Fig. 4.10b, it is noticeable that around the vortices, the axial velocity component  $v_x$  is predominantly non-zero, indicating a wake-like flow directed towards the wing. Intense axial flow can be observed in the core of the vortices. The remnants of the wake of the strut are also noticeable in the mid-plane region but, as shown in Fig. 4.10a, they do not introduce significant axial vorticity in the flow.

The symmetry of the vortex trajectories is now discussed. The procedure to identify the centroid of the vortices is detailed in section 4.2.1. Here, it suffices to say that  $W_v$  and  $W_d$  are the vertical descent velocity of the vortices, as obtained from measurements and from theory, respectively. Also,  $x_c(t)$  is the vortex position as

obtained from the  $G1$  criterion. Fig. 4.11 illustrates the horizontal and vertical components of the left and right side vortex trajectory for the *Ref* configuration. These trajectories demonstrate a downward motion of the vortices. Non-symmetrical cases (not shown), where the lateral effect caused by the strut generates flow disturbances, exhibit uneven vortex strengths and deviations from a straight descending path.

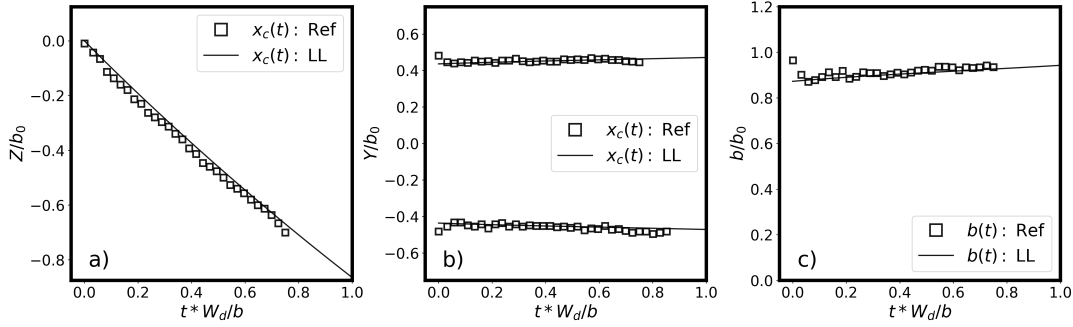


FIGURE 4.11: Vortex trajectory  $\mathbf{x}_c$  as a function of time, for configuration (*Ref*,  $U_0 = 3 \text{ m/s}$ ,  $\alpha = 0.5^\circ$ ) and as predicted by lifting line theory. Time is normalized on the vertical drift speed  $W_d$  and vortex separation  $b$  and data is decimated by 4, for clarity : **a)** vertical component of the left-side vortex trajectory, **b)** horizontal component for the right and left side vortices and **c)** vortex separation distance.

The parameter  $b(t)$ , defined by eq. 4.6, is used to evaluate the vortex separation. Fig. 4.11c provides insight into the evolution of  $b(t)$  with time. It is evident that upon formation, the vortices move slightly inward about the wing tip due to the vortex wake roll-up. This is followed by a slight outward motion, observable in the growth of  $b(t)$ . The trajectories of the vortices as predicted by the lifting line model (*LL*) are plotted on the figures. Details on the model are provided in section 4.1.1. The model is parametrized by the lift coefficient obtained experimentally.  $\mathbf{x}_c(t)$  and  $b(t)$  match perfectly with the lifting line predictions shown in the figure. It thus seems that the tank induced effects play a significant role in the outward motion of the vortices.

Let  $t_0, \dots, t_n$  be the  $n$  PIV measurements realized during an experiment. The operator  $\langle x \rangle_t$  is used to translate a time average over the PIV measurements of an experiment.

$$\langle X \rangle_t = \frac{1}{n} \sum_{i=0}^n X(t_i) \quad (4.16)$$

Thus,  $\langle b \rangle_t$  is introduced to represent the averaged distance between vortices. The evaluation yields a value of 0.86 for the *Ref* wing. Generally,  $\langle b \rangle_t / b_0$  falls within the range of 0.82 to 0.9 across the parameter map and it is consistently well predicted by lifting line calculations.

The values of  $W_d$  and  $\langle b \rangle_t$  obtained for different experiments at the same towing configuration are then averaged following the usual methodology (see appendix D for further information) to obtain  $\overline{W_d}$  and  $\overline{b}$ . The analytical lifting line model  $W_d$  from equation 2.72 is preferred over the direct measurement  $W_v$  as it allows for comparison between different experiments of the same configuration. Thus, in Fig. 4.11, time is normalized based on the vertical drift speed  $\overline{W_d}$  and vortex separation  $\overline{b}$ . In these reference scales the monitoring duration is approximately the same for all wing configurations. The end of monitoring is limited by the vertical size of the PIV frames, which is approximately  $0.7b_0$ .

Furthermore, the left and right-side vortices descend at an equal velocity, suggesting equal circulation for both vortices and thus confirming the flow symmetry about the wing mid-plane. However, in some cases, a slight asymmetry between the left and right sides of the wake is observed, resulting in a low-amplitude lateral drift of the vortices. This indicates that the vortex descending at a faster rate has weaker circulation compared to its counterpart. We consider this asymmetry significant when the vortices trajectory drift towards one side, in which case the data is discarded.

#### 4.1.2.5 Intermediate summary

In this section, a thorough assessment of the wake generated during typical experiments in this study is conducted by analyzing the raw data obtained from PIV measurements. Despite the significant measurement noise that affects the left-side vortex (see section 3.2.2.4), one can confidently consider both vortices in the wake to be symmetric with respect to the wing mid-plane. Furthermore, indicators of this symmetry are established to include a low lateral force compared to the lift force and a vortex trajectory characterized by a vertical, straight descent at a constant velocity. Moving forward, the focus is directed towards analyzing the right side of the wake.

It is important to note that in certain camera configurations, the left-side of the wake may be purposely excluded. In such cases, the sound aerodynamic efforts and the trajectory of the right-side vortex serves as sufficient indicators of wake symmetry. In the next section, the physical characteristics of the right-side vortex are analyzed.

## 4.2 Extraction of vortex characteristics from PIV measurements

In this section the physical characteristics of the vortex are estimated. This characterization precedes the identification of physical phenomena present in the flow. To do this characterization, the measured velocity field  $v = (u, v, w)$  is exploited. To illustrate our purposes, we choose to show data from the wing towed under configuration  $C_{27}$ . This data is taken at  $tU_0/b_0 = 30$  since this is a conservative time at which we can consider that the physical phenomenon related to the wake formation are not present anymore, and that physical phenomena related to the vortex aging are still negligible. Indeed, at  $tU_0/b_0 \sim 30$  most of vorticity has rolled-up around the vortex, the vortex has reached an axisymmetric state, the wake from the strut is effectively dispersed. Also, vortex 3D deformations are negligible, the action of viscous diffusion is weak, and so is the action of the tank boundaries.

### 4.2.1 Identification of the vortex center

The procedure for vortex detection in the PIV measurements is described. The detection is done in three steps that are presented hereafter. To initialize the procedure, the extremum  $\mathbf{x}_m$  of the axial vorticity field is located

$$\mathbf{x}_m = \underset{\mathbf{x}_\perp}{\operatorname{argmax}} (\omega_x) \quad (4.17)$$

By construction,  $\mathbf{x}_m$  is restrained to the vertices of the PIV mesh. To refine this localization, we then calculate  $\mathbf{x}_w$  the barycenter of the axial vorticity over a reduced

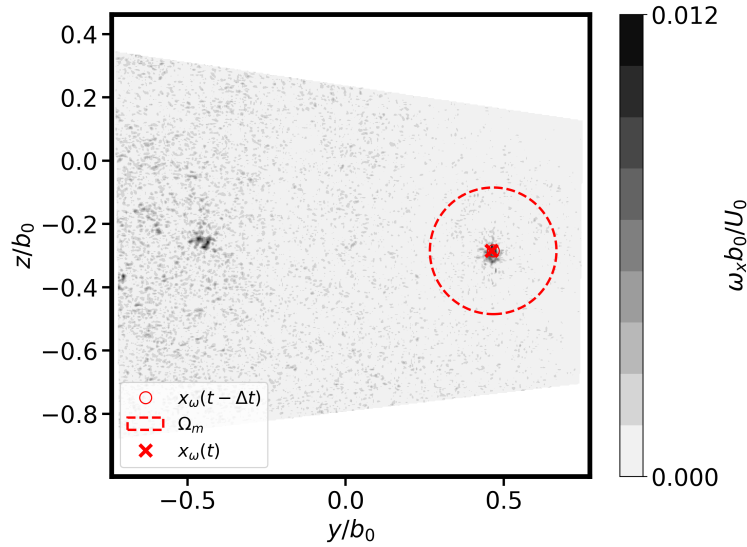


FIGURE 4.12: Measured axial vorticity field  $\omega_x$  trailing 70 wingspans behind the wing towed under configuration (*Ref*,  $U_0 = 3 \text{ m/s}$ ,  $\alpha = 0.5^\circ$ ).

region  $\Omega_m$  of diameter  $0.25b_0$  centered about  $\mathbf{x}_m$  following

$$\mathbf{x}_\omega \int_{\Omega_m} \omega_x dy dz = \int_{\Omega_m} \mathbf{x}_\perp \omega_x dy dz \quad (4.18)$$

For the subsequent measurements, this procedure is repeated but it is initialized by centering  $\Omega_m$  on  $\mathbf{x}_\omega(t - \Delta t)$ . An illustration of the vorticity field trailing behind the *Ref* wing is provided in Fig. 4.12.  $\mathbf{x}_\omega(t - \Delta t)$  is shown by a small red circle.  $\Omega_m$  and  $\mathbf{x}_\omega$  are shown in Fig. 4.12 by a red dashed circle and a red cross, respectively. The  $\Omega_m$  region is large enough to contain the compact axial vorticity field of the vortex and allows to exclude the outside vorticity which is overwhelmed by the freestream turbulent vorticity and measurement noise.

Fig. 4.13 presents the temporal evolution of  $\mathbf{x}_\omega$  computed on the port-side of the wake. The dashed line indicates the lower limit of the PIV window. The detection routine is halted when  $\mathbf{x}_\omega$  approaches this limit. The trajectory of the vortex in the transverse plane is depicted by the locus  $\mathbf{x}_\omega(t)$ . From this trajectory, one can calculate the effective downward velocity  $W_v$  using the following equation:

$$W_v = \frac{d\mathbf{x}_\omega(t)}{dt} \quad (4.19)$$

Fig. 4.14 displays the relationship between the obtained  $W_v$  and the analytical estimation of the wake descent  $W_d$  (refer to equation 2.72) for various towing configurations. It is worth noting that  $W_v$  and  $W_d$  exhibit a strong correlation, which validates our characterization of the vortex descent. Few outlier points, where  $W_v$  is lower than the prediction  $W_d$  are also observed. These are cases where the descent of the vortex is interrupted and will be described further down.

The final step in localizing the vortex uses the G1 criterion, initially introduced by Graftiaux [36]

$$G1(\mathbf{x}_p) = \frac{1}{N} \sum_S \sin(\theta_M) \quad (4.20)$$

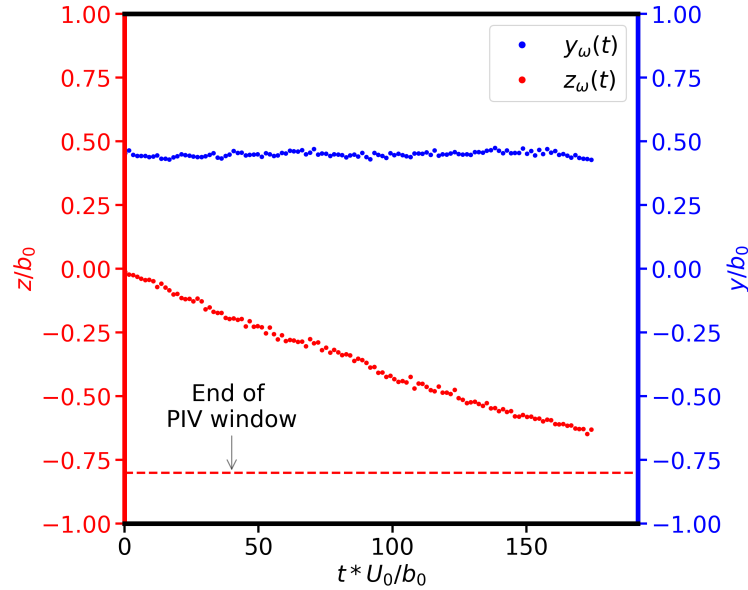


FIGURE 4.13: Time evolution of the coordinates  $y_\omega$  and  $z_\omega$  of the barycenter of vorticity on the wake under configuration (Ref,  $U_0 = 3 \text{ m/s}$ ,  $\alpha = 0.5^\circ$ ).

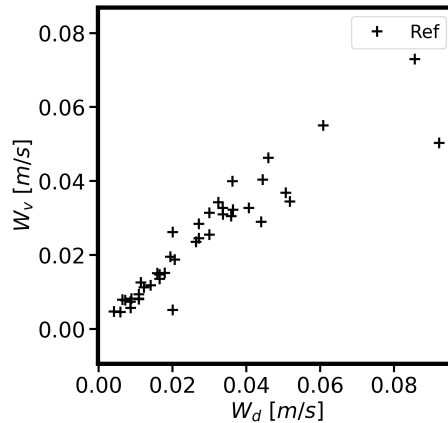


FIGURE 4.14: Vortex estimated descent velocity  $W_d$  as a function of measured descent velocity  $W_v$ .

This criterion relies on the rotation rate of the in-plane velocity field  $v_\perp$  around the vertex  $\mathbf{x}_p = (y_p, z_p)$  of the PIV mesh. In 4.20  $S$  is an area defined around  $\mathbf{x}_p$ ,  $v_M = v_\perp(y_M, z_M)$  the velocity at point  $x_M = (y_M, z_M)$ , and  $\theta_M$  is the angle between  $v_M$  and  $PM = \mathbf{x}_M - \mathbf{x}_p$ . This criterion being not Galilean invariant, subtracting the descent velocity  $W_v$  is necessary before evaluating it.

In this study, vortex characteristics are analyzed by averaging velocity fields in the azimuthal ( $\theta$ ) direction, as will be detailed later. Among the criteria used, the G1 criterion outperforms others due to its direct use of PIV velocity data, while methods like barycenter of vorticity are noisier due to vorticity field calculations. However, the localized barycenter of vorticity  $x_\omega$  works well for  $W_v$  calculation. The distinction is evident when comparing fields of  $v_\perp$ , and  $\omega_x$  (Fig. 4.15), with  $\max|G1|$  and  $x_\omega$  marked. The value of the vortex radius averaged over the azimuthal direction is shown to provide a length scale for the comparison of  $\max|G1|$  and  $x_\omega$ . In the fields shown, the localization of both criteria differ by about  $0.5R_a$  and this trend is

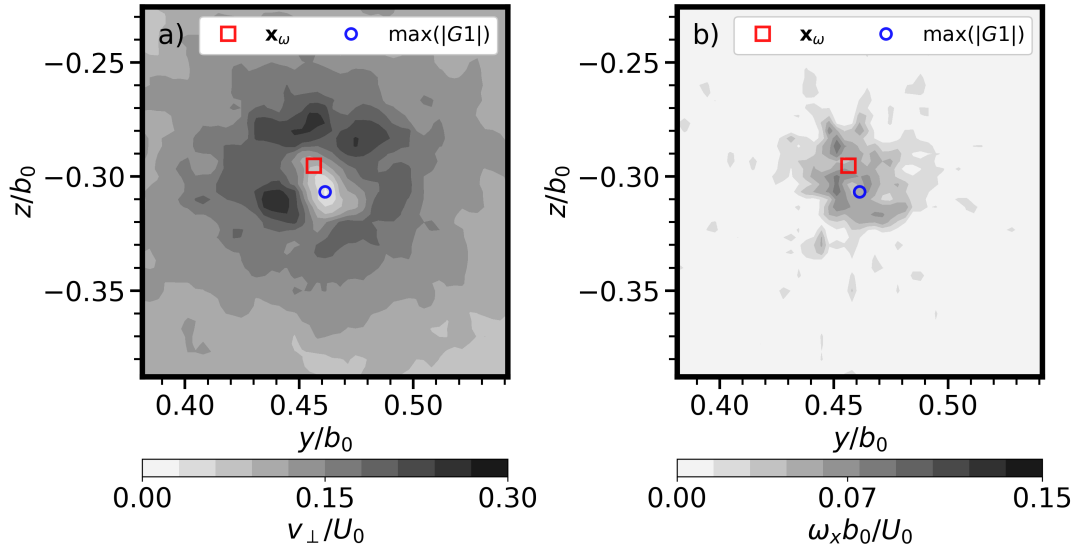


FIGURE 4.15: Location of  $\mathbf{x}_\omega$  and  $\max(|G1|)$  for the right side vortex 70 wingspans downstream on the wake under configuration ( $Ref, U_0 = 3 \text{ m/s}, \alpha = 0.5^\circ$ ). These locations are represented on the **a)**  $v_\perp$  and **b)**  $\omega_x$  fields

observed for all experiments. This length scale is non-negligible when assessing the center of the vortex, since large velocity gradients exist for  $|\mathbf{x} - \mathbf{x}_c| < R_a$ . It is evident that  $\max|G1|$  provides velocity measurements which will yield lesser variation when averaged over the  $\theta$  direction. In other words, the vortex field has a better axial symmetry when the center is determined by  $G1$ . This is why the vortex center  $\mathbf{x}_c = (y_c, z_c)$  is defined based on  $G1$  following

$$\mathbf{x}_c = \operatorname{argmax}(G1) \quad (4.21)$$

#### 4.2.2 Extraction of the 2D vortex velocity field

We shift to the reference frame that is attached to the vortex and is denoted  $\mathcal{R}_V = (O_V, x, y, z)$ .  $\mathcal{R}_V$  is sketched in figure 4.16. This reference frame has the same axis as  $\mathcal{R}_M$ , however its origin  $O_V$  is set at the instantaneous centroid of the vortex  $\mathbf{x}_c$ . Therefore, seen from the galilean reference frame  $\mathcal{R}_M$ ,  $\mathcal{R}_V$  descends vertically with the vortex at velocity  $W_v$ . The transfer from  $\mathcal{R}_M$  to  $\mathcal{R}_V$  is achieved by correcting the vertical velocity field  $w$  from the descent velocity  $W_v$  such that, in  $\mathcal{R}_V$ :

$$\mathbf{v} = (u, v, w - W_v) \quad (4.22)$$

Therefore, in what follows  $\mathbf{v}_\perp = (0, v, w - W_v)$

In the following the velocity field of the vortex is more closely investigated and recast into a cylindrical coordinate system about the vortex center yielding  $\mathbf{v} = (v_\theta, v_r, v_x)$ . To do this, the data on the polar grid is interpolated from that on the original cartesian grid (given by the PIV) on a domain limited to the radial distance  $r_{max} = 0.4b_0$ . The polar coordinates and  $r_{max}$  are shown in figure 4.16, the latter by a black dashed line.

The azimuthal, radial and axial velocity fields  $v_\theta, v_r$  and  $v_x$  are shown in Fig. 4.17. The fields are zoomed-in to  $y, z \in [-0.2b_0, 0.2b_0]$  for clarity. The azimuthal velocity field  $v_\theta$ , shown in Fig. 4.17a, is mostly axisymmetric about the vortex center. In

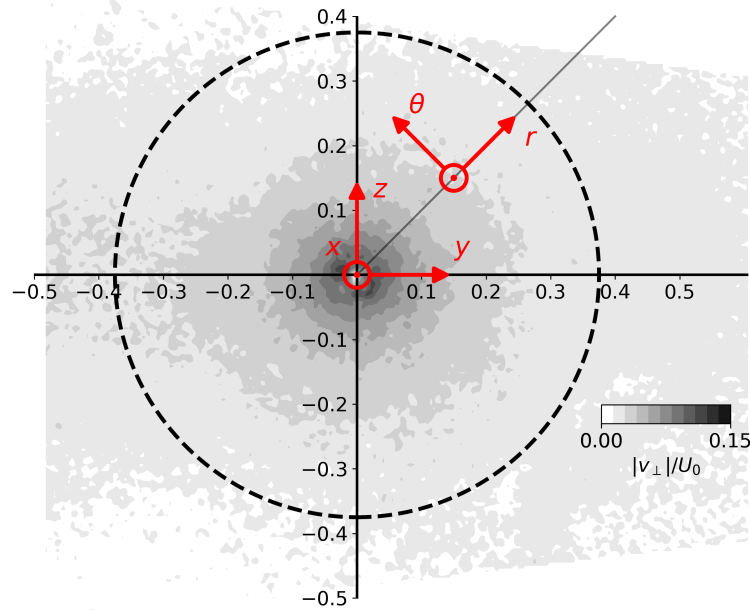


FIGURE 4.16: Diagram of the reference frame attached to the vortex  $\mathcal{R}_V$ , the radius  $r_{max}$  is shown by a dashed line

Fig. 4.17b, the radial velocity field  $v_r$  feature weak values. Residual radial velocities realistically result from the unavoidable slight error made in detecting the vortex core. A significant wake-type stream-wise velocity  $v_x$  (corresponding to positive  $v_x$  velocities, that is, in the direction of the wing), is observed in the core of the vortices, as shown in Fig. 4.17c. The axial velocity in the vortex core results from the axial pressure gradient imposed by the roll-up and the external flow, and the effect of the roll-up of the velocity deficit associated with the boundary layer at the wing surface (see, for instance, Batchelor [5], Moore & Saffman [66]).

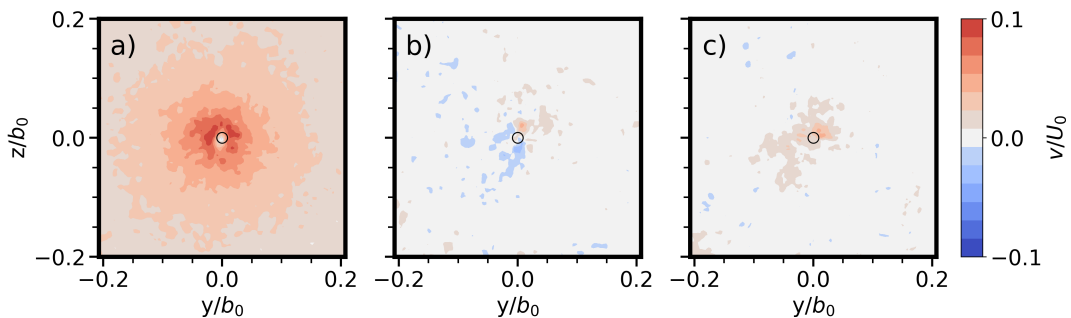


FIGURE 4.17: Instantaneous velocity fields a)  $v_\theta/U_0$ , b)  $v_r/U_0$  and c)  $v_x/U_0$  for the reference wing under configuration  $C_{27}$  and  $tU_0/b_0 = 30$ . The centroid  $x_c$  is shown with a black circle.

### 4.2.3 Extraction of the 1D velocity profile

An overall procedure of velocity averaging is then performed to allow a fine characterization of the vortex parameters like radius and circulation. The same procedure is realized for the three velocity components,  $v_x$ ,  $v_\theta$  and  $v_r$ . The first step of the procedure is to calculate a sliding time average velocity field using finite time windows

centered around each instant  $t$ . This is necessary to filter the unsteadiness between successive instantaneous flow fields. To compute the length of the windows we define a timescale of viscous diffusion in the vortex as  $t_\nu = \pi R_d^2 / \nu$ , with  $R_d$  a measure of the vortex radius and  $\nu$  the kinematic viscosity of water. We then set a duration  $\tau$  so that the viscous diffusion of the vortex is negligible compared to the duration of the time window used when averaging ( $\tau \ll t_\nu$ ), here,  $\tau = 1$  s is considered sufficient for the purpose of filtering some unsteadiness off the vortex field. Thus the operator  $\langle x \rangle_\tau$  is defined to translate the time average of variable  $x$  over a time-frame  $[t - \tau/2, t + \tau/2]$ . The operator is written explicitly below, in eq. 4.23.

The velocity fields resulting from the time averaging procedure are shown in Fig. 4.18. The axial symmetry of the  $\langle v_\theta \rangle_\tau$  field has been enhanced without significant modifications of the magnitude of velocity in the field (see Fig. 4.18a). Also, the radial velocity field  $\langle v_r \rangle_\tau$  is almost nill, which further suggests that instantaneous  $v_r$  values stem from random errors in the center detection step (see Fig. 4.18b). The axial velocity field  $\langle v_x \rangle_\tau$  is not axi-symmetric but its magnitude does decrease when moving away from the vortex center, as expected.

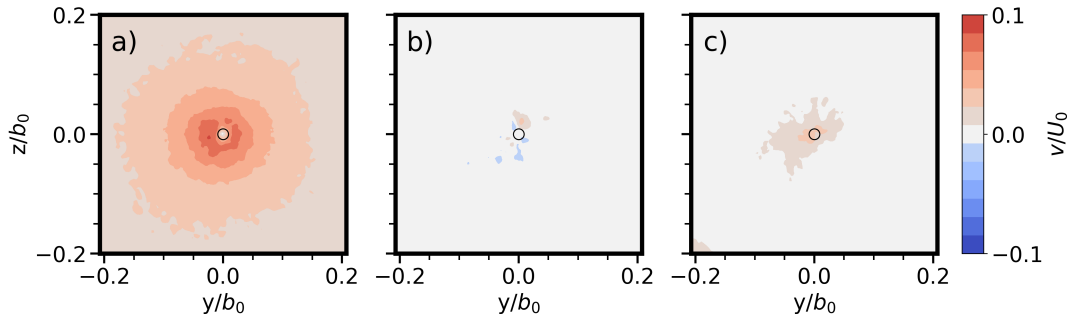


FIGURE 4.18: Velocity fields averaged over a time frame of 1 s **a)**  $\langle v_\theta \rangle_\tau / U_0$  **b)**  $\langle v_r \rangle_\tau / U_0$  and **c)**  $\langle v_x \rangle_\tau / U_0$  field for the reference wing under configuration  $C_{27}$  and  $tU_0/b_0 = 30$ . The centroid  $x_c$  is shown with a black circle.

From each sliding time-average velocity field, an azimuthal average in the  $\theta$ -wise direction is further performed to produce a vortex velocity profile  $v_\theta(r, t)$  for  $r \in [0 : r_{max}]$ . An operator  $\langle x \rangle_{\tau, \theta}$  is thus defined to encompass both average computations :

$$\langle v_\theta(r, t) \rangle_{\tau, \theta} = \frac{1}{2\pi} \frac{1}{\tau} \int_0^{2\pi} \int_{t-\tau/2}^{t+\tau/2} v_\theta(r, \theta', t') dt' d\theta' \quad (4.23)$$

Following the usual methodology (see appendix D) the resulting data  $\langle v_\theta(r, t) \rangle_{\tau, \theta}$  is finally averaged over the  $N$  different realizations which were repeated yielding  $\bar{v}_\theta(r, t)$  and the dispersion of data  $s_{v_\theta}(r, t)$ . Explicitly, for the average operation :

$$\bar{v}_\theta(r, t) = \frac{1}{N} \sum_{i=1}^N \langle v_\theta(r, t) \rangle_{\tau, \theta, i} \quad (4.24)$$

The number of repetitions is between none ( $N = 1$ ) to  $N = 4$  depending on the configuration (this information is available in appendix A). In what follows, we use the notation  $\bar{v}_x(r, t)$ ,  $\bar{v}_\theta(r, t)$  and  $\bar{v}_r(r, t)$  to refer to the velocity profiles obtained through this averaging operation.

Further characterization requires the radial profile of axial vorticity  $\bar{\omega}_x(r, t)$ . The average procedure is applied yielding

$$\bar{\omega}_x(r, t) = \frac{1}{r} \left[ \frac{d}{dr} (r\bar{v}_\theta(r, t)) \right] \quad (4.25)$$

The evolution of  $\bar{\omega}_x(r, t)$ , shown in Fig. 4.20, follows a Gaussian profile where  $\bar{\omega}_x(r, t)$  is concentrated in a region of small  $r$ . This region will be discussed on the following.

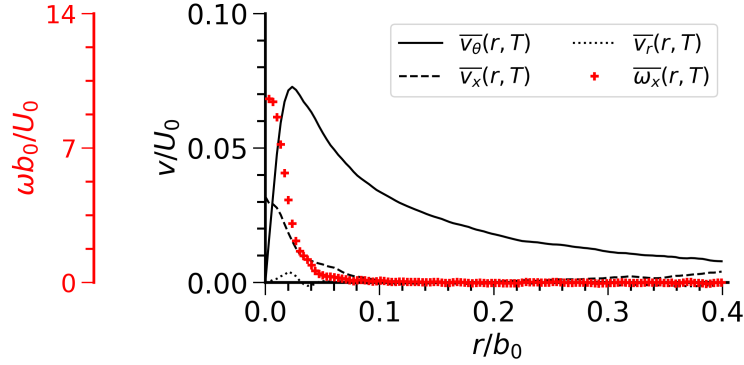


FIGURE 4.19: velocity and vorticity profiles obtained for the reference wing towed under configuration  $C_{27}$  and  $tU_0/b_0 = 30$ .

The resulting 1D profiles of vortex velocity and vorticity are shown in Fig. 4.19. It can be seen that the 1D velocity and vorticity profiles follow the same trend as observed from the 2D velocity distributions. Namely, azimuthal velocity follows a distribution similar to that of a gaussian vortex. This can also be seen on the evolution of axial vorticity which is concentrated around the vortex center. Also, axial velocity is also concentrated around the vortex center and radial velocity is almost nill. Some axial velocity is observed to develop for  $r/b_0 > 0.3$ , this is thought to be related to the remanents of the wake of the strut but this is negligible for our purposes.

Numerical fits of the velocity profile are performed against the q-vortex model [5]. The q-vortex model is defined by

$$v_r^Q(r) = 0 \quad ; \quad v_\theta^Q(r) = \frac{\Gamma}{2\pi r} \left( 1 - e^{-\left(\frac{r}{R_d}\right)^2} \right) \quad ; \quad v_x^Q(r) = \Delta U e^{-\left(\frac{r}{R_d}\right)^2} \quad (4.26)$$

where the superscript  $Q$  is used to indicate the matched velocity field.  $\Delta U$  is the difference between far-field velocity ( $r \rightarrow \infty$ ) and the maximum axial flow in the core of the vortex. Here  $\Delta U(t) = v_x^Q(r = 0, t)$ .  $R_d$  is the dispersion radius and  $\Gamma$  the circulation. The ratio of azimuthal to axial velocity in the vortex, also called swirl number  $q$ , is an important factor regarding for instance stability. It is defined as

$$q = \frac{\Gamma}{2\pi R_d \Delta U}. \quad (4.27)$$

A comparison between a sample of the experimental data and the q-vortex fit is shown in Fig. 4.19. It confirms that there is a good agreement of the experimental data with the gaussian profile.

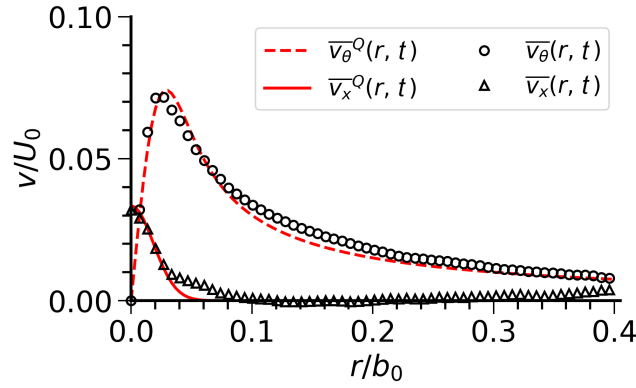


FIGURE 4.20: q-vortex fitted over the velocity profiles, for the reference wing towed under configuration  $C_{27}$  and  $tU_0/b_0 = 30$ . For clarity, data has been decimated by 3

At this stage, the measured velocity field is treated into a format suitable for analyzing the instantaneous vortex velocity field. To do this, it is first demonstrated that the instantaneous vortex velocity field can be averaged over a short time window to filter the flow unsteadiness. Then, this two-dimensional velocity field is processed to derive a one-dimensional average velocity profile. Through analysis of our extensive database, we have obtained  $\bar{v}_x(r, t)$ ,  $\bar{v}_\theta(r, t)$ , and  $\bar{v}_r(r, t)$ , which represent the vortex velocity distribution for a given time and under a specific towing configuration. In the next section, these results are utilized to characterize the vortex.

#### 4.2.4 Estimation of vortex characteristics

In this section, we discuss the physical characteristics of the vortex. Particular emphasis is placed on the vortex characteristics that define its potential hazard in a wake-encounter scenario. The hazard is commonly related to the magnitude of the rolling moment that a vortex can induce on the follower aircraft. This magnitude scales proportionally to the vortex circulation and it is reduced with a larger vortex core radius. Owing to the good match between the experimental data ( $v_\theta(r)$ ) and the q-vortex fit ( $v_\theta^Q(r)$ ), the fit (see eq. 4.26) also provides the vortex radius and circulation through  $R_d$  and  $\Gamma$ . Here, these quantities are discussed and compared to direct measurements realized on  $v_\theta(r)$ .

##### 4.2.4.1 Measurement of vortex size

Of the various definitions of vortex size, we begin by considering the radius of the compact vorticity region, denoted as  $R_\omega(t)$ . This measure is established by identifying where the vorticity magnitude surpasses the level of PIV noise, which serves as a practical threshold. The determination of  $R_\omega(t)$  is key in our methodology to measure the vortex circulation, as it is shown below. The process developed to compute  $R_\omega(t)$  is illustrated in Fig. 4.21. In short, the process involves first a statistical analysis of  $\bar{\omega}_x(r)$  to estimate the noise magnitude.

In Fig. 4.21a, the radial evolution of  $|\bar{\omega}_x|$  is plotted. It exhibits a smooth evolution as a function of  $r$  when its magnitude exceeds approximately  $10^{-1} \text{ s}^{-1}$ . To draw a first estimation of the region where noise is dominant,  $R_1$  is set such that  $|\bar{\omega}_x|(r \geq$

$R_1) \leq 0.1s^{-1}$ . Within the region defined by  $r \geq R_1$ , we introduce  $\omega_n(r)$  following

$$\omega_n(r) = \begin{cases} 0 & r \leq R_1 \\ \bar{\omega}_x(r) - \frac{1}{r_{max}-R_1} \int_{R_1}^{r_{max}} \bar{\omega}_x(r) dr & r > R_1 \end{cases} \quad (4.28)$$

It is recalled that  $r_{max} = 0.4b_0$  defines the extent of the circular domain from which the measured velocity field is extracted. Fig. 4.21b illustrates the density distribution of  $\omega_n(r)$ . The noise magnitude is estimated from the standard deviation of  $\omega_n(r)$ , denoted as  $\sigma_\omega$ . Values are considered indistinguishable from the noise level when  $\bar{\omega}_x(r) \leq 2\sigma_\omega$ . Finally,  $R_\omega$  is determined where

$$\bar{\omega}_x(r \geq R_\omega) \geq 2\sigma_\omega \quad (4.29)$$

which is indicated by the red dashed line in Fig. 4.21a. This boundary highlights the dominant vorticity concentration within  $r \leq R_\omega$ , while beyond this radius, vorticity values are comparable to the noise level.

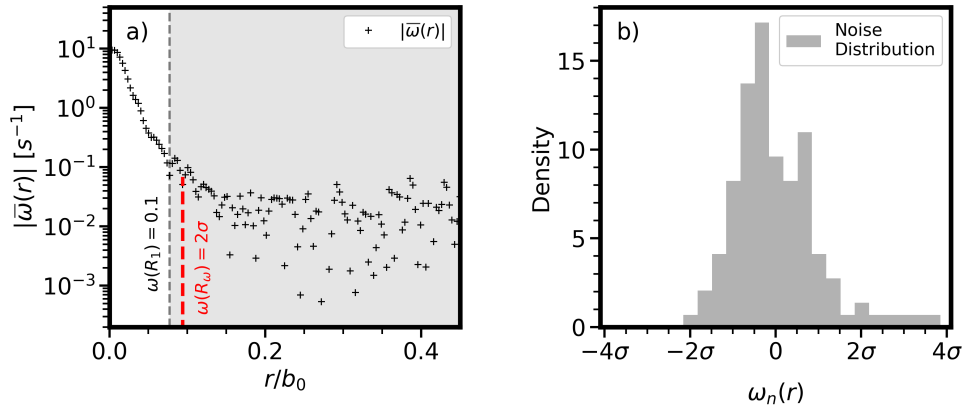


FIGURE 4.21: Illustration of the procedure to compute  $R_\omega$  on the vortex generated under configuration  $C_{27}$ , at  $tU_0/b_0 = 30$ . **a)** Magnitude of  $|\bar{\omega}_x|$  over  $r/b_0$ . The region where  $r > R_1$  is colored in grey and  $R_\omega$  is indicated by a red dashed line. **b)** Density distribution of  $\omega_n$

The next radius to be defined is the radius of maximum azimuthal velocity  $R_a(t)$ , which is computed using a cubic interpolation scheme on the discrete grid of the PIV set.

$$\bar{v}_\theta(r = R_a, t) = \max(\bar{v}_\theta(r, t)) \quad (4.30)$$

$R_a$ ,  $R_d$  and  $R_\omega$  are presented with respect to the vortex velocity and vorticity profiles in Fig. 4.22. Notably,  $R_a$  and  $R_d$  exhibit comparable values, whereas  $R_\omega$  is approximately four times larger than  $R_d$ . This trend is maintained over the whole dataset. In what follows,  $R_\omega$  is useful for the computation of circulation. Between  $R_a$  and  $R_d$ , our focus is on the later when studying the vortex size due to its common usage in relevant references [5, 24, 45].

The value of the vortex size soon after formation and its subsequent time evolution are now described. The magnitude of  $R_d$  is measured at  $t_{10}U_0/b_0 = 10$ , which is a conservative time to obtain a representative assessment of the vortex state shortly after roll-up completion. These measurements are shown in Fig. 4.23a. Data is plotted as a function of the towing angle of attack  $\alpha$ . Overall, it is observed that  $0.02 \leq R_d(t_{10})/b_0 \leq 0.05$ . The normalized radius  $R_d(t_{10})/b_0$  demonstrates a tendency to increase with  $\alpha$ , although larger values of  $R_d(t_{10})/b_0$  are also observed at

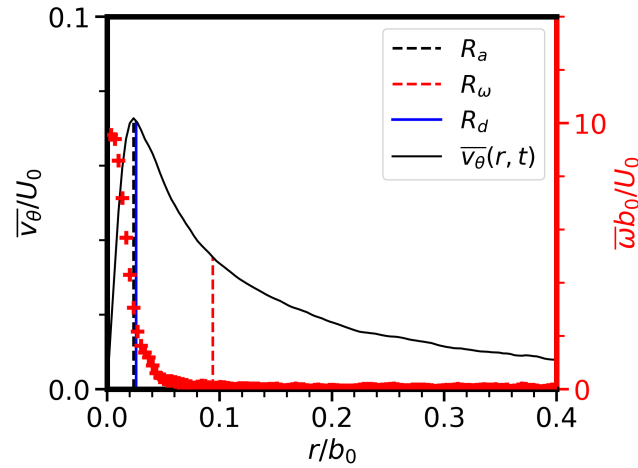


FIGURE 4.22: Measurements of the radius of a vortex generated in configuration  $C_{27}$ , at  $tU_0/b_0 = 30$

moderate angles of attack, around  $\alpha \sim 5^\circ$ .

The time evolution of vortex radius measurements is shown in Fig. 4.23b. To track the evolution of the vortices at large times, a repetition of the experiment is realized with the measurement frame placed at a lower vertical distance (see section 3.2.2.1 for details). Data is shown from the towing configuration ( $Ref, U_0 = 3m/s, \alpha = 3^\circ$ ) which was measured using the upper and lower frames. Through this method, measurements are provided until  $t_{max} \frac{U_0}{b_0} \sim 375$ . A good match is observed for the measurements of vortex radius  $R_a(t)$ ,  $R_d(t)$  and  $R_\omega(t)$ , plotted in Fig. 4.23b.  $R_a(t)$  and  $R_d(t)$  increase with time at a slow rate, while  $R_\omega(t)$  does not show any particular trend. Also, the value of  $R_\omega(t)$  is subjected to strong variability, nevertheless it is sufficient for our purposes as it is shown in the following section. The fact that measurements between both frames coincide is a good indicator of the validity of the procedure. The cause for radius growth is analyzed in section 4.3.1.

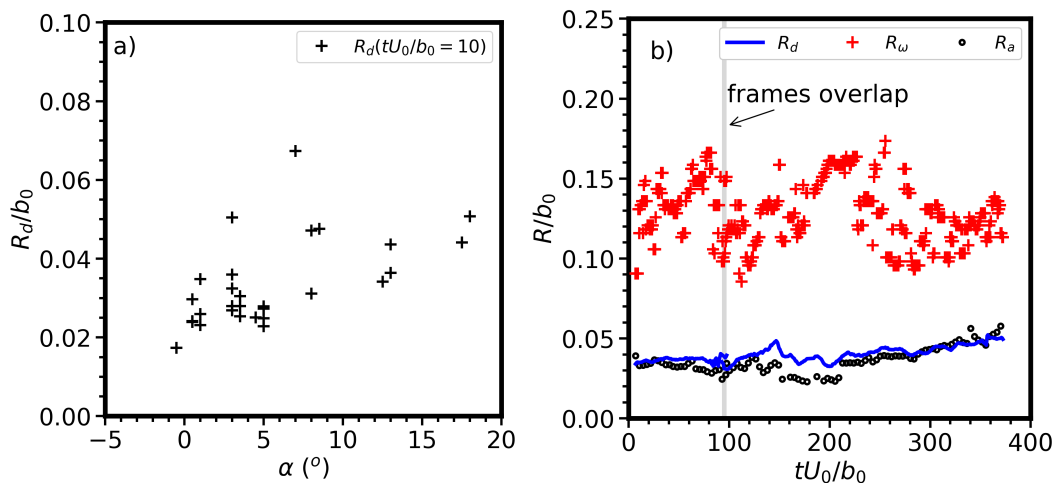


FIGURE 4.23: Characteristics of the vortex radius : **a)** Normalized dispersion radius for the right side vortex trailing 10 wingspans downstream from the reference wing as a function of towing angle of attack  $\alpha$  and **a)** time evolution of vortex radius downstream from the reference wing under configuration ( $U_0 = 3m/s, \alpha = 3^\circ$ )

#### 4.2.4.2 Measurement of vortex strength

The strength of the vortex is now characterized by analyzing its circulation and its maximum azimuthal and axial velocities.

The vortex circulation can be computed by integrating the tangential component of velocity along a closed contour encircling the vortex. In our measurements, this is equivalent to using the equation :

$$\Gamma_r(r, t) = 2\pi r \overline{v_\theta}(r, t) \quad (4.31)$$

where  $\Gamma_r$  represents the circulation at a specific radial distance  $r$  and time  $t$ . The evolution of  $\Gamma_r(r, t)$  as a function of radial distance is shown in Fig. 4.24 for a specific time  $t$ . It is expected that at a sufficiently large  $r$ , the value of  $\Gamma_r(r, t)$  evolves asymptotically to that of the vortex total circulation. Thus the total circulation of the vortex, denoted as  $\Gamma^{exp}(t)$ , is obtained by averaging  $\Gamma_r(r, t)$  in the region outside the vortex core. This region is estimated to start at  $r = R_\omega$  and is limited by the radius of the analysis domain which is  $r = r_{max}$ . This yields

$$\Gamma^{exp}(t) = \frac{1}{r_{max} - R_\omega} \int_{R_\omega}^{r_{max}} \Gamma_r(r, t) dr \quad (4.32)$$

This approach allows us to handle situations where no clear asymptotic value is observed in the evolution of  $\Gamma_r(r, t)$ . Most experiments yield however an asymptote for  $\Gamma_r(r, t)$ .

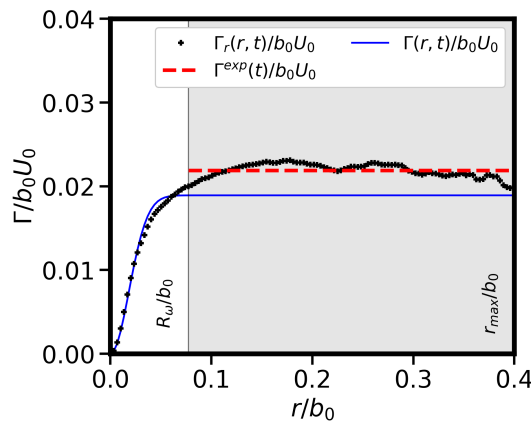


FIGURE 4.24: Circulation profile for the vortex trailing 30 wingspans downstream from the reference wing under configuration  $C_{27}$ . Data is decimated by 2 for clarity.

It is observed that the circulation obtained from the  $q$ -vortex fit ( $\Gamma$ ) underestimates the value obtained through a direct analysis of the measurements  $\Gamma^{exp}$ . This is the case in most of the experimental dataset and can be attributed to the fact that the velocity distribution of the real vortex is not exactly gaussian. However,  $\Gamma(t)$  and  $\Gamma^{exp}(t)$  follow the same time evolution which makes the use of  $\Gamma(t)$  adequate to characterize the evolution of the vortex properties.

The normalized magnitude of vortex circulation soon after roll-up ( $t_{10}U_0/b_0 = 10$ ) is plotted in Fig. 4.25a.  $\Gamma(t_{10})/U_0b_0$  evolves in a linear fashion with the wing angle of attack. This is expected based on the relationship between  $\alpha$  and the wing lift (see eq. 4.3). Next, the time evolution of the normalized circulation is shown, measured at configuration  $C_{29}$  in Fig. 4.25b. Circulation is seen to decrease with

time at a monotonous rate. There is a good match in circulation magnitude in the region where the measurement frames overlap. Since the vortex strength is reduced at large times, its vertical descent is rendered slower. On the other hand, very close to the PIV frame lower border, the vortex descent might decelerate due to the action of ground effects as is shown in section 4.3. This explains that the measurement duration on the lower frame is longer.

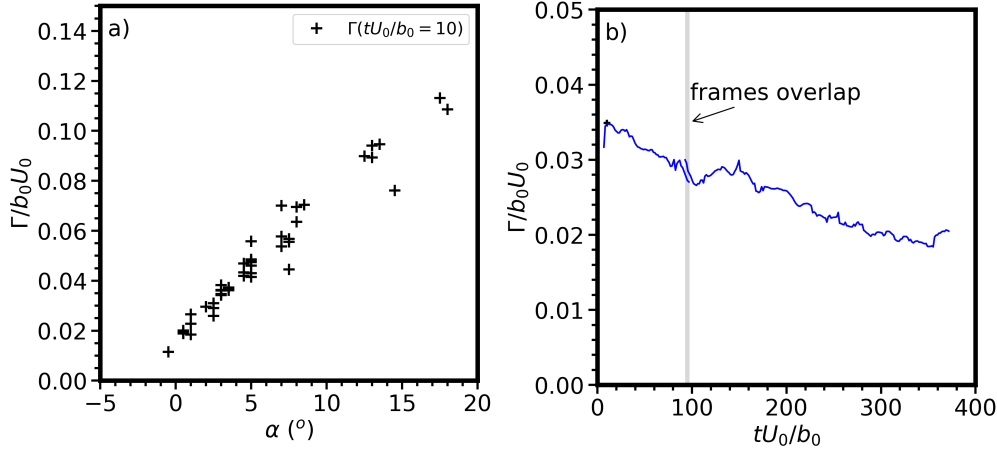


FIGURE 4.25: **a)** Normalized circulation for the right side vortex trailing 10 wingspans downstream from the reference wing as a function of towing angle of attack  $\alpha$  and **b)** time evolution of normalized circulation downstream from the reference wing under configuration  $C_{29}$  : ( $U_0 = 3m/s, \alpha = 3^\circ$ ).

The maximum azimuthal velocity, maximum axial velocity and maximum axial vorticity, respectively  $\max(v_\theta^Q)$ ,  $\max(v_x^Q)$  and  $\max(\omega_x^Q)$ , are directly taken from the fitted velocity profiles.

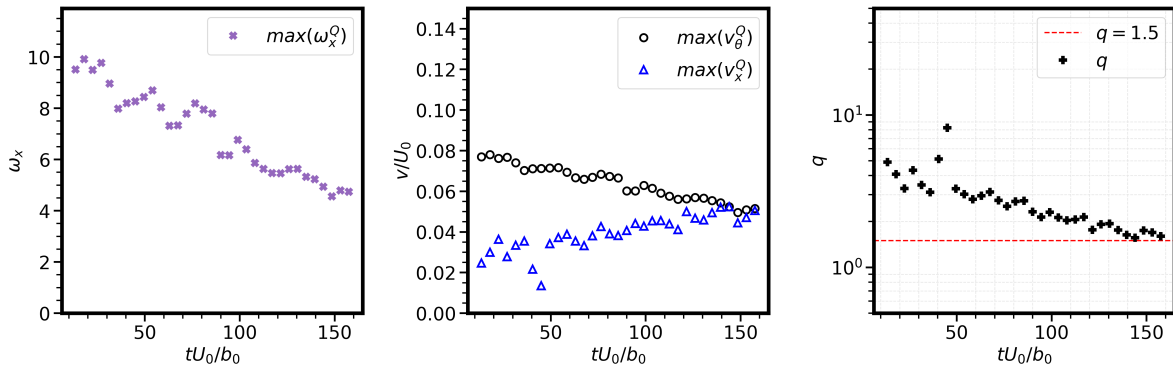


FIGURE 4.26: Flow intensity in the vortex core over time computed through a fit of the q-vortex over the experimental data (configuration  $C_{27}$ ) and expressed by **a)** maximum vorticity  $\max(\omega_x^Q)$ , **b)** maximum azimuthal and axial velocities  $\max(v_\theta^Q)$  and  $\max(v_x^Q)$  and **c)** swirl parameter  $q$ . Data has been decimated by 3 for clarity.

The time evolution of  $\max(\omega_x^Q)$ ,  $\max(v_\theta^Q)$  and  $\max(v_x^Q)$  is depicted for configuration  $C_{27}$  in Fig. 4.26. The time evolution of the swirl number  $q(t)$  is also shown in Fig. 4.26c. Remarkably, despite performing independent fits for each dataset  $t$ , there is a smooth consistency in the results for adjacent data points.

It is observed that the in-plane flow intensity, represented by  $\max(\omega_x^Q)$  and  $\max(v_\theta^Q)$ , decreases monotonically with time. On the other hand, the out-of-plane flow, indicated by  $\max(v_x^Q)$ , increases with time. This behavior is reflected in  $q$ , which also decreases monotonically. The behavior of these quantities is further explored in the subsequent analysis.

#### 4.2.4.3 Vortex trajectories

The trajectories of the vortex are now analyzed in the laboratory reference frame  $\mathcal{R}_M$ . The trajectory of the barycenter of vorticity  $x_\omega(t)$ , generated under a specific configuration  $C_{15}$  : (*Ref*,  $U_0 = 2\text{m/s}$ ,  $\alpha = 3.5^\circ$ ), is shown in Fig. 4.27. In this experiment, the trajectories are seen to be disturbed. These perturbations could arise from 3D effects influencing the flow. Indeed, the trailing vortex evolves over a large longitudinal distance in this experiment so one could ask the question whether tridimensional effects are present or not. In principle, to do this would be difficult in our case since in our experiment we dispose of only one measurement plane which is fixed in space. However, the presence of random or long-wavelength motion in the vortex can be determined by comparing its trajectory with an unperturbed 2D trajectory which we estimate.

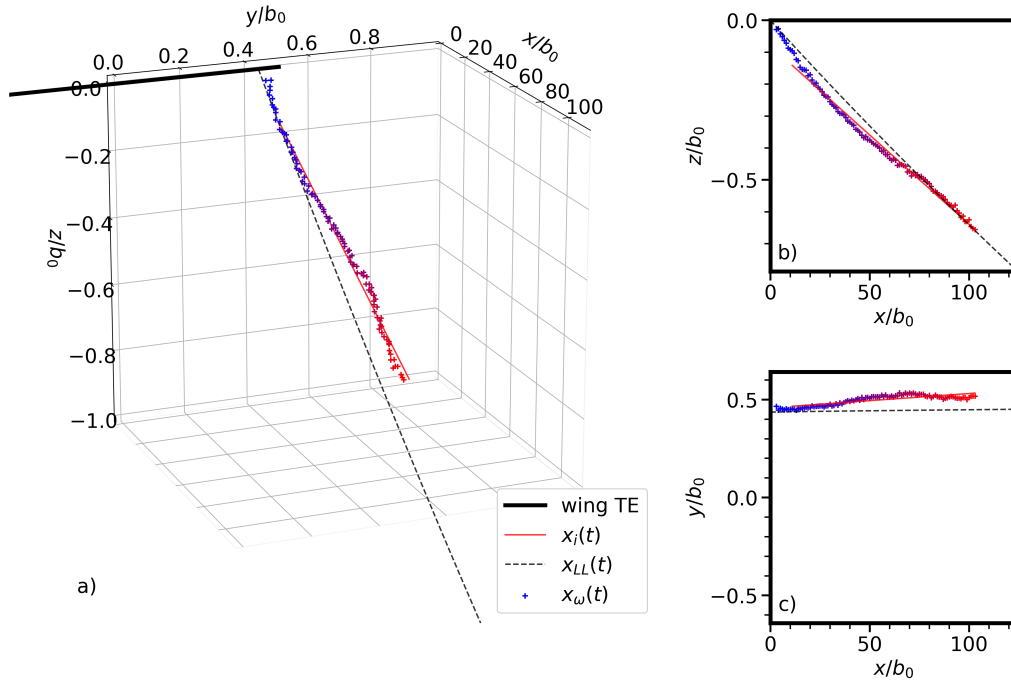


FIGURE 4.27: Characterization of the trajectory of the vorticity barycenter  $x_\omega(t)$ , the unperturbed vortex  $x_i(t)$  and of the position predicted by lifting line theory  $x_{LL}$ , generated under configuration  $C_{15}$ . Subsequent positions overtime are colored in from  $tU_0/b_0 \sim 0$  (blue) to  $tU_0/b_0 \sim 100$  (red) : **a**) trajectories in a 3D space, note that scales are adapted from their original size. **b**) vertical trajectory of the vortex. **c**) plot of the vorticity barycenter in the reference frame centered around the unperturbed position.

First, the ideal trajectory of the vortex is estimated from that predicted by 2D theory. An analytical trajectory of the vortex, denoted  $\mathbf{x}_{LL}(t)$ , is obtained through a combination of lifting line theory and predicted 2D effects induced by the tank boundaries (further details are found in 4.1.1). The trajectory of the barycenter of vorticity  $\mathbf{x}_\omega(t)$  is compared to the 2D prediction  $\mathbf{x}_{LL}(t)$  in Fig. 4.27. Both  $\mathbf{x}_{LL}(t)$  and  $\mathbf{x}_\omega(t)$  exhibit similar descent velocities and a similar span-wise position. However, the trajectory of  $\mathbf{x}_\omega(t)$  is not straight, and is located lower than  $\mathbf{x}_{LL}(t)$  for  $x/b_0 < 50$  and more outwards than  $\mathbf{x}_{LL}(t)$  after a similar  $x$ . Since this behavior cannot be explained by the arguments that allow to compute  $\mathbf{x}_{LL}(t)$ , one can enounce the hypothesis that the vortex position is perturbed from its original trajectory by an additional effect. Possible causes to explain this behavior are discussed in section 4.3.3.

The procedure utilized to isolate the position perturbation is described now. The focus is on characterizing the offset that occurs between the unperturbed trajectory of the vortex  $\mathbf{x}_i(t)$  and the measured position of the vortex  $\mathbf{x}_\omega(t)$ . To estimate the unperturbed trajectory  $\mathbf{x}_i(t)$ , the subsequent positions  $\mathbf{x}_\omega(t)$  are broken down in horizontal and vertical components. Then, a linear regression of this data is used to estimate  $\mathbf{x}_i(t)$ . The roll-up stage is excluded from the trajectory data when performing this linear regression.  $\mathbf{x}_i(t)$  is shown by a red line in figure 4.27. Finally, the offset  $\mathbf{x}_\delta$  about the ideal trajectory is computed following

$$\mathbf{x}_\delta(t) = \mathbf{x}_\omega(t) - \mathbf{x}_i(t) \quad (4.33)$$

$\mathbf{x}_\delta(t)$  thus obtained is in the order of magnitude of the core size  $R_d$ .

### 4.3 Analysis of physical phenomena causing the evolution of vortex characteristics

We examine how the vortex radius, circulation, swirl parameter and perturbations in its trajectory change with time, but also how they evolve in response to a change in towing parameters ( $U_0$  and  $\alpha$ ).

#### 4.3.1 Physical mechanisms driving vortex decay

##### 4.3.1.1 Laminar diffusion of the vortex core

First, we wish to identify the cause for radius growth observed in the experiments. The time evolution of normalized dispersion radius is shown in Fig. 4.28. In order to simplify our purposes, we show the results only for three cases which are towed at the same velocity ( $U_0 = 3m/s$ ) but at different angles of attack ( $\alpha = 0.5^\circ, \alpha = 3^\circ$  and  $5^\circ$ ). The normalized dispersion radius  $R_d(t)/b_0$  exhibits an increase with time, that can be correlated to the laminar diffusion process, even in the presence of turbulence [43].

$$R_d(t)^2 = R_d(t_0)^2 + 4vt \quad (4.34)$$

When scaled by the dispersion radius found at  $t_0$ , this yields

$$\left( \frac{R_d(t)}{R_d(t_0)} \right)^2 - 1 = \frac{4vt}{R_d^2(t_0)} \quad (4.35)$$

The experimental measurements are compared to the prediction yielded by in Fig. 4.28. Here, time is scaled by the viscous time scale  $t_\nu$ . The good agreement obtained here shows that vortices do increase in size by laminar diffusion.

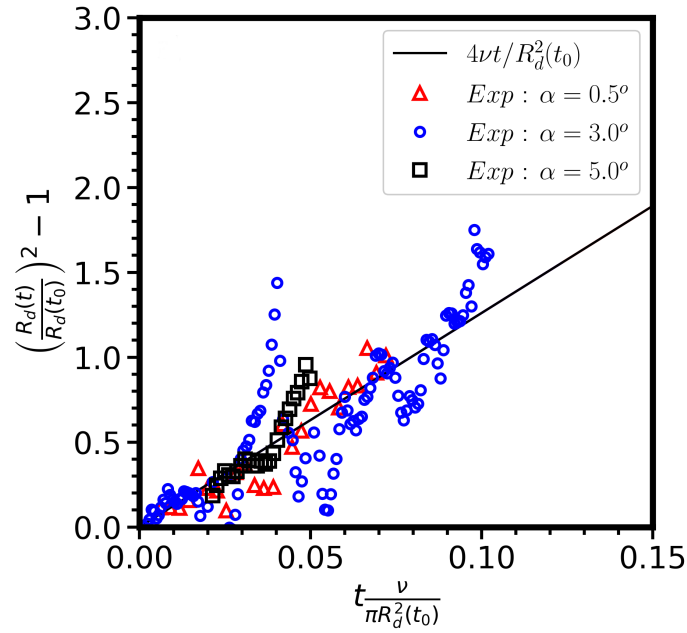


FIGURE 4.28: Evolution of normalized dispersion radius (experimental and predicted) for the right side vortex trailing downstream from the reference wing towed at  $U_0 = 3m/s$  and  $\alpha = 0.5^\circ, 3^\circ, 5^\circ$  : time is normalized by the viscous time-scale

#### 4.3.1.2 Analysis of the circulation decrease

Now, we wish to identify the cause for the circulation decrease that is observed in the experiments. In theory, for a vortex in an infinite medium, the circulation is a constant. The decrease of the circulation that is observed here can be the result of boundary effects or measurement inaccuracies.

Indeed, in order to obtain the rate of change of vorticity one can consider the Helmholtz equation [39] :

$$\frac{D\boldsymbol{\omega}}{Dt} = (\boldsymbol{\omega} \cdot \nabla)\mathbf{u} + \nu\Delta\boldsymbol{\omega} + \frac{\nabla \times \mathbf{f}}{\rho} \quad (4.36)$$

One should note that the term  $\frac{\nabla \times \mathbf{f}}{\rho}$  takes the form of a source term if the fluid is stratified, as would be the case if there is a vertical temperature gradient in the tank. This, however, could not be confirmed in this work. From the Helmholtz equation an expression for the rate of change of circulation can be derived (see equations 2.51 to 2.52). If one neglects stratification effects, the resulting equation shows that circulation decreases due to viscous friction at the wall :

$$\frac{d\Gamma}{dt} = -\nu \int_{-\infty}^{\infty} \frac{\partial \omega_x}{\partial y} \Big|_{y=0} dz \quad (4.37)$$

This could be the case in our experiments, if the vortex field extends to a distance comparable with that separating it from the tank walls. In this experiment, the distance separating the vortex from the lateral walls is  $1.375b_0$ . It is shown in section 4.1.1 that the image effect induced by the lateral walls amounts to an induced upwash  $W_w$  (see eq. 4.9), which is non-negligible with respect to the dipole downwash

$W_d$ . Since the tank width is not large enough to isolate vortices from significant image effects induced by the walls, it is also possible that the effect of viscous friction occurring at the lateral walls are also significant. Furthermore, the distance separating the vortices from the walls is often reduced from the initial estimation, since portside vortices are observed to drift side-wise towards the wall during their evolution. This outwards drift is promoted by the effect of image vorticity about the tank ground (see sec. 4.1.1).

In these experiments, circulation is observed to decrease with time on all configurations. This is seen in Fig. 4.29a, where the normalized evolution of  $\Gamma(t)/U_0 b_0$  is plotted for experiments towed at  $U_0 = 3\text{ m/s}$  and various angles of attack in the range  $0.5^\circ \leq \alpha \leq 8^\circ$ . Circulation decreases for all configurations and the rate of change  $|\frac{\Delta\Gamma/b_0 U_0}{\Delta t W_d/b}|$  seems to increase at higher angles of attack. This suggests that the mechanism responsible for circulation decrease scales with the magnitude of  $|\Gamma|/b_0 U_0$ . This observation is in agreement with the hypothesis that the tank frontiers play a significant role on the evolution of the circulation.

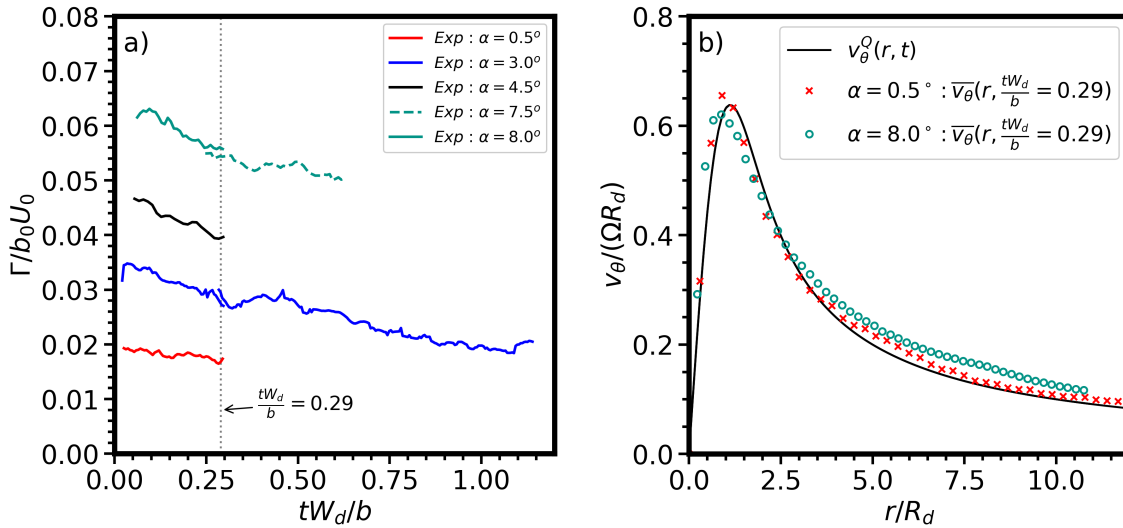


FIGURE 4.29: Circulation and velocity distributions measured on the right side vortex trailing downstream from the reference wing. **a)** Evolution of normalized circulation for experiments at configuration  $U_0 = 3\text{ m/s}$  and various angles of attack  $\alpha$ . Time is scaled by the induction based time. **b)** Vortex velocity distributions for the cases (*Ref*,  $U_0 = 3\text{ m/s}$ ,  $\alpha = 0.5^\circ$ ) and (*Ref*,  $U_0 = 3\text{ m/s}$ ,  $\alpha = 8^\circ$ ). The fitted  $q$ -vortex model  $v_\theta^Q(r)$  is plotted with a solid line. Data is decimated by 3, for clarity. The radial coordinate is normalized by the radius  $R_d$  and velocity is normalized by  $\Omega R_d$ .

In Fig. 4.29b, the normalized velocity distribution of the vortex at  $tW_d/b = 0.29$  is shown for the configurations where  $U_0 = 3\text{ m/s}$  and the angle of attack is  $\alpha = 0.5^\circ$  and  $\alpha = 8^\circ$ . Here, the measured velocity distribution  $\bar{v}_\theta(r, t)$  is compared to that of the  $q$ -vortex fit,  $v_\theta^Q(r, t)$ . It can be seen that at radii larger than the core (say,  $r > 3R_d$  in the figure)  $\bar{v}_\theta(r, t) > v_\theta^Q(r, t)$ . This suggests that the real flow is not fully irrotational at these large radial distances. The observation that vorticity extends beyond large radial distances is also in agreement with the hypothesis that the tank is not large enough to impede viscous friction from occurring at the lateral wall.

Further confirmation of this hypothesis would require a larger domain of  $r$ . However in our case the domain is limited to  $r \leq r_{max} = 0.4b_0$  which is defined with respect to the dimensions of the PIV window.

Measurement inaccuracies may also have an effect on the evolution of circulation. On one hand, laminar diffusion may distribute vorticity radially outwards, eventually surpassing the extent of our integration domain,  $r > r_{max}$ . In this case, the measured circulation decreases artificially. We show above that the flow seems to be not fully irrotational at  $r \sim r_{max}$ , so circulation measurement might be indeed affected.

### 4.3.2 Evolution of the peak vortex velocities and of the swirl number

The stability of a trailing vortex can be much affected by the axial flow in its core. Following [24, 56, 72], the swirl parameter  $q$  that compares the azimuthal velocity to the axial velocity distinguish a stable region for  $q > 1.5$  and an unstable one below this threshold, for a  $q$ -vortex, when the axial flow is strong enough. The experiment offers a long time observation of the trailing vortices that is ideally suited to evaluate the evolution of the azimuthal and axial velocity and of the swirl number. It is interesting to note first, that for an axisymmetric vortex column the azimuthal and axial velocities are related through the cyclostrophic equilibrium. This can be shown by considering the equations of continuity and of momentum for an isolated and axisymmetrical vortex. Here, we neglect the viscous term when analyzing the flow on a time-scale small with respect to  $t_v$ . The equation of continuity reduces to :

$$\frac{\partial v_x}{\partial x} = 0 \quad (4.38)$$

For  $v_r$ , the equation of motion becomes :

$$\rho \frac{v_\theta^2}{r} = \frac{\partial p}{\partial r} \quad (4.39)$$

and for  $v_x$  :

$$\rho \frac{\partial v_x}{\partial t} = - \frac{\partial p}{\partial x} \quad (4.40)$$

Following 4.39, pressure at the center of the vortex ( $r = 0$ ) translates to

$$p(r = 0) = p_\infty - \rho \int_0^\infty \frac{v_\theta^2}{r} dr \quad (4.41)$$

These equations show that when the vortex is subjected to a perturbation along its core, the pressure difference arising in the axial direction will disrupt the cyclostrophic equilibrium. A modification of the axial flow is created in this way, because of the fluid that is moved axially by the inhomogeneous pressure.

The evolution of the azimuthal and axial velocity is shown for two particular configurations in Fig. 4.30. One can observe that the azimuthal velocity decreases with time, while axial velocity (deficit) increases. This is in line with the expected dynamics as discussed above. The decrease of azimuthal velocity generates a higher pressure in the core of the vortex, which tends to push the flow towards the wing, and thus amplify the velocity deficit. However, we observe that for configuration C<sub>30</sub>, the increase of axial flow seems to stop when the axial velocity reaches a similar magnitude to that of azimuthal velocity (this occurs at  $tU_0/b_0 > 150$  in the figure).

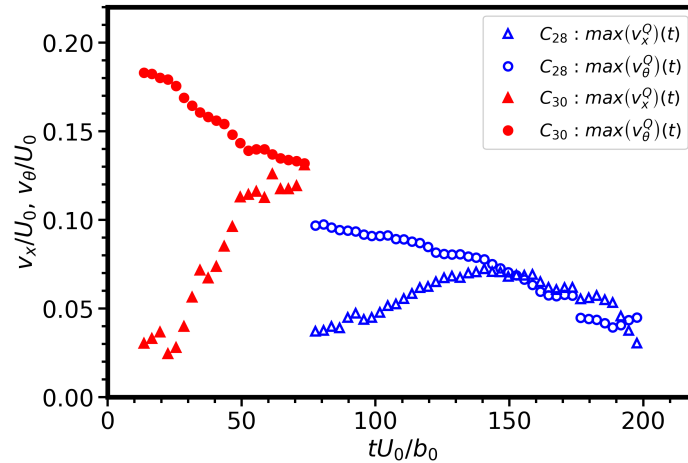


FIGURE 4.30: Evolution of peak axial and azimuthal velocities for the right side vortex trailing behind the *Ref* wing towed at configuration  $C_{28}$  : (*Ref*,  $U_0 = 3\text{m/s}$ ,  $\alpha = 2.5^\circ$ ) and at configuration  $C_{30}$  : (*Ref*,  $U_0 = 3\text{m/s}$ ,  $\alpha = 4.5^\circ$ ). Data is decimated by 4 ( $C_{28}$ ) and by 2 ( $C_{30}$ ) for clarity

The temporal evolution of  $q(t)$ , shown in Fig. 4.31, corresponds to all experiments of the *Ref* wing. The plot draws the threshold  $q = 1.5$  with a red dashed line. As a consequence of the evolution of the azimuthal and axial velocities  $q$  first decreases with time but one observes that as the value reaches the stability threshold, the decrease stops. For instance, for the experiment  $C_{30}$ ,  $q$  decreases sharply until  $tU_0/b_0 = 50$  when  $q$  approaches 1.5 and for  $tU_0/b_0 > 50$ , the value of  $q$  remains constant. For configuration  $C_{28}$ ,  $q$  decreases until  $tU_0/b_0 = 150$  when the condition  $q \leq 1.5$  is reached. Soon after  $tU_0/b_0 > 150$ , the value of  $q$  increases sharply. This behavior is found for all experiments, suggesting that the vortex tends to keep out of the instability.

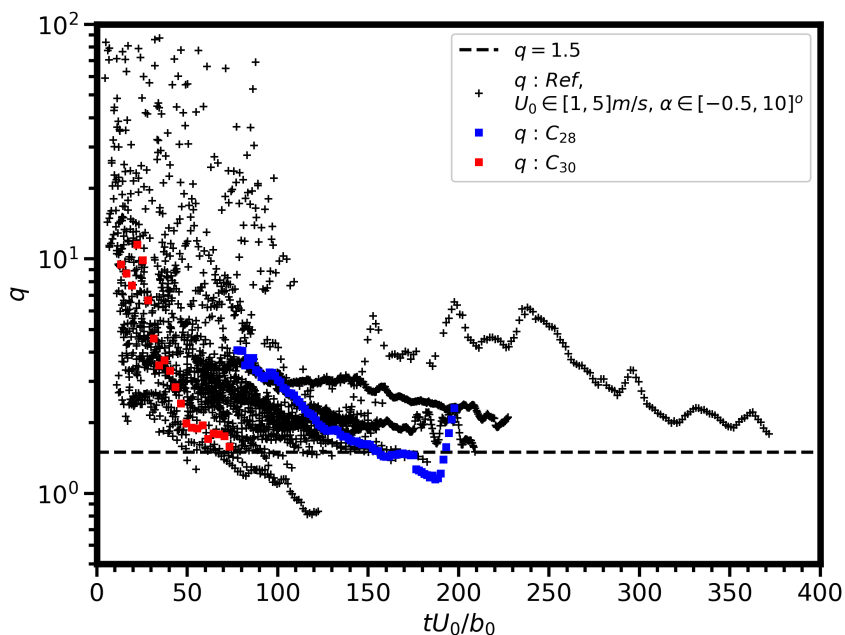


FIGURE 4.31: Evolution of the swirl number  $q$  for the right side vortex trailing behind the *Ref* wing configuration.

### 4.3.3 Random and periodic components in the trajectories of the trailing vortices

The nature of the periodic and non-periodic components observed in the trajectories of the vortices are discussed in this paragraph. Indeed, when analyzing the evolution of  $\mathbf{x}_\omega(t)$  about  $\mathbf{x}_i(t)$ , a periodic component is observed in the vortex trajectories of some experiments, while non-periodic motion is observed in other experiments of the dataset. Some characteristics of the offset  $\mathbf{x}_\delta(t)$  are shown for two different experiments in Fig. 4.32.

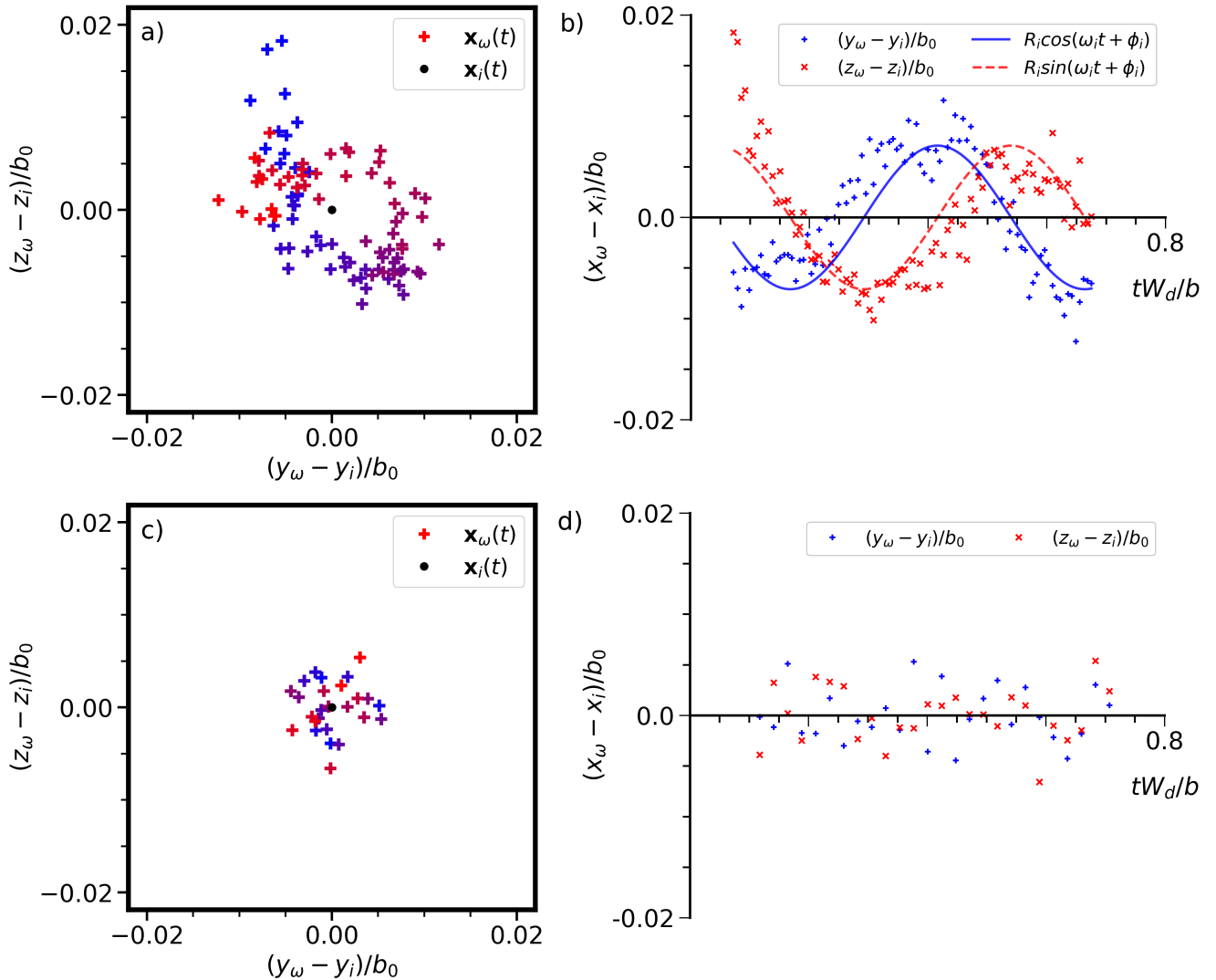


FIGURE 4.32: Characteristics of the trajectory of the vortex centroid in the reference frame centered around the unperturbed trajectory  $\mathbf{x}_i$ . Two towing configurations are explored, **a)** and **b)** :  $C_{15}$  and **c)** and **d)**  $C_{53}$ . The plot of  $\mathbf{x}_\omega(t)$  is shown in **a)** and **c)**. Subsequent positions overtime are colored from  $t \frac{W_d}{b} \sim 0$  (blue) to  $t \frac{W_d}{b} \sim 0.7$  (red). The evolution over normalized time  $t \frac{W_d}{b}$  of  $\mathbf{y}_\omega(t)$  and  $\mathbf{z}_\omega(t)$  is shown in **b)** and **d)**. In **b)**, trajectories as predicted by a sine and cosine fit are shown.

On one hand, the results for an experiment realized in configuration  $C_{15}$  : ( $Ref$ ,  $U_0 = 2$  m/s,  $\alpha = 3.5^\circ$ ) are shown in Figs. 4.32a and 4.32b. This experiment is the same as the one shown in Fig. 4.27. In a reference frame centered about  $\mathbf{x}_\omega(t)$ , the

trajectory of  $\mathbf{x}_\delta(t)$  reveals a slow circling motion of  $\mathbf{x}_\omega(t)$  around  $\mathbf{x}_i(t)$ . Then,  $y_\delta(t)$  and  $z_\delta(t)$  is plotted as a function of time in Fig. 4.32b. The motion of  $\mathbf{x}_\omega(t)$  about  $\mathbf{x}_i(t)$  shows a clear sinusoidal regime. We repeated this experiment and observed again a periodic motion. This periodic motion is studied through a fit of sine and cosine functions (shown by lines in Fig. 4.32b), the result is characterized by the motion amplitude, pulsation and phase, respectively  $r_i$ ,  $\omega_i$  and  $\phi_i$ .

On the other hand, in Figs. 4.32c and 4.32d, the same plot is shown for an experiment realized in configuration  $C_{53}$  : ( $Ref$ ,  $U_0 = 5$  m/s,  $\alpha = 3.5^\circ$ ). Towing velocity has been increased with respect to the previous configuration. Here, no oscillation is observed, suggesting that the phenomenon present in the former case does not occur. We realized a second and a third instance of this experiment and consistently observed no periodicity.

A Fourier transform analysis is realized on  $\mathbf{x}_\omega(t)$  for the same experiments of configurations  $C_{15}$  and  $C_{53}$ . The power spectrum  $P(f)$  of the output is shown in Fig. 4.33. Here, frequency is normalized by the vortex time scale  $\frac{2\pi R_d^2}{\Gamma}$ . For conf.  $C_{15}$ , the pulsation  $\omega_i$  obtained through the cosine fit is in good agreement with the main frequency obtained through the FFT analysis. The slight discrepancy observed is related to the condition of  $\omega_i(y_\delta) = \omega_i(z_\delta)$  which we impose during the cosine fit analysis. Moreover, for conf.  $C_{53}$ , the FFT analysis yields no "preferred" frequency for the temporal signal of  $\mathbf{x}_\omega(t)$ . The power spectrum of both  $y_\delta(t)$  and  $z_\delta(t)$  in this case resembles that of a "white-noise" distribution. The trajectories obtained for the rest of the experiments are categorized as "periodic motion" or as "non-periodic motion" following an examination analogous to this one. In this dataset, the apparition of periodic motion is a phenomenon which does not seem to depend on vortex strength, since both periodic and non-periodic cases are obtained in the whole range of circulation based Reynolds  $0.1 \times 10^4 < Re_\Gamma < 4 \times 10^4$ . Also, the detection of periodic motion does not seem to be limited by our measurement resolution (namely the acquisition rate  $\Delta t$  and the measurement grid  $\Delta x$ ), since both periodic and non-periodic cases are obtained for conditions where the vortex displacement velocity is smaller or larger than  $\Delta t / \Delta x$ .

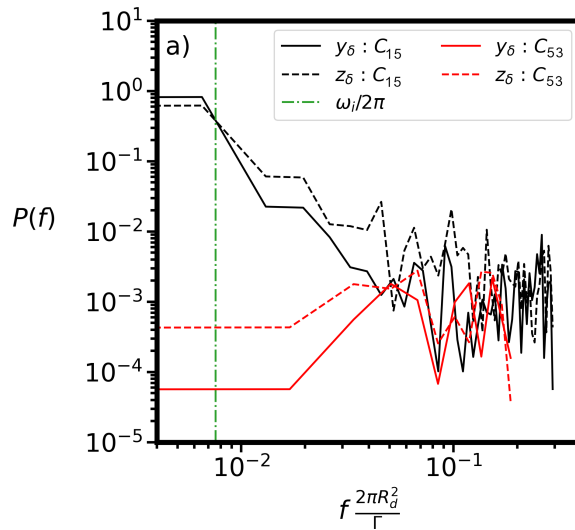


FIGURE 4.33: Power spectrum as a function of the normalized frequency for  $\mathbf{x}_\delta(t)$ , for configurations  $C_{15}$  and  $C_{53}$ .

In order to investigate the characteristics of the non-periodic motion, a proper orthogonal decomposition (POD) is realized on the flow field of configuration  $C_{53}$

[99]. This analysis was performed on consecutive velocity fields in a reference frame centered on  $\mathbf{x}_\omega(t)$ , with the mean flow subtracted. The first and second modes extracted from the POD analysis are depicted in Fig. 4.34a and b, respectively. The green line in these figures represents the vortex radius  $\overline{R}_d$ , time-averaged.

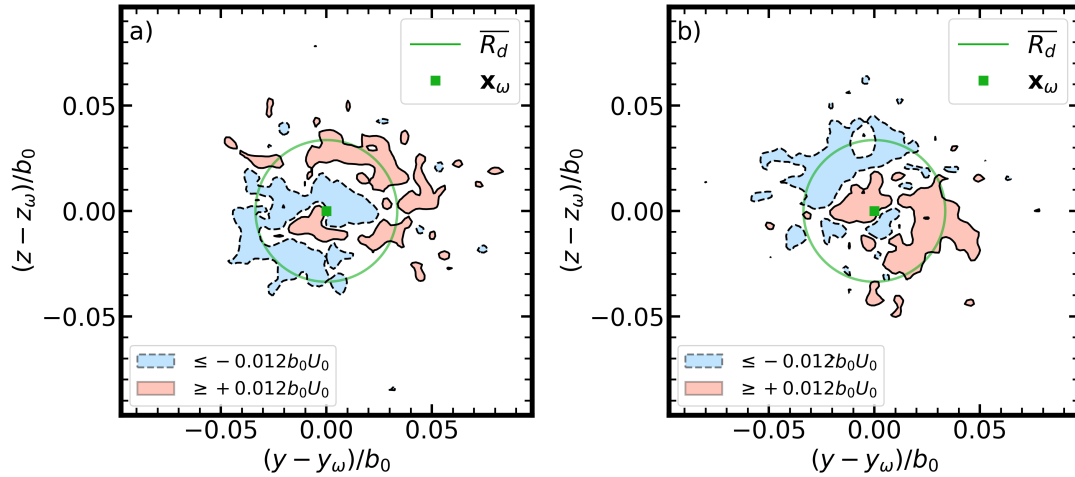


FIGURE 4.34: POD analysis of the vortex flow of an experiment at configuration  $C_{53}$ . Iso-contours ( $\pm 0.012b_0U_0$ ) of the **a)** first and **b)** second modes of normalized axial vorticity. Positive and negative contours are drawn with solid and dashed lines and are colored red and blue, respectively. The center of the vortex and a representation of its dispersion radius  $\overline{R}_d$  averaged over time is shown.

These modes exhibit a distinct structure, resembling two overlapping vorticity dipoles. Notably, the poles within these dipoles possess alternating signs and align along an axis inclined at  $\pm 45^\circ$ . Furthermore, the axis of the second mode is orthogonal to that of the first mode. The outer dipole extends beyond the vortex radius. This pattern is recurrent in most experiments displaying non-periodic motion. For configuration  $C_{53}$ , an FFT analysis applied to the temporal components of the POD identifies a primary frequency of  $f_1 = 0.2\text{Hz}$  for the first mode (Fig. 4.34a) and  $f_2 = 1.8\text{Hz}$  for the second mode (Fig. 4.34b).

The structure of these modes is reminiscent of helical modes (see for instance Fabre, Sipp, & Jacquin [33]). More specifically, the effect induced by modes with two overlapping dipoles, akin to the structures observed in Fig. 4.34, is described in ref. [33] to result from the superimposed effects of each dipole. The outer dipole primarily displaces the vortex center in a countergrade manner. Conversely, the inner dipole operates exclusively within the vortex core, causing stretching and compression of vorticity on either side of the dipole through pressure perturbations. Ultimately, the inner dipole contributes to a cograde wave. This wave competes with the countergrade wave induced by the outer dipole. Therefore, the presence of mechanisms with opposing characteristics in the most energetically dominant flow modes could explain the absence of periodic components in the vortex displacement, as observed in the present experiments. Nevertheless, confirming this hypothesis is a challenge given the limitations of our dataset. Moreover, precision errors in the computation of the vortex center could potentially lead to the appearance of dipole modes (smaller than the core radius) localized at the center of the flow.

Now, we wish to interrogate the nature of the periodic motion. The two most energetic modes yielded by the POD analysis for configuration  $C_{15}$  are shown in

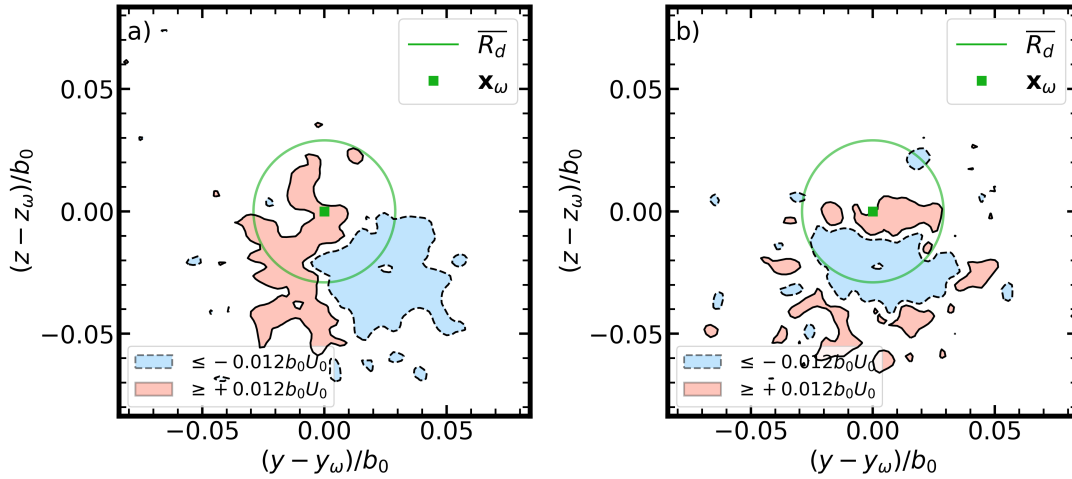


FIGURE 4.35: POD analysis of the vortex flow of an experiment at configuration  $C_{15}$ . Iso-contours ( $\pm 0.012b_0U_0$ ) of the **a)** first and **b)** second modes of normalized axial vorticity. Positive and negative contours are drawn with solid and dashed lines and are colored red and blue, respectively. The center of the vortex and a representation of its dispersion radius  $\bar{R}_d$  averaged over time is shown.

Fig. 4.35. Both modes exhibit a dipolar structure, and the axis of the dipole of the second mode is orthogonal to that of the first mode. The temporal frequency of the mode is  $f_1 = 0.36\text{Hz}$  for that in Fig. 4.35a and  $f_2 = 0.12\text{Hz}$  for that in Fig. 4.35b. The normalized frequency of the first mode is  $f_1 \frac{2\pi R_d^2}{\Gamma} = 8.8 \times 10^{-3}$  and this is coherent with the frequency of the periodic motion obtained from the analysis above (see, for instance, Fig. 4.33). The center of the dipoles seems to be offsetted below  $x_\omega$ , which could be attributed to the quality of the measurement procedure. Nevertheless, the dipolar structure of the modes is coherent with the observation that the center of the vortex is displaced in this experiment.

We choose to characterize this motion by  $\omega_i$ , which is the angular pulsation of the motion of  $x_\omega(t)$  about  $x_i(t)$ . It is hypothesized that this deformation is related to tridimensional effects, such as the development of Kelvin waves in the columnar vortex. Since we measure the displacement of the vortex centroid, the particular family of Kelvin waves that could be causing this periodic motion would have an azimuthal wavenumber  $m = \pm 1$ . Furthermore, this family of Kelvin waves is also called *displacement waves* and relate to the self-induced rotation rate of a vortex column [33]. This is why the angular pulsation is normalized by the time scale of vortex rotation, following  $\omega_i \frac{2\pi R_d^2}{\Gamma}$ . The values of  $\omega_i \frac{2\pi R_d^2}{\Gamma}$  for the different towing configurations are shown in Fig. 4.36a. For most of the experiments,  $\omega_i < 0$ , indicating a rotation sense that is countergrade with respect to the portside vortex, which turns in the counter-clockwise direction. The countergrade nature of the periodic component aligns with the hypothesis that this phenomenon is caused by a Kelvin displacement wave. An average of the absolute value of the data shown in the figure yields  $|\omega_i \frac{2\pi R_d^2}{\Gamma}| \approx 0.07$ . Following our hypothesis, we oppose these experimental results to analytical predictions from Fabre [33] (see Fig. 4.36b). These small values of  $\omega_i \frac{2\pi R_d^2}{\Gamma}$  correspond to a longitudinal wavenumber of  $k \sim 0.33$ , which indicates that, if the displacement of the vortex is in fact caused by Kelvin waves, then the longitudinal wavelength of the modes measured is large with respect to the vortex

core.

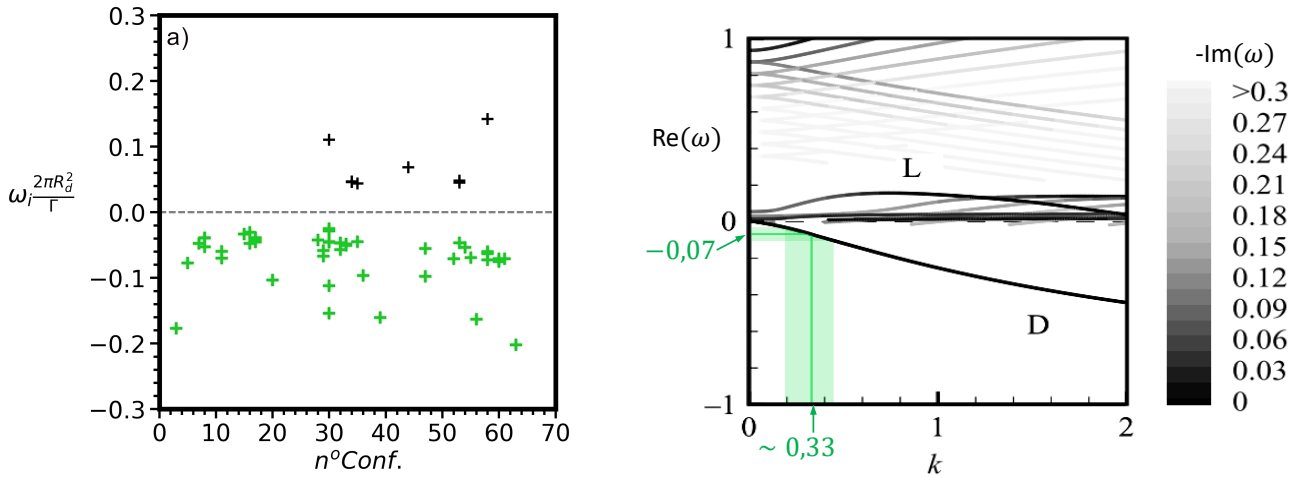


FIGURE 4.36: Characteristics of the periodic motion observed in the vortices generated by the *Ref* wing configuration. **a)** normalized angular frequency of periodic motion across the towing configurations. Countergrade motion is colored in green. **b)** Snapshot (taken from Fabre [33]) of normalized angular frequency  $\omega$  ( $\omega_i$  in our notations) as a function of longitudinal wavenumber as predicted by stability analysis. The curve corresponding to displacement waves is labeled *D*. Our experimental results are shown in the figure : the mean normalized angular frequency (countergrade) of  $\omega_i \frac{2\pi R_d^2}{\Gamma} = -0.07$  (solid green line) and its standard deviation (light green region).

#### 4.3.4 Intermediate summary

In the paragraphs above, the time evolution of the vortex properties is analyzed in order to identify the physical mechanisms that act on the wake flow during an experiment. The vortex radius is observed to grow under the effect of laminar diffusion. A decay in circulation is observed, and it is hypothesized that it is due to the effect of the tank frontiers. The evolution of axial flow is found to be promoted by longitudinal pressure gradients but it seems to also depend on stabilizing effects occurring in the vortex core. The vortex is observed to be displaced from its mean trajectory during an experiment and this displacement exhibits a random distribution or a periodic one depending on the configuration. The periodic displacements are analyzed in order to verify the hypothesis that this perturbation is related to the action of Kelvin waves in the vortex.

Overall, the results show that the vortices of this rectangular wing model (*Ref*) are persistent structures. This means that in the time frame considered ( $tU_0/b_0 < 300$ ) and in the absence of the tank frontiers (i.e. in unbound flow), these vortices would exhibit constant circulation and a very slow decay, only driven by viscous diffusion. This is why our next purpose is to promote a faster decay of the vortices through a passive flow control strategy applied at the wing.

## 4.4 Analysis of the impact of a modification of the wing geometry on the characteristics of its vortex wake

In this section we study the wake of rectangular wing models designed to attempt the excitation of high-order spanwise disturbances into the trailing vortices they generate. The excitation strategy consists in modifying the trailing edge of a rectangular wing into a sinusoidal shape in order to excite a flow mode identified by Edstrand *et al.* [28]. This work was performed in collaboration with Prof. L. Cattafesta from Florida State University.

### 4.4.1 Modification of the wing geometry in order to introduce a span-wise perturbation on the flow

The wings designed to study the effect of a trailing edge undulation on the wake vortices have a different baseline geometry : they are rectangular with a NACA 0012 profile -instead of a NACA44112 for the previous wing- their chord and span are  $c_0 = 0.16 \text{ m}$  and  $b_0 = 0.4 \text{ m}$ , respectively, which results in an aspect ratio of 2.5. The present wing configuration is purposely identical to the one considered by Edstrand *et. al* [28].

The concept of the wake control investigated here derives from the work of Navrose *et. al* [70] and Edstrand *et. al* [28] who demonstrated that the zones of sensitivity to excite vortex dynamics behind a rectangular wing are distributed on the full wingspan. The present apparatus is specifically based on the results of [28] whose parabolized stability analysis provides the conceptual shape of perturbation able to target each unstable mode of the wake. In their work the desired mode was excited by adding a body force in the wake of a rectangular wing. Here the perturbation is installed in a passive way using the sinusoidal undulations of the trailing edge. Hence the focus of the work is the outcome of a parametric variation of the rectangular planform, where the trailing edge is modified into this sinusoidal shape with increasing amplitude  $A$ . The test set of amplitudes is selected as  $A/c_0 = \{0, 0.01, 0.05, 0.10\}$ , in which the case  $A = 0$  constitutes the reference undeformed case. Based on the best case identified by Edstrand *et al.* [28], the chosen wavelength of the undulations is  $b_0/6$ . A top view and cross-sections of the four wing models are displayed in Fig.4.37. The undulation is made so that the airfoil profile is constant along the span, while the chord and thickness vary as a consequence of the trailing edge undulations. The mean chord length remains equal to the reference configuration  $c_0$ .

### 4.4.2 Results

For all experiments in this study, the wing model is towed at velocity  $U_0 = 2 \text{ m/s}$  and at an angle of attack of  $5^\circ$ . Two repetitions of an experiment are realized for each undulation amplitude in the set  $A/c_0 = \{0, 0.01, 0.05, 0.10\}$ .

Measurements of the aerodynamic coefficients generated by each wing model during the constant towing velocity phase are provided in table 4.1. No effect of the trailing edge undulation is observed on the aerodynamic coefficients. This is expected since the wing models feature the same planform area so they exhibit the same lift and drag coefficients in spite of the trailing edge undulation.

PIV snapshots of the wake generated under configuration ( $A/c_0 = 0$ ) and ( $A/c_0 = 0.1$ ) are shown in Fig. 4.38. The time at which the first measurement is available is denoted  $t_0$ . Despite the modification in the wing geometry, the topology of the wake

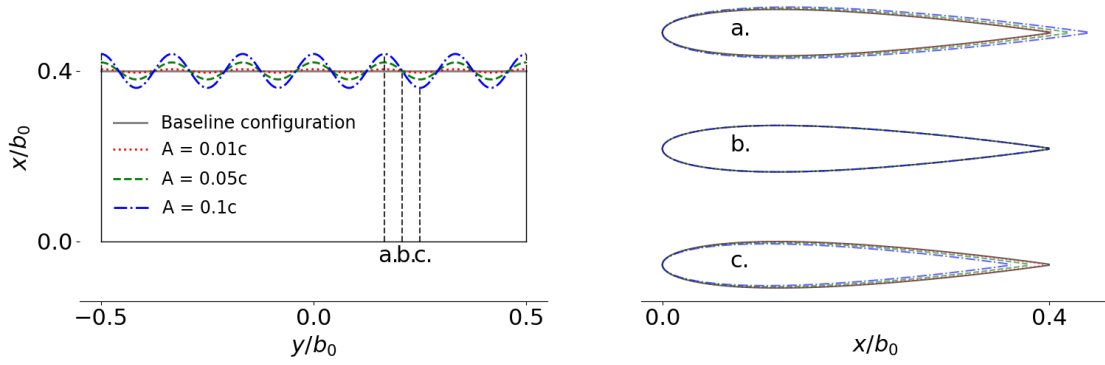


FIGURE 4.37: Top view (left) and cross-sections (right) of the wing design for all the amplitudes of the trailing edge undulations.

$A$	0.0	$0.01c_0$	$0.05c_0$	$0.1c_0$
$C_z$	0.211	0.217	0.216	0.212
$C_x$	0.018	0.018	0.018	0.017

TABLE 4.1: Aerodynamic coefficients for wings of different trailing edge undulation amplitudes ( $A$ ). The uncertainty on the lift and drag coefficients is on the order of  $10^{-3}$  at maximum.

of the wing when  $A/c_0 = 0.1$  is similar to that of a plain configuration  $A/c_0 = 0$ . Namely, the undulation of the trailing edge does not introduce additional vortices in the flow. Therefore the methodology described in section 4.2 is applied. In what follows, we describe the results obtained from the evaluation of the vortex characteristics as a function of the undulation amplitude  $A$ .

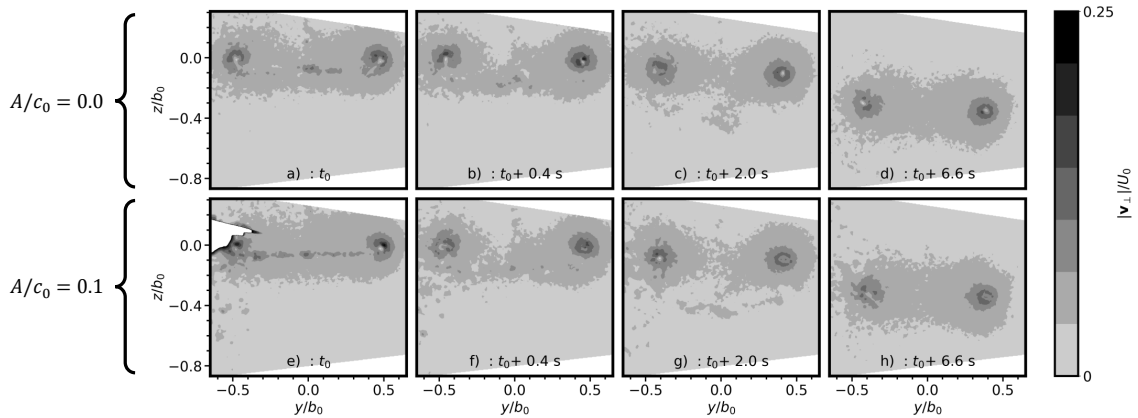


FIGURE 4.38: Description of the wake of the baseline wing,  $A/c_0 = 0$ , in the top row and (a-d) and of the modified wing,  $A/c_0 = 0.1$ , in the bottom row (e-g), using the field of normalized in-plane velocity  $v_{\perp}/U_0$  obtained from the PIV measurement in a plane transverse to the wing motion. Four time instants are shown for each wing model, from 0 to 6.6s. In both cases, the towing configuration is  $U_0 = 2 \text{ m/s}$ ,  $\alpha = 5^\circ$ .

Vortex characteristics as a function of time for each trailing edge undulation amplitude,  $A$  are shown in Fig. 4.39. Error bars are used in the figures to indicate the standard deviation upon the two different realisations of the same experiment. The

characteristics are scaled by the circulation, radius and maximum azimuthal velocity measured on the vortex at configuration  $A = 0$  at  $t = t_0$ .

Fig. 4.39a shows the time evolution of the circulation  $\Gamma(A, t)/\Gamma(0, t_0)$  for each value of  $A$ . It is found that the trailing edge undulation does not affect the vortex circulation. Furthermore, the circulation is almost constant in time as expected from the conservation of circulation.

Fig. 4.39b shows the effect of  $A$  on the normalized core size  $R_a(A, t)/R_a(0, t_0)$ . An increase of  $R_a(t)$  with the undulation amplitude is observed. The magnitude of increase of  $R_a(t)$  is comparable between  $A/c_0 = 0.01$  and  $A/c_0 = 0.05$ . For  $A/c_0 = 0.1$  a magnitude of increase in  $R_a(t)$  between 20% and 30% is observed.

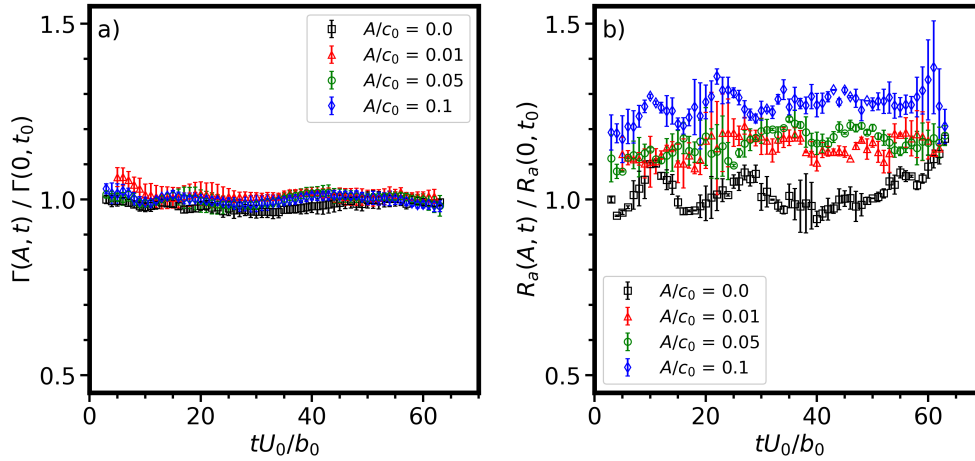


FIGURE 4.39: Effect of trailing edge undulation amplitude  $A$  on the downstream evolution of **a)** vortex circulation  $\Gamma(A, t)$  and of **b)** core size  $R_a(A, t)$ .

A comparison of the temporal evolution of the maximum azimuthal velocity,  $\max(v_\theta)$ , as a function  $A$  is made in Fig. 4.40a. It is found that the maximum velocity decreases with  $A$ . Overall the increase in core size (observed in Fig. 4.39b) and decrease in maximum tangential velocity (visible in Fig. 4.40a) from 0 to  $\sim 60$  wing spans downstream suggests an increased diffusion of the vortex with the undulations of the trailing edge. The velocity profile  $v_\theta(r)$  at  $tU_0/b_0 = 50$  is plotted for all values of  $A$  in Fig. 4.40b. The decrease of  $\max(v_\theta)$  is observed while  $A$  increases. The asymptotic velocity profile at large radius is little changed by  $A$ , which is coherent with the absence of change of the circulation.

Since the magnitude of the increase in core size  $R_a$  does not evolve proportionally to  $A$ , We can assume that this diffusion is linked to non-linear effects. In experiments with synthetic jet actuation, Dghim *et. al* [25] attributed a similar diffusive effect as the result of the presence of additional turbulent structures in the vortex core, which act to effectively enhance disorder and mixing of fluid layers in this region.

In conclusion, the effect of the undulation amplitude shows original results on the vortex properties. An increase of the core radius  $R_a$  and a decrease of the maximum tangential velocity are observed, while the lift and circulation are unchanged by the undulation. We interpret this as an increased diffusive effect of the inner region of the vortices due to additional turbulent structures associated with the undulation. This effect is local and does not change the overall circulation. Although

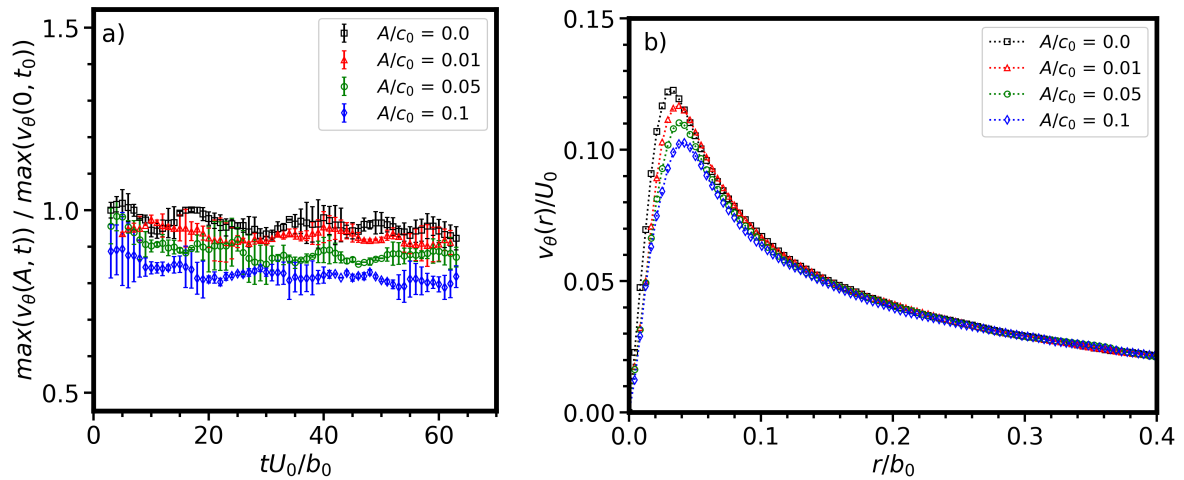


FIGURE 4.40: Effect of trailing edge undulation on **a)** the maximum angular velocity  $\max(\bar{v}_\theta)$  and on **b)** the angular velocity profile  $\bar{v}_\theta(r, tU_0/b_0 = 50)$  for the right side vortex trailing behind wings of different trailing edge undulation amplitudes  $A$ .

the circulation is not affected, these results remain interesting as they imply the possibility to modify the vortex structure by acting simply on the wing design, in a passive manner.

## 4.5 Intermediate conclusion

In this chapter, we establish a methodology to characterize wake physics at extended downstream locations in towing tank experiments. This methodology is applied across various wing and towing configurations to assess their impact on alleviating the hazard represented by wake vortices. The experiments herein use elliptic-like wing-loads typical of aircraft in cruise configuration, resulting in long wake dissipation times where a single counter-rotating vortex dipole is shed from the near wake of the wing. In contrast, wake vortex hazard in commercial aviation primarily manifest at airports, where wing-load distributions resemble the landing/take-off configuration, generating multi-polar vortex wakes. On subsequent chapters the reference wing geometry is modified to produce a multi-polar wake, featuring co-rotating dipoles on each side, mimicking landing/take-off conditions. The impact of this modification will be explored to understand its influence on wake physics at distant downstream locations, including the potential for unstable perturbations within the vortex system.

## Chapter 5

# Analysis of vortex interaction in a co-rotating trailing vortex system

In the previous section we define the general characteristics of the vortex wake generated by a rectangular NACA 4412 wing. We now discuss of the properties of the wake generated by a wing with flaps. This configuration generates two additional vortices, resulting in a wake of four vortices where there are two co-rotating vortices on each side. Studying co-rotating systems is of interest for the understanding of the physics of the wake of a commercial aircraft at specific points of its flight envelope, for example in the landing or take-off configuration, also called "high-lift" configuration. In this configuration, the lift coefficient of the aircraft is increased by deploying wing flaps and this reduces the distance and velocity necessary for landing/take-off. Drag coefficient is however also increased by the flaps. Each side of the wake of a high-lift flapped wing is characterized by the formation of a co-rotating pair of vortices that eventually fuse to form a single vortex. First, the decisions made concerning the design of the experimental setup aimed at studying a co-rotating vortex flow are discussed in section 5.1. The dynamics of the vortex pair before the fusion event are studied next, in section 5.3.2. Finally, a comparative analysis of the properties of a fused vortex with respect to the *Ref* vortex (presented in chapter 4) is conducted in section 5.3.3, with the objective of evaluating the consequences of this flow modification on wake hazard.

### 5.1 Generation of a co-rotating pair of vortices

In this section, the design of the wing models of the study is discussed. We begin by describing the objectives with respect to the properties of the generated flow. As seen in section 2.3, the motion of a system of 4 vortices can be periodic or divergent and this is a function of the conditions  $\beta = b_2/b_1$  and  $\gamma = \Gamma_2/\Gamma_1$  summarized in the Donaldson-Bilanin diagram, in Fig. 5.1. However, the following design constraints apply : The wing geometry is modified by adding a twist angle  $\Theta$  to its inboard region. This allows for the modified wings to have the same planform as the reference model. Furthermore, the ratio of distances between the shed vortices  $\beta$  can be estimated from the ratio of flap-span to wing-span. This is because the discontinuity at flap tip introduces locus around which the shed vorticity sheet rolls-up (see [26, 86]). The twist angle  $\Theta$  is constant and sets the value of the circulation ratio  $\gamma$  at null incidence  $\alpha = 0$ . Modifying  $\alpha$  brings about a change in  $\Gamma_1$  while keeping similar magnitudes of  $\Gamma_2$  [64], thus allowing for a fine control of  $\gamma$ . However incidence values are limited so as to not generate negative lift (at small  $\alpha$ ) nor detached flow (at large  $\alpha$ ).

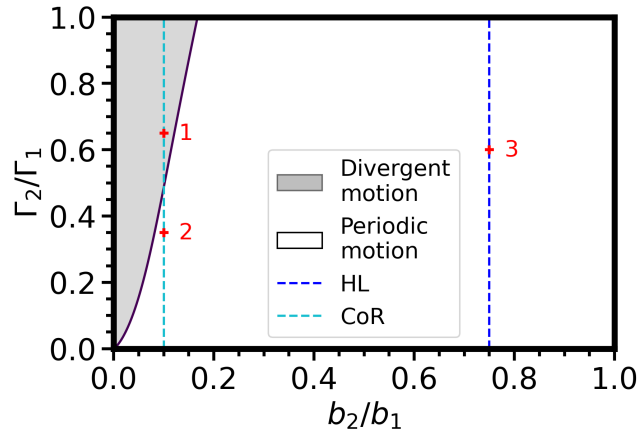


FIGURE 5.1: Donaldson-Bilanin diagram for co-rotating vortex pairs. A modelization of vortex trajectories for points 1,2 and 3 is shown in Figs. 5.3, 5.4 and 5.6 respectively

To attain both periodic and divergent wakes under the constraint of constant twist angle, one must keep the distance ratio  $\beta$  small. In particular, for a co-rotating system,  $\beta < 0.16$  (see Fig. 5.1). Moreover at moderate  $\beta$  co-rotating vortices tend to fuse quickly. However, if the flap-span is too small, the shed vorticity loses intensity, which reduces  $\gamma$ . Thus, the design of these wings results from a compromise that aims to generate strong secondary vorticity far from the wing-tips. In Fig. 5.1, two values of  $\beta$  which correspond to two wing models (*HL* and *CoR*) are plotted. The design of these wings is described on what follows.

The design of the wings is sketched in Fig. 5.2. The first model was designed to reproduce *high-lift* wing-loading conditions, which are adopted by commercial aircraft in landing/take-off configuration and also generates co-rotating vortices. Its geometry is obtained by adding an inboard twist of  $\Theta = 6^\circ$  from the midplane to  $y = 0.375b_0$ , yielding  $\beta_{HL} = 0.75$ . For the outboard section, from  $y = 0.375b_0$  to  $y = 0.5b_0$  (the wing-tip), the twist angle is  $\Theta = 0^\circ$ . This geometry is sketched in Fig. 5.2b, it is denoted *HL* since the resulting wing-loading is similar to that of a *high-lift* configuration. The evolution of  $\Theta$  from the outboard to the inboard region is discontinuous due to construction constraints.

The next model was designed to generate strong secondary vorticity at a span-wise position far from the wing-tip. This model is denoted *CoR* wing due to its co-rotating vortex system. In the *CoR* wing, a twist angle of  $\Theta = 8^\circ$  is added from the midplane to  $y = 0.05b_0$ , yielding  $\beta_{CoR} = 0.1$ . This geometry is sketched in Fig. 5.2c.

Let  $l_y$  be the local lift generated at a span-wise  $y$  station along the wing. Each wing configuration feature different distributions of lift  $l_y(y)$ . We also introduce the bound circulation  $\Gamma_y(y)$  which scales as  $l_y(y)$ . The wings load distributions  $\Gamma_y(y)$  are shown in Fig. 5.2a. The curves are obtained by an application of the lifting line theory where the model velocity and total generated lift are set to  $5 \text{ m/s}$  and  $175 \text{ N}$  respectively. The wing-load of the reference geometry (*Ref*) resembles a cruise configuration with a nearly elliptic distribution. As a consequence of the inboard twist the *HL* and *CoR* configurations feature more lift inboard compared to the *Ref* model. At the zone of geometrical discontinuity, a strong variation of  $\Gamma_y(y)$  is observed in both wings yielding positive values of  $d\Gamma_y/dy$ . It is expected that trailing vortices roll-up and be shed from the flap tips, in accordance with the results of Betz [26,

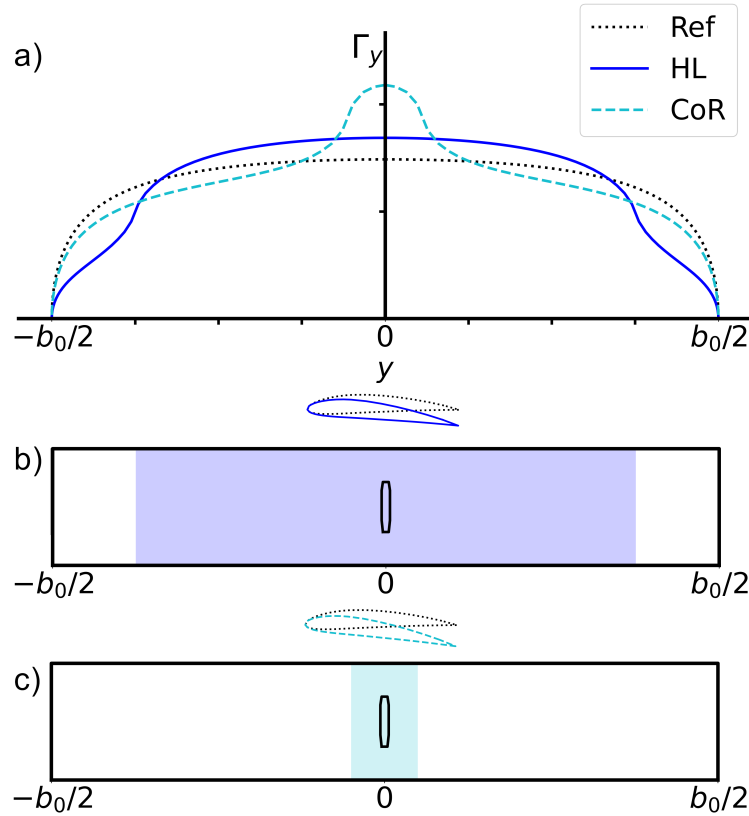


FIGURE 5.2: Properties of the *Ref*, *HL* and *CoR* wing models. **a)** Bound circulation  $\Gamma_y$  as a function of span-wise station  $y$  for the wing models generating equal total lift. Side and top views of the *HL* and *CoR* geometries are sketched in **b)** and **c)**, respectively. The twisted inboard zones are colored. The contour occupied by the strut is drawn at the center of the top-views.

86] which state that secondary vorticity concentrates around span locations where  $d\Gamma_y/dy$  is large.

## 5.2 Wake of the CoR wing

The *CoR* wing is designed to generate co-rotating pairs that display both periodic and divergent motion, allowing for the study of a wide range of behaviors in a vortex system. This can be seen in Fig. 5.1 since for  $\beta_{CoR}$ , the critical regime is attained when  $\gamma_{CoR} = 0.5$ . Thus, experiments aim to generate vortices with  $\gamma < 0.5$  for periodic motion and  $\gamma > 0.5$  for divergent motion.

### 5.2.1 Estimation of the wake behavior from a numerical model

A numerical estimation of vortex trajectories in the conducted experiments is derived through point vortex calculations. The trajectories of point vortices shed from the *CoR* wing with  $\gamma = 0.35$  and  $\beta = 0.1$  are illustrated in Fig. 5.3, showing wing-tip vortices  $(x_1, x_4)$ , flap vortices  $(x_2, x_3)$ , and the portside barycenter of vorticity  $x_{1+2}$ . The vortices path in the laboratory reference frame is depicted in Fig. 5.3a. The portside vortices exhibit a pseudo-periodic motion around  $x_{1+2}(t)$ , as seen in Fig. 5.3b,

where the reference frame is centered on  $\mathbf{x}_{1+2}(t)$ . In this example, the trajectory completes a pseudo-revolution every  $tU_0/b_0 = 30$  normalized time units. The point vortex simulations suggest that flap and tip vortices separate from each other during each rotation period. However, referring to established experiments [8, 17], actual flap and tip vortices are anticipated to draw closer and eventually fuse. This fusion event marks the end of the measurement window for investigating the co-rotating vortex pair interactions. Nevertheless, in the case of the *CoR* wing, flap and wing tip vortices are initially shed at a significant distance from each other, leading to an expected prolonged time until their fusion. When  $\gamma = 0.65$ , as depicted in Fig. 5.4, the motion becomes divergent. Specifically, in the reference frame centered on  $\mathbf{x}_{1+2}(t)$ , the vortices move away from the barycenter, indicating a minimal interaction once they are shed.

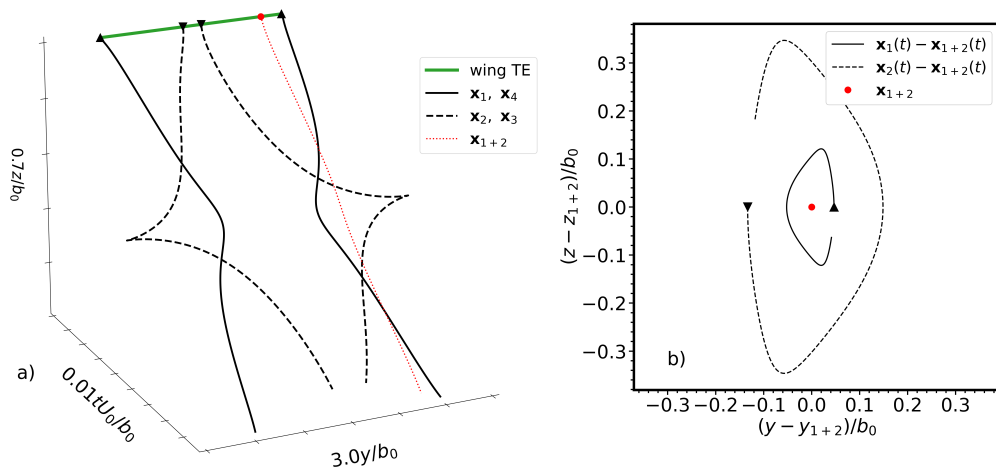


FIGURE 5.3: Periodic trajectories of point-vortices in a co-rotating dipole for  $\gamma = 0.35$ ,  $\beta = 0.1$  (point 2 in Fig. 5.1) : **a)** in the laboratory reference frame and **b)** in a reference frame centered around the portside barycenter of vorticity.

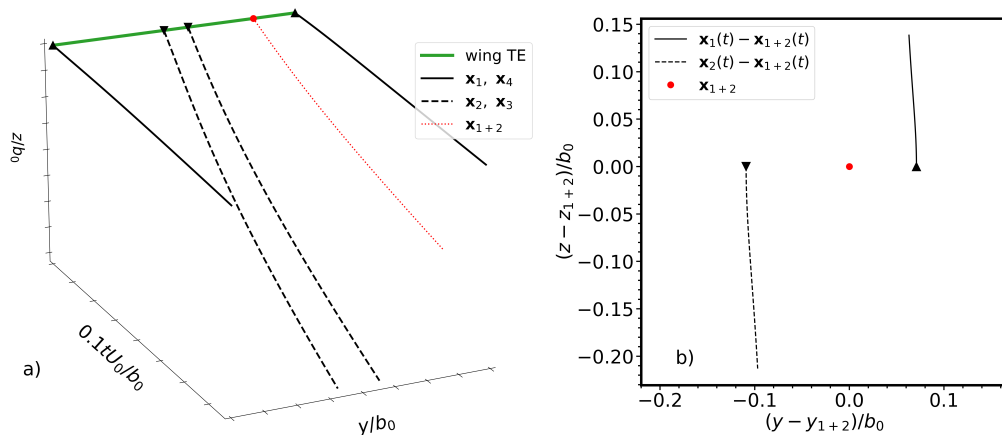


FIGURE 5.4: Divergent trajectories of point-vortices in a co-rotating dipole for  $\gamma = 0.65$ ,  $\beta = 0.1$  (point 1 in Fig. 5.1) : **a)** in the laboratory reference frame and **b)** in a reference frame centered around the portside barycenter of vorticity.

### 5.2.2 Analysis of experimental results

Experiments cover a wide range of towing configurations for the CoR wing, enabling an exploration of the wake general characteristics within this setup. Fig. 5.5 provides an example of the observed wake during an experiment. Vorticity measurements are presented for two key instances : immediately following the wing passage ( $tU_0/b_0 = 6$ , Fig. 5.5a), and 50 wingspans downstream from the wing ( $tU_0/b_0 = 50.3$ , Fig. 5.5c).

While vorticity indeed emerges in the region where the presence of flap vortices is expected ( $|y/b_0| < 0.15$ ), this vorticity is primarily associated with the strut wake and swiftly diffuses during the experiment. At  $tU_0/b_0 = 6$ , a region of significant vorticity ( $|\omega_x b_0/U_0| > 1$ ) is widely distributed around the  $y/b_0 = 0$  axis. However, by  $tU_0/b_0 = 50.3$ , most of this vorticity has diffused.

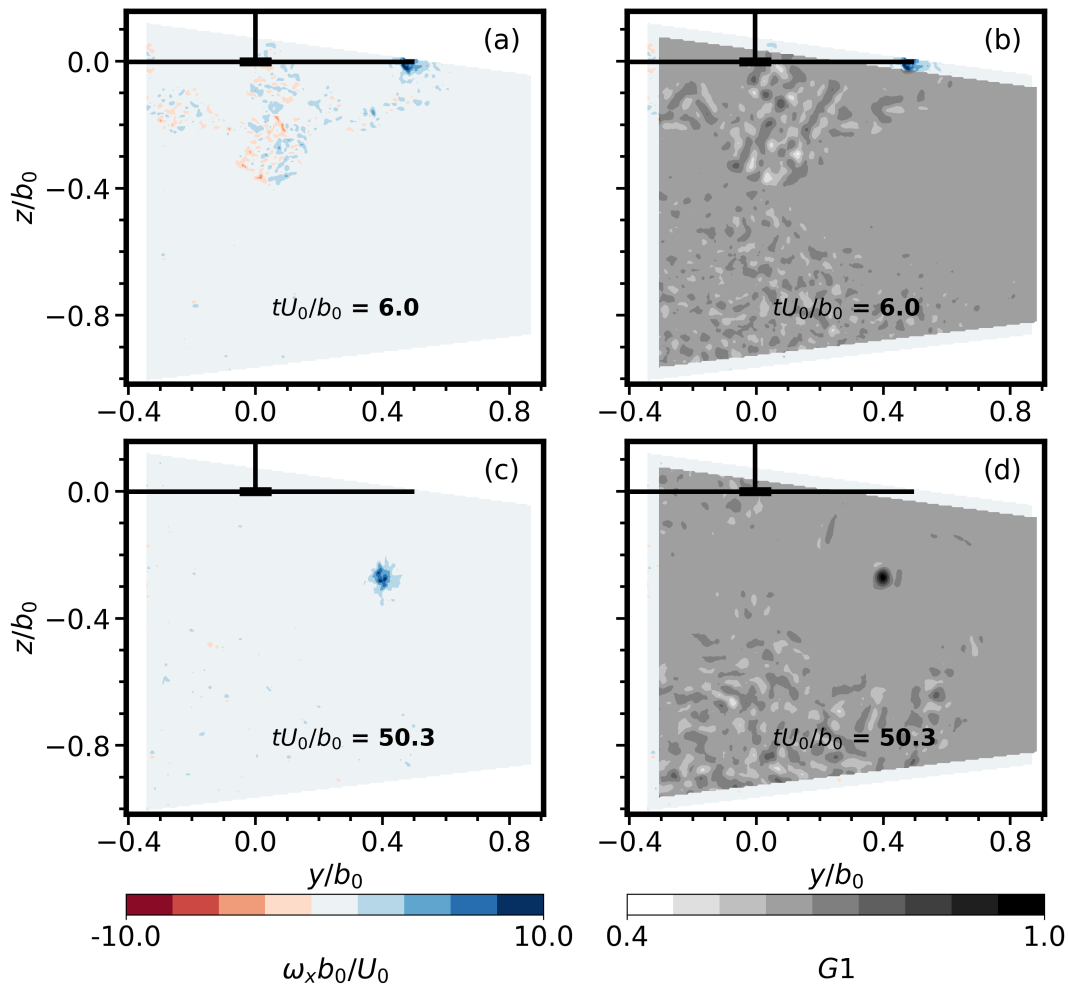


FIGURE 5.5: Measurements of the wake generated by the CoR wing model towed at  $U_0 = 1\text{m/s}$  and  $\alpha = 0^\circ$ . The normalized vorticity field  $\omega_x b_0/U_0$  is represented on the left column while the G1 field is represented on the right one. The flapped wing and the strut are schematized with black lines, the flap is shown with a thicker line. Measurements are shown for two normalized times, **a**) and **b**) :  $tU_0/b_0 = 6$  and **c**) and **d**) :  $tU_0/b_0 = 50.3$

A vorticity roll-up process is expected to occur near the wing-flap tips, giving rise to symmetric flap vortices at each side of the symmetry plane. The flap vortices thus

formed should persist downstream from the wing. However, no flap vortex formation is observed in the experiments. In contrast, vorticity roll-up is observed near the wing-tip : the formation of the wing-tip vortex is nearly completed at  $tU_0/b_0 = 6$ . It is characterized by a vorticity magnitude of  $|\omega_x b_0/U_0| > 5$ . Downstream, at  $tU_0/b_0 = 50.3$ , the wing-tip vortex retains its coherence and vorticity magnitude.

Therefore it appears that this wing model fails at generating flap vortices. Further insights are sought by conducting an analysis of the  $G1$  criterion over the measurement window. Figs. 5.5b and 5.5d represent the  $G1$  field, derived from the 2D velocity fields (not shown). The computation of  $G1(y, z)$ , as per equation 4.20, utilizes a circular computation window with a radius of 15 gridpoints. Thus  $G1(y, z)$  cannot be computed at points within a distance of less than 15 gridpoints from the borders of the measurement window. To depict regions where  $G1(y, z)$  remains uncomputed, the vorticity field is overlaid on Figs. 5.5b and 5.5d.

Fig. 5.5d shows a compact region where  $G1 \sim 1$  forms around the wing-tip vortex. However, no analogous compact region with  $G1 \sim 1$  manifests around the midplane of the wake. This absence is noticed both in proximity to the wing (see Fig. 5.5b) and further downstream (see Fig. 5.5d). Consequently, the analysis methodology did not confirm the presence of flap vortices.

We propose a hypothesis to explain this : The wake vorticity generated by the strut is prominent in the midplane region of the wake, precisely where flap vortices are expected to form. If flap vortices do come into existence, they may become overwhelmed by the pre-existing vorticity within the strut wake, ultimately resulting in their diffusion. Furthermore, the presence of the strut on the wing model surface might hinder the natural formation of vortices. It is noteworthy that during the design phase of the wing models in this study, the aerodynamic impact of the strut was not taken into account. The surface occupied by the strut is sketched in Fig. 5.2c. Taking into consideration these effects, the load distributions illustrated in Fig. 5.2a would yield  $\Gamma_y(y) = 0$  in the span occupied by the strut in the  $y$ -direction. For the *CoR* wing, where the flap constitutes only a small portion of the total span, this effect cannot be dismissed. For these reasons, we decided not to further study the wake of the *CoR* wing. However, our subsequent discussion on the *HL* wing provides insights into the behavior of co-rotating vortices.

### 5.3 Wake of the HL wing

The general properties of the wake of the *HL* wing are discussed. In this case,  $\beta = 0.75$  so only periodic motion of the vortex pair is expected (see Fig. 5.1). Vortex trajectories as predicted by point vortex simulations are shown in Fig. 5.6. Vortices display pseudo-periodic circular trajectories around the barycenter of vorticity, as seen in Fig. 5.6b, where the reference frame is centered around  $x_{1+2}(t)$ .

#### 5.3.1 Analysis of experimental results

In the case of the *HL* wing, the flap covers a span of  $0.75b_0$ , so the effect of the strut can be neglected. Co-rotating flap vortices are observed on the wake of this wing. These vortices fuse rapidly, since in this case the flap and tip vortices are shed close to each other.

A comparison of the span-wise trajectories of the vortices generated by *Ref* and the *HL* configurations is displayed in Fig. 5.7. For the *HL* configuration, the wing-tip ( $y_1$ ) and flap ( $y_2$ ) vortices are shown until their fusion event, after which the

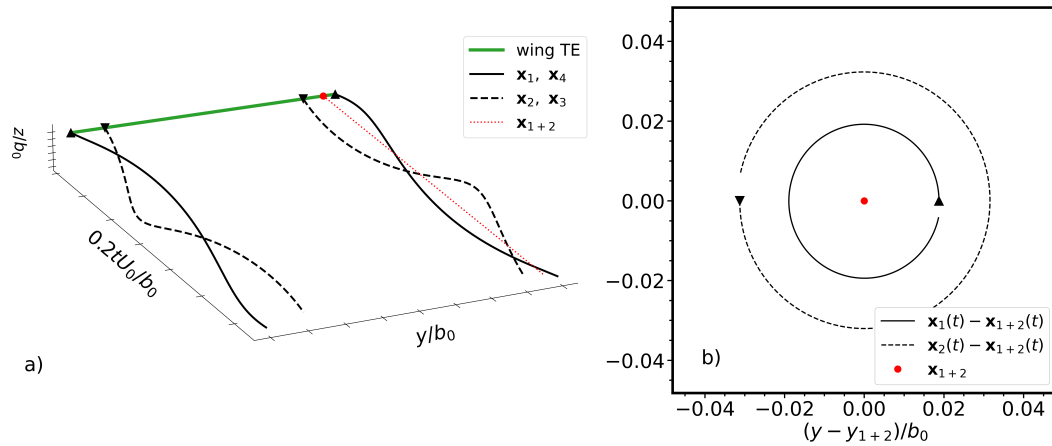


FIGURE 5.6: Periodic trajectories of point-vortices in a co-rotating dipole for  $\Gamma_2/\Gamma_1 = 0.6$ ,  $b_2/b_1 = 0.75$  (point 3 in Fig. 5.1) : **a)** in the laboratory reference frame and **b)** in a reference frame centered around the portside barycenter of vorticity.

vortex is labeled  $y_c : HL$ . The wing-tip *Ref* vortex is labeled  $y_c : Ref$ . The towing configurations for the *Ref* and *HL* wings are distinct, yet generate an equal total lift of  $F_z = 33N$ . The configuration for *Ref* is  $C_{16} = (Ref, U_0 = 2 \text{ m/s}, \alpha = 5^\circ)$  and for *HL* is  $C_{68} = (HL, U_0 = 2 \text{ m/s}, \alpha = -0.5^\circ)$ . It can be seen that in the *HL* case, the fusion event occurs little before vortices can complete a full period of orbital movement, at  $t = t_f$ .

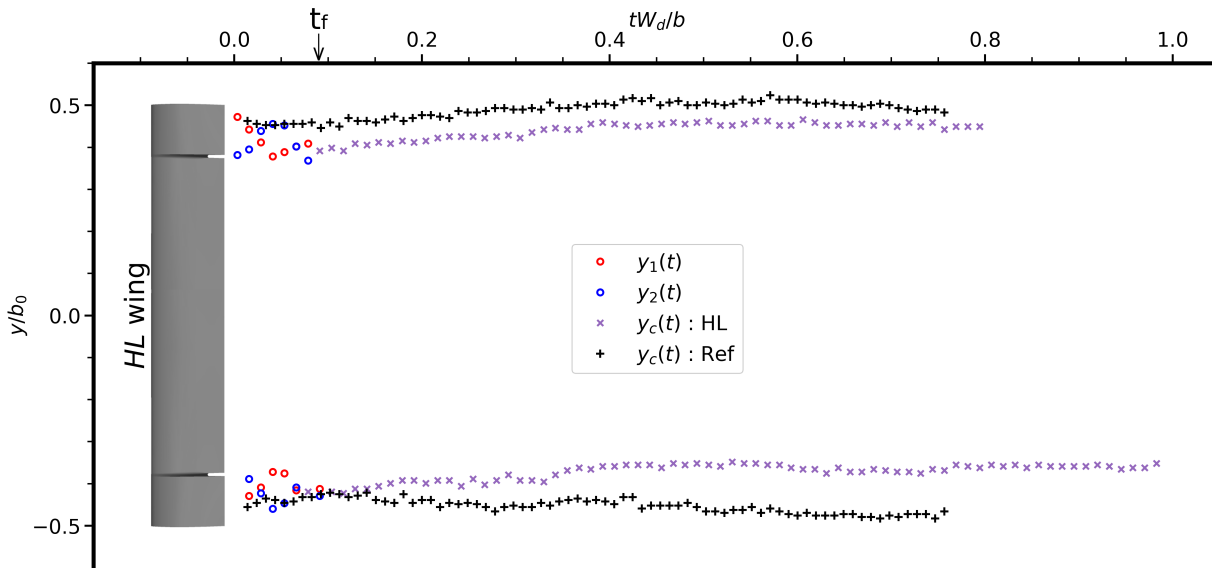


FIGURE 5.7: Horizontal component of the vortex trajectory as a function of time, for configurations  $(Ref, U_0 = 2 \text{ m/s}, \alpha = 5^\circ)$  and  $(HL, U_0 = 2 \text{ m/s}, \alpha = -0.5^\circ)$ . Time is normalized on the vertical drift speed  $W_d$  and vortex separation  $b$ . In the *HL* case, the tip and flap vortices that coexist before fusion ( $t = t_f$ ) are shown with circle symbols. The *HL* wing geometry is shown for illustrative purposes.

The vortices generated by the wing descend towards the floor of the towing tank

as a consequence of the downwash. The vertical component of the trajectory for configurations  $C_{16}$  and  $C_{68}$  is shown in Fig. 5.8a. Data before fusion ( $t < t_f$ ) is excluded in the *HL* case. Portside and starboardside vortices move down at a constant velocity. Fig. 5.8b shows the vortex separation, computed from eq. 4.6. In this plot one can observe a closing of the *Ref* vortices in the first instants after the wing passage. This is associated with the roll-up of the vorticity sheet released by the wing, about the barycenter of vorticity, located inward about the wing tip. Measurements show that  $\frac{b}{b_0}$  is 0.91 and 0.82 for the *Ref* and *HL* wings, respectively. These values are indicative of those found in the rest of the database, exhibiting little dependence on the parameter others than the loading profile. The subsequent increasing vortex separation is attributed to the effect of the frontiers of the flow. From an inviscid point of view, the hard walls and the free surface (supposed to be flat) play on the vortices as image and opposite vortices. As detailed in sec. 4.1.1, a two-dimensional numerical model of this situation has been constructed to evaluate the trajectory of the vortices. Here, the model is initialized using a lifting line model parameterized by the lift coefficient obtained experimentally. The numerical prediction, indicated by a subscript *th* in Fig. 5.8b, is shown by solid and dashed lines for *Ref* and *HL* respectively. A good match is found with the experimental data, suggesting the validity of the wall effect explanation.

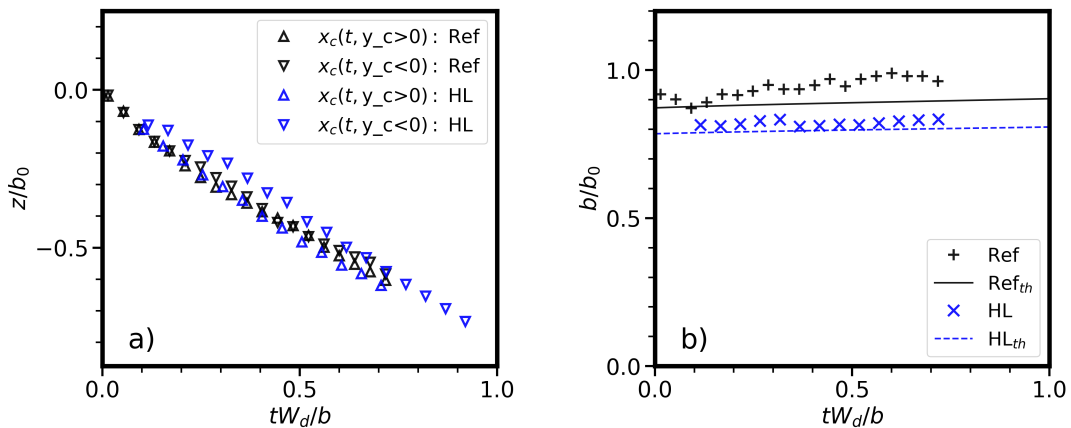


FIGURE 5.8: Vortex trajectory as a function of time, for configurations (*Ref*,  $U_0 = 2 \text{ m/s}$ ,  $\alpha = 5^\circ$ ) and (*HL*,  $U_0 = 2 \text{ m/s}$ ,  $\alpha = -0.5^\circ$ ). Time is normalized on the vertical drift speed  $W_d$  and vortex separation  $b$ . **a)** vertical component and **b)** vortex separation measured (symbols) and predicted by lifting line theory (lines)

The recording of the vortex trajectory is limited by the size of the PIV measurement plane. Recasting this limited duration in the normalized set formed by the convective time scale of the flow past the wing or that associated with the vortex descent is interesting to infer the portion of the vortex age that is captured by the present experiments. Table 5.1 summarizes the maximum time using the convective and vortex scales for both *Ref* and *HL* configurations. Towing configurations that provide the minimal and maximal duration have been selected. In vortex time scales, the observation time varies between roughly 70 to 170 for the *Ref* wing and from 40 to 50 for the *HL* wing. The smaller observation time of the *HL* wing relates to the increased circulation of the vortices, when comparing the two configuration for the same lift, and increased proximity, which together promote a faster descent.

The set of test cases (*Ref* and *HL*) compared in this study is now described. Because of the difference of wing loading, the high-lift and reference wing models

$U_0$ m/s	1.0	5.0	$U_0$ m/s	1.0	5.0
$\alpha = 0^\circ$	134 ( <b>0.59</b> )	170 ( <b>0.74</b> )	$\alpha = 0^\circ$	45.5 ( <b>0.52</b> )	52.5 ( <b>0.88</b> )
$\alpha = 5^\circ$	79 ( <b>0.63</b> )	75 ( <b>0.64</b> )	$\alpha = 5^\circ$	44 ( <b>0.68</b> )	—

TABLE 5.1: Maximum vortex age measured before the exit of the vortices of the SPIV window in terms of  $t \frac{U_0}{b_0}$  and in terms of  $t \frac{W_d}{b}$  (inside parenthesis) as a function of angle of attack  $\alpha$  and towing velocity  $U_0$  for the reference (left) and high-lift (right) configurations

exhibit different lift forces for identical  $(U_0, \alpha)$  conditions. The high-lift wing generates more lift than the reference wing. Incidentally, it is interesting to evaluate the wake dynamics at the same lift force, on the account that a given aircraft must balance a given weight at constant flight speed and altitude, irrespective of its wing loading. Therefore we define a sub-group of towing configurations realized in this work, shown in table 5.2, that gather tests of *Ref* and *HL* that have the same lift force (given a maximum error of 5%). The equality of lift is achieved by playing on the model angle of attack, while keeping the same flow speed. The selected cases feature a  $C_z$  value of approximately 0.55 corresponding to a cruise like situation. As a consequence the reduced database is also useful to evaluate the effect of Reynolds number for instance by considering **F1**, **F2**, **F3** and the *HL* model, or **F1**, **F2**, **F4**, **F5** and the *Ref* model.

Configuration	F1	F2	F3	F4	F5
$Re_{b_0}$	4.0e+05	8.0e+05	1.2e+06	1.6e+06	2.0e+06
$C_z$	$0.57 \pm 7e-03$	$0.59 \pm 9e-03$	$0.57 \pm 8e-03$	$0.57 \pm 5e-03$	$0.55 \pm 1e-02$
<b>HL Wing</b>	1m/s, $-0.5^\circ$	2m/s, $-0.5^\circ$	3m/s, $-0.5^\circ$	4m/s, $-1^\circ$	5m/s, $-1^\circ$
<b>Ref Wing</b>	1m/s, $5^\circ$	2m/s, $5^\circ$	3m/s, $4.5^\circ$	4m/s, $5^\circ$	5m/s, $5^\circ$

TABLE 5.2: Description of the selected test cases.

### 5.3.2 High-lift wake before vortex fusion ( $t < t_f$ ) : characterization of the fusion mechanism

#### 5.3.2.1 Characterization of the vortices

The case of *HL* wing which generates four vortices in the near wake deserves further post-processing to locate the vortices. The two vortices and their merging are illustrated in Fig. 5.9 with three subsequent snapshots of the PIV measurements for the configuration **F2** : *HL*. The vortices generated by the high lift flap rotate in the same direction as the tip vortices. These two vortices rotate about each other and, after a time  $t_f$ , merge into one single vortex. The localization of the vortices is obtained by first using the barycenter of vorticity  $\mathbf{x}_\omega$ , computed over  $\Omega_m$  which contains both vortices. Because the two vortices are co-rotating, the barycenter of the entire vorticity field defines  $\mathbf{x}_\omega \equiv \mathbf{x}_{1+2}$  the center of rotation of the two vortex system.  $\mathbf{x}_{1+2}$  is shown by a black square in Fig. 5.9. The descent motion of the dipole  $W_v$  is subtracted from the velocity field. The detection of the two vortices is then made using the  $G1$  criterion with  $\mathbf{x}_1$  and  $\mathbf{x}_2$  the centers of the wing-tip and flap vortices, respectively.

We locate each vortex as a distinct compact region of  $G1(\mathbf{x}) > G1_{crit}$  where  $G1_{crit} = 0.75$ . These regions are shown by red dashed lines in Fig. 5.9. The center

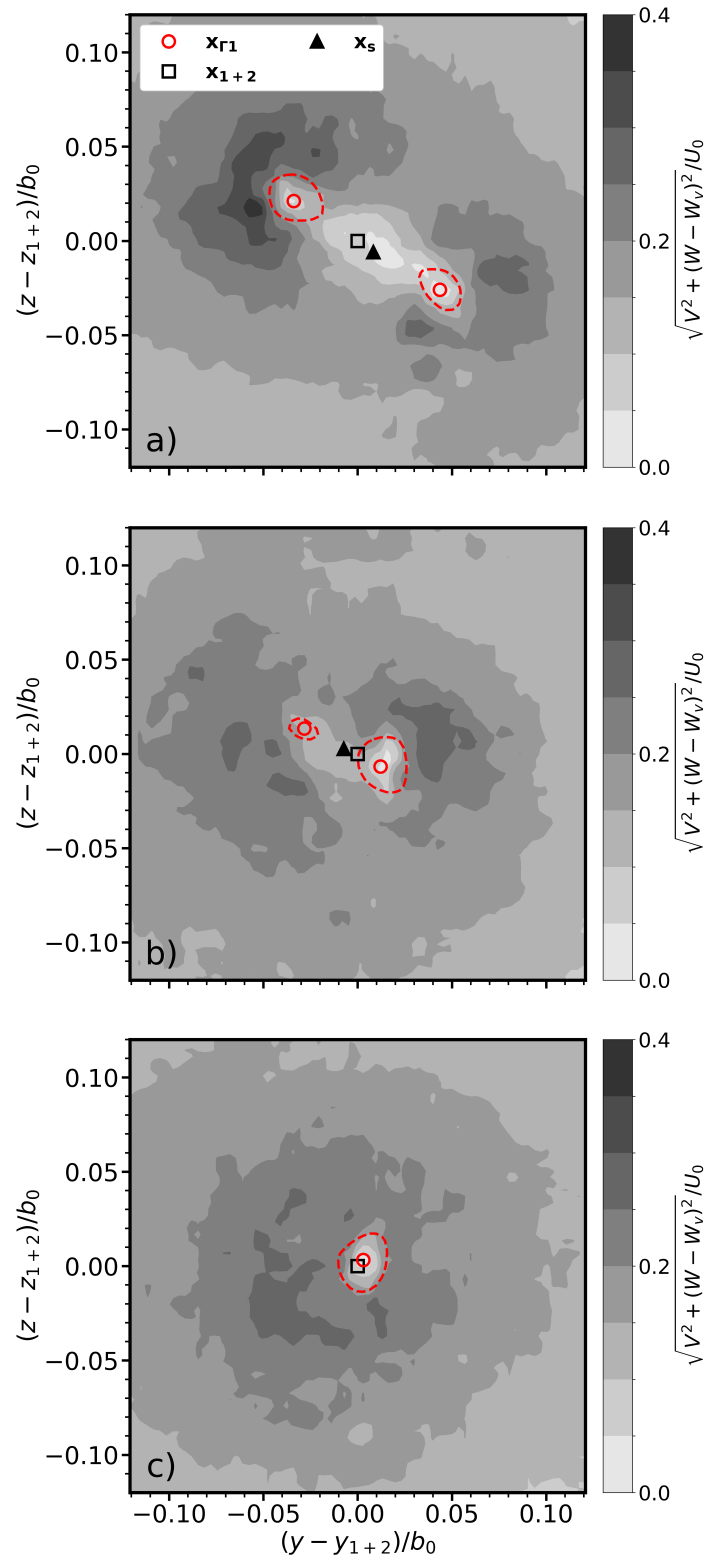


FIGURE 5.9: View of the wake of the *HL* wing under configuration *F2 : HL*. The figure shows the field of velocity  $v_{\perp} = \sqrt{V^2 + (W - W_v)^2}$  at normalized times of  $tb_0/U_0 =$  a) 3.25, b) 6.25 and c) 8.25. The regions where  $G1 > G1_{crit}$  are shown by a red dashed line.

of each vortex is then the local maxima of the  $G1$  criterion. This threshold methodology allows for an approximate detection of the end of the fusion phase, when a unique compact region of  $G1(\mathbf{x}) = G1_{crit}$  is detected, see Fig. 5.9c. In the experiment shown in Fig. 5.9, the two vortices are approximately  $0.1b_0$  apart initially and rotate together in the trigonometric sense around  $\mathbf{x}_{1+2}$ . Within  $\approx 8$  normalized time units their distance reduces and the vortices merge into one single vortex. Before fusion, a stagnation point  $\mathbf{x}_s$  is formed in a region where the velocity fields of both the tip vortex and the flap vortex cancel out. When considering the distance from each of the vortices to  $\mathbf{x}_s$  along the axis that links both vortices, one obtains :

$$x_s = \frac{\Gamma_1 x_2 + \Gamma_2 x_1}{\Gamma_1 + \Gamma_2} \quad (5.1)$$

Which is a simple way to show that  $\mathbf{x}_s \neq \mathbf{x}_{1+2}$ . Notably,  $\mathbf{x}_{1+2}$  is located closer to the stronger vortex while  $\mathbf{x}_s$  is closer to the weaker one.

It is useful to separate the regions of  $v_\perp$  that are mainly influenced by each of the vortices. We illustrate our procedure in Fig. 5.10. In short, we trace a line perpendicular to the axis of the dipole and passing through  $\mathbf{x}_s$ . In particular, this allow us to characterize the circulation of each vortex separately. We integrate the velocity field around contours drawn around each vortex centroid ( $x_1$  and  $x_2$  in the figure). It can be seen in Fig. 5.10 that each contour mainly contains the vorticity of one of the vortices of the pair.

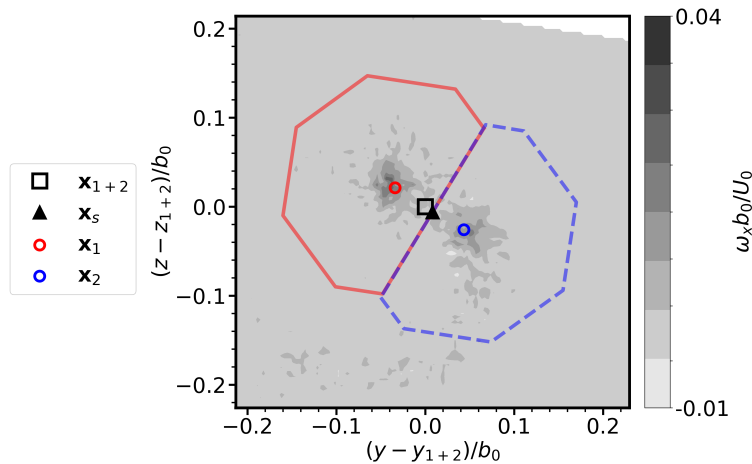


FIGURE 5.10: Contours of integration to compute the circulation ratio of co-rotating vortices in the wake of the HL wing under configuration F2 : HL. The figure shows the field of normalized axial vorticity  $\omega_x b_0 / U_0$  at  $tb_0 / U_0 = 3.25$ . The contour of the wingtip vortex is shown by a red solid line while that of the flap vortex is shown by a blue dashed line.

### 5.3.2.2 Evolution of the properties of the co-rotating pair

The dynamics of the co-rotating pair from their formation to their fusion are studied. The main characteristics of the pair are defined first. In the pair, the wing tip vortex is defined as the primary vortex and the flap tip vortex as the secondary vortex. The primary and secondary vortices are denoted with subscripts 1 and 2. At  $t \approx 0$ , the secondary vortex is located at the trailing edge of the wing flaps and then undergoes an orbital motion around the wing-tip vortex. The time scale of the orbital period

for point vortices of same circulation as those from our experiment is defined as

$$t_{orb} = \frac{(2\pi d)^2}{\Gamma} = \frac{8b(\pi d)^2}{C_z U_0 S} \quad (5.2)$$

With  $d$  the distance between vortices 1 and 2. A non-dimensional time scaled by the orbital motion  $t/t_{orb}$  is thus defined. The pair is also characterized by the ratio of vortex circulation  $\gamma_0 = \Gamma_2/\Gamma_1$  and by the ratio of distances between vortices at the right and left sides of the wake  $\beta_0 = b_2/b_1$ .  $\beta_0$  is estimated from the wing geometry (as per Betz's method [86], see sec. 5.1), yielding  $\beta_0 = 0.75$  for all experiments. Therefore  $d$  in equation 5.2 is set as  $d_0$  the distance between the flap and wing tips. The magnitude of  $\gamma_0$ , however, is dependent on both time and towing conditions. This is why the characteristic ratio  $\gamma_0$  of each pair is estimated from the ratio measured at the earliest available time.

$U_0 m/s$	1.0	2.0	3.75	5.0
$\alpha = -0, 5^\circ$	0.93	1.01	0.88	1.11
$\alpha = 2.5^\circ$	—	—	0.79	—
$\alpha = 5^\circ$	0.68	0.62	0.58	—

TABLE 5.3: Characteristic ratio  $\gamma_0$  measured at time  $t/t_{orb} = 0.1$  as a function of angle of attack  $\alpha$  and towing velocity  $U_0$  for the HL wing.

The characteristic ratio of circulations between the flap and wing-tip vortices,  $\gamma_0$ , is shown in Table 5.3 at a normalized time of  $t/t_{orb} = 0.1$  which is often the earliest time at which measurements are available. If PIV measurements are not available at that time, the ratio is estimated by linear interpolation of  $\gamma(t)$  over non-dimensional time  $t/t_{orb}$  based on measurements in the range of  $0.1 < t/t_{orb} < 1$ . Table 5.3 reveals that the circulation ratio is weakly dependent on  $U_0$  and decreases with  $\alpha$ . At  $\alpha \approx 0^\circ$ , both vortices have similar strength at their formation. For  $\alpha = 5^\circ$ , the flap vortex circulation is approximately 0.58 to 0.68 that of the wing-tip vortex.

The characteristic ratio of circulation  $\gamma_0$  has a direct influence on the orbital behavior of the vortices within the pair. Specifically, these vortices orbit around their shared barycenter of vorticity  $x_{1+2}(t)$ . Consequently, when  $\gamma_0$  approaches unity, both vortices assume relatively equidistant orbits from  $x_{1+2}(t)$ . Conversely, when  $\gamma_0$  is less than unity, the trajectory of  $x_1(t)$  exhibits a tighter orbit around  $x_{1+2}(t)$  compared to that of  $x_2(t)$ . This distinction is evident in Fig. 5.11, where the positions of  $x_1(t)$ ,  $x_2(t)$ , and  $x_{1+2}(t)$  are presented for two distinct configurations: one with  $\gamma_0 = 1.01$  (Fig. 5.11a and b) and the other with  $\gamma_0 = 0.62$  (Fig. 5.11c and d).

The vortex trajectories in the laboratory reference frame are shown on the first column of Fig. 5.11, followed by their representation in a reference frame centered around  $x_{1+2}(t)$  (second column of Fig. 5.11), which accentuates the orbital motion of the vortices. These trajectories generally align with the predictions derived from point vortex simulations (not shown). However, it is worth noting that in the experiments, the vortices approach each other during their orbit, a characteristic indicative of the time dependency of the properties of the pair (see, for example Fig. 5.11b). This behavior is not replicated in the simulations, where the properties of the vortices are constant.

At this stage, the main characteristics of the co-rotating pair are defined. The time evolution of the properties of the pair is now analyzed in order to characterize the process of vortex fusion. To achieve this, the evolution of the circulation ratio  $\gamma(t)$ , of the distance between the vortices  $d(t)$  and of  $\phi(t)$  which is the angle between  $x_1$  and

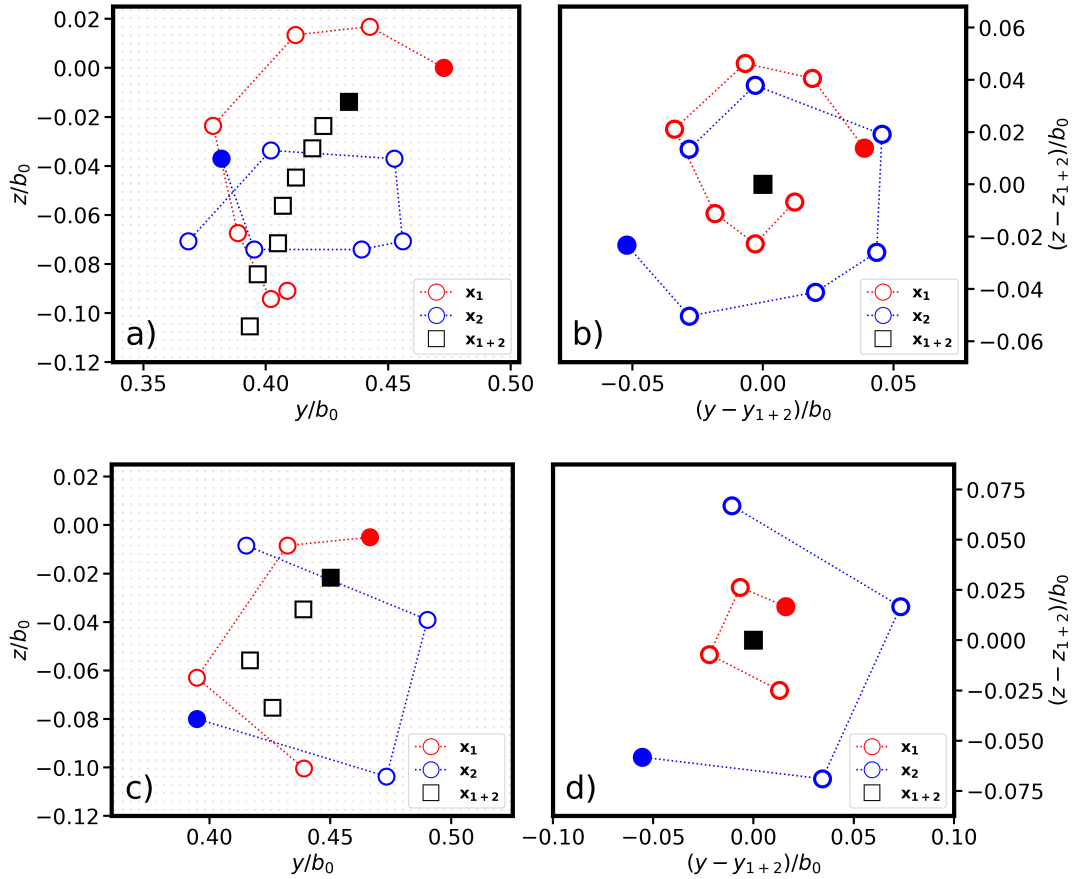


FIGURE 5.11: Vortex 2D trajectories as a function of time (the first instant is indicated by a filled symbol) for the wing-tip and flap vortices of configurations **a)** and **b)** :  $\gamma_0 = 1.01$  ( $HL, U_0 = 2m/s, \alpha = -0,5^\circ$ ) and **c)** and **d)** :  $\gamma_0 = 0.62$  ( $HL, U_0 = 2m/s, \alpha = 5^\circ$ ). Trajectories are represented in the laboratory reference frame (first column) and in a reference frame centered around the barycenter of vorticity (second column).

$x_{1+2}$  are studied. The time evolution of these variables is shown in Fig. 5.12.  $\phi(t)$  characterizes the orbital motion of the pair.  $\phi(t)$  is also of practical interest since it allows us to define an origin of time as the instant where  $\phi(t) = 0$ . The data in Fig. 5.12 has been thus corrected from this origin of time.

It is found that  $\gamma(t)$  decreases with time, meaning that the secondary vortex loses circulation, and the primary vortex gains circulation. All the experiments follow this trend in a self-similar fashion. The distance between the pair depends on the circulation of the vortices  $\Gamma_1$  or  $\Gamma_2$  because of the conservation of angular momentum  $J$  considering

$$J = \int_{\Omega} (\mathbf{x} - \mathbf{x}_{1+2})^2 \omega_x(\mathbf{x}) d\Omega \quad (5.3)$$

$d(t)$  decreases with time meaning that the two vortices get closer to each other. The rate of decrease is larger when  $\gamma_0 \sim 1$  than when  $\gamma_0$  is lower. This can be seen in Fig. 5.11b and d : when  $\gamma_0 = 1.01$ , the initial distance between  $x_1$  and  $x_2$  (shown by the filled circles) is larger than that of the last measurement, i.e. prior to fusion. On the contrary, when  $\gamma_0 = 0.62$ , the distance between the vortices on the first measurement and on the last measurement are of similar magnitude.

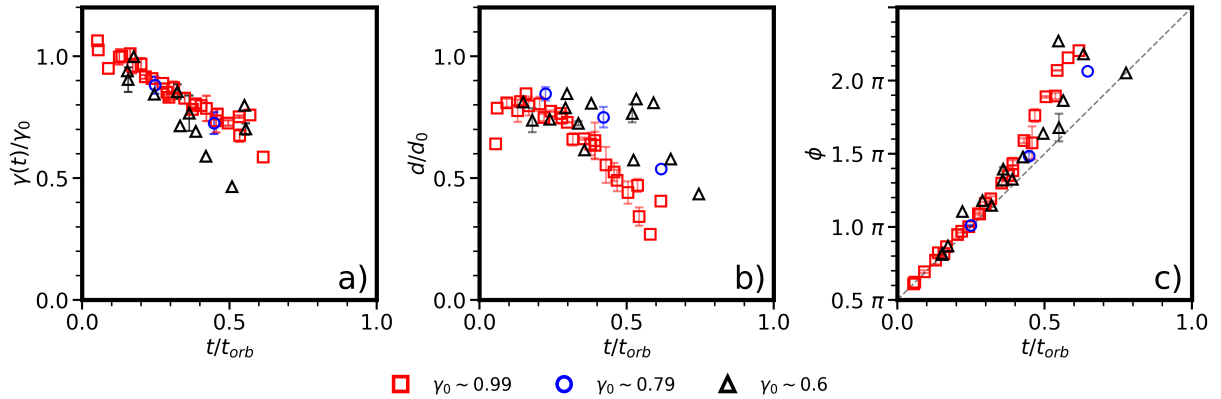


FIGURE 5.12: Time evolution, of the co-rotating pair characteristics for different values of characteristic circulation ratio  $\gamma_0$ : **a)** circulation ratio  $\gamma(t)/\gamma_0$ , **b)** distance between the co-rotating pair  $d(t)/d_0$  and **c)** orbit angle  $\phi_1(t)$  for the wing-tip vortex, (the evolution of  $\phi_{th}$ , the orbit angle calculated by using an inviscid model, is represented by a dashed line), Dispersion between runs is represented by error bars.

Following these previous points, the evolution of the angle  $\phi(t)$  relates to the evolution  $d(t)$ . The angle  $\phi(t)$  is compared to  $\phi_{th}$  which is the theoretical angle predicted by the inviscid model for the orbital period  $1/t_{orb}$ . The evolution of  $\phi_{th}$  is defined by equation 5.2. It is observed that  $\phi$  closely matches  $\phi_{th}$  until what can be denoted as a threshold, that is when  $t/t_{orb} \sim 0.4$ . Beyond this threshold, the orbital velocity of the wing-tip vortex,  $\dot{\phi}$ , appears to accelerate, suggesting a completion of a full turn ( $2\pi$ ) by  $t/t_{orb} \sim 0.75$ . However, in all experiments, vortex fusion occurs before a complete rotation of the two vortices is completed.

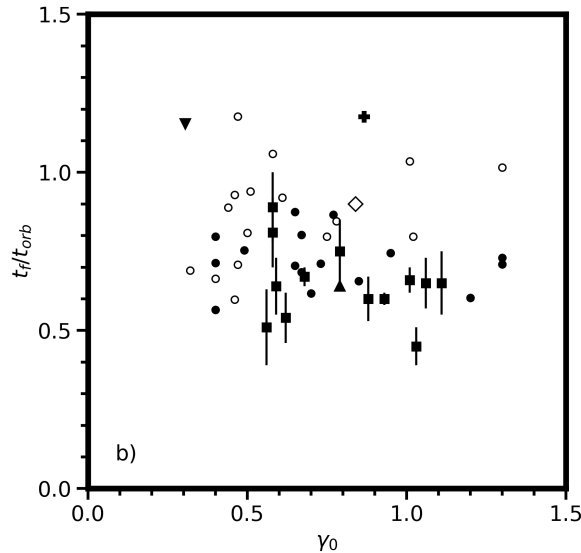


FIGURE 5.13: Fusion time as a function of initial ratio of circulations scaled by the orbit time scale  $t_{orb}$ .  $\diamond$ : Bristol *et al.* [12] ( $d/b_0 = 0.25$ ),  $\circ$ : Chen *et al.* [17] ( $d/b_0 = 0.351$ ),  $\bullet$ : Chen *et al.* [17] ( $d/b_0 = 0.164$ ),  $\blacktriangle$ : Breitsamter [8] ( $d/b_0 = 0.175$ ),  $\blacktriangledown$ : Breitsamter [8] ( $d/b_0 = 0.04$ ),  $+$ : Meunier [61],  $\blacksquare$ : present study ( $d/b_0 = 0.125$ )

In our measurements, the fusion time  $t_f$  refers to the moment when the separate regions with  $G1(x) > G1_{crit}$  coalesce into a single continuous region (see Fig. 5.9 for an illustration). Fusion times from our experiments and from the literature show consistent values when scaled by the orbital period of the vortex pair. Fig. 5.13 shows the fusion times of the present experiment along with other results from the literature [12, 8, 17, 61]. When analyzing fusion times scaled by the orbit time scale, a consistent trend emerges - fusion typically occurs when  $t/t_{orb} = \mathcal{O}(1)$ .

Here fusion occurs before one rotation period, indicating a faster process than predicted by 2D theory. Previous studies [85] used point vortex simulations to examine merging parameters, such as circulation ratio and initial spacing, and found that vortices might deform and orbit without merging. Comparing our results to these studies, one observes a faster fusion than expected for our initial conditions. This finding confirms those of the literature where  $t_f/t_{orb} < 1$  was also observed.

### 5.3.3 High-lift wake after vortex fusion ( $t > t_f$ ) : Comparison of the far wake evolution of the fused vortex characteristics with that of the baseline vortex in order to estimate the impact of a high-lift configuration on the vortex wake hazard

We wish to assess the effect of the loading distribution on the properties of the trailing vortices. To do this, the post-fusion vortex from the *HL* configuration is compared to the vortex of the *Ref* configuration. The vortices are compared under equal conditions of  $Re_{b_0}$  and  $C_z$ , and also at equal normalized time. For each configuration of Table 5.2,  $U_0^{Ref} = U_0^{HL}$ , since  $Re_{b_0}^{Ref} = Re_{b_0}^{HL}$  and both wings have the same span.

The temporal evolution of vortex radius ( $R_d(t)$ ) is presented in Fig. 5.14, for the *Ref* and *HL* configurations of case F2. This analysis draws upon the insights gained from the investigation of the behavior of  $R_d(t)$  in the *Ref* configuration, which is detailed in detailed in sec. 4.3.1. The vortex behavior in the high-lift configuration mirrors that of the reference vortex. Specifically, the *HL* vortex exhibits an increase in size attributed to laminar diffusion. This relationship is evident in Fig. 5.14a, where the analytical prediction derived from eq. 4.34 is plotted with solid and dashed lines, corresponding to the *Ref* and *HL* configurations, respectively.

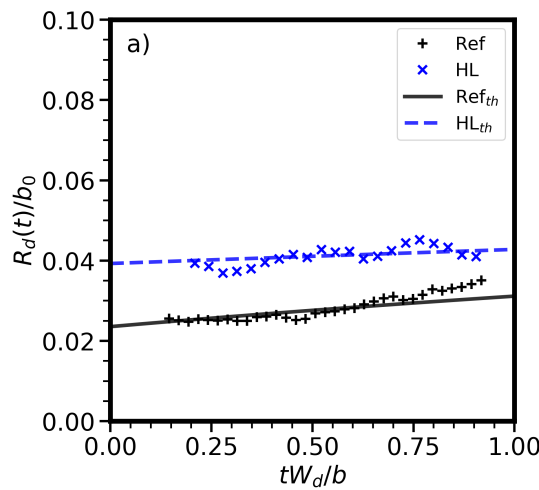


FIGURE 5.14: Vortex normalized dispersion radius as a function of the induction based time for the right side vortex trailing downstream from the reference and high-lift wings under configurations F2 .

Fig. 5.15 shows the azimuthal velocity and axial vorticity profiles of the *Ref* and *HL* vortices of all cases from Table 5.2. The difference in peak azimuthal velocities is on average  $\max(\overline{v_\theta}^{HL})/\max(\overline{v_\theta}^{Ref}) \sim 0.65$ . On the other hand, we note an average increase of the dispersion radius of  $R_d^{HL}/R_d^{Ref} \sim 1.65$ . The complete set of values is summarized in table 5.4.

In all configurations  $b^{HL}/b^{Ref} < 1$ , which indicates that the vortex separation  $b$  is reduced on the high-lift case compared to the reference case. This reduction in separation is expected due to the increase in root circulation  $\Gamma_0$  caused by the presence of an inboard flap on the *HL* wing (see equation 4.6).  $\Gamma^{HL}/\Gamma^{Ref} > 1$ , indicating a higher circulation in the high-lift configuration compared to the reference configuration. The increase in circulation goes from 8% to 20% at  $tU_0/b_0 = 30$ . The measured change in circulation confirms the increase in root circulation in the *HL* case, also it is in good agreement with the inference made from comparing the separation  $b$ , namely  $\Gamma^{HL}/\Gamma^{Ref} = b^{Ref}/b^{HL}$ .

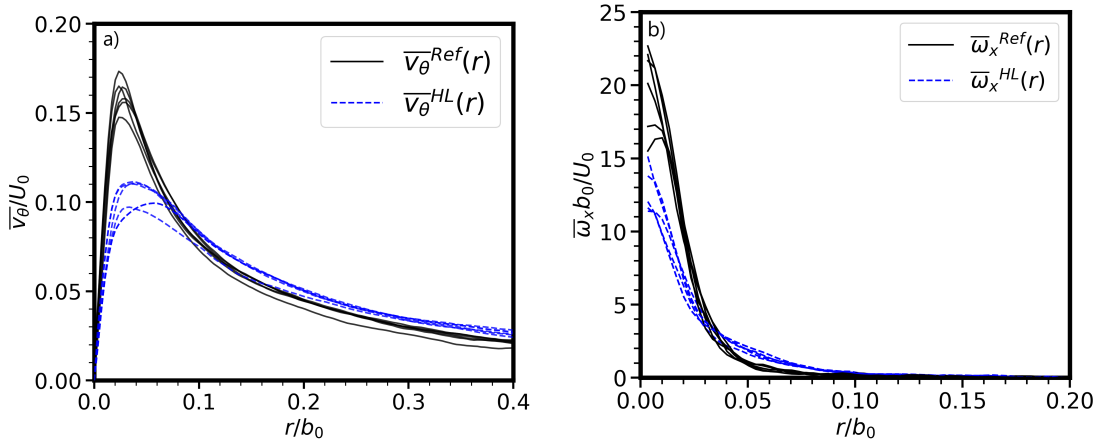


FIGURE 5.15: Scaled profiles of vortices generated under configurations of table 5.4,  $t\frac{b_0}{U_0} = 30$ . **a)** azimuthal velocity, **b)** axial vorticity

Configuration	F1	F2	F3	F4	F5
$\Gamma^{HL}/\Gamma^{Ref}$	1.08	1.15	1.20	1.20	1.17
$b^{HL}/b^{Ref}$	0.89	0.87	0.88	0.85	0.85
$\max(\overline{v_\theta}^{HL})/\max(\overline{v_\theta}^{Ref})$	0.62	0.64	0.67	0.67	0.63
$R_{d0}^{HL}/R_{d0}^{Ref}$	1.62	1.67	1.51	1.49	1.67

TABLE 5.4: Towing configurations, noted as  $(U_0, \alpha)$  for which the reference and high-lift wings generate comparable lift. Ratios of vortex characteristics between configurations for  $T = 30 \pm 1$  wingspans downstream on the wake are shown.

## 5.4 Intermediate conclusion

In this chapter, the behavior of a co-rotating pair of trailing vortices is investigated. Our study involves the development of a methodology for analyzing this vortex pair, allowing for the characterization of their trajectories and circulation ratios.

The fusion of the co-rotating vortices is consistently observed over a time scale corresponding to the period of the vortices orbital motion. The load distribution on

the generating wing mimics that of a commercial aircraft in its high-lift configuration. To understand the impact of this modified wing-load on the wake, we compare the generated vortices with those generated by a plain configuration (*Ref*). The comparison is performed under the same conditions of lift coefficient ( $C_z$ ) and Reynolds number ( $Re_{b_0}$ ).

The *HL* vortex is found to possess a 8% to 20% higher normalized circulation than the *Ref* vortex. However, the vortex core of the *HL* configuration is more diffused, exhibiting an average reduction of 35% in maximum azimuthal velocity and an average increase of 65% in its dispersion radius compared to the *Ref* case.

In the following section, we introduce counter-rotating vorticity into the wake, as interactions between flap and wing-tip vortices in this configuration are known to promote the development of viscous and three-dimensional effects, potentially leading to a rapid decay in vorticity intensity.



## Chapter 6

# Analysis of vortex interaction in a counter-rotating trailing vortex system and properties in the far wake

In this chapter, we analyze the results of experiments using a wing configuration that generates two counter-rotating pairs of vortices. This wing configuration is denoted *CnR* and the particular flow generated in its wake is referred to as a counter-rotating system hereafter. In a commercial aircraft, a counter-rotating system can result from the interaction between the vortices shed by the wing-tip and those shed by the horizontal stabilizers. First, in section 6.1 we discuss the design and objectives set for the experiments involving the *CnR* wing. Then in section 6.2 we describe the methodology developed to assess the characteristics of the counter-rotating pair during an experiment. Finally, in section 6.3 we characterize the diffusion that affects the flap and wing tip vortices.

### 6.1 Modification of the wing geometry in order to generate a counter-rotating vortex system

In the *CnR* wing, a twist angle of  $\Theta = -8^\circ$  is applied to the baseline geometry (described in sec. 3.1.1) from the midplane to  $y = 0.075b_0$ , leading to the wing-load distribution illustrated in Fig. 6.1a, with the grey area indicating the region of twist variation. At this point of geometrical discontinuity, a significant change in bound circulation  $\Gamma_y(y)$  is observed, resulting in a negative value of  $d\Gamma_y/dy$ . According to Betz theory [26, 86], vorticity roll-up occurs around regions of peak vorticity strength, typically situated close to the wing and flap tips. Consequently, the *CnR* wing design is expected to enable the generation of strong counter-rotating vorticity, referred to as secondary vorticity, alongside the primary wingtip vortex. A sketch of the counter rotating system is recalled in Fig. 6.2.  $b_1$  (and similarly,  $b_2$ ) represents the distances between the primary (and secondary) vortices on each side of the plane. Following Betz theory (see sec. 2.3.1.1 for details)  $\beta_{CnR} = b_2/b_1$  can be estimated to be approximately equal to the ratio of the flap span to the wing span, resulting in  $\beta_{CnR} = 0.15$ . As discussed in section 2.3, the behavior of vortex pairs is determined by their ratio of circulation  $\gamma = \Gamma_2/\Gamma_1$  and of distances  $\beta$ . This relationship is graphically represented in the Donaldson-Bilan diagram [26] depicted in Fig. 6.1b. For  $\beta_{CnR} = 0.15$ , three types of motion can occur: a divergent motion, a steady motion and a periodic motion. The critical value of  $\gamma$  at which the behavior transitions between periodic and divergent motion is approximately  $\gamma_s \sim -0.425$ .

The subscript  $s$  is employed to denote that at this critical value, vortices are expected to exhibit steady motion. Hence, the present  $CnR$  wing is expected to generate pairs of vortices that demonstrate divergent, steady and periodic motion.

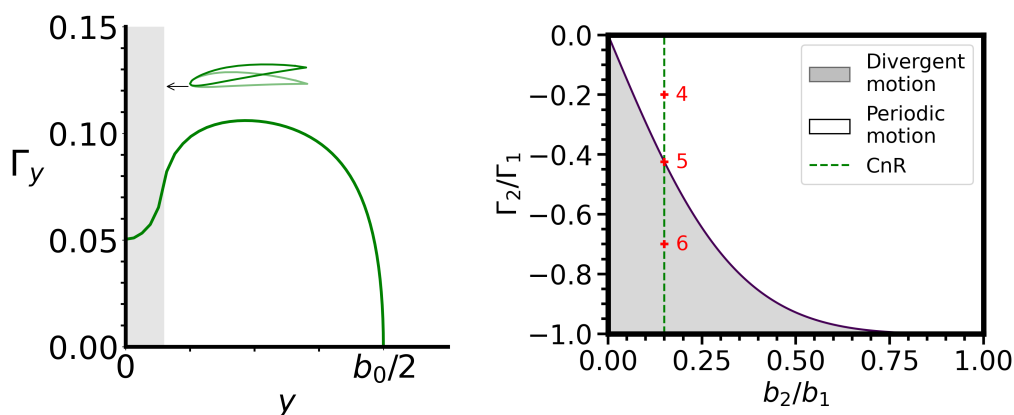


FIGURE 6.1: Design of the  $CnR$  wing model **a)** Supersposed view of the wing geometry and bound circulation  $\Gamma_y$  as a function of spanwise station, as predicted by lifting line theory. **b)** Donaldson-Bilanin diagram for counter-rotating vortex pairs. The zone of divergent motion is colored gray while the zone of periodic motion is colored white. The value of  $b_2/b_1$  for the  $CnR$  wing is shown by a dashed line. A modelization of vortex trajectories for points 4,5 and 6 is shown in Figs. 6.3, 6.5 and 6.4 respectively

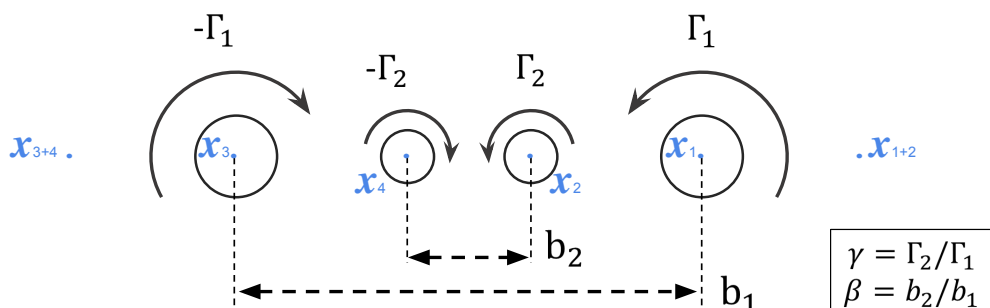


FIGURE 6.2: Diagram of a system of four vortices

Point-vortex motion simulations are conducted as a preliminary step to predict the expected outcomes of our experiments. In these simulations, the trajectories of a system comprising four point vortices are calculated using, as input, values for  $\gamma$  and for  $\beta$ . Initially, the point vortices are aligned in the spanwise direction. Their subsequent positions over time are then determined according to eq. 6.1 (see sec. 2.3.1.2 for details) :

$$\frac{dY_n}{dt} = \sum_{m \neq n} -\frac{\Gamma_m}{2\pi} \frac{(Z_n - Z_m)}{(Y_n - Y_m)^2 + (Z_n - Z_m)^2} \quad (6.1)$$

$$\frac{dZ_n}{dt} = \sum_{m \neq n} \frac{\Gamma_m}{2\pi} \frac{(Y_n - Y_m)}{(Y_n - Y_m)^2 + (Z_n - Z_m)^2} \quad (6.2)$$

The simulation is advanced in time using a first-order explicit time scheme. The trajectories of point vortices in a periodic, steady and divergent configuration are displayed in Figs. 6.3, 6.4 and 6.5, respectively. In these figures, we depict the trajectories of the portside wing-tip vortex  $\mathbf{x}_1$  and the portside flap vortex  $\mathbf{x}_2$ , relative to the reference frame centered around the barycenter of vorticity  $\mathbf{x}_{1+2}$  (highlighted in red). Additionally, the trajectories of vortices are presented in the laboratory reference frame. In the counter-rotating system (be it a divergent, steady or periodic configuration), the barycenter of vorticity is located beyond the spanwise station of the wing-tip.

Consider the periodic case depicted in Fig. 6.3. All four vortices follow circular trajectories as they descend in the laboratory reference frame. The downwash from tip vortices dominates, causing a general downward motion for each pair. Examining the trajectories relative to  $\mathbf{x}_{1+2}(t)$ , shows that each pair orbits around this point. The rotation period is approximately  $\Delta t U_0 / b_0 = 100$  for this configuration.

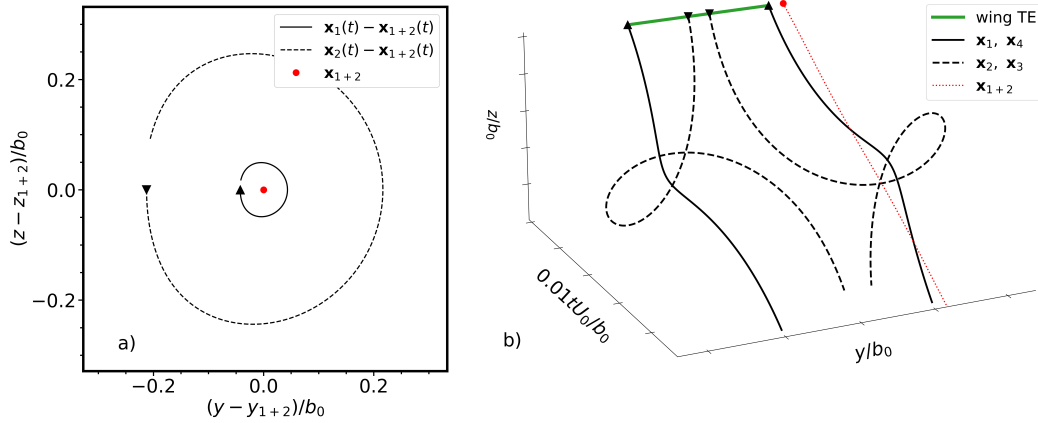


FIGURE 6.3: Periodic trajectories of point-vortices in a counter-rotating dipole for  $\gamma_0 = -0.2$ ,  $b_2/b_1 = 0.15$  (point 4 in Fig. 6.1) : **a)** in a reference frame centered around the portside barycenter of vorticity and **b)** in the laboratory reference frame.

In the steady case (depicted in Fig. 6.4), vortices descend linearly in the laboratory reference frame. Here, the velocities induced by flap and tip vortices counteract each other as per eq. 2.77, resulting in a purely descending motion. In the  $\mathbf{x}_{1+2}$  centered frame, the vortices appear stationary.

In the divergent case (depicted in Fig. 6.5), flap vortices move upward in the laboratory reference frame, while tip vortices descend as usual. The barycenter  $\mathbf{x}_{1+2}$  follows a downward trajectory. In the  $\mathbf{x}_{1+2}$  centered frame, both tip and flap vortices appear to ascend. This behaviour is due to the strong upward velocity induced by flap vortices on each other, overpowering the downwash from tip vortices. Vortex interaction in this case is less prominent than for periodic and steady cases.

Our first goal in this study is to develop a methodology for assessing the value of  $\gamma(t)$  during an experiment. Subsequently, we analyze vortex trajectories to distinguish between divergent and periodic motion, allowing us to estimate the experimental value of  $\gamma_s$ . Finally, we focus on the periodic motion cases, examining the flow's evolution over extended periods in order to characterize the effects of the interactions within the vortex pair.

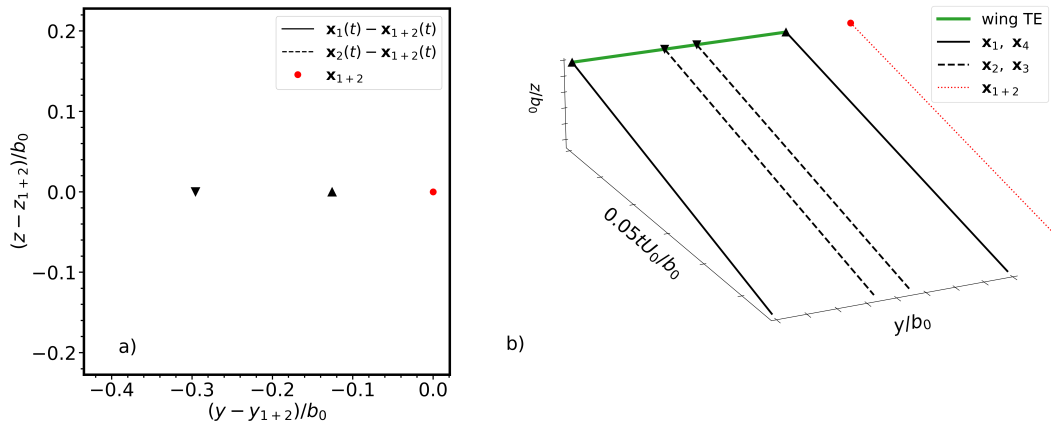


FIGURE 6.4: Steady trajectories of point-vortices in a counter-rotating dipole for  $\gamma_0 = -0.425$ ,  $b_2/b_1 = 0.15$  (point 5 in Fig. 6.1) : **a**) in a reference frame centered around the portside barycenter of vorticity and **b**) in the laboratory reference frame.

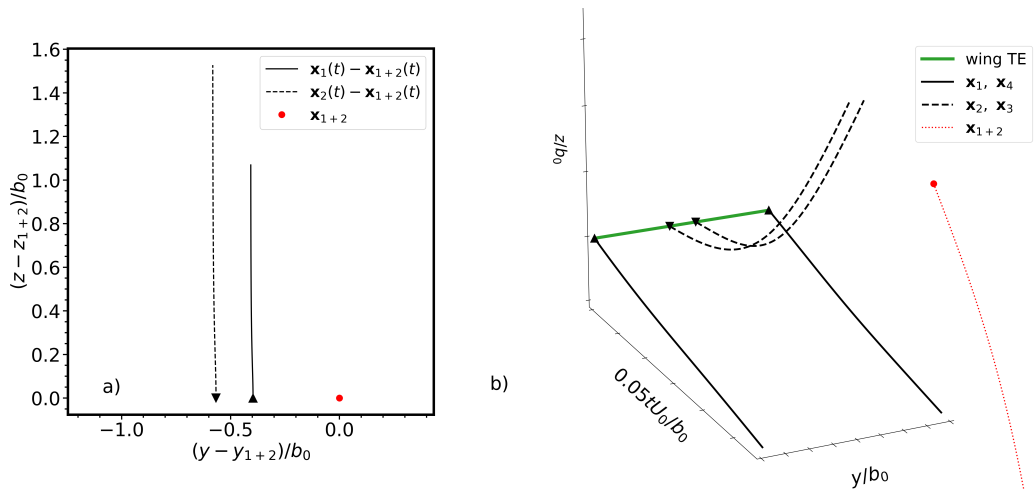


FIGURE 6.5: Divergent trajectories of point-vortices in a counter-rotating dipole for  $\gamma_0 = -0.7$ ,  $b_2/b_1 = 0.15$  (point 6 in Fig. 6.1) : **a**) in a reference frame centered around the portside barycenter of vorticity and **b**) in the laboratory reference frame.

## 6.2 Analysis of vortex trajectory and circulation in a counter-rotating system

### 6.2.1 Identification of the vortices

The methodology employed for vortex identification is adapted from the previous case of co-rotating vortices to the challenges posed by the counter-rotating vortex system. The data measured for an experiment realized at configuration  $C_{126} = (CnR, U_0 = 3m/s, \alpha = 10^\circ)$  is used in this chapter to visually represent the steps of the procedure. 3D iso-surfaces of vorticity obtained from the PIV field are provided in Fig. 6.6. The positive vorticity (red) is linked to the wing-tip vortex while the negative vorticity (blue) is linked to the flap vortex.

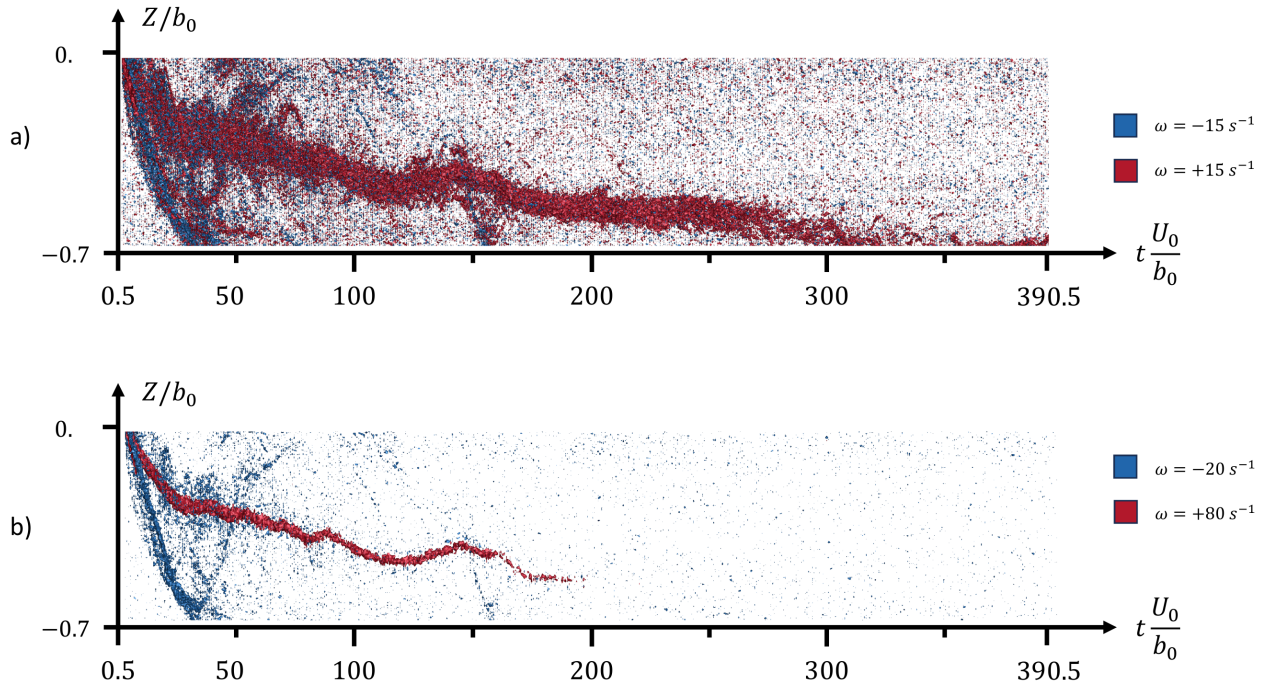


FIGURE 6.6: Vorticity iso-surfaces (side-view), reconstructed from the PIV measurements, for the wake generated at configuration  $C_{126}$  (periodic motion). **a)** Iso-surfaces  $\omega = \pm 15 \text{ s}^{-1}$  and **b)**  $\omega = -20$  and  $+80 \text{ s}^{-1}$ .

Analyzing this pair of counter-rotating vortices is challenging due to the significant separation between vortices relative to the measurement window's size. Depending on the experiment, the trajectories of these vortices may exit the measurement window from various sides, necessitating adjustments to the window's position accordingly. Consequently, the vortices are often situated near the measurement window's borders, potentially obstructing the measurement of vortex characteristics like location and circulation. This is observed in Fig. 6.6a: the wing tip vortex descends vertically and has exited through the lower border of the measurement window almost completely at  $tU_0/b_0 = 390.5$ . Also, it can be seen that the flap vortex nears the upper and lower borders of the measurement window during its life time. A substantial loss of circulation is experienced by the vortices during the experiment, sometimes leading to an apparently complete diffusion. This is observed in Fig. 6.6b, which displays iso-surfaces for high magnitudes of positive and negative vorticity: the vorticity of the wing tip vortex is higher than  $+80 \text{ s}^{-1}$  only for  $tU_0/b_0 < 200$ . Hence, the adopted methodology for vortex identification must be robust in the face of vortex disappearance, either due to them exiting the measurement window or diffusing.

On the following,  $t = t_0$  corresponds to the time of the first measurement available after the passage of the wing through the PIV plane ( $t_0U_0/b_0 = 0.5$  in the case of Fig. 6.6). Also  $t = t_{max}$  is the time of the last measurement for which one of the vortices is still detected in the PIV window.

First, the barycenters of vorticity of each vortex in the pair, denoted  $\mathbf{x}_{\omega,1}$  and  $\mathbf{x}_{\omega,2}$ , are computed. Let  $i \in \{1,2\}$  :

$$\mathbf{x}_{\omega,i}(t) = \frac{\int_{\Omega_i} \mathbf{x}\omega(\mathbf{x})d\Omega_i}{\int_{\Omega_i} \omega(\mathbf{x})d\Omega_i} \quad (6.3)$$

Where  $\Omega_1 = \Omega_1(t)$  and  $\Omega_2 = \Omega_2(t)$  are two distinct regions of radius  $0.1b_0$ . At  $t = t_0$ , these regions are centered on the locations of the flap and wing tips, respectively. This process is visually represented in Fig. 6.7 for an experiment conducted under the towing configuration  $C_{126}$  at  $tU_0/b_0 = 11.8$ . At each subsequent time step  $t + n\Delta t$ , the integration surfaces are recentered yielding :

$$\mathbf{x} \in \Omega_i(t + n\Delta t) \iff |\mathbf{x} - \mathbf{x}_{\omega,i}(t + (n - 1)\Delta t)| \leq 0.1b_0 \quad (6.4)$$

This provides an initial approximation of the vortices trajectories within the measurement window. Additionally, by analyzing the field over a region  $\Omega_m$  encompassing both vortices, we determine  $\mathbf{x}_{1+2}(t)$ , the shared barycenter of the vortex pair. This methodology faces challenges, particularly when  $\mathbf{x}_{\omega,1}(t)$  and  $\mathbf{x}_{\omega,2}(t)$  are near the measurement window borders, causing  $\Omega_m$  to extend beyond the window's boundaries. In most cases, the shared barycenter of vorticity of the pair,  $\mathbf{x}_{1+2}(t)$ , lies outside the measurement window. Nevertheless, this approach for locating  $\mathbf{x}_{1+2}(t)$  yields satisfactory results, as shown further down.

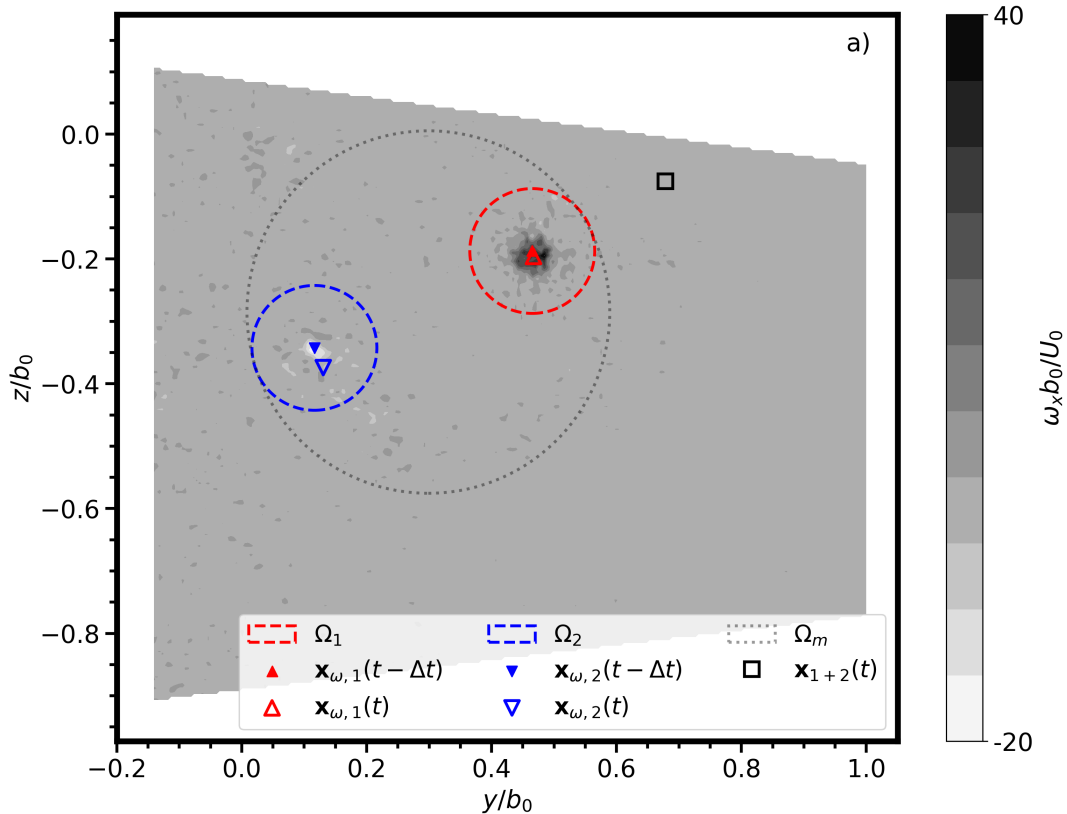


FIGURE 6.7: Procedure to assess the location of the barycenters of vorticity  $\mathbf{x}_{\omega,1}(t)$  and  $\mathbf{x}_{\omega,2}(t)$  and  $\mathbf{x}_{1+2}(t)$ , respectively attributed to the flap vortex, wing tip vortex and to the barycenter of the pair. The wake is generated at the configuration  $C_{126}$ , here  $tU_0/b_0 = 11.8$

A front view (the  $(z, y)$  plane) of the iso-surfaces of vorticity for the wake generated at  $C_{126}$  is shown in Fig. 6.8a. Negative vorticity, which for the most part is shed from the portside wing flap-tip, is seen to "wrap-up" around strong positive vorticity (shed from the wing-tip). The trajectories of  $\mathbf{x}_{\omega,1}(t)$  and  $\mathbf{x}_{\omega,2}(t)$  are illustrated in Fig. 6.8b. Initially, both trajectories display a circular motion, with  $\mathbf{x}_{\omega,2}(t)$  seemingly circling  $\mathbf{x}_{\omega,1}(t)$ . This suggests a periodic regime in the vortex system. However, around  $t_1 U_0/b_0 = 84.5$ , the trajectory of the flap vortex,  $\mathbf{x}_{\omega,2}(t)$ , starts to exhibit random behavior. This is due to the weakening of the vorticity magnitude of the flap vortex over the duration of the experiment at this point. The calculation of  $\mathbf{x}_{\omega,2}(t)$  is affected when vorticity levels are overcome by surrounding vorticity or by measurement noise. Similar issues arise when  $\mathbf{x}_{\omega,2}(t)$  approaches the measurement window's border, since this places  $\Omega_2(t)$  partially outside the measurement window, rendering the barycenter operation ill-defined. In Fig. 6.8b, it can be observed that the computation of  $\mathbf{x}_{\omega,1}(t)$  continues until  $t_{max} U_0/b_0 = 387.5$ , at which point  $\mathbf{x}_{\omega,1}(t > t_{max})$  exits the measurement window. The behavior described by  $\mathbf{x}_{\omega,1}(t)$  and  $\mathbf{x}_{\omega,2}(t)$  is similar to the one observed in the iso-surfaces of vorticity. Thus, this step of the identification procedure is validated.

At this stage of our study, the trajectories of the vorticity barycenters for both the flap and wing-tip vortices ( $\mathbf{x}_{\omega,1}(t)$  and  $\mathbf{x}_{\omega,2}(t)$ ) are defined along with a rough estimate of when vortices either diffuse or exit the measurement window. Thus, the next objective is to refine this computation by introducing a criterion to assess when a vortex diffuses. To achieve this, we calculate the G1 criterion for both  $\Omega_1$  and  $\Omega_2$ , defined in eq. 6.4. The computation of the G1 field necessitates an examination of the flow within a reference frame that moves with the vortices. To do this, the vortices vertical and lateral motion is subtracted from the wake flow. Vertical and lateral motions of the vortex pair are defined as  $W_v$  and  $V_v$  respectively:

$$V_v = \frac{dy_{\omega,1}}{dt} ; W_v = \frac{dz_{\omega,1}}{dt} \quad (6.5)$$

Only the trajectory data from the wing tip vortex  $\mathbf{x}_{\omega,1}(t)$  is used in eq. 6.5 as its location remains consistent throughout the experiment in this dataset, unlike the flap vortex. Note that in previous studies (*Ref* and *HL*), subtracting only the vertical motion from the flow sufficed for our purposes, as  $V_v$  was negligible compared to  $W_v$ . In the case of counter-rotating systems,  $W_v$  and  $V_v$  are of similar magnitude and significant with respect to the vortices azimuthal velocity. Thus, on the following, the velocity field is defined as:

$$\mathbf{v}(y, z, t) = u(y, z, t)\mathbf{e}_x + (v(y, z, t) - V_v(t))\mathbf{e}_y + (w(y, z, t) - W_v(t))\mathbf{e}_z \quad (6.6)$$

therefore the in-plane velocity field  $\mathbf{v}_{\perp}(y, z, t)$  is

$$\mathbf{v}_{\perp}(y, z, t) = (v - V_v)\mathbf{e}_y + (w - W_v)\mathbf{e}_z \quad (6.7)$$

The G1 criterion computation over  $\Omega_1(t)$  and  $\Omega_2(t)$  is illustrated for the configuration  $C_{126}$  in Fig. 6.9. In this process, the vortex is defined as a region where  $G1(y, z) > 0.7$ , and its centroid as  $\mathbf{x}_i = \max(G1(y, z))$ . These vortex regions are shown with colored dashed lines for the flap and tip vortices, respectively, in Figs. 6.9b and 6.9c.

In Fig. 6.9c, it is seen that the condition  $G1(y, z) > 0.7$  is satisfied in multiple connected regions within  $\Omega_2(t)$ . This is primarily due to the stretching of the flap vortex resulting from its interaction with the wing-tip vortex. In such cases, priority is given to the region where  $\max(G1(y, z))$  is located.

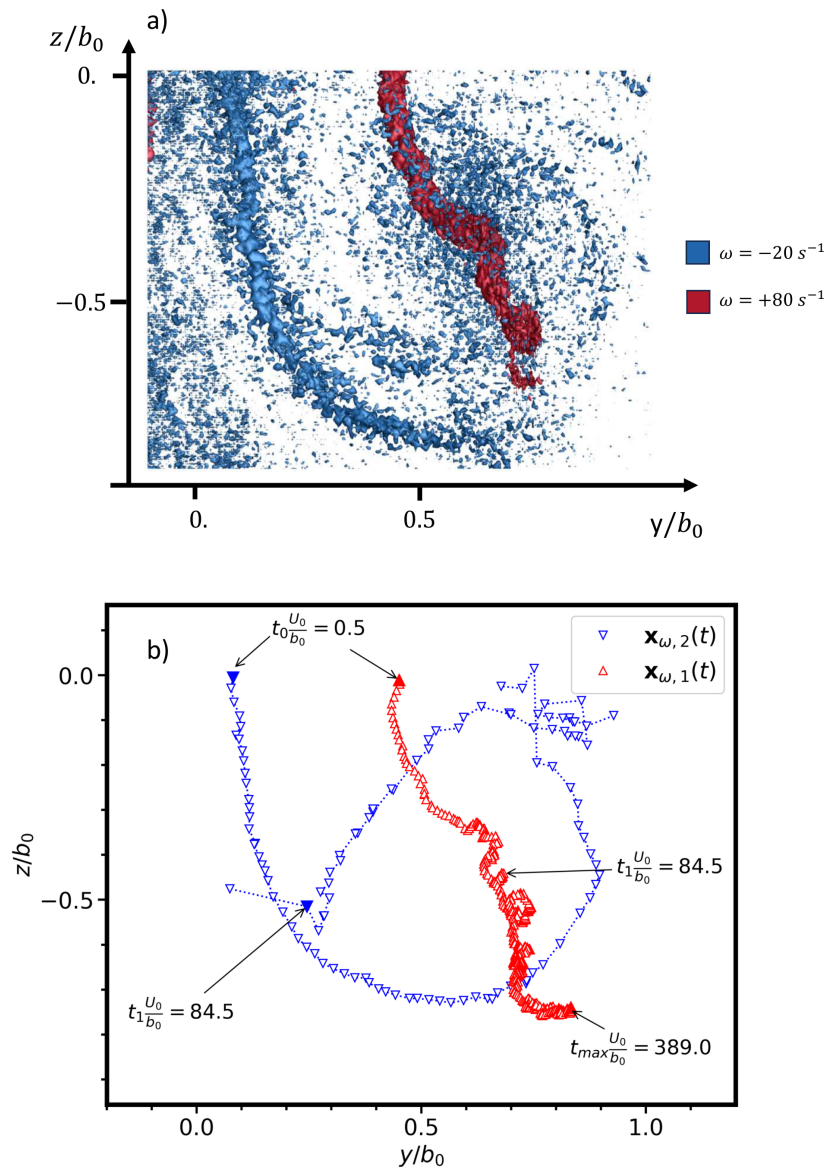


FIGURE 6.8: Analysis of the vorticity field in order to obtain an estimation of vortex trajectories : **a)** Vorticity iso-surfaces, reconstructed from the PIV measurements, in the  $(z, y)$ -plane for the wake generated at configuration  $C_{126}$  (periodic motion). **b)** Trajectories of  $\mathbf{x}_{\omega,1}(t)$  and  $\mathbf{x}_{\omega,2}(t)$  on the measurement plane. The first and last measurements for each vortex are shown by filled symbols. Normalized times of interest are indicated : the time of the first measurement is denoted  $t_0$ , while the times of the last measurement for the flap and wingtip vortices are, respectively,  $t_1$  and  $t_{max}$

Similarly to our observations in the co-rotating case, this threshold-based approach effectively determines the moment at which the vortex intensity significantly decreases (i.e.,  $G1(y, z) < 0.7$  over  $\Omega_i(t)$ ). This reduction in intensity is attributed either to the vortex exiting the measurement window or reaching a point that can be considered, for our purposes, as the end of its lifespan. The precise value produced by  $G1(y, z)$  is dependent on factors such as the PIV resolution and computation parameters, including the size of  $\Omega_i(t)$ . However, these parameters remain constant

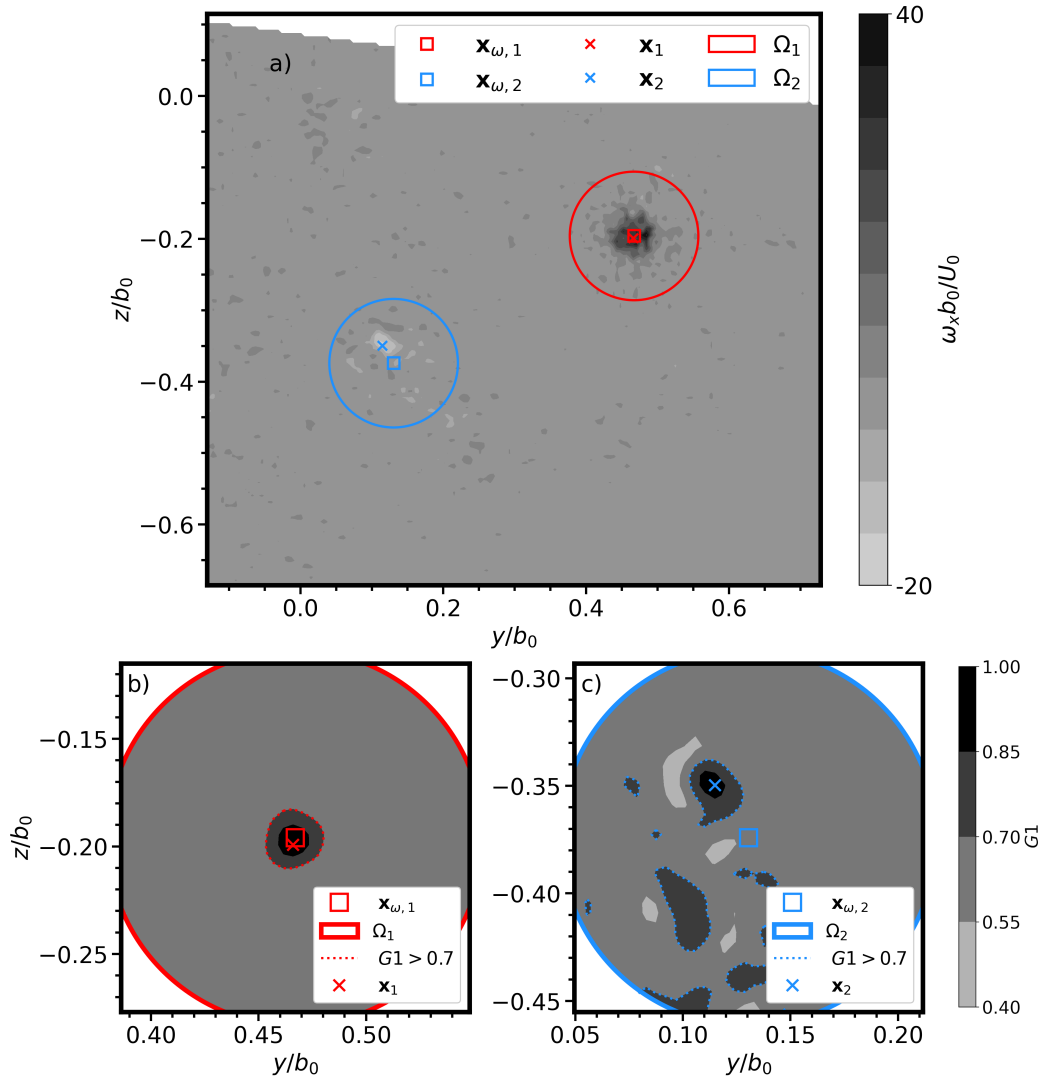


FIGURE 6.9: Computation of vortex locations  $\mathbf{x}_1(t)$  and  $\mathbf{x}_2(t)$  with the  $G1$  criterion for vortices generated in the configuration  $C_{126}$  at  $tU_0/b_0 = 12$ . **a)** locus of  $\mathbf{x}$ ,  $\mathbf{x}_\omega$  and the region for  $G1$  computation superposed over the axial vorticity field, **b)**  $G1$  field computed over the region  $\Omega_1$  and **c)**  $G1$  field computed over the region  $\Omega_2$ .

throughout the entire dataset, ensuring the consistency of results across the tested towing configurations. Consequently, this enables us to terminate the computation of vortex locations at an appropriate time.

In summary, this methodology developed for identifying vortices in the counter-rotating system proves efficient for the analysis of PIV measurements, delivering robust and coherent results for experiments with both periodic and divergent behaviors. In this way, large datasets are efficiently analyzed without the need for manual computation of flow characteristics in each PIV measurement.

Moving forward, we utilize this methodology to characterize each vortex within the counter-rotating pair separately.

### 6.2.2 Assessment of the flap and tip vortices circulation in order to characterize the counter-rotating system

The vortex position  $\mathbf{x}_1(t)$  and  $\mathbf{x}_2(t)$  is used to calculate the vortices individual circulations  $\Gamma_1(t)$  and  $\Gamma_2(t)$ , respectively, and derive the circulation ratio,  $\gamma(t)$ . The total portside ( $y > 0$ ) circulation  $\Gamma_{Tot}(t)$  is also estimated from the PIV measurements using an integral method :

$$\Gamma_{Tot}(t) = \oint_{\Lambda_{Tot}} \mathbf{v}_{\perp}(t) \cdot d\boldsymbol{\ell} \quad (6.8)$$

Where  $\Lambda_{Tot}$  is a rectangular contour which extends up until the borders of the measurement plane and  $d\boldsymbol{\ell}$  is the unit vector tangent to  $\Lambda_{Tot}$ . This is illustrated in Fig. 6.10.

To compute the circulation pertaining to the wing-tip vortex, a closed contour, denoted  $\Lambda_1$  and centered about  $\mathbf{x}_1(t)$  is defined. The dimensions of  $\Lambda_1$  are the same for all measurements. The velocity field is then integrated around this contour to compute  $\Gamma_1(t)$ , as follows:

$$\Gamma_1(t) = \oint_{\Lambda_1} \mathbf{v}_{\perp}(t) \cdot d\boldsymbol{\ell} \quad (6.9)$$

where  $d\boldsymbol{\ell}$  is the unit vector tangent to  $\Lambda_1$ . The analogous procedure is realized for  $\Gamma_2$ . The velocity in the contours is interpolated using a 2D cubic scheme from the measurements in the PIV grid points. For  $\Gamma_{Tot}(t)$ , eq. 6.9 is also utilized but over a squared contour defined on the portside of the wake. Here, the PIV velocity field is directly integrated with no interpolation.

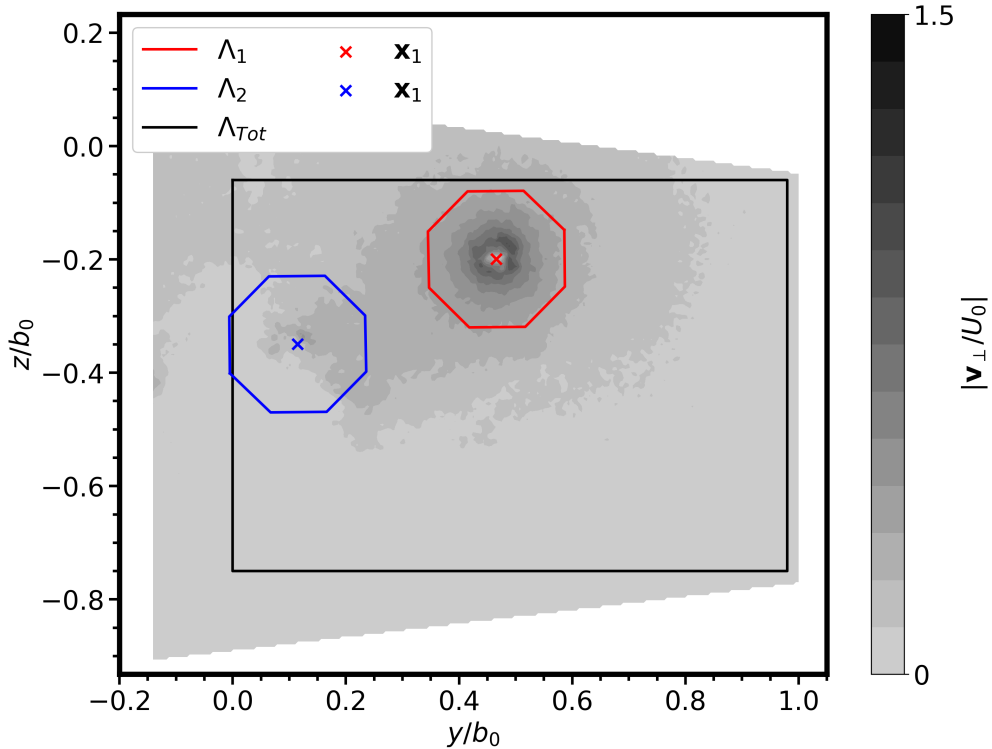


FIGURE 6.10: Contours of integration  $\Lambda_1$ ,  $\Lambda_2$  and  $\Lambda_{Tot}$  superposed to the measured velocity field of the wake generated in the configuration  $C_{126}$  at  $tU_0/b_0 = 11.8$

The evolution of  $\Gamma_1(t)$  and  $\Gamma_2(t)$  thus computed is shown in Fig. 6.11a and that of the resulting ratio of circulations,  $\gamma(t)$ , is shown in Fig. 6.11b. The primary focus is on the downstream stations where both the flap and wingtip vortices coexist. Subsequent measurements and the evolution of total circulation are discussed further down, in section 6.3. Despite the independent measurement of circulation at each time step  $t$ , the values are quite similar from one time step to the next.

On one hand, the normalized circulation magnitude for both the flap and the wingtip vortices decreases with time. On the other hand,  $\gamma(t)$  decreases with time and becomes nearly negligible when  $tU_0/b_0 > 50$ . This is explained by the fact that  $\Gamma_2(t)$  also approaches zero at this approximate time, whereas the magnitude of  $\Gamma_1(t)$  remains significant in the meantime.

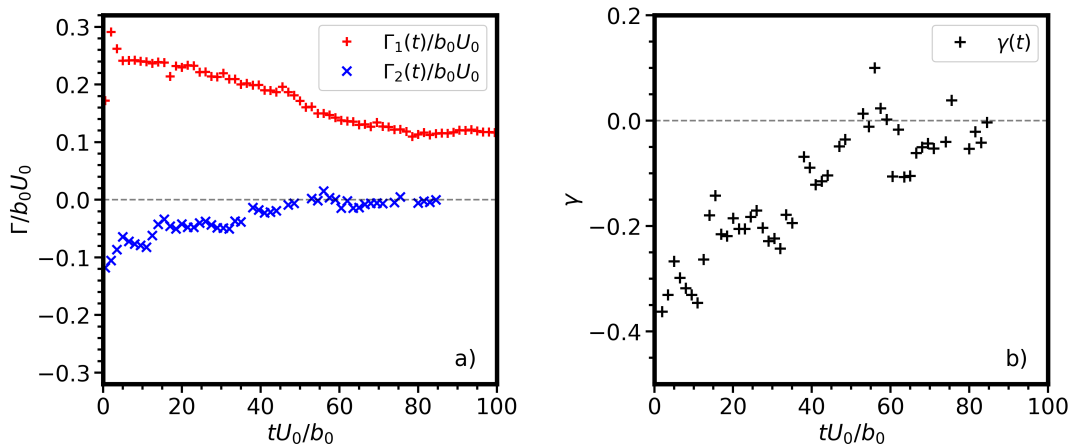


FIGURE 6.11: Estimated characteristics of the counter-rotating vortex pair generated at the configuration  $C_{126}$  (periodic motion) for  $tU_0/b_0 < 100$ . **a)** Evolution of the normalized vortex circulations  $\Gamma_1(t)/U_0b_0$  and  $\Gamma_2(t)/U_0b_0$  and **b)** evolution of the vortex pair circulation ratio  $\gamma(t)$ . The sampled data is decimated by 2 for clarity.

In this context, the decrease in measured circulation magnitude can be attributed to two distinct causes. Firstly, as time progresses, the vortex experiences diffusion, causing a portion of its circulation to exit the integration contour  $\Lambda_i(t)$  (whose size remains constant over time). This results in a reduction of  $|\Gamma_i(t)|$  (measured). Secondly, an additional factor may come into play: if the vorticity undergoes reorientation and is no longer normal to the measurement plane, a portion of the vortex's circulation becomes inaccessible for measurement within  $\Lambda_i(t)$ .

The temporal evolution of  $\gamma(t)$ , as depicted in Fig. 6.11b, demonstrates notable change with time, starting almost immediately after the onset of vortex shedding (at approximately  $t \sim t_0$ ). In cases where the counter-rotating system exhibits a divergent regime, the flap vortices depart from the measurement window shortly after formation (not shown). This constrains the availability of data for the estimation of  $\gamma(t)$ . Consequently, the prompt measurement of  $\gamma(t)$  is key to characterize the counter-rotating system. Because of this, the characteristic circulation ratio,  $\gamma_0$ , is assessed by averaging the circulation measurements taken for  $tU_0/b_0 < 5$ . At later times, the diffusion of flap vortices may have already begun, or flap vortices may have exited the measurement window. Consequently,  $\Gamma_{i,0}$ , a value representing the

initial circulation of the  $i^{th}$  vortex, is defined as :

$$\Gamma_{i,0} = \frac{1}{N_5} \sum_{j=1}^{N_5} \Gamma_i(t_j) \quad (6.10)$$

where  $N_5$  is the number of measurements available for  $tU_0/b_0 < 5$ . It follows that

$$\gamma_0 = \Gamma_{2,0}/\Gamma_{1,0} \quad (6.11)$$

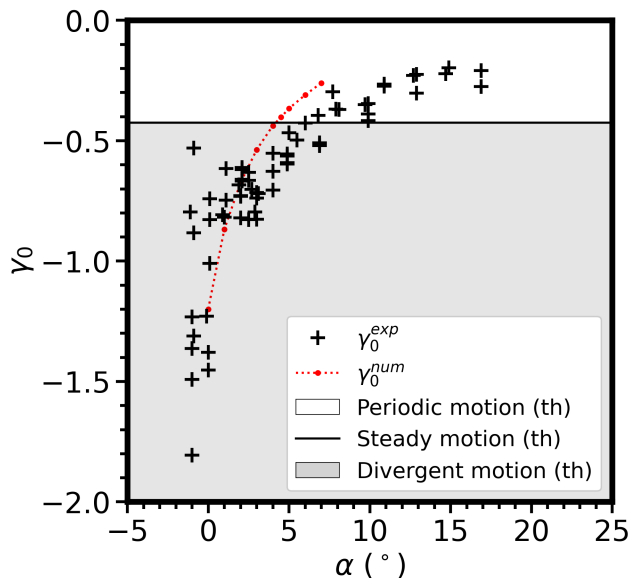


FIGURE 6.12: Characteristic ratio of circulation  $\gamma_0(t)$  as predicted by numerical simulations and as measured through the integral method for the experiments realized with the  $CnR$  wing.

The values obtained for  $\gamma_0$  across the towing configurations tested are now discussed. In this work, three towing velocities were tested  $U_0 \in \{1, 3, 5\} m/s$  for which a range of wing-tip angle of attack  $\alpha \in [-1^\circ, 17^\circ]$  was explored (see appendix A for the complete set of configurations). A large range of  $\alpha$  was chosen since it is expected for  $\gamma_0$  to exhibit strong dependence on  $\alpha$  and little dependence on  $U_0$ . The evolution of  $\gamma_0$  as a function of  $\alpha$  is shown in Fig. 6.12. At low angles of attack, both the flap and wingtip vortices exhibit similar circulation magnitudes, with some experiments even showing  $\gamma_0 < -1$ , signifying that the flap vortex circulation is larger than that of the wingtip vortex at  $tU_0/b_0 < 5$ . As the angle of attack increases,  $\gamma_0$  diminishes in magnitude, indicating that the wingtip vortex becomes dominant. This trend aligns well with results obtained from simulations conducted using the panel method during the wing geometry design phase [64]. Within the range of  $\gamma_0$  values observed, and considering the analytical results discussed earlier (e.g., Fig. 6.1), it is expected that experiments with  $\gamma_0 > -0.425$  display periodic behavior and those with  $\gamma_0 < -0.425$  divergent behavior. Steady motion is anticipated at  $\gamma_0 = -0.425$ . This is shown in the figure with the grey colored region representing that of divergent motion. Therefore, in the following sections, we examine the trajectories of the vortices to characterize the flow regime in each experiment. Furthermore, on the upcoming analysis, the variable  $\gamma_0$  here computed (and also  $\beta_0 = 0.15$ , as discussed earlier) serves to parametrize the point vortex numerical model in order to oppose an analytical prediction of the vortex trajectories to the measurements.

### 6.2.3 Analysis of vortex trajectories in order to identify the system regime

We now aim to characterize the flow regime of the counter-rotating vortex system based on the trajectories of the portside vortices.

#### 6.2.3.1 Periodic motion

The trajectories  $\mathbf{x}_1(t)$  and  $\mathbf{x}_2(t)$ , representing the tip and flap vortices of configuration  $C_{126}$ , are depicted in Fig. 6.13a. These experimental trajectories are juxtaposed with those predicted by the point vortex (*PV*) model, which is described in sec. 6.1. For the flap vortex, both the experiment and the *PV* model show a circular trajectory. However, the *PV* model trajectory extends more downward and outward compared to the experimental results. In the case of the wingtip vortex, the *PV* model predicts a "looping" trajectory, which is not observed in the experiment. This is because the shape of the vortices trajectory is highly dependent on the ratio of circulations  $\gamma(t)$  (this is easily shown by analyzing eqs. 2.75). In particular the loop shape of  $\mathbf{x}_1(t)$  is promoted in cases where  $\Gamma_2(t)$  is comparable to  $\Gamma_1(t)$ . Such behavior is consistent with the simulation, where  $\gamma(t)$  is constant ( $\approx -0.35$  in this case), but it does not align with the experimental data, where  $|\gamma(t)|$  decreases over time.

To better study the difference between the experiment and the model prediction, we recast the results into a reference frame centered around  $\mathbf{x}_{1+2}$ . The *PV* trajectories display circular orbits around  $\mathbf{x}_{1+2}$ , characteristic of a periodic vortex system. The vortex positions  $\mathbf{x}_1(t)$  and  $\mathbf{x}_2(t)$  also exhibit a circular orbit around  $\mathbf{x}_{1+2}(t)$ . In contrast to the *PV* model orbit, it can be seen in Fig. 6.13b that the radius of the orbit of  $\mathbf{x}_1(t)$  and  $\mathbf{x}_2(t)$  decreases over time. This is explained by the fact that the circulation of the vortices in the experiment decreases over time (see Fig. 6.11b). For instance, the center of rotation of the system  $\mathbf{x}_{1+2}(t)$  is located closer to the wing-tip vortex  $\mathbf{x}_1(t)$  when  $\gamma(t) \rightarrow 0$  resulting in a smaller radius of orbit for  $\mathbf{x}_1(t)$ . From these results, it can be inferred that in the configuration  $C_{126}$ , the system of counter-rotating vortex pairs exhibits a periodic regime. To confirm that the vortex system behaves like a periodic system, we compare the velocity at which the pair orbits its center of rotation to that predicted by the periodic model.

Similar to the periodic trajectories observed for the co-rotating system (see eq. 5.2 from Chapter 5), we analyze the period of rotation of the counter-rotating system, denoted as  $t_{orb}$ , given by:

$$t_{orb} = \frac{(2\pi d)^2}{\Gamma_1 + \Gamma_2} = \frac{8b(\pi d)^2}{C_z U_0 S} \quad (6.12)$$

The variables in eq. 6.12 can be seen in the sketch of Fig. 6.2.

$$b(t) = |\mathbf{x}_{1+2}(t) - \mathbf{x}_{3+4}(t)| \quad (6.13)$$

$$d(t) = |\mathbf{x}_1(t) - \mathbf{x}_2(t)| = |\mathbf{x}_3(t) - \mathbf{x}_4(t)| \quad (6.14)$$

It is useful to define a time scale from this period of rotation when analyzing the properties of the vortex pair. Thus, we define the scale  $t_{orb}$  from an estimation of  $b(t)$  and  $d(t)$  at  $t = 0$ . Since at this time the vortices are aligned in the spanwise direction,  $b(0)$  is equal to

$$b(0) = b_0 \frac{1 + \beta_0 \gamma_0}{1 + \gamma_0} \quad (6.15)$$

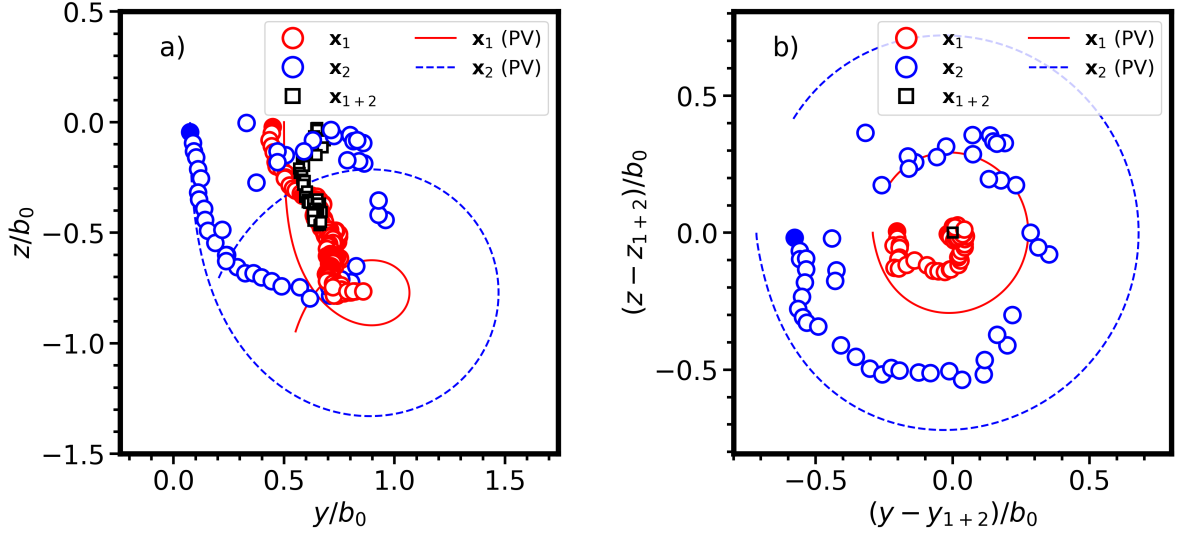


FIGURE 6.13: Periodic motion : Trajectories of the vortices trailing on the portside of the wing towed in the configuration  $C_{126}$ . The data is decimated by 2, for clarity. The trajectories as predicted by a point vortex model (PV) are shown by dashed and solid lines. **a)** Trajectories in the laboratory reference frame and **b)** in a reference frame centered around the barycenter of vorticity of the pair  $x_{1+2}(t)$

Furthermore one can estimate  $d(0) \approx d_0$  which is the geometrical distance between the flap and wing tips. On the following analysis,  $t_{orb}$  is the time scale computed with  $d(0)$  and with  $b(0)$  unless specified.

The evolution of the distance  $d(t)$  and of the angle  $\phi_i(t)$  between vortex  $i$  and  $x_{1+2}(t)$  is visualized in Fig. 6.14a and b, respectively. In these figures, time is scaled separately by  $t_{orb}$  and by  $b_0/U_0$ . The distance measured between the vortices is compared to that predicted by the PV model in Fig. 6.14a.  $d^{PV}(t)$  fluctuates around a constant mean value which is  $\approx d_0$ . This is in line with the fact that in the PV model the vortex circulations are constant. However, the distance measured in the experiments,  $d^{exp}(t)$ , seems to decrease around  $t/t_{orb} = 0.2$ . The angle  $\phi$  in this system of vortices can be inferred from  $t_{orb}$  following :

$$\phi = 2\pi \frac{t}{t_{orb}} + \pi \quad (6.16)$$

$\phi(t)$  is thus plotted in Fig. 6.14b for  $t_{orb}(t) = t_{orb}(d^{exp}(t))$  and for  $t_{orb}(t) = t_{orb}(d^{PV}(t))$ . The time evolution of the angle  $\phi^{PV}$ , shown by a dashed line in Fig. 6.14b, is quasi-linear. This means that in the model the velocity at which the vortices orbit each other ( $\dot{\phi}$ ) is approximately constant with time. For  $t/t_{orb} < 0.2$ , it can be seen that the angles  $\phi_1 \sim \phi_2 \sim \phi^{PV}$ . Thus the measured velocity of the orbit movement of the vortices is in good agreement with the PV model. However, for  $t/t_{orb} \geq 0.2$ , both  $\dot{\phi}_1(t)$  and  $\dot{\phi}_2(t)$  exceed  $2\pi/t_{orb}(d^{PV})$ , indicating an increase in the rotational velocity of the vortices about each other. One can derive from eq. 6.12 that an increase in rotational velocity (i.e. a reduction of the period of rotation  $t_{orb}$ ) could be caused by a decrease of vortex distance  $d$  or by a decrease in the total circulation of the system. We observe in Fig. 6.14b that the evolution of  $\phi_1(t)$  and of  $\phi_2(t)$  correlates well with the one obtained by accounting only for the evolution of the vortex distance  $d^{exp}(t)$  (which is represented by the solid line). This indicates that the increase in rotational velocity is mostly due to the decrease of distance between the vortices  $d^{exp}(t)$ .

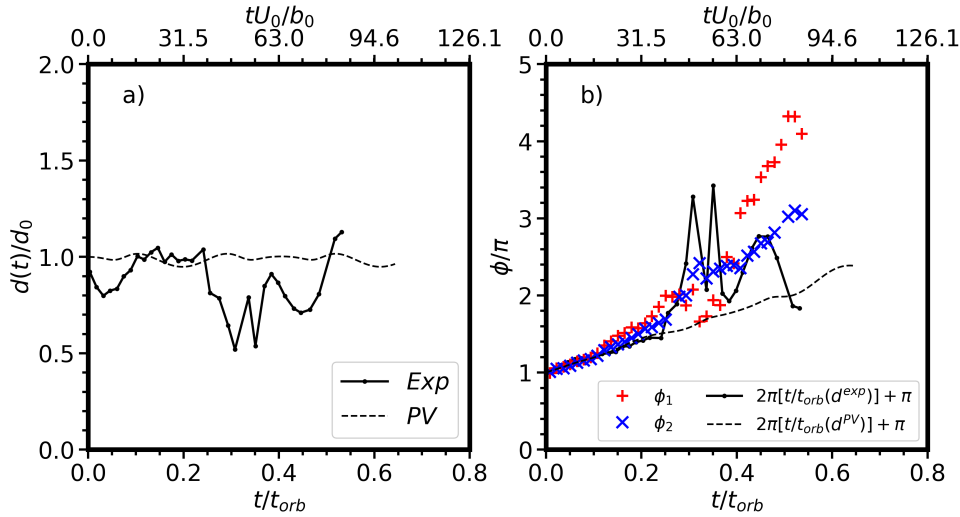


FIGURE 6.14: Evolution of properties of the vortices trajectories as predicted by a point vortex model and as observed experimentally for configuration  $C_{126}$  (periodic motion). Time is scaled by the period of rotation  $1/t_{orb}(d_0)$  and by  $b_0/U_0$ . The data is decimated by a factor 4, for clarity. **a) b)** the angle  $\phi_i(t)$  between vortex  $i$  and  $\mathbf{x}_{1+2}(t)$

These results confirm that the vortex system can be approximated by the periodic model. Additionally, the results presented in Fig. 6.14 provide an estimate of the point at which the real flow deviates from the model prediction (in which vortex circulation is constant), as  $\phi_i(t)$  becomes greater than  $2\pi/t_{orb}$  at around  $t = 0.2t_{orb}$ .

### 6.2.3.2 Divergent motion

Consider the iso-surfaces of vorticity shown in Fig. 6.15, which illustrate a case of divergent motion obtained at configuration  $C_{118} = (CnR, U_0 = 3 \text{ m/s}, \alpha = -1^\circ)$ . On the side-view, in Fig. 6.15a, it can be seen that the portside flap vorticity (in blue) ascends and exits the measurement plane soon after formation while the wing tip vortex (in red) descends.

This behavior can be analyzed with more precision on the vortex trajectories, which are shown for this case in Fig. 6.16a. The flap and wing tip vortices exit the window around  $tU_0/b_0 \sim 30$  and  $t_{max}U_0/b_0 \sim 350$ , respectively. The measured trajectories align with the point-vortex predictions, as expected. In all experiments showing divergent motion, the wing tip vortex consistently moves downward upon formation. In most instances, like the one shown in Figs. 6.16 and 6.15, the flap vortex ascends and exits the upper measurement window relatively quickly.

However, in certain cases with a divergent trajectory, a different behavior is observed. When the circulation ratio  $\gamma_0$  approximates  $\gamma_s$ , (which indicates the critical value at which the regime is steady), the flap vortex may descend but at a slower rate than the wing tip vortex. In a reference frame centered around  $\mathbf{x}_{1+2}(t)$ ,  $\mathbf{x}_1(t)$  and  $\mathbf{x}_2(t)$  invariably move in opposite directions.

Consider now the evolution of normalized circulation, shown for this experiment in Fig. 6.16b. The magnitude of the circulation of both vortices decreases slowly up until  $t \frac{U_0}{b_0} \sim 20$ . Beyond this time, the flap vortex circulation seems to decrease abruptly, but this is due to the vortex exiting from the measurement plane. At  $t \frac{U_0}{b_0} \sim 30$ , the flap vortex has exited completely from the measurement plane. The circulation

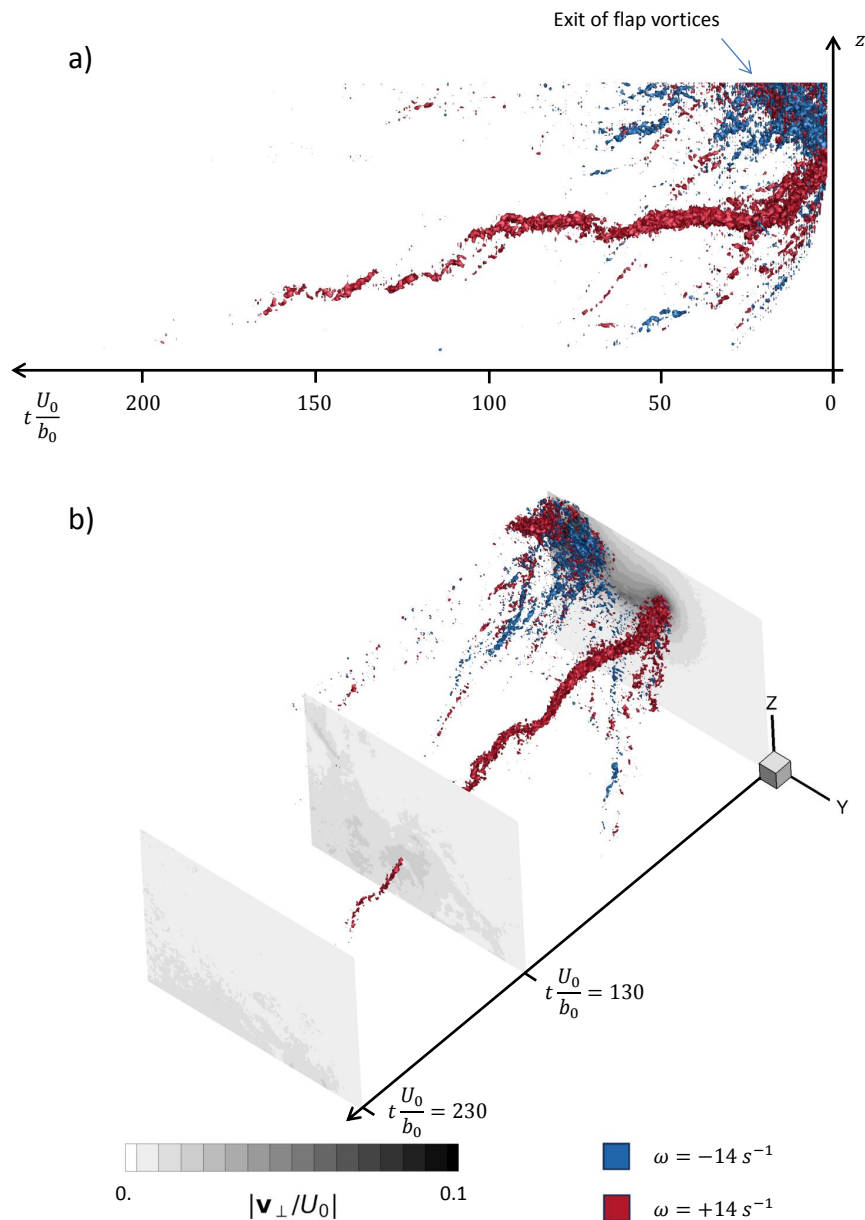


FIGURE 6.15: Divergent motion : Axial vorticity iso-surfaces  $\omega_x = \pm 14 \text{ s}^{-1}$  for the wake generated at configuration  $C_{118}$ . **a)** Side-view and **b)** isometric view. The field of velocity modulus in the Trefftz plane is shown at three instances :  $tU_0/b_0 = 0$ ,  $tU_0/b_0 = 130$  and  $tU_0/b_0 = 230$ .

of the wing-tip vortex decreases with time. Contrary to what is observed for the flap vortex, the circulation decrease of the wing-tip vortex is not related to it exiting the measurement plane for  $t \frac{U_0}{b_0} < 200$ . Indeed, it can be seen in Fig. 6.15a that the vorticity magnitude of the wing tip vortex diminishes during its descent, crossing below the threshold  $\omega_x < +15 \text{ s}^{-1}$  around  $t \frac{U_0}{b_0} \sim 150$ . On the isometric view in Fig. 6.15b, one can see that at  $t \frac{U_0}{b_0} = 130$  the structure of the vortex is less coherent than upon formation, which is consistent with the observation that some of its circulation has been lost. At  $t \frac{U_0}{b_0} = 350$ , the wing tip vortex has exited the measurement plane

completely.

The loss of circulation by the wing tip vortex is intriguing and may be due to a particular interaction with the counter-rotating vortex from the flap. Unfortunately, it is challenging to establish any link between the vortices in the flow because of the swift departure of the flap vortex from the measurement plane.

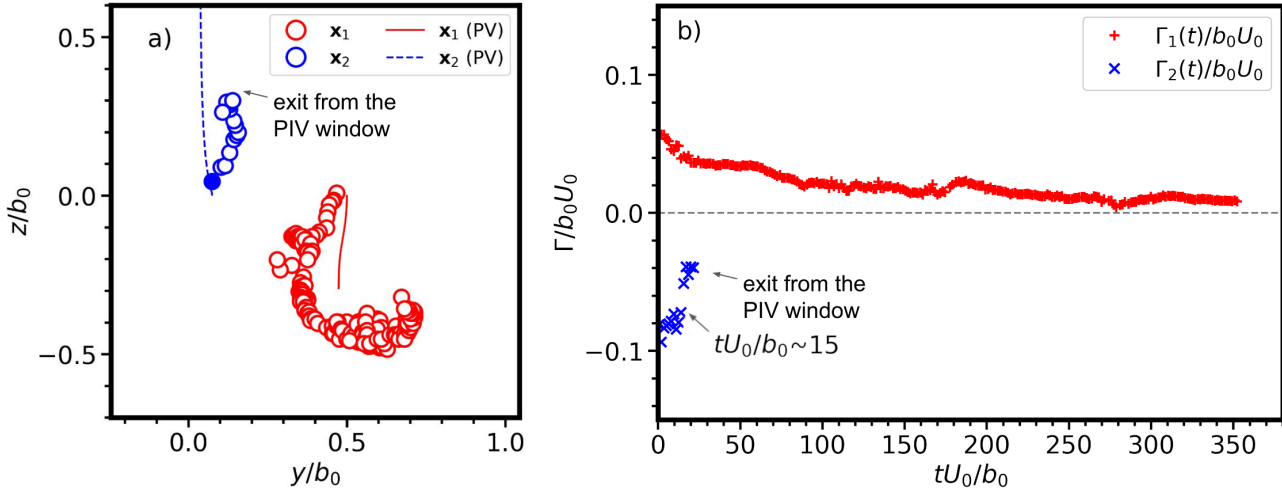


FIGURE 6.16: Divergent motion : Characteristics measured on the portside vortices generated in the configuration  $C_{118} = (CnR, U_0 = 3 \text{ m/s}, \alpha = -1^\circ)$  : **a)** Trajectories measured and predicted by a point vortex model (PV), in the laboratory reference frame. **b)** Time evolution of the normalized circulation. The data is decimated by 2, for clarity

### 6.2.3.3 Steady motion

Experiments that display steady motion are now analyzed. The trajectories of vortices in a steady regime are shown in Fig. 6.17. The condition to achieve steady motion is defined in Chapter 2.3.1.2. In particular, equation 2.77 expresses that steady motion results from the balance between the motion that the four vortices in the wake induce on each other, so that only the wake descent motion remains. In order to identify a steady motion regime in the experiments, we simplify this condition to one where  $x_{1+2}(t)$ ,  $x_1(t)$  and  $x_2(t)$  display a similar descent velocity, resulting in a somewhat vertical and straight trajectory of the vortices of the system, i.e., at any instant  $t$  at which both the flap and wing tip vortices are present in the measurement window :

$$z_1(t) \sim z_2(t) \sim z_{1+2}(t) \quad (6.17)$$

This behavior is exemplified by vortices generated in the configuration  $(CnR, U_0 = 3 \text{ m/s}, \alpha = 4^\circ)$ , as shown in Figs. 6.17 and 6.18. In Fig. 6.17a, the vortices trajectories are shown and compared to that predicted by the *PV* model. In Fig. 6.17b the focus is put on the vertical coordinates.

In Fig. 6.18, 3D iso-contours of velocity modulus for this same configuration (reconstructed from the PIV measurements) are displayed. The measurement window contains both flap-tip vortices but only the portside wing-tip vortex.

It is important to note that in our observations of the vortex trajectories for the present database, we did not witness perfectly straight motion in any experiment. Achieving fully steady motion (i.e. verifying condition 2.77) during an experiment is

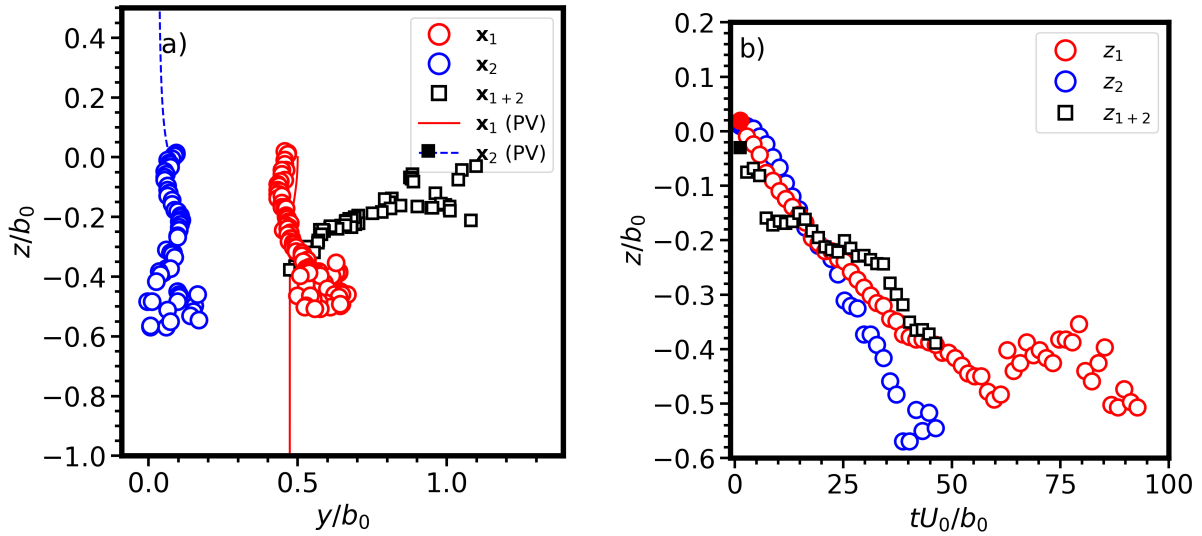


FIGURE 6.17: Steady motion : Evolution of coordinates of the port-side vortices generated in the configuration  $(CnR, U_0 = 3 \text{ m/s}, \alpha = 4^\circ)$ . **a)**  $\mathbf{x}_{1+2}(t)$ ,  $\mathbf{x}_1(t)$  and  $\mathbf{x}_2(t)$  in the laboratory reference frame and **b)** evolution of  $z_{1+2}(t)$ ,  $z_1(t)$  and  $z_2(t)$  as a function of normalized time. The data is decimated by 2, for clarity

challenging due to the evolving characteristics of the vortices with time. However, the behavior of the vortices in some configurations where  $\alpha \sim 4^\circ$ , seem to indicate that condition 6.17 is indeed verified in the early stages of the experiment.

Take for instance the flow of configuration  $C_{143} = (CnR, U_0 = 3 \text{ m/s}, \alpha = 4^\circ)$  shown in Figs. 6.17 and 6.18. The trajectory of  $\mathbf{x}_1(\mathbf{t})$  and of  $\mathbf{x}_2(\mathbf{t})$  is somewhat straight from  $z_i/b_0(t) = 0$  to  $z_i/b_0(t) \sim -0.3$  (see Fig. 6.17a). During the same time, the trajectory of the vorticity barycenter  $\mathbf{x}_{1+2}(\mathbf{t})$  goes from a far span-wise location to blending with  $\mathbf{x}_1(\mathbf{t})$ . This indicates that vortex 2 undergoes diffusion, since most of the vorticity integrated in the contour used to compute  $\mathbf{x}_{1+2}(\mathbf{t})$  is now located around vortex 1. A similar conclusion can be reached from analyzing the iso-contours in Fig. 6.18. The intensity of the flap-tip vortices rapidly diminishes after formation, with velocities dropping below the threshold  $|\mathbf{v}_\perp| \leq 0.235 \text{ m/s}$  soon after. A similar phenomenon occurs for the wing tip vortex, albeit at a later time. This decline in flow velocity translates into a decline of the measured circulation of the vortices. This is explored further in section 6.3.

When analyzing the vertical component of the trajectories (shown in Fig. 6.17b), it is seen that the vortices descend at a similar rate until  $tU_0/b_0 \sim 25$ , after which the wing-tip vortex descends at a slower rate than the flap vortex. This behavior suggests that the conditions for steady motion were reunited during the early stages of the experiment, until  $tU_0/b_0 \sim 25$ . This is further supported by the shape of the iso-contours of velocity, which exhibit a nearly straight profile (see Fig. 6.18). Interestingly, in the case of configuration  $C_{143}$ , where  $\gamma_0 < \gamma_s$ , the point vortex model predicts divergent motion (as seen in Fig. 6.17a). This is discussed in the paragraphs below.

The evolution of  $\Gamma_2(t)$  and  $\Gamma_1(t)$  in this steady case is shown in Fig. 6.19a. The circulation magnitude of both vortices decreases with time, resulting in a complete

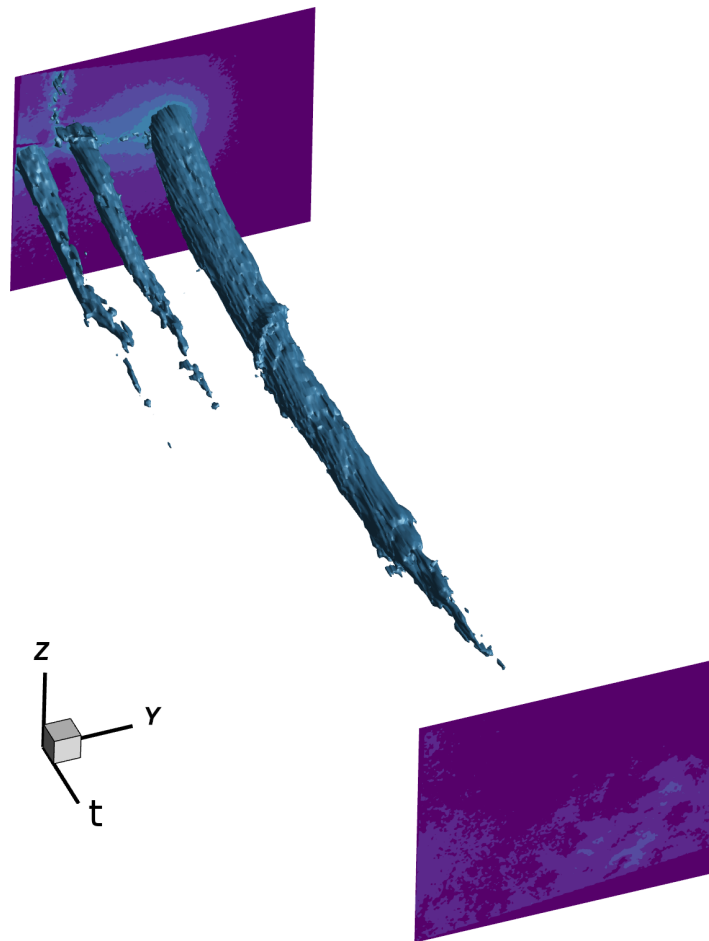


FIGURE 6.18: Steady motion : Iso-contours of velocity modulus,  $|\mathbf{v}_\perp| = 0.235 \text{ m/s}$ , measured on the wake generated under configuration  $C_{143} = (CnR, U_0 = 3 \text{ m/s}, \alpha = 4^\circ)$

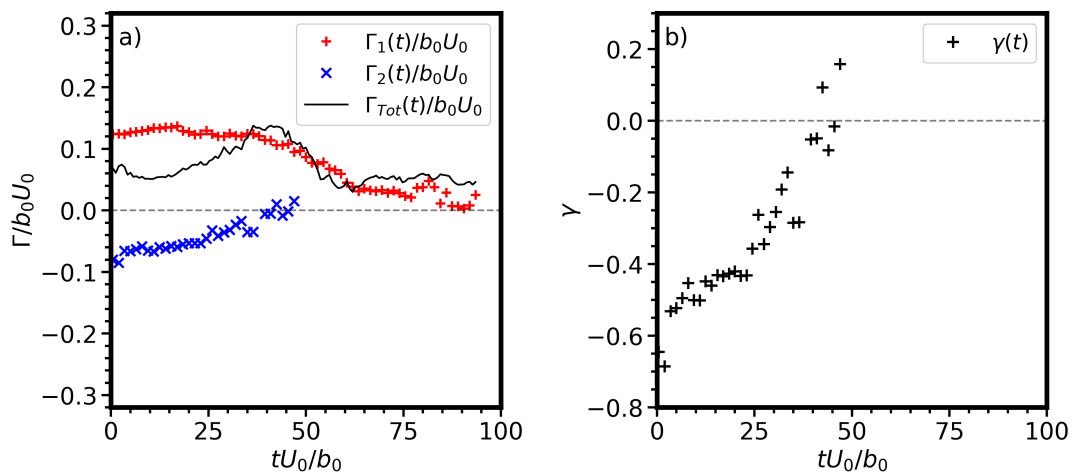


FIGURE 6.19: Steady motion : Estimated characteristics of the counter-rotating vortex pair generated at the configuration  $C_{143}$ . **a)** Evolution of the normalized vortex circulations  $\Gamma_1(t)/U_0b_0$ ,  $\Gamma_2(t)/U_0b_0$  and  $\Gamma_{Tot}(t)/U_0b_0$  and **b)** evolution of the vortex pair circulation ratio  $\gamma(t)$ . The sampled data is decimated by 2 for clarity.

diffusion of the flap vortex and a partial diffusion for the wing tip vortex. The evolution of total circulation is coherent with that of  $\Gamma_2(t)$  and  $\Gamma_1(t)$ . For instance  $\Gamma_{Tot} \sim \Gamma_1$  when  $\Gamma_2 \sim 0$ , which occurs around  $tU_0/b_0 = 50$ . Furthermore, the  $\Gamma_1(t)$  appears to remain mostly constant for  $tU_0/b_0 \sim 50$ , time at which the flap vortex seems to diffuse completely. For  $tU_0/b_0 > 50$  the wing-tip vortex circulation  $\Gamma_1(t)$  starts to decrease with time, this is in part due to the diffusion it endures, but also to its exit from the measurement window, which starts soon after  $tU_0/b_0 = 50$ .

It can be seen in Fig. 6.19b that the ratio of circulation  $\gamma(t)$  decreases quickly with time. This is consistent with the observation that the conditions for steady motion may be reunited at the initial stages of the wake evolution, but may be lost further downstream.

#### 6.2.3.4 Analysis of the three regimes

After analyzing the trajectories across all the experiments of this study,  $\gamma_0$  is plotted as a function of  $\alpha$  in Fig. 6.20a and as a function of  $\beta$  in Fig. 6.20b.  $\gamma_0$  is color-coded according to the observed flow regime (divergent, steady or periodic). We note that the flow regime changes from divergent to periodic motion at approximately  $\alpha_s \geq 4^\circ$ . Also, some experiments where  $\alpha_s \approx 4^\circ$  exhibit steady motion. Experimental and analytical limits between the periodic and the divergent regime, denoted as  $\gamma_s^{exp}$  and  $\gamma_s^{th}$ , are shown with a dotted and with a solid line, respectively.  $\gamma_s^{exp}$  is smaller than  $\gamma_s^{th}$ , which can be attributed to three main factors : Firstly,  $\gamma_s^{th}$  is a function of  $\beta_0$ . Thus our approximation of  $\beta_0 = 0.15$  may be improved with a more accurate estimation based on the measured vortex positions. Secondly, the limitations of the integral method used to assess vortex circulation can affect accuracy when the vortices circulation exits the integration contours as a consequence of diffusion. This is specially true when vortices approach the measurement window borders, which occurs in some configurations where the measurement window is adjusted to maximize the observations in downstream stations. Thirdly, one could question the validity of the hypothesis made to obtain  $\gamma_s^{th}$ , which assumes that, in this experiment, vortices behave like line vortices, i.e. the vortex radius is small with respect to the distances  $b_1$  and  $b_2$ .

With this extensive analysis, the behavior of the counter-rotating vortex pair is effectively characterized across various towing configurations. The observations align well with simple models, such as those using point vortices with constant circulation. However, it is clear that vortices undergo diffusion causing the measured circulation to diminish with time. Moreover, it's consistently observed that the diffusion of the flap vortex is promoted in the periodic and steady motion scenarii, whereas the wing tip vortex persists further downstream. Consequently, in the following section, we delve into the evolution of  $\Gamma_1(t)$  and  $\Gamma_2(t)$  to identify the underlying physical mechanisms responsible for the observed reduction in measured circulation within the experiments.

### 6.3 The effect of flap vortex diffusion on the evolution of the vortex system

In this section, we analyze the evolution of the counter-rotating vortex wake at large downstream stations. We quantify the decay of vortex strength, based on the hypothesis that it is related to the interaction between wing-tip and flap-tip vortices.

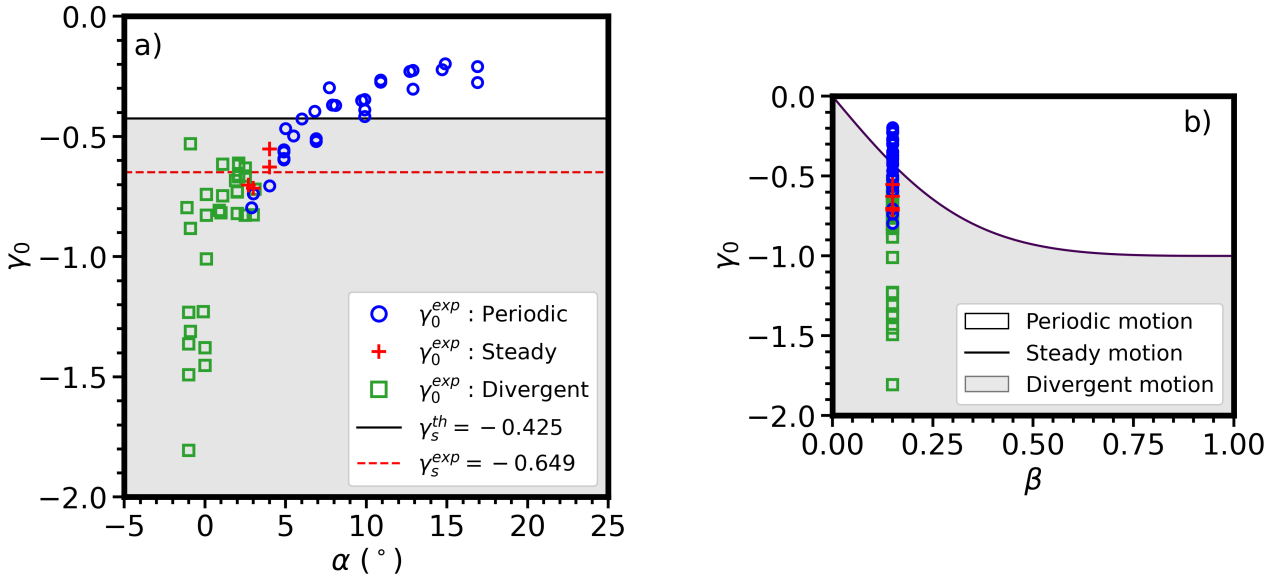


FIGURE 6.20: Ratio of circulations measured with the integral method (refer to sec. 6.2.2 for details) **a)** as a function of angle of attack and **b)** as a function of separation ratio  $\beta$ , for the counter-rotating vortices at  $tU_0/b_0 = 2 \pm 0.5$ .

The time evolution of the wake for configuration  $C_{126}$  is examined. A top-view of the iso-vorticity surfaces of the wake is shown in Fig. 6.21. Also, the evolution of  $\Gamma_1(t)$  and  $\Gamma_2(t)$  is shown in Fig. 6.22. Time is scaled using both  $b_0/U_0$  and  $t_{orb}$ . The wingtip vortex remains within the measurement window until approximately  $t_{max}U_0/b_0 \sim 390$  or 2.5 times  $t_{orb}$ .

### 6.3.1 $t < t_\Delta$ : Analysis of the diffusion of the flap vortex through viscous cancellation

The flow is analyzed for  $tU_0/b_0 < 100$ , which is a good estimation of the time span in which both the flap and wing-tip vortices are detected in the measurement window. As previously observed, vorticity levels in the wake decay shortly after formation. This is seen in the vorticity measurements of Fig. 6.21b. A quantitative evaluation is obtained from  $\Gamma_1(t)$  and  $\Gamma_2(t)$  which experience an initial drop in magnitude that extends until  $tU_0/b_0 \sim 100$  (see Fig. 6.22). At  $tU_0/b_0 \sim 100$ , the measured circulation of the flap vortex has diminished practically to zero, while that of the wing tip vortex retains significant magnitude. However, total circulation  $\Gamma_{Tot}(t)$  remains constant over this time span (with the exception of  $tU_0/b_0 < 10$ , for which the contour  $\Lambda_{Tot}$  does not contain both vortices). These observations suggest that counter-signed vorticity is undergoing a viscous cancellation effect along the interface between the two vortices.

At  $tU_0/b_0 = 100$ , only the wing tip vortex is detected in the flow, however,  $\Gamma_{Tot} > \Gamma_1$ . This suggests that the contour of integration  $\Lambda_1$  (see Fig. 6.10) is not large enough to contain all of the vorticity in the wake at this point in time. However, the dimensions of the contours  $\Lambda_1$  and  $\Lambda_2$  are constrained by the fact that vortices often locate close to the window borders, which is why we could not enlarge these contours in order to improve the procedure. Nevertheless, as shown above, these results are sufficient to characterize the viscous cancellation occurring for  $tU_0/b_0 = 100$ .

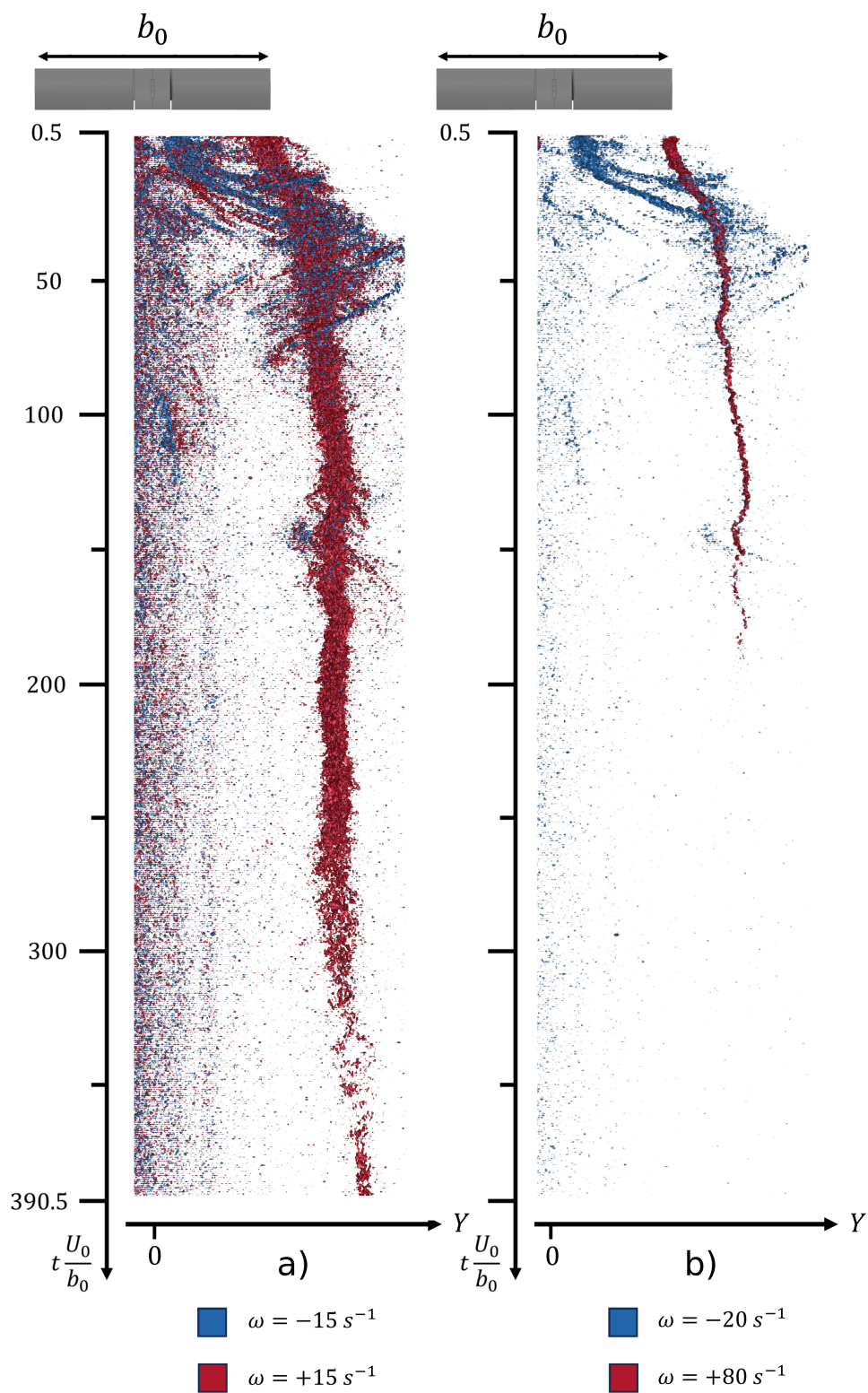


FIGURE 6.21: Axial vorticity iso-surfaces (top-view), reconstructed from the PIV measurements, for the wake generated at configuration  $C_{126}$ . **a)** Iso-surfaces  $\omega = \pm 15 \text{ s}^{-1}$  and **b)**  $\omega = -20$  and  $+80 \text{ s}^{-1}$ .

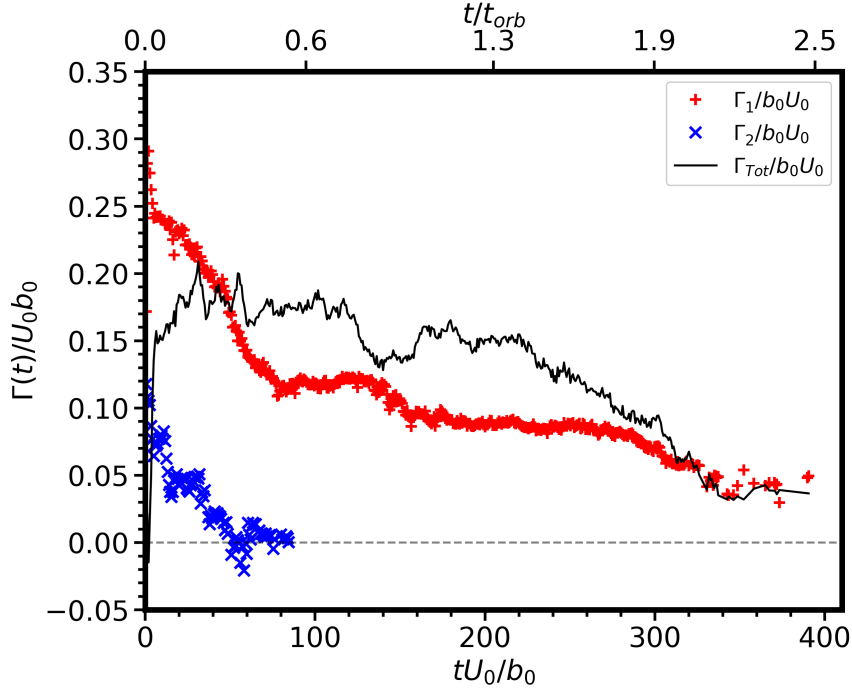


FIGURE 6.22: Evolution of normalized circulation for the flap and wingtip vortices generated at configuration  $C_{126}$ .

### 6.3.2 $t > t_{\Delta}$ : Analysis of the wing-tip vortex after the complete diffusion of the flap vortex

In this section, we explore the causes contributing to the observed decay in measured circulation beyond  $tU_0/b_0 > 100$ . Two distinct events of circulation loss are identified, as depicted in Fig. 6.22: First, a sudden loss of circulation is observed during the time span of  $100 < tU_0/b_0 < 200$  in both  $\Gamma_{Tot}(t)$  and  $\Gamma_1(t)$ . This first event appears to be localized within approximately  $tU_0/b_0 \in [120, 160]$ , as the total circulation magnitude remains stable outside of this temporal frame. A second loss of circulation is noticed, commencing (in  $\Gamma_{Tot}(t)$ ) at around  $tU_0/b_0 \sim 240$  and continuing until  $t_{max}$ . This second phase of circulation loss is primarily associated with the wing-tip vortex leaving the measurement window and therefore it is less relevant for our analysis.

The flow evolution within  $tU_0/b_0 \in [100, 200]$  is examined based on the iso-vorticity surfaces presented in Fig. 6.21b. At  $tU_0/b_0 = 100$ , there are no discernible structures of negative vorticity (below  $-20s^{-1}$ ) in proximity to the wing-tip vortex. However, around  $tU_0/b_0 \sim 150$ , a substantial structure with  $\omega < -20s^{-1}$  emerges, orbiting the wing-tip vortex. The structure of the wing-tip vortex deviates from a straight shape as a result from the presence of this negative vorticity spot. Additionally, during this period, the vorticity levels of the tip-vortex drop below the threshold of  $+80 s^{-1}$ . Notably, the abrupt decay in circulation within the flow (seen in Fig. 6.22) corresponds to the appearance of this negative vorticity spot at  $tU_0/b_0 \sim 150$ .

The loss of measured circulation is observed in both  $\Gamma_1(t)$  and  $\Gamma_{Tot}(t)$ , contrary to the behavior observed for  $tU_0/b_0 < 100$ , where only  $\Gamma_1(t)$  experiences a reduction, while  $\Gamma_{Tot}(t)$  remains constant. This suggests that during this short time interval, the wing-tip vortex experiences substantial diffusion, leading to the dissipation of a portion of its circulation outside of the contour  $\Lambda_{Tot}$ . Another plausible cause for the decline in measured circulation could be the tilting of the vortices, causing their

axes to deviate from a perpendicular orientation to the PIV plane. This hypothesis aligns with the abrupt emergence of the negative vorticity spot at  $tU_0/b_0 \sim 150$ , suggesting that this vorticity spot was not initially aligned with the plane. Consequently, the negative vorticity spot may simply be the remnants of the flap vortex, which, aside from viscous cancellation, also tilted out of the measurement window around  $tU_0/b_0 \sim 100$ , and is reorienting into the plane at  $tU_0/b_0 \sim 150$ , subsequently resuming viscous cancellation as well. However, this interpretation remains unverified due to limitations in the available dataset.

Finally, it is worth mentioning that this decay of circulation in the wing tip vortex also leads to the stagnation of the vortex in the vertical plane, and to the outwards position of the vortex, as seen in the figure.

The decrease in vorticity magnitude within the wake is characterized here based on the circulation data. We define  $t_\Delta$  as the time at which the measured circulation of the flap vortex reaches zero. This parameter serves as an indicator of the duration during which viscous cancellation is likely to occur. The evolution of normalized  $t_\Delta U_0/b_0$  as a function of the ratio  $\gamma_0$  is plotted in Fig. 6.23a. A general trend is observed where the diffusion of the flap vortex occurs earlier at lower  $|\gamma_0|$ . This behavior is expected, since at low  $|\gamma_0|$ , the velocity field induced by the wing-tip vortex significantly exceeds that of the flap vortex. We further introduce the ratio  $\Delta_\Gamma$  to quantify the average loss in circulation within the wingtip vortex following the diffusion of the flap vortex :

$$\Delta_\Gamma = \frac{1}{t_{max} - t_\Delta} \int_{t_\Delta}^{t_{max}} \frac{\Gamma_1(t)}{\Gamma_{1,0}} dt \quad (6.18)$$

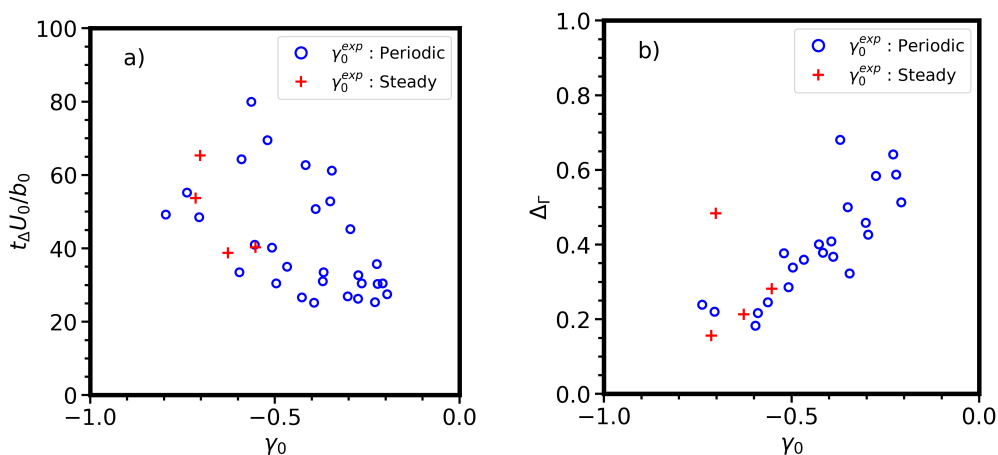


FIGURE 6.23: Characteristics of the diffusion occurring in the counter-rotating pair of vortices as a function of the initial ratio of circulation  $\gamma_0$ . **a)**  $t_\Delta$  and **b)** Ratio  $\Delta_\Gamma$ . Experiments where the flow regime is periodic and steady are shown. Data is plotted as a function of lift coefficient  $C_z$ .

The evolution of  $\Delta_\Gamma$  as a function of  $\gamma_0$  is provided in Fig. 6.23b. Cases in which the wingtip vortex exits the measurement window shortly after  $t_\Delta$  have been excluded from this analysis due to limited data availability for assessing the circulation of the wing-tip vortex. Significant reductions in the circulation of the wing-tip vortex are observed, ranging from  $\Delta_\Gamma \sim 0.7$  to approximately  $\sim 0.2$ .

This reduction demonstrates a proportional relationship with  $\gamma_0$ . This implies that, in the experiments, viscous cancellation is the primary mechanism driving the diffusion of the wingtip vortex. It is noteworthy that these reductions occur while preserving an aerodynamic lift coefficient comparable to that of a planar wing configuration. When  $\Delta_\Gamma \sim 0.7$ , the lift coefficient  $C_z$  approximates 1.1, and for  $\Delta_\Gamma \sim 0.2$ , the  $C_z$  ranges between approximately 0.3 and 0.5. This outcome aligns with expectations, as both  $\gamma_0$  and the lift coefficient increase with the wing's angle of attack in this specific  $\alpha$  range.

## 6.4 Intermediate conclusion

In this chapter, we analyze the wake generated by the *CnR* wing configuration, characterized by the presence of counter-rotating vortex pairs on each side of the wake. Vortices in this flow exhibit time-dependent intensity which can be challenging to characterize when it is overcome by surrounding vorticity and measurement noise, or when it is located at the borders of the measurement window (as it is often the case in these experiments). We apply methodologies tailored to these unique challenges in order to identify the vortices and assess their main characteristics. Our characterization of each vortex proves robust, even in cases where the flap vortex diffuses during the course of an experiment. Periodic, divergent, and steady trajectories were observed across the tested towing configurations. Upon formation, the measured ratio of circulation between the flap and wing-tip vortices is in good agreement with numerical predictions. Notably, the characteristic circulation ratio,  $\gamma_s$ , at which steady motion occurs is found to be close to, yet slightly smaller, than what is predicted by analytical arguments.

In cases featuring periodic, divergent, and steady motion, the motion of the vortices within this flow aligns remarkably well with simple models like point vortex simulations. Discrepancies between experimental data and the model arise primarily due to the rapid decrease in circulation magnitude observed experimentally, often leading to the complete diffusion of the flap vortex.

Both vortices in a pair experience a similar decrease in circulation magnitude over comparable time-frames while the total circulation measured in the flow remains constant. This indicates that viscous cancellation is the mechanism responsible for this diffusion. Following this phenomenon, the wake is left with only the wing-tip vortices for which the circulation has been significantly reduced compared to its magnitude upon formation. This reduction of the vorticity intensity in the wake is achieved while maintaining lift coefficients comparable to that of the plain wing configuration.



## Chapter 7

# General conclusion and perspectives

### 7.1 Conclusion

In this work we realize an experimental study of the impact of the lift span-wise distribution on the dynamics of a wing's vortex wake. The reference geometry (*Ref*) is rectangular with no twist and a NACA 4412 airfoil. Variations about this wing model are designed from a different span-wise evolution of geometrical twist with respect to four main subjects of study :

1. The physics of vortices trailing from a baseline configuration.
2. The impact of a trailing edge undulation on the properties of the trailing vortices.
3. The impact of flaps-down wing configurations, including a high-lift wing configuration, on the generated co-rotating vortex system.
4. The impact of the introduction of counter-rotating vortices in the wake of the wing.

These experiments are performed in a towing tank facility and the vortex wake is investigated through stereoscopic particle image velocimetry. The span based Reynolds number is  $Re_{b_0} \approx 10^5$  and the circulation based Reynolds number is  $10^4 < Re_{\Gamma} < 10^5$ . For the reference wing, our experimental configuration has a maximum Strouhal number of  $f_{PIV} b_0 / U_0$  on the order of 4, and a maximum time of observation on the order of 2 times the time scale of the dipole mutual induction which is  $t_b = 2\pi b^2 / \Gamma$ . The experiments in this work are designed to characterize the wingtip vortices for each load profile under a wide range of towing velocities ( $[1, 5]m/s$ ) and angles of attack ( $[-3^\circ, 20^\circ]$ ). The vortex flow is measured in a reference frame descending with the barycenter of vorticity. In this way, we inspect the properties of the vortices from vortex formation to a maximum of 300 wingspans downstream.

With respect to subject **1.**, the main results are : Vortex properties are tracked as a function of time, and it is confirmed that the vortex radius follows the growth predicted by viscous theory. Additionally, a decrease in circulation is observed. We attribute this to tank boundary effects and, to a lesser degree, to measurement inaccuracies. Measurements  $\Gamma(t)$  suggest that the rate of change of circulation is larger with a larger circulation magnitude. Also the velocity distribution of the vortices seems to not be fully irrotational at large radial distances in the order of  $r \sim 10R_d$ . Both of these observations align with the hypothesis of a circulation decay driven by wall effects. Vortex trajectories are analyzed, revealing periodic components that

suggest the development of countergrade Kelvin waves with a high axial wavenumber. However, the consistency of this phenomenon across experiments is variable, and the precise conditions for its occurrence remain unknown. In experiments exhibiting non-periodic motion, Proper Orthogonal Decomposition (POD) is applied revealing that the most energetic vorticity modes exhibit a structure resembling an overlap of dipoles, potentially explaining the erratic, non-periodic displacement of the vortex centroid.

The development of wake-type axial flow downstream, represented as  $v_x(t)$ , exposes two opposing mechanisms. Initially, an increase in the magnitude of axial flow as a function of time is noted, likely linked to the evolution of azimuthal velocity through cyclostrophic equilibrium. Subsequently, axial flow reduction is observed as it approaches the magnitude of azimuthal velocity, attributed to stabilizing effects within the vortex core. When the swirl parameter ( $q$ ) approaches approximately 1.5, perturbations induced by strong  $v_x(t)$  are transported away from the vortex centroid and dispersed, causing a decline in  $v_x(t)$ . However,  $q$  approximates 1.5 mainly at large downstream stations. Hence, most configurations necessitate measurements at greater downstream locations to offer deeper insights into the evolution of  $v_x(t)$  under such conditions. Further investigation should focus on the impact of these events on other properties like radius and circulation and also their correlation with vortex stability.

The analysis of vortex trajectories and properties does not reveal the development of the Crow instability before the vortices exit the measurement window, which occurs at  $t = 2t_b$ .

With respect to subject 2., Experiments were conducted using wings featuring undulating trailing edges with equal wavelengths but varying amplitudes. All wings maintained equivalent aerodynamic characteristics, exhibiting consistent  $C_z$  values. The design of our wing model was based on a numerical solution obtained through a parabolized stability analysis of the wing wake.

The principal discovery of this study is that as the undulation amplitude increases, the vortex core becomes more diffused, yet the circulation of the vortex remains unaltered. While the diffusion of the core results in a reduction of the maximum induced rolling moment of the vortex, the scale of this reduction is not substantial for applications related to hazard alleviation.

Notably, our experimental results did not replicate the characteristics of the wake seen in the numerical solution. However, our experiments were constrained to a specific towing configuration (symmetrical profile,  $U_0 = 2 \text{ m/s}$ ,  $\alpha = 5^\circ$ ) due to experimental limitations. This raises questions about how the flow perturbation introduced by this wing geometry might behave under higher load conditions, such as increased towing velocities or a cambered wing profile. Furthermore, it is essential to determine whether the geometry modification accurately represents the intended mode excitation from the numerical reference. In-depth analysis of the flow in the near wake of the modified wings could provide a more precise understanding of the effects of this geometry modification. Additionally, examining flow measurements for unsteady phenomena, potentially through a POD analysis, could identify modified flow characteristics guiding future experiments.

With respect to subject 3., We analyze the wake generated by a wing with an inboard region of constant positive twist similar to an airplane flaps. In this way flap vortices are introduced in the wake. These are co-rotating with the wing-tip

vortices. The key characteristics governing the behavior of the vortex pairs are the ratios of circulation and span-wise distances, denoted as  $(\gamma, \beta)$ .

In the case of co-rotating configurations generated by an inboard flap of span  $10\%b_0$ , the flap vortices appear relatively weak and are often overcome by the wake generated by the strut, yielding no significant results. Instead, we investigate the co-rotating pairs formed in the near-wake a wing model with a flap of 75% inboard span. An analysis of the pair time evolution is performed with particular focus on the orbital movement of the vortices around the vorticity barycenter and on the occurrence of vortex fusion. A point vortex model is used to predict vortex trajectories based on initial characteristics  $(\gamma_0, \beta_0)$ , yielding accurate predictions during the early stages of the wake. Vortex fusion commences as vortices approach each other, leading to a sudden acceleration in their orbital velocity around the vorticity barycenter. During this process,  $\gamma(t)$  decreases, translating the transfer of circulation from the flap vortex to the tip vortex. The fusion concludes when vortices within the dipole became indistinguishable, a phenomenon typically occurring within a time frame corresponding to one period of the orbital movement of a point vortex dipole with analogous attributes.

Furthermore, in the case of the wing model with a flap of span  $75\%b_0$ , the resulting wing-load profile is of type *high-lift (HL)*. This allows for the study of the impact of the lift distribution on the physics of the wake when transitioning from a cruise (*Ref*) to a landing/take-off (*HL*) wing configuration. Here, a single dipole of trailing vortices results from the fusion of the dipole of co-rotating vortices on each side of the near wake. The normalized circulation of the *HL* vortex exceeds that of the *Ref* vortex by a maximum of 20%. Nonetheless, the *HL* vortex displays a more diffuse structure near its centroid, characterized by lower velocities and a larger radius compared to the *Ref* configuration. This diffusive effect is attributed to the upstream fusion event.

In both configurations, the characteristics of the dipole were mapped, offering experimental references for future studies. It also lays the groundwork for investigations involving the interaction of trailing vortices with the ground, as aircraft adopt a flaps-down configuration during take-off and landing. Indeed, our observations near the lower boundary of the measurement window highlighted ground effects on the vortices. While not our primary focus, this suggests the experimental setup potential for studying the ground effect and the effect of flow control localized at the wall.

With respect to subject 4., counter-rotating vortices are generated by towing a wing with an inboard flap of span  $15\%b_0$ . This setup allows for the experimental study of counter-rotating systems that display divergent, steady or periodic motion. We develop a methodology that allows for tracking and characterizing the flap and tip vortices separately until they exit the measurement window or until they diffuse. Indeed, it is found that the interaction between the tip and flap vortices leads to a diffusion process occurring over a time scale ranging from  $20 \frac{b_0}{U_0}$  to  $80 \frac{b_0}{U_0}$ . In steady and periodic cases, the flap vortex eventually diffuses completely, while the tip vortex persists in a modified state with its circulation reduced by 30% to 80% relative to its initial magnitude. Before the diffusion of the flap vortex is completed, at  $t = t_\Delta$ , both vortices follow orbital paths. The diffusion process appears to be primarily driven by viscous cancellation, suggesting that cooperative instabilities did not manifest significantly within the temporal frame defined by  $t < t_\Delta$ . In the counter-rotating configuration, vortex trajectories in the "steady" regime are

observed at  $\beta_0 \sim 0.15$ ,  $\gamma_0 \sim -0.65$ , which is not entirely aligned with model predictions, (for theory  $\beta_0 \sim 0.15$ ,  $\gamma_0 \sim -0.425$ ). The point vortex model described above is used here too yielding a good prediction of vortex trajectories in the early stages of the development of the wake. Beyond the early stages of the wake, events such as vortex diffusion induce time-dependent changes in  $(\gamma, \beta)$ , which are currently beyond the scope of our model. Future work could involve using experimental data in order to develop a model, that accounts for circulation transfer between vortices. Such a model would permit precise predictions of the evolution of the vortex system.

## 7.2 Discussion of results and perspectives

The methodologies, main results and limitations encountered in this work are discussed now. The towing tank installation in which we realize the experiments of this work allows for the observation of vortex evolution from its formation up to  $tU_0/b_0 = 200$ , for the baseline wing geometry. We exploited the extent of this frame of observation to investigate physical phenomena that are not commonly characterized in other experiments (for instance, the interplay between axial and azimuthal flow in the regime where  $q \sim 1.5$ ). However, the maximum observation time turned out to be small with respect to the time-scale of vortex mutual induction,  $t_b = 2\pi b^2/\Gamma = b/W_d$ . This renders the observation time insufficient to characterize the development of vortex instabilities, such as the Crow instability. This constraint is primarily attributed to the vertical dimensions of the tank, since vortices travel vertically during their evolution and exit the measurement plane resulting in a maximum observation time of  $t_{max} \sim 2t_b$ . In order to observe the full-fledged instability, one would require  $t_{max} \sim 5t_b$ . One potential axis for improvement involves the design of experiments employing wings with reduced spans. In such cases, the objective is to bring the shed vortices within a distance small with respect to the tank and measurement window dimensions. Prolonged observation periods would be attained in this way. However, such experiments may require exceptionally small wing spans, raising concerns about the detectability and lifespan of the generated vortices due to the low Reynolds number and to the effects of the wake of the strut. For instance, if the wing is towed 0.5 meters below the water surface, with significant ground effects considered only within a distance of approximately one wingspan above the ground level, then the maximum vertical descent length for observation is estimated to be 0.8 meters. If one considers that the angle of vortex descent is the same as observed in the experiments of this work, where  $b_0 = 0.4$  m, then in order to achieve an observation time equivalent to 5 induction time scales, a minimal vortex spacing of  $b = 0.16$  meters is required, corresponding to a wing span of  $b_0 = 0.2$  meters. While the vortices generated under such conditions would be smaller in dimensions, the existing spatial resolution may still suffice for their detection, potentially facilitating observations of the Crow instability.

Another limitation inherent to the towing tank installation is that it is challenging to study the measured data with a statistical approach. The limitation is tied to the availability of only a single velocity field for discrete downstream stations, rendering the results highly sensitive to the quality of each measurement. In this work, we address this challenge by averaging the measurements spatially (on the azimuthal direction) but also over small time-frames. On top of this, we used a synchronization procedure that allowed us to average the results of multiple realizations of each experimental configuration. This methodology yields data that allows us to track

the vortex time evolution. However, in some instances of our study, this data is insufficient to conclude on the hypothesis raised, (for example when characterizing the periodic and non-periodic motion of vortices in the plane). In this context, we propose another axis of amelioration : given the now-established knowledge of particular downstream stations where significant physical phenomena occur, focusing measurements on smaller, better-resolved temporal/spatial windows is suggested. Employing a smaller PIV window for improved spatial resolution and specialized equipment for time-resolved PIV can enhance data quality and yield more robust findings.

As said above, this experimental setup enables the study of the interaction between axial and azimuthal flow in the limit where  $q \sim 1.5$ . In this work we identify the underlying physical mechanisms governing this interaction. Notably, it has become apparent that the longitudinal gradients in azimuthal and axial velocity are linked, a phenomenon consistent with classical theory on cyclostrophic equilibrium. Then, in the limit where  $q \sim 1.5$ , there is a discernible dampening of axial velocity, a characteristic reminiscent of stabilization mechanisms that have been predicted analytically in other works.

Conversely, a limitation in our work arises from the absence of concrete confirmation regarding whether these stabilization mechanisms indeed are the cause of the observed behavior. Ideally, to fully characterize the dampening of axial velocity, one would require measurements of the flow over a large time period in which  $q(t)$  is not changing with time. This would allow us to confirm that although  $q$  decreases over the first stages of evolution, the vortex does not enter a state where  $q(t) < 1.5$  during its life time. However, in numerous experimental configurations, the vortices exit the measurement window soon after  $q$  begins its stabilization, leaving open the question of whether the threshold of 1.5 is crossed or not. In some less common cases,  $q(t) < 1.5$  occurs. For some of these experiments, the flow quickly returns to a state where  $q(t) > 1.5$  before the vortex exits the measurement window, but for other, the vortex exits the measurement window soon after  $q(t) < 1.5$  occurs, impeding further observation. It is thus evident that the limitations of our observation frame is the main constraint in this part of our work. Another constraint arises in specific configurations, where intense axial flow impedes measurement due to experimental limitations of the PIV setup. In these instances, particles exit the laser plane in a direction perpendicular to it, rendering accurate measurements impossible.

Multiple avenues for improvement are proposed. Firstly, there exists an opportunity for more in-depth analysis of the available data, particularly through a POD study of the axial flow field. This can offer a deeper understanding of the underlying dynamics.

Secondly, it remains essential to study the impact that the development (or the dampening) of axial velocity has on other vortex characteristics, such as radius and circulation. Particular emphasis is placed on the question of whether conditions of strong axial flow contribute to the decay of vortices.

Thirdly, a targeted measurement campaign can be conducted at specific downstream locations where  $q \sim 1.5$ , as identified in this study. The ability to perform time-resolved PIV measurements at these locations can facilitate a more precise assessment of whether the stabilization mechanisms are indeed taking place.

Another notable result in this work lies in the study of analytical investigations

into practical experiments. Specifically, we characterize the impact of a passive control strategy involving the undulation of the wing trailing edge. This design modification is grounded in theoretical studies of wake stability, where a body force whose shape matches a specific perturbation mode is introduced numerically into the near wake of a wing.

However, one limitation in our experiment is evident as the measurements did not provide confirmation that the trailing edge undulation successfully introduces the desired perturbation in the wake. Additionally, the analytically identified mode is time-dependent, a characteristic that is not replicated by our passive control.

One potential avenue for improvement involves testing new wing geometries while adhering to the same underlying principle of reproducing a perturbation mode that is periodic in the spanwise direction. For example, the implementation of wings with evenly spaced bumps along their span could introduce time-dependent perturbations through the physical mechanism of vortex shedding. Other wing designs could be aimed at targeting alternative perturbation modes, such as those obtained through optimal perturbation analysis of Navrose [70]. The wing models in these experiments were 3D printed. This caused cavitation issues to arise at high towing velocities, limiting the experimental configurations that we could test. New wings would need to be constructed using more homogeneous materials to mitigate this problem.

A strength of this work is the study of the wake of a wing configuration that has a flap of large span. This geometry generates a co-rotating vortex pair on each side of the wake and its wingload is representative of a high-lift configuration of commercial aircraft. Although it was not the intended objective of this study, the data collected here serves as valuable initialization for investigating vortex behaviors in ground effect, since high-lift configurations are typically adopted during take-off and landing. Presently, some numerical studies in this domain initiate wake properties using a wing elliptic configuration, which, as demonstrated here, deviates from the high-lift case. Furthermore, during the experimental campaign, it was confirmed that the tank ground has a strong impact on the vortices as they approach within one wingspan's height (refer to Fig. 7.1). Therefore, it is evident that further work

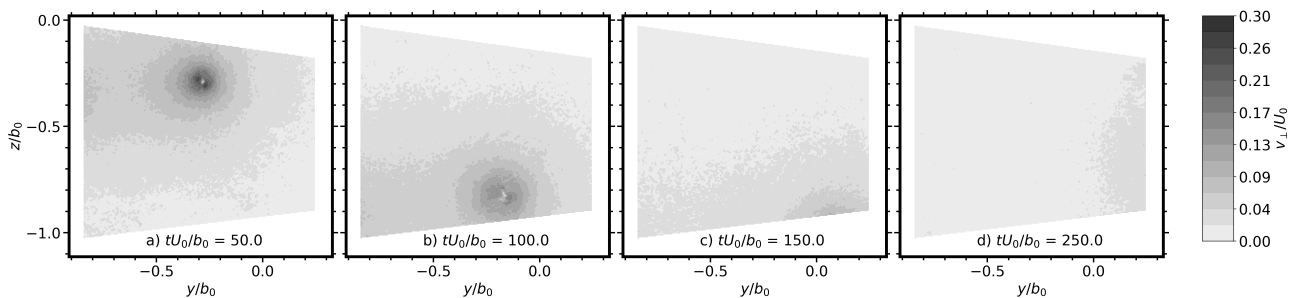


FIGURE 7.1: Wake downstream evolution for an experiment at configuration ( $Ref, U_0 = 5 \text{ m/s}, \alpha = 7.5^\circ$ ). Subsequent times are represented,  $tU_0/b_0 = \text{a) } 50, \text{ b) } 100, \text{ c) } 150 \text{ and d) } 250$

could involve adapting the experiment to investigate the ground effect on high-lift vortices. This adaptation could include the introduction of a dedicated solid surface parallel to the water's surface. A key experimental parameter in this setup would be the vertical distance between the wing and the horizontal solid surface. This parameter governs the extent to which the vortices can develop independently before ground effect becomes the predominant mechanism. Moreover, the design

of the surface that serves as the ground can incorporate either smooth features or passive control strategies through deformations. This modified setup is particularly intriguing since image vorticity around the ground represents another pathway for the development of cooperative instabilities.

As a preliminary assessment of this scenario, numerical simulations were conducted to predict the timescale of Crow instability development in proximity to the ground. The results, shown in Fig. 7.2, reveal that a height  $h$  in the order of the vortex distance  $b$  is necessary for the instability to manifest between the tip vortex and its image vorticity at a rate observable within our experimental framework. These simulations, however, neglect the effect of other phenomena that stem from ground interaction, such as the the boundary layer induced by the vortex flow, which may be a significant factor to consider in the design of the experiments.

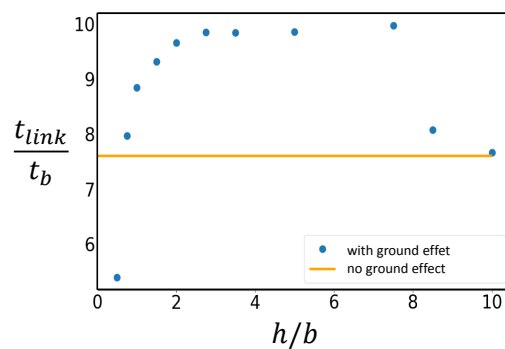


FIGURE 7.2: From [63] : Normalized time to linking  $t_{link}/t_b$  as a function of initial vertical distance to the ground  $h/b$  as predicted by numerical simulations.

Finally, this work encompasses the study of a wing that generates a counter-rotating vortex pair on each side of its wake. Here, the time evolution of circulation for each vortex within the pair is measured by employing a contour of integration that moves with the center of each vortex. Furthermore, we quantify the total circulation using a large contour that extends over the entire measurement frame.

A notable strength of this study is the analysis of the impact of flap vortex diffusion on the evolution of the vortex system. Scenarios involving divergent, steady, and periodic motion of the dipole system are achieved during the experiments. We provide data on the time required for flap vortex diffusion as a function of the initial circulation ratio in the pair. Additionally, the magnitude of the wingtip vortex decay is quantified after the complete diffusion of the flap vortex. These results contribute to forthcoming experiments focused on the development of control strategies that involve counter-rotating flow.

However, a limitation of this experimental setup is that only the axial vorticity data is measurable. Indeed, in other experiments in the literature, it is confirmed through dye visualizations that the flap vortex undergoes a particular instability that causes the reorientation of its vorticity out of the 2D plane. With only the planar PIV data available, it is challenging to confirm that this occurs in our experiments.

Furthermore, due to the wide trajectories that the vortices describe, in some instances the measurement plane is not large enough to encompass the whole flow. This is evident for the experiments involving divergent motion but it is also a limitation in some cases of periodic motion. These limitations do not impede us from concluding that viscous cancellation operates between the flap and wing-tip vortices during the earlier stages of the wake evolution, since the total circulation is

kept constant while that of the vortices decreases. However, in the later stages of evolution, the total circulation in the flow decreases, and it becomes challenging to fully attribute this and subsequent occurrences to one particular cause. In summary, the measurement of total circulation reveals that in these experiments the vorticity exits the measurement plane, but it is unclear whether vorticity remains axial and exits through the sides of the PIV window, or if vorticity is being reoriented and exits the PIV plane altogether.

In order to answer these questions, it is interesting to further study the state of the wing-tip vortex after the dissipation of the flap vortex. This is because experimental [73] and analytical [29] references describe the wingtip vortex state as "altered" by the influence of the flap vortex before its complete diffusion. Indeed, our results show that the interaction between the flap and wing-tip vortices has an impact in their diffusion and in their trajectory. It follows that if the flap vortex does undergo strong deformations due to instability, then the wavelength of these deformations will impact in some way the structure of the wing-tip vortex structure. Thus, using the available data one could explore the presence of periodic components in the trajectories or in the radius of the wing-tip vortex after the diffusion of the flap vortices. The existence (or the absence) of these periodic components could provide insights into the question of whether the flap vortex is being deformed. Then, if it is established that the wing-tip vortex exhibits periodic deformations, and if these characteristics are dependent on the initial ratios of distances and circulations, it could signify that this perturbation could be fine-tuned to incite a deformation corresponding to the wavelength of the Crow instability.

## Appendix A

# Description of the database

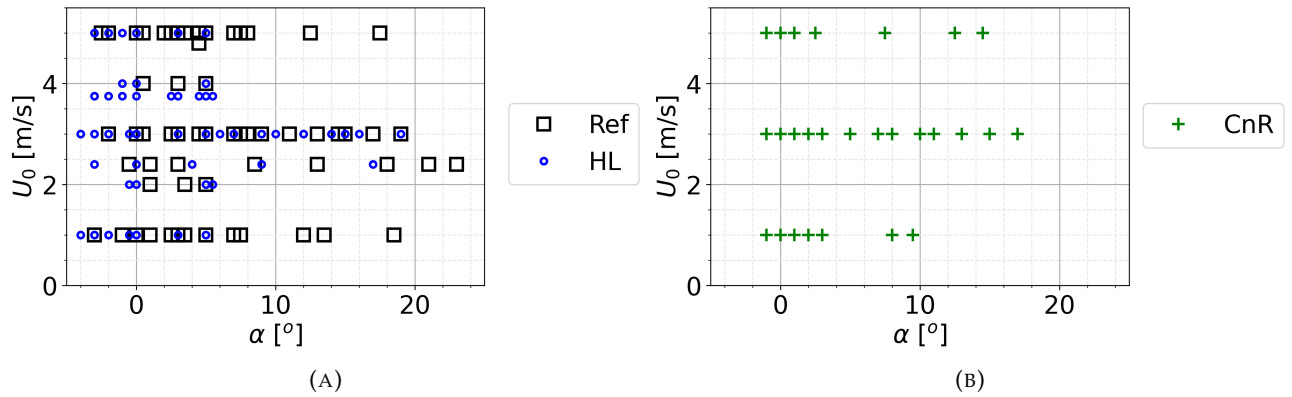
The experiments realized with the *Ref*, *HL* and *CnR* wing configurations are shown in the table below. This information is also represented visually in Fig. A.1.

$n^o$	Wing	$H$	$U_0$ m/s	$\alpha^o \pm 0.25^o$	Efforts	PIV (high frame)	PIV (low frame)
C <sub>1</sub>	Ref	0.5	1.0	-3.0	✓(1)		
C <sub>2</sub>	Ref	0.5	1.0	-1.0	✓(2)		
C <sub>3</sub>	Ref	0.5	1.0	0.0	✓(2)		
C <sub>4</sub>	Ref	0.5	1.0	1.0	✓(3)	✓(2)	
C <sub>5</sub>	Ref	0.5	1.0	2.5	✓(3)		✓(2)
C <sub>6</sub>	Ref	0.5	1.0	3.0	✓(2)		
C <sub>7</sub>	Ref	0.5	1.0	3.5	✓(3)	✓(3)	
C <sub>8</sub>	Ref	0.5	1.0	5.0	✓(8)	✓(3)	✓(2)
C <sub>9</sub>	Ref	0.5	1.0	7.0	✓(3)	✓(1)	✓(2)
C <sub>10</sub>	Ref	0.5	1.0	7.5	✓(1)		✓(1)
C <sub>11</sub>	Ref	0.5	1.0	12.0	✓(1)		
C <sub>12</sub>	Ref	0.5	1.0	13.5	✓(3)	✓(1)	
C <sub>13</sub>	Ref	0.5	1.0	18.5	✓(1)		
C <sub>14</sub>	Ref	0.5	2.0	1.0	✓(3)	✓(3)	
C <sub>15</sub>	Ref	0.5	2.0	3.5	✓(2)	✓(2)	
C <sub>16</sub>	Ref	0.5	2.0	5.0	✓(3)	✓(3)	
C <sub>17</sub>	Ref	0.5	2.4	-0.5	✓(1)	✓(1)	
C <sub>18</sub>	Ref	0.5	2.4	1.0	✓(1)	✓(1)	
C <sub>19</sub>	Ref	0.5	2.4	3.0	✓(4)	✓(1)	
C <sub>20</sub>	Ref	0.5	2.4	8.5	✓(1)	✓(1)	
C <sub>21</sub>	Ref	0.5	2.4	13.0	✓(1)	✓(1)	
C <sub>22</sub>	Ref	0.5	2.4	18.0	✓(1)	✓(1)	
C <sub>23</sub>	Ref	0.5	2.4	21.0	✓(1)		
C <sub>24</sub>	Ref	0.5	2.4	23.0	✓(1)		
C <sub>25</sub>	Ref	0.5	3.0	-2.0	✓(2)		
C <sub>26</sub>	Ref	0.5	3.0	0.0	✓(2)		
C <sub>27</sub>	Ref	0.5	3.0	0.5	✓(4)	✓(4)	
C <sub>28</sub>	Ref	0.5	3.0	2.5	✓(2)		✓(2)
C <sub>29</sub>	Ref	0.5	3.0	3.0	✓(15)	✓(6)	✓(2)
C <sub>30</sub>	Ref	0.5	3.0	4.5	✓(3)	✓(3)	
C <sub>31</sub>	Ref	0.5	3.0	5.0	✓(4)		✓(2)
C <sub>32</sub>	Ref	0.5	3.0	7.0	✓(4)		✓(2)
C <sub>33</sub>	Ref	0.5	3.0	7.5	✓(2)		✓(2)

C <sub>34</sub>	Ref	0.5	3.0	8.0	✓(2)	✓(1)	
C <sub>35</sub>	Ref	0.5	3.0	9.0	✓(1)		
C <sub>36</sub>	Ref	0.5	3.0	11.0	✓(1)		
C <sub>37</sub>	Ref	0.5	3.0	13.0	✓(4)	✓(1)	
C <sub>38</sub>	Ref	0.5	3.0	14.5	✓(1)		✓(1)
C <sub>39</sub>	Ref	0.5	3.0	15.0	✓(1)		
C <sub>40</sub>	Ref	0.5	3.0	17.0	✓(1)		
C <sub>41</sub>	Ref	0.5	3.0	19.0	✓(1)		
C <sub>42</sub>	Ref	0.5	4.0	0.5	✓(5)	✓(5)	
C <sub>43</sub>	Ref	0.5	4.0	3.0	✓(5)	✓(7)	
C <sub>44</sub>	Ref	0.5	4.0	5.0	✓(3)	✓(3)	
C <sub>45</sub>	Ref	0.5	4.8	4.5	✓(2)	✓(2)	
C <sub>46</sub>	Ref	0.5	5.0	-2.5	✓(1)		
C <sub>47</sub>	Ref	0.5	5.0	-2.0	✓(2)		
C <sub>48</sub>	Ref	0.5	5.0	0.0	✓(2)		
C <sub>49</sub>	Ref	0.5	5.0	0.5	✓(3)	✓(3)	
C <sub>50</sub>	Ref	0.5	5.0	2.0	✓(3)		✓(3)
C <sub>51</sub>	Ref	0.5	5.0	2.5	✓(2)		✓(1)
C <sub>52</sub>	Ref	0.5	5.0	3.0	✓(2)	✓(2)	
C <sub>53</sub>	Ref	0.5	5.0	3.5	✓(3)	✓(3)	
C <sub>54</sub>	Ref	0.5	5.0	4.5	✓(2)	✓(2)	
C <sub>55</sub>	Ref	0.5	5.0	5.0	✓(9)	✓(3)	✓(2)
C <sub>56</sub>	Ref	0.5	5.0	7.0	✓(4)		✓(4)
C <sub>57</sub>	Ref	0.5	5.0	7.5	✓(1)		✓(1)
C <sub>58</sub>	Ref	0.5	5.0	8.0	✓(2)	✓(2)	
C <sub>59</sub>	Ref	0.5	5.0	12.5	✓(2)	✓(1)	
C <sub>60</sub>	Ref	0.5	5.0	17.5	✓(1)	✓(1)	
C <sub>61</sub>	HL	0.5	1.0	-4.0	✓(1)		
C <sub>62</sub>	HL	0.5	1.0	-3.0	✓(1)		
C <sub>63</sub>	HL	0.5	1.0	-2.0	✓(3)		
C <sub>64</sub>	HL	0.5	1.0	-0.5	✓(3)	✓(3)	
C <sub>65</sub>	HL	0.5	1.0	0.0	✓(4)		✓(1)
C <sub>66</sub>	HL	0.5	1.0	3.0	✓(3)		
C <sub>67</sub>	HL	0.5	1.0	5.0	✓(22)	✓(8)	✓(6)
C <sub>68</sub>	HL	0.5	2.0	-0.5	✓(2)	✓(2)	
C <sub>69</sub>	HL	0.5	2.0	0.0	✓(5)		✓(4)
C <sub>70</sub>	HL	0.5	2.0	5.0	✓(1)		
C <sub>71</sub>	HL	0.5	2.0	5.5	✓(3)	✓(3)	
C <sub>72</sub>	HL	0.5	2.4	-3.0	✓(1)		
C <sub>73</sub>	HL	0.5	2.4	0.0	✓(1)		
C <sub>74</sub>	HL	0.5	2.4	4.0	✓(1)		
C <sub>75</sub>	HL	0.5	2.4	9.0	✓(1)		
C <sub>76</sub>	HL	0.5	2.4	17.0	✓(1)		
C <sub>77</sub>	HL	0.5	3.0	-4.0	✓(1)		
C <sub>78</sub>	HL	0.5	3.0	-3.0	✓(1)		
C <sub>79</sub>	HL	0.5	3.0	-2.0	✓(3)		

C <sub>80</sub>	HL	0.5	3.0	-0.5	✓(3)	✓(2)	✓(1)
C <sub>81</sub>	HL	0.5	3.0	0.0	✓(10)		✓(6)
C <sub>82</sub>	HL	0.5	3.0	3.0	✓(5)		
C <sub>83</sub>	HL	0.5	3.0	5.0	✓(16)	✓(6)	✓(6)
C <sub>84</sub>	HL	0.5	3.0	6.0	✓(1)		✓(1)
C <sub>85</sub>	HL	0.5	3.0	7.0	✓(1)		
C <sub>86</sub>	HL	0.5	3.0	9.0	✓(1)		
C <sub>87</sub>	HL	0.5	3.0	10.0	✓(1)		✓(1)
C <sub>88</sub>	HL	0.5	3.0	12.0	✓(1)		
C <sub>89</sub>	HL	0.5	3.0	14.0	✓(1)		
C <sub>90</sub>	HL	0.5	3.0	15.0	✓(1)		
C <sub>91</sub>	HL	0.5	3.0	16.0	✓(1)		
C <sub>92</sub>	HL	0.5	3.0	19.0	✓(1)		
C <sub>93</sub>	HL	0.5	3.75	-3.0	✓(1)		
C <sub>94</sub>	HL	0.5	3.75	-2.0	✓(1)		
C <sub>95</sub>	HL	0.5	3.75	-1.0	✓(2)	✓(2)	
C <sub>96</sub>	HL	0.5	3.75	0.0	✓(1)		
C <sub>97</sub>	HL	0.5	3.75	2.5	✓(4)	✓(4)	
C <sub>98</sub>	HL	0.5	3.75	3.0	✓(4)		✓(2)
C <sub>99</sub>	HL	0.5	3.75	4.5	✓(3)	✓(3)	
C <sub>100</sub>	HL	0.5	3.75	5.0	✓(8)	✓(6)	✓(2)
C <sub>101</sub>	HL	0.5	3.75	5.5	✓(1)		✓(1)
C <sub>102</sub>	HL	0.5	4.0	-1.0	✓(2)	✓(2)	
C <sub>103</sub>	HL	0.5	4.0	0.0	✓(1)		✓(1)
C <sub>104</sub>	HL	0.5	4.0	5.0	✓(8)	✓(6)	
C <sub>105</sub>	HL	0.5	5.0	-3.0	✓(1)		
C <sub>106</sub>	HL	0.5	5.0	-2.0	✓(2)		
C <sub>107</sub>	HL	0.5	5.0	-1.0	✓(5)	✓(5)	
C <sub>108</sub>	HL	0.5	5.0	0.0	✓(7)		✓(2)
C <sub>109</sub>	HL	0.5	5.0	3.0	✓(3)		
C <sub>110</sub>	HL	0.5	5.0	5.0	✓(5)		✓(3)
C <sub>111</sub>	CnR	0.5	1.0	-1.0	✓(1)	✓(1)	
C <sub>112</sub>	CnR	0.5	1.0	0.0	✓(1)	✓(1)	
C <sub>113</sub>	CnR	0.5	1.0	1.0	✓(1)	✓(1)	
C <sub>114</sub>	CnR	0.5	1.0	2.0	✓(1)	✓(1)	
C <sub>115</sub>	CnR	0.5	1.0	3.0	✓(1)	✓(1)	
C <sub>116</sub>	CnR	0.5	1.0	8.0	✓(1)	✓(1)	
C <sub>117</sub>	CnR	0.5	1.0	9.5	✓(2)	✓(2)	
C <sub>118</sub>	CnR	0.5	3.0	-1.0	✓(4)	✓(4)	
C <sub>119</sub>	CnR	0.5	3.0	0.0	✓(3)	✓(3)	
C <sub>120</sub>	CnR	0.5	3.0	1.0	✓(2)	✓(2)	
C <sub>121</sub>	CnR	0.5	3.0	2.0	✓(4)	✓(4)	
C <sub>122</sub>	CnR	0.5	3.0	3.0	✓(1)	✓(1)	
C <sub>123</sub>	CnR	0.5	3.0	5.0	✓(4)	✓(4)	
C <sub>124</sub>	CnR	0.5	3.0	7.0	✓(2)	✓(2)	
C <sub>125</sub>	CnR	0.5	3.0	8.0	✓(1)	✓(1)	

C <sub>126</sub>	CnR	0.5	3.0	10.0	✓(3)	✓(3)
C <sub>127</sub>	CnR	0.5	3.0	11.0	✓(2)	✓(2)
C <sub>128</sub>	CnR	0.5	3.0	13.0	✓(2)	✓(2)
C <sub>129</sub>	CnR	0.5	3.0	15.0	✓(1)	✓(1)
C <sub>130</sub>	CnR	0.5	3.0	17.0	✓(2)	✓(2)
C <sub>131</sub>	CnR	0.5	5.0	-1.0	✓(1)	✓(1)
C <sub>132</sub>	CnR	0.5	5.0	0.0	✓(1)	✓(1)
C <sub>133</sub>	CnR	0.5	5.0	1.0	✓(1)	✓(1)
C <sub>134</sub>	CnR	0.5	5.0	2.5	✓(1)	✓(1)
C <sub>135</sub>	CnR	0.5	5.0	7.5	✓(1)	✓(1)
C <sub>136</sub>	CnR	0.5	5.0	12.5	✓(1)	✓(1)
C <sub>137</sub>	CnR	0.5	5.0	14.5	✓(1)	✓(1)
C <sub>138</sub>	CnR	0.6	3.0	-1.0	✓(3)	✓(3)
C <sub>139</sub>	CnR	0.6	3.0	0.0	✓(1)	✓(1)
C <sub>140</sub>	CnR	0.6	3.0	2.0	✓(3)	✓(3)
C <sub>141</sub>	CnR	0.6	3.0	2.5	✓(3)	✓(3)
C <sub>142</sub>	CnR	0.6	3.0	3.0	✓(2)	✓(3)
C <sub>143</sub>	CnR	0.6	3.0	4.0	✓(3)	✓(3)
C <sub>144</sub>	CnR	0.6	3.0	5.0	✓(1)	✓(1)
C <sub>145</sub>	CnR	0.6	3.0	5.5	✓(1)	✓(1)
C <sub>146</sub>	CnR	0.6	3.0	6.0	✓(1)	✓(1)
C <sub>147</sub>	CnR	0.86	3.0	-0.5	✓(1)	✓(1)

FIGURE A.1: Test cases for the *Ref*, *HL* and *CnR* wing configurations.

The experiments realized to study the effect of an undulated trailing edge are shown in the table below.

$n^o$	$A/c_0$	$H$	$U_0$ m/s	$\alpha^o \pm 0.25^o$	Efforts	PIV (high frame)	PIV (low frame)
C <sub>138</sub>	0.0	0.5	2.0	5.0	✓(2)	✓(2)	
C <sub>139</sub>	0.01	0.5	2.0	5.0	✓(2)	✓(2)	
C <sub>140</sub>	0.05	0.5	2.0	5.0	✓(2)	✓(2)	
C <sub>141</sub>	0.10	0.5	2.0	5.0	✓(2)	✓(2)	

## Appendix B

# Calibration procedure on the experimental installation

### B.1 Calibration of the wing angle of attack

The wing angle of attack ( $\alpha$ ) and towing speed ( $U_0$ ) are used to characterize the results of this work. The following section describes the calibration procedure to obtain an accurate ( $\pm 0.25^\circ$ ) measurement of  $\alpha$ .

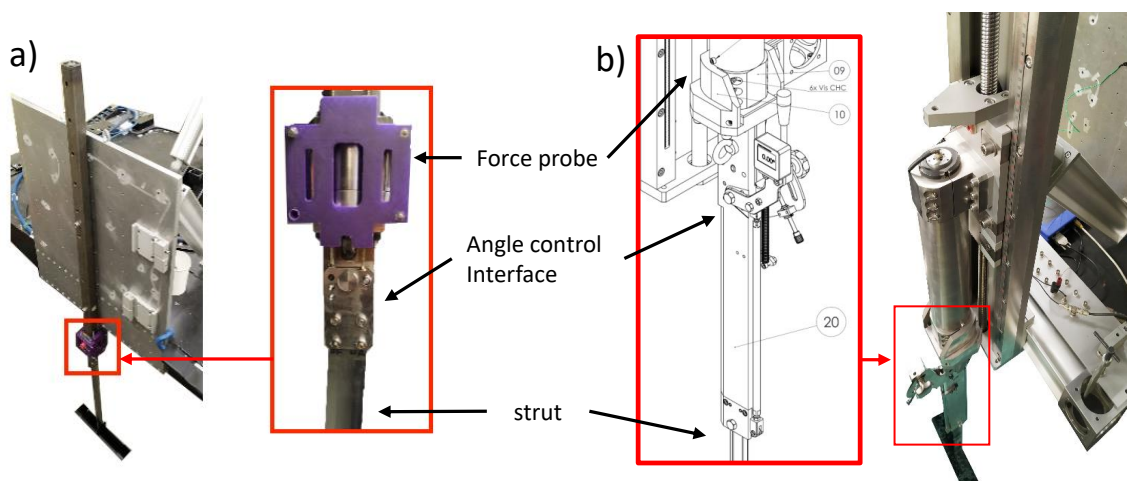


FIGURE B.1: Structures used to attach the strut and wing ensemble to the chariot. **a)** structure S20 and **b)** structure S23

The angle of attack is defined as the angle between the wing tip chord and the longitudinal direction ( $X$ ). Before each experiment, we set the angle of attack by tilting the strut and wing together. This is accomplished using a structure attached to the chariot, which holds the strut and wing ensemble during towing. During this research project, we had two different structures, referred to as S20 and S23 (shown in Fig. B.1a and B.1b, respectively). In both structures, the pivot point for adjusting  $\alpha$  is situated approximately  $0.53\text{ m}$  above the wing. The range of  $\alpha$  allowed by each structure is  $\alpha \in [0^\circ, 5^\circ]$  for S20 and  $\alpha \in [-3^\circ, 25^\circ]$  for S23. During the experimental campaign, it often becomes necessary to unmount the structure from the chariot, which introduces ambiguity regarding the true value of  $\alpha$  before and after the unmounting. To achieve precise control of  $\alpha$ , we have developed a specific methodology, which is presented in what follows.

Our calibration procedure can be summarized as follows:

1. First, the exact geometric angle of attack ( $\pm 0.01^\circ$ ) is obtained on a calibration rig (Fig. B.2). The angle is determined using an inclinometer and the analysis of digital images.
2. Then, force probe measurements are performed during towing to obtain a calibrated data curve of  $C_z^{cal}(\alpha)$ .
3. The values of  $\Delta C_z^{cal} / \Delta \alpha$  in the linear regime and of  $C_z^{cal}(\alpha = 0^\circ)$  are identified to be used as a reference.
4. The data from experiments is compared to this reference to compute a correction factor  $\alpha_{corr}$  for the angle of attack set at the angle control interface.
5. Finally, experiments performed between two unmountings of the structure (S20 or S23) are grouped and compared in order to assign a single value of  $\alpha_{corr}$  to the group.

This approach provides a rigorous *a posteriori* calibration of  $\alpha$  and allows for the harmonization of experiments done with both structures. However, the precision and repeatability of the real towing velocity ( $U_0$ ) and force probe measurements ( $F_z$ ) can introduce limitations to the methodology. The error introduced by the former is neglected, as velocity measurements show consistent and repeatable values due to a closed-loop command system. The latter can be significant when dealing with towing configurations that generate a lift force comparable to the measuring resolution of the force probe. To address this, experiments generating strong lift forces are realized before unmounting the structure and the data from these experiments reduce the impact of weaker lift force experiments on  $\alpha_{corr}$ .

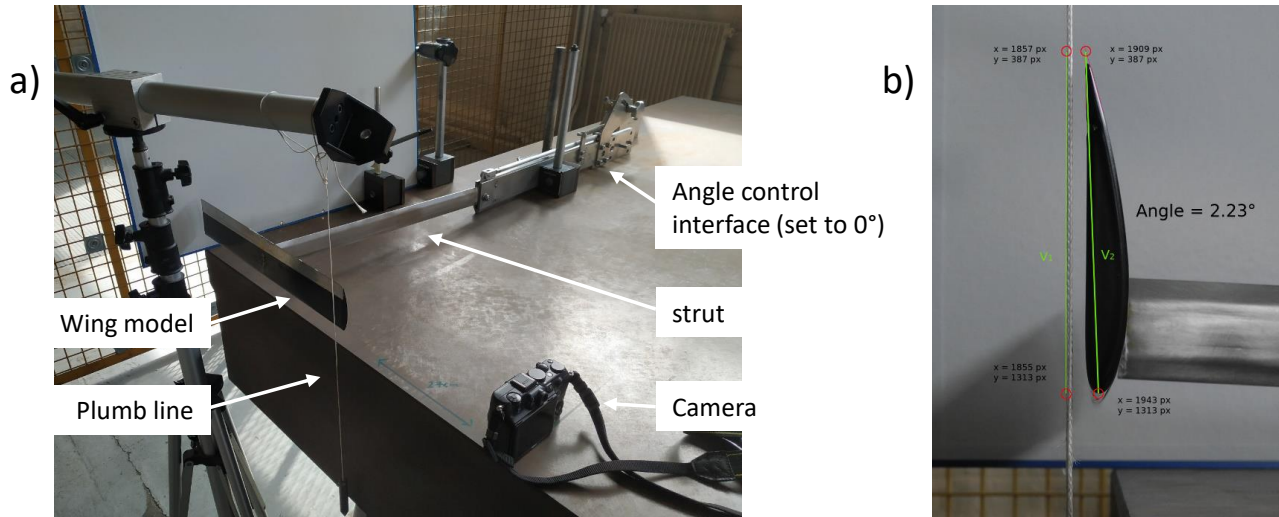


FIGURE B.2: Calibration procedure for the angle of incidence of the wing model.

### Description of step 1.

In the first step of the process, the real angle of the wing tip chord is determined in relation to the angle indicated by the angle control interface. To achieve this, the wing model, strut, and angle control interface are placed in a calibration rig, as depicted in Fig. B.2a. The angle control interface is initially set to  $0^\circ$  using an inclinometer. A plumb line is then positioned next to the wing tip, as shown in Fig. B.2b,

to assess the angle between the chord and the vertical direction. To ensure minimal image deformation caused by the camera's optical lenses, we carefully control the positions of the elements in the rig using meters and the inclinometer. This ensures that the camera plane remains parallel to both the line and the wingtip plane. We place the line and wing at the center of the image plane, where optical deformation is minimal. Also when analyzing the image we confirm that the line appears perfectly vertical, indicating no optical distortion. For instance, upon analysis of the image in Fig. B.2b, we find that the wing angle of attack is approximately  $2.2^\circ$  when the angle control interface is set to  $0^\circ$ . This procedure allows us to accurately assess the real angle of the wing tip chord in comparison to the indicated angle at the control interface.

### Description of steps 2. and 3.

Next, the calibrated ensemble is mounted into the towing tank facility and force probe measurements are conducted to obtain a calibrated dataset,  $C_z^{cal}(\alpha)$ . The results for the reference wing are shown in Fig. B.3a. From this dataset, the values of  $C_z^{cal}(\alpha = 0^\circ)$  and  $\Delta C_z^{cal} / \Delta \alpha$  are extracted, this is presented in Table B.1. To ensure accuracy, we focus on the range  $\alpha \in [-3^\circ; 7^\circ]$ , in which  $C_z^{cal}(\alpha)$  is linear. Measurements are conducted at three different towing velocities,  $U_0 \in [1, 3, 5]m/s$ , as the evolution of  $C_z(\alpha)$  may vary with the Reynolds number. By performing three repetitions of each measurement point  $(U_0, \alpha)$ , we ensure the consistency and reliability of our data. This is indicated in Table B.1 : the maximum standard deviation between repetitions of the experiments,  $\max(s_{C_z^{cal}})$ , is remarkably small. We conclude that the calibration of the dataset  $C_z^{cal}(\alpha)$  is accurate enough for the purpose of providing reference data.

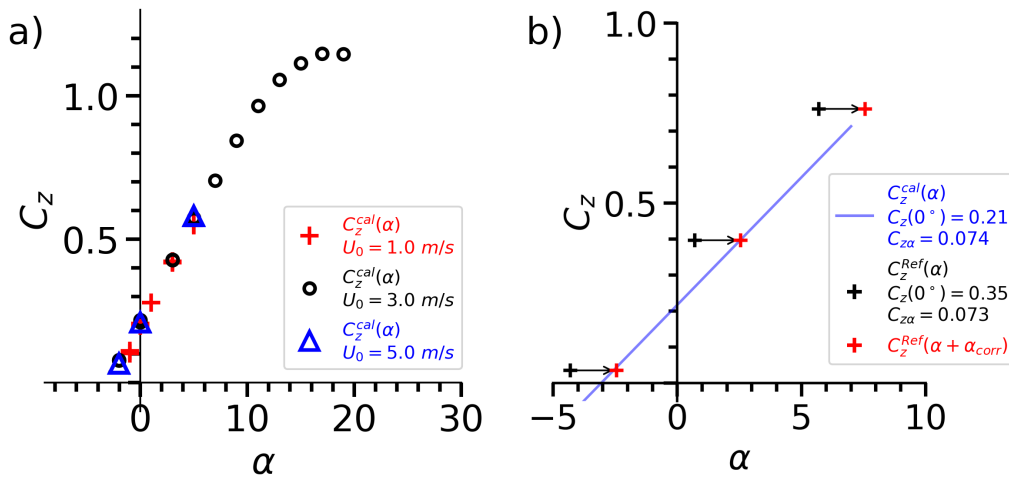


FIGURE B.3: Calibration procedure for  $\alpha$  : a) Reference measurements of lift coefficient obtained with the calibrated setup. b) Determination of  $\alpha_{corr}$  for experiments with the *Ref* wing towed at  $U_0 = 5 m/s$ . Note that scales are adapted to each figure for clarity.

### Description of steps 4. and 5.

The values of  $C_z^{cal}(\alpha = 0)$  and  $\Delta C_z^{cal} / \Delta \alpha$  are used to determine the corrective angle  $\alpha_{corr}$ , which adjusts the angle set at the control interface during experiments.

$U_0$	1 m/s	3 m/s	5 m/s
$C_z^{cal}(\alpha = 0)$	0.20°	0.22°	0.21°
$\Delta C_z^{cal} / \Delta \alpha$	0.073	0.071	0.074
$max(s_{C_z^{cal}})$	$4 \times 10^{-3}$	$3 \times 10^{-3}$	$9 \times 10^{-4}$

TABLE B.1: Characteristics of the calibrated dataset  $C_z^{cal}(\alpha)$ 

$C_z^{Ref}(\alpha)$  data obtained from experiments on the *Ref* wing at  $U_0 = 5 \text{ m/s}$  are shown with black symbols in Fig. B.3b. The strut and wing structure remained unchanged throughout the series of plotted experiments. In Fig. B.3b, the solid line represents the calibrated data. A close match is observed between  $\Delta C_z^{Ref} / \Delta \alpha$  and  $\Delta C_z^{cal} / \Delta \alpha$ , confirming the validity of this approach – the sole adjustment needed to align experimental and calibrated data is a correction in the angle of attack. Hence,  $\alpha_{corr}$  is defined as follows:

$$C_z^{Ref}(\alpha_{corr}) = C_z^{cal}(\alpha = 0^\circ) \quad (\text{B.1})$$

The value of  $C_z^{Ref}(\alpha_{corr})$  is interpolated from available data. This corrected data is depicted in Fig. B.3b using red symbols, and for the given data,  $\alpha_{corr} = 1.83^\circ$ . For the other experiments in this work the range of  $|\alpha_{corr}|$  lies within  $[0^\circ, 2.5^\circ]$ . While the correction magnitude seems substantial, this can be attributed to the challenge of precisely verifying the wing model chord angle during the experimental campaign, where the rig and camera setup is not always available. Nonetheless, this calibration method is well-suited for this experimental setup, offering a retrospective dataset correction.

## B.2 Verification of the calibration of force measurements

The calibration of the force is verified probe to ensure reliable measurements throughout the experiments. This procedure is summarized as follows:

1. Before the experimental campaign, the precision of the probe measurement bridges is verified using precise weights.
2. Identification of strut and wing forces: measurements of the aerodynamic forces generated solely by the strut (without any wing model attached) are realized for each velocity and angle of attack.
3. Correction for random drift: Prior to each experiment, measurements are performed with the wing model at rest.

### Description of step 1.

The 6-component force probes (AMTI-MC3A and PHI-70) are calibrated by subjecting them to calibration weights and measuring the forces and moments applied at the center of the probe. Each channel is calibrated separately by placing the weights only on the axis of the respective channel. The choice of the weight used depends on the channel uncertainty, which is determined by its maximum measurable weight. This calibration procedure is initially performed by the manufacturer and then verified in our laboratory.

An illustration of the test procedure is shown in Fig. B.4. 1kg and 2kg weights are applied on the isolated channels. Each test is repeated three times. The measured forces are compared to the theoretical values (approximately 9.81 N and 19.62

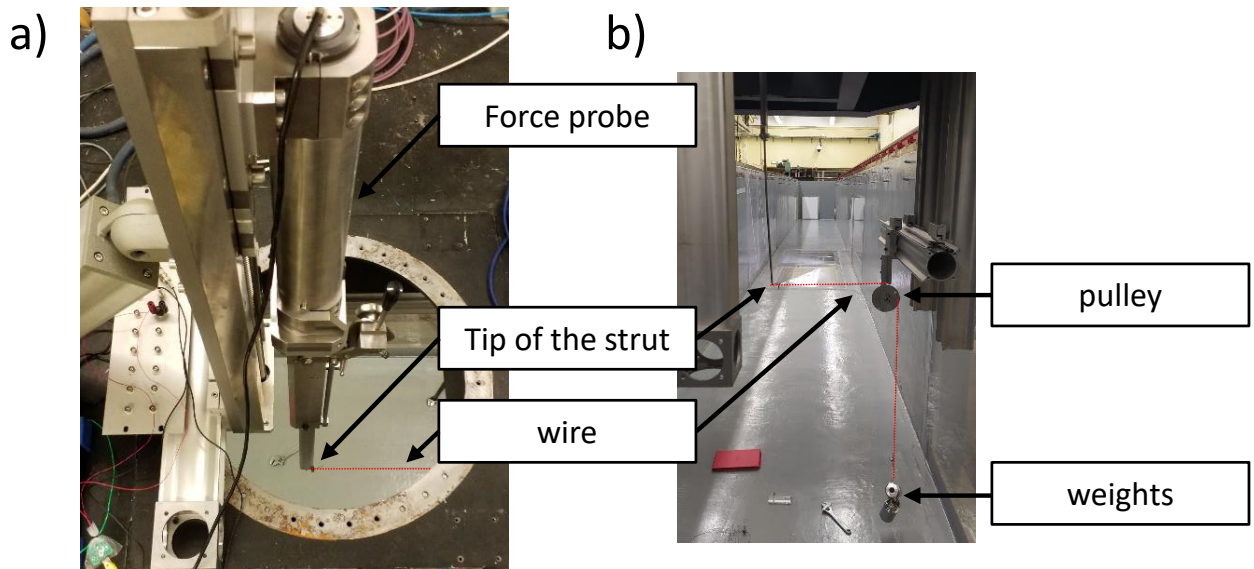


FIGURE B.4: Calibration verification tests performed in the laboratory **a)** as viewed from above the chariot and **b)** as viewed from below. In the images, the wire is overlaid in red for clarity.

N). During these tests the mean error obtained for the measured forces is 0.26 N, and for the moments, it is 0.59 N·m. These errors are lower than the inherent error of the force probe and are deemed sufficient for our purposes.

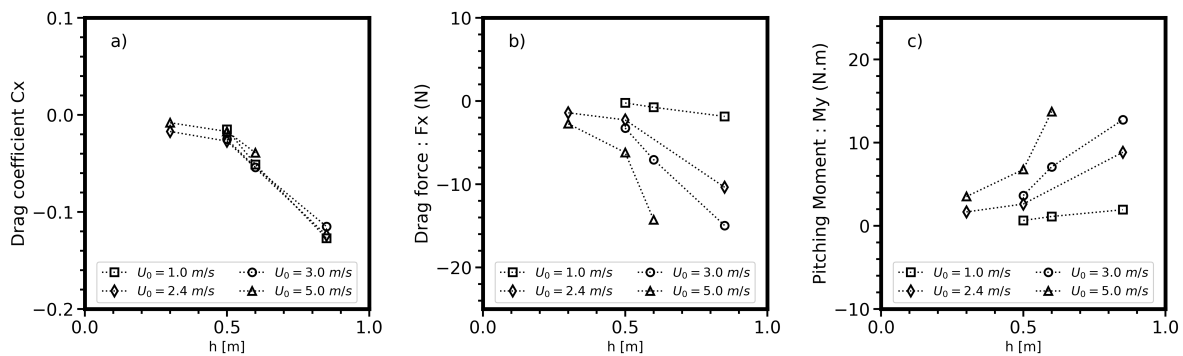


FIGURE B.5: Evolution of **a)** drag coefficient, **b)** drag force and **c)** pitching moment generated by towing the strut alone as a function of depth  $h$ .

### Description of step 2.

During these experiments, the measured drag  $F_x$  is approximated to be the sum of the drag generated by the wing and the drag generated by the strut, which gives us the expression:

$$F_{x,wing} = F_x - F_{x,strut} \quad (B.2)$$

The strut is towed alone as a preliminary step yielding measurements of  $F_{x,strut}$  and  $M_{y,strut}$ . The effect of  $\alpha$  is neglected and so are the forces and moments generated

in the  $Y$  and  $Z$  directions. Measurements of  $F_{x,\text{strut}}$  and  $M_{y,\text{strut}}$ , realized at various water depths ( $h$ ) and towing velocities are presented in Fig. B.5. Each measurement point is repeated 2 times. The results show that  $F_{x,\text{strut}}(h, U_0)$  increases linearly with  $h$ , as expected, because more of the strut is immersed during towing and generates drag. The geometry of the strut is thin and faired over 0.50 m and thicker above 0.50 m. Thus a stronger increase is observed in  $F_{x,\text{strut}}(h, U_0)$  for  $h > 0.5$  at any given towing velocity. The dataset of measurement points ( $h, U_0$ ) is utilized to correct the values of experiments conducted at the same  $h$  and  $U_0$ . If no drag measurements are available for a specific point ( $h, U_0$ ) during the campaign, the value of  $F_{x,\text{strut}}(h, U_0)$  is interpolated from the available dataset.

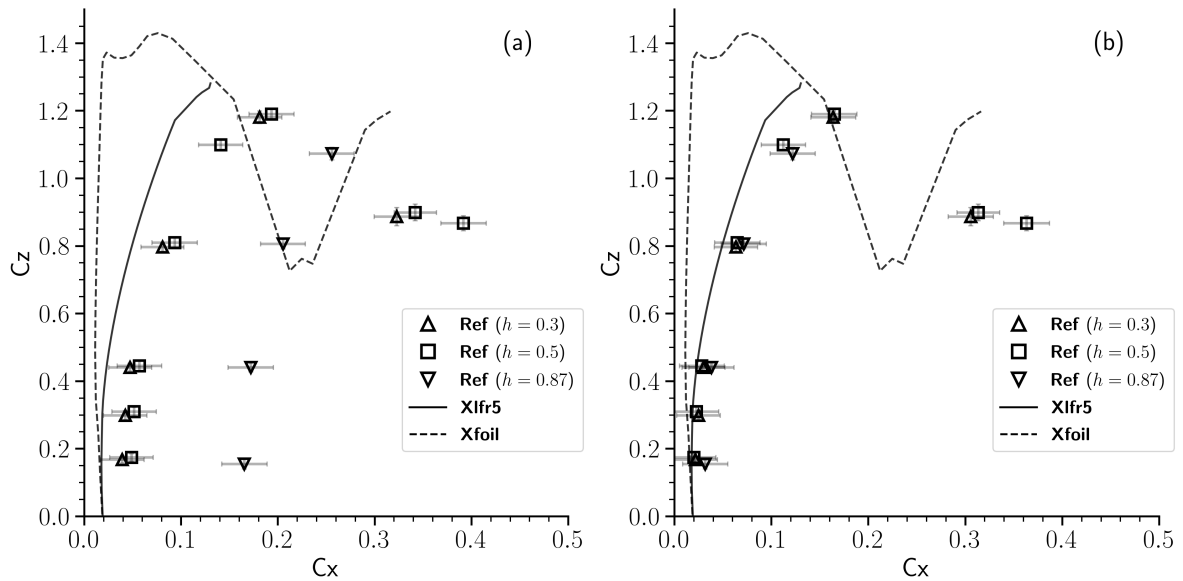


FIGURE B.6: Polars obtained experimentally (symbols) and numerically (lines) for the *Ref* wing towed at  $U_0 = 2.4 \text{ m/s}$  ( $Re_c \sim 2 \times 10^5$ ), **a)** without the correction for the strut drag, **b)** with the correction for the strut drag.

The dataset  $F_{x,\text{strut}}(h, U_0)$  allows us to mitigate the effects of water depth levels when comparing the aerodynamic force results from experiments conducted during the campaign. Fig. B.6 shows the polars obtained for experiments performed with the *Ref* wing at  $U_0 = 2.4 \text{ m/s}$  at three different water depths:  $h = 0.3 \text{ m}$ ,  $0.5 \text{ m}$ , and  $0.87 \text{ m}$ . In Fig. B.6a, where no correction is applied to the data, one can observe the effect of  $h$  on the polar. However, when the correction using the measurements from  $F_{x,\text{strut}}(h, U_0)$  is applied (as shown in Fig. B.6b) the results collapse, indicating that the effect of the water level has been successfully corrected. Furthermore, the corrected results yield values closer to the numerical prediction. This supports our previous assumption that the strut generates no efforts in the  $Z$  direction.

### Description of step 3.

Prior to each experiment in the campaign, a "self-zeroing" procedure is performed on the force probe to correct for any random drift that may occur over time. This drift can be caused by factors such as changes in ambient temperature or warm-up of the probe upon activation. Therefore, the "zeroing" procedure needs to be carried out recurrently and as close to the start of the experiment as possible. During this

procedure, the weight of the strut and wing is also corrected, which is beneficial for the purposes of measuring the generated lift only. However, to cope with cases where the initial "self-zeroing" results are not consistent, a second "self-zeroing" step is consistently conducted during the post-processing of results. This second step takes into account the data measured at the end of the experiment when the wing is once again at a standstill.

### B.3 Calibration of velocity field measurements

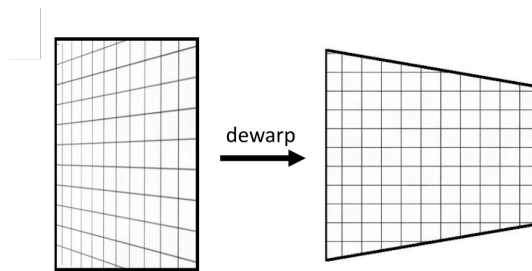


FIGURE B.7: Schematics of the image dewarping process.

The calibration of the cameras field of view is crucial for reconstructing the real space in which particles move. The dewarp image process is sketched in Fig. B.7. The precision of the spatial calibration directly impacts the reliable assessment of particle displacements. Our setup is stereoscopic, with two cameras positioned on opposite sides of the measurement plane. It is generally admitted [80] that measurement precision is enhanced by aligning the cameras orthogonal to each other. As explained in section 3.2.2.1, this is achieved in most experiments by placing  $45^\circ$  prisms between the cameras and the tank windows. The camera's point of view is defined by its position and orientation with respect to the measurement plane, along with lens focal length and its nominal magnification factor. Additionally, a slight angle is set between the lens plane and image plane of the cameras in order to obtain uniform focus across the measurement plane. This is referred to as a Sheimpflug setting and it is set on each camera by trial and error during the calibration process. Theoretically, knowing all of the information regarding the camera point of view allows us to correct for perspective deformations and perform image dewarping, enabling us to retrieve accurate space displacements. However, achieving precise control of the PIV setup parameters and accounting for nonlinear effects like lens distortions can pose challenges, making complete image dewarping often unfeasible.

Instead, a polynomial dewarping process that overcomes these limitations is used. To achieve this, a flat calibration target is employed, as depicted in Fig. B.8a, and analyze the image-to-object point pairs derived from it. This calibration procedure is analogous to a numerical determination of the geometric characteristics of the camera point of view. Regarding the accuracy of the velocity measurements, PIV studies where the accuracy of different stereo-reconstruction algorithms are compared [76, 95] show that the results obtained by image-mapping methods (such as the one employed in this work) give comparable results to those of more classical approaches, like the Soloff method, where the calibration target is displaced along the  $x$  direction during the calibration process. Thus, by representing the image deformation through a polynomial expression, one can accurately reconstruct the dewarped

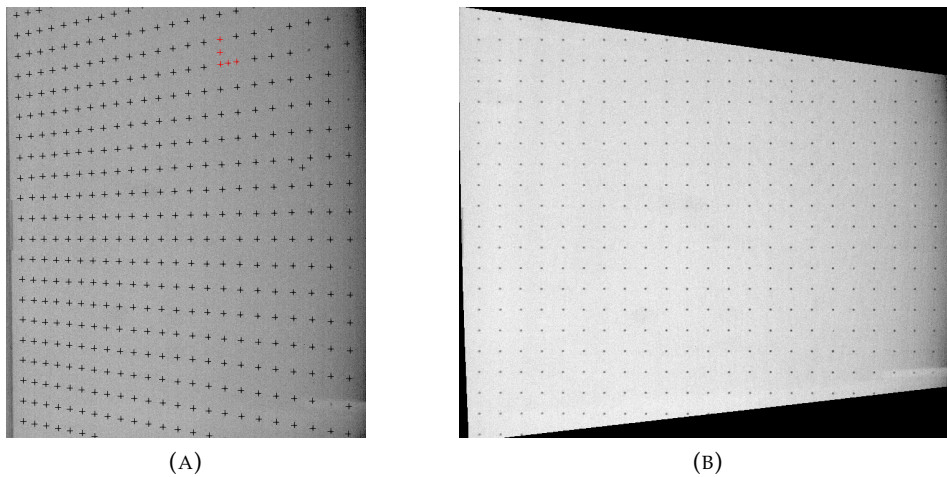


FIGURE B.8: Images, taken by camera 1, of the calibration target : **a)** warped image and **b)** dewarped image.

images. The dewarped image of camera 1 is shown in Fig. B.8b. An additional benefit of this process is the determination of the magnification factor. The calibration process was conducted approximately every two days, accounting for any minor displacements in the measurement setup that may occur during usage. The quality of the dewarping process is controlled by computing the error between the cartesian grid used as reference and the actual gridpoints that are detected in the dewarped image of the target (Fig. B.8b).

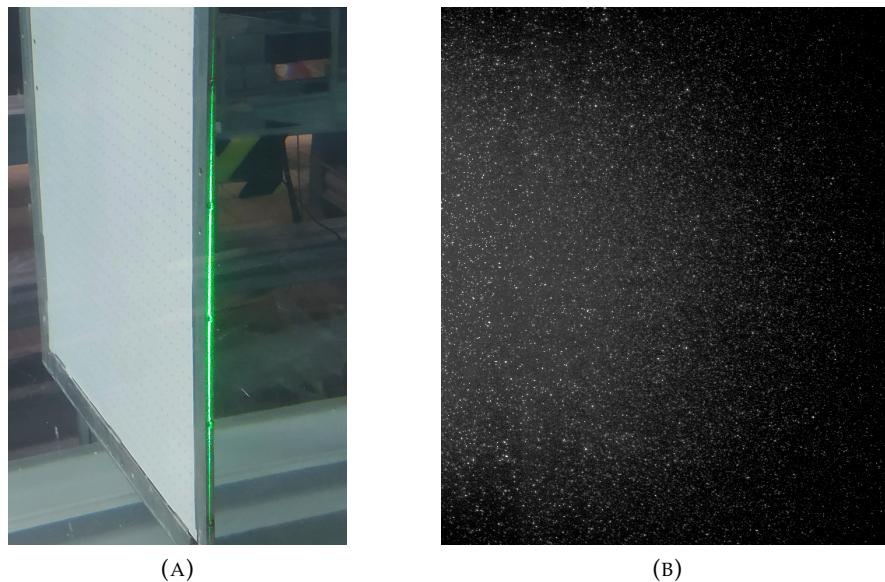


FIGURE B.9: **a)** Alignment of the laser plane with the calibration target. **b)** PIV picture of quiescent flow.

It is crucial that during measurements, the laser plane remains aligned with the position previously occupied by the calibration target to ensure accurate image dewarping. This alignment is first done manually, as shown in Fig. B.9a. Besides plane alignment, one also needs to address uneven lighting conditions across the image plane, as it can affect the accuracy of our measurements. An example of a warped

PIV image is depicted in Fig. B.9b, where the left side of the picture appears brighter than the right side. This uneven lighting occurs due to the diffusion of light in the water medium and the distribution of light along the laser plane, influenced by the optical setup. Notably, Fig. B.9a demonstrates that more laser light is focused at the middle of the plane than at the top and bottom regions (the mean laser plane thickness is of 3 mm). The uneven distribution of particles across the image space also contributes to the uneven lighting in the final image, as light reaches the cameras only when it bounces off a particle.

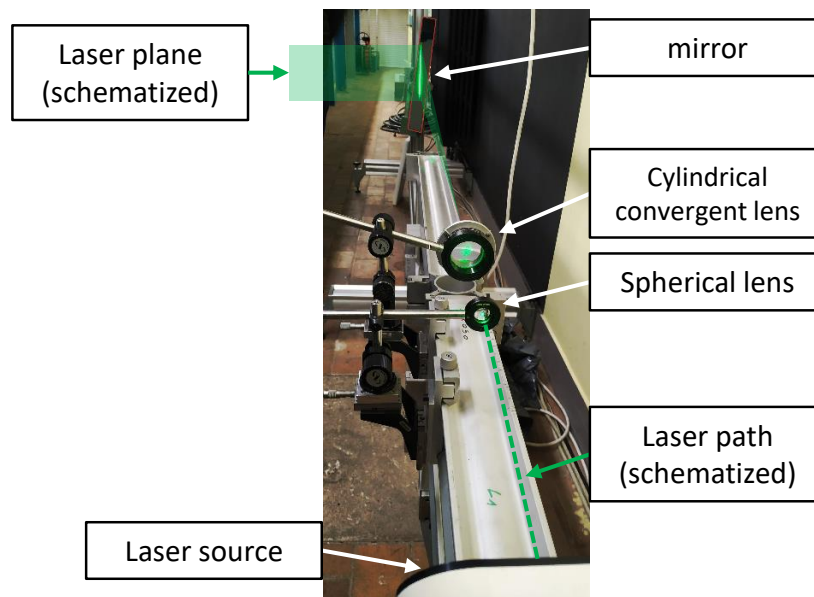


FIGURE B.10: Elements of the laser setup.

To ensure optimal lighting conditions, measurements of the flow are conducted in quiescent conditions. The setup quality is assessed by quantifying the correlation obtained across the plane and fine-tuning the optical setup of the laser through trial and error to achieve even correlation scores throughout the space. The components of the optical setup, as depicted in Fig. B.10, are adjusted to achieve this goal. Specifically, the parameters modified are the power output of the laser, the position and orientation of the optical lenses generating the laser plane, and the orientation of the mirror that directs the plane into the tank. Fig. B.11 illustrates the correlation fields on the still flow before and after this optimization procedure. In Fig. B.11a, the quality of measurements is degraded on the left side of the picture. However, after adjusting the elements of the optical setup, Fig. B.11b shows a correlation field with consistently good quality measurements across the entire space.

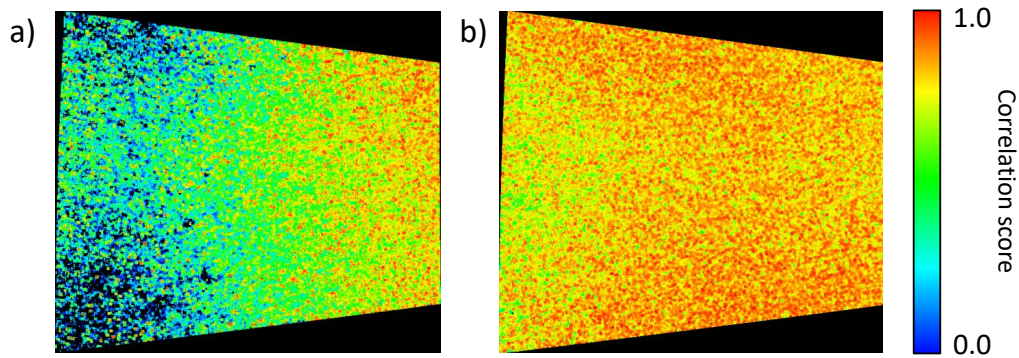


FIGURE B.11: Fields of correlation score measured **a)** before and **b)** after the laser alignment procedure.

## B.4 Time-synchronisation of the measurements

The timings in the movement of the wing  $X_{TE}(t)$ , force probe measurements  $F_i(t)$  and PIV measurements  $\mathbf{v}(X = X_{PIV}, t)$  are synchronized using a master clock that generates a TTL signal at 10Hz (denoted,  $TTL_{10}(t)$ ). The specialized hardware and acquisition rate corresponding to each quantity are provided in table B.2. In this paragraph the procedure to synchronize these measurements is detailed. This procedure is summarized in table B.3. An example of the synchronization data for an experiment is provided in Fig. B.12. The synchronization procedure is realized in the reference frame of the towing tank ( $X', t'$ ), where  $X'$  is the longitudinal position from the edge of the tank and  $t'$  the time elapsed since the onset of towing motion. In Fig. B.12a the evolution of the trailing edge position  $X_{TE}(t)$  is shown. The position of the sensors that trigger the acquisition of data is shown by a blue line and that of the PIV plane by a green line. Two gray regions are colored in Fig. B.12a : the first marks the time frame that is displayed in Fig. B.12b and the second marks the time frame displayed in Fig. B.12c.

To ensure synchronization of the data, the following procedure is carried out :

1. The time origin  $t' = 0$  is defined by the experiment initiation (the onset of the towing motion). The towing motion is triggered on the next rising edge of  $TTL_{10}(t)$ .
2. The towed wing pass through two gates, denoted  $trig, 1$  and  $trig, 2$ , located at the beginning of the course :  $X(t' = t_{trig,i}) = X_{trig,i}$ . In Fig. B.12a,  $X_{trig,1}$  is shown by a blue line.
3. The times  $t_{trig,1}$  and  $t_{trig,2}$  are precisely identified through an interpolation of the discrete  $X_{TE}(t')$  measurements.
4. The crossing of the gates results in two square signals  $TTL_{trig,1}$  and  $TTL_{trig,2}$  which are recorded by the force probe and by the PIV installation : These trigger signal is shown with a blue line in Fig. B.12b. Only the square wave of  $TTL_{trig,2}$  can be observed. The force probe acquisition is triggered on the falling edge of  $TTL_{trig,1}$ . The PIV acquisition is triggered on the falling edge of  $TTL_{trig,2}$ .

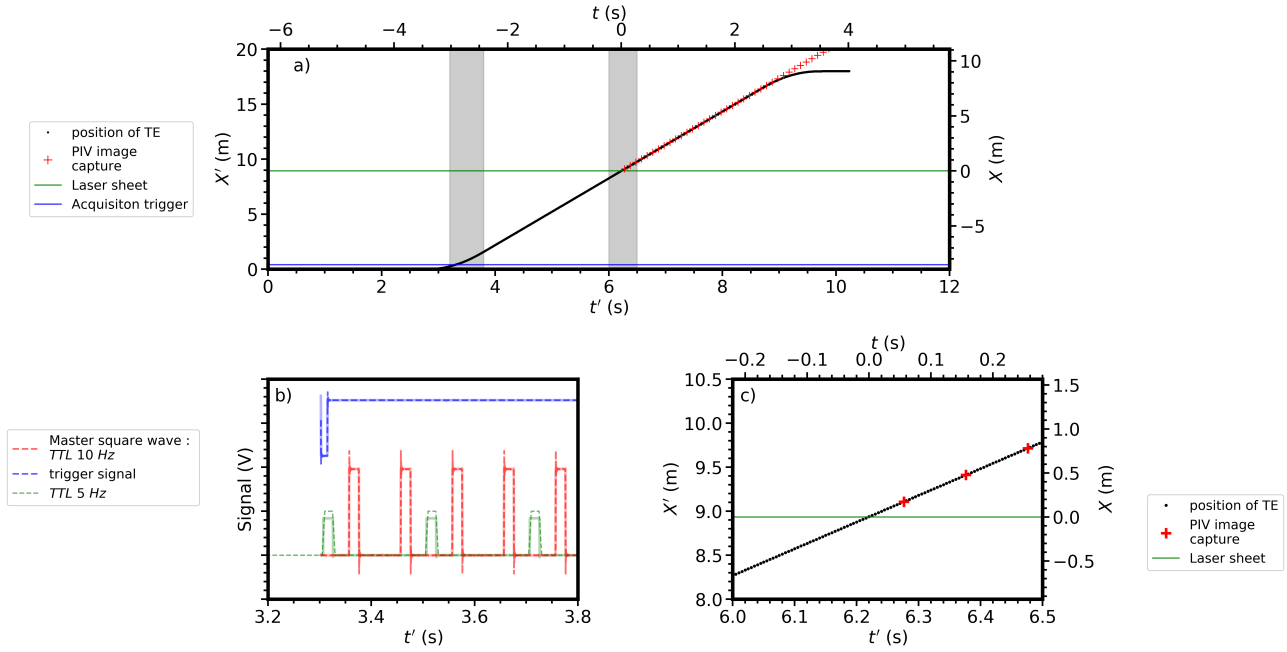


FIGURE B.12: Synchronisation procedure. **a)** Evolution of the trailing edge position  $X_{TE}(t)$  as a function of time. **b)** Synchronization signals recorded by the measurement hardware during  $3.2 < t' < 3.8$  s. **c)** Data recorded around  $t_{PIV}$  such that  $X_{TE}(t_{PIV}) = X_{PIV}$ .

5. Thus, the timing of the  $X_{TE}(t')$  data is synchronized with that of  $F_i(t')$  by comparing the signals  $TTL_{trig,1}$ . Conversely the  $X_{TE}(t')$  data is synchronized with that of  $\mathbf{v}(t')$  by comparing the signals  $TTL_{trig,2}$ .
6. Additionally, both the force probe and the PIV hardware record  $TTL_{10}(t)$  (shown in red in Fig. B.12b). Both the force probe and the position sensors record a reference signal at 5Hz,  $TTL_5(t)$  (shown in green in Fig. B.12b). The sound overlap of these signals in the synchronized data is an indicator that validates the procedure.
7. The towed wing crosses the PIV plane at  $t' = t_{PIV}$ . This instant is determined through an interpolation of  $X_{TE}(t)$  and accounting for the  $x$ -wise offset caused by the wing's angle of attack. Thus  $X_{TE}(t_{PIV}) = X_{PIV}$ .
8. By setting the origin at  $t' = t_{PIV}$ , the time  $t$  elapsed since crossing the PIV plane becomes the common time reference for all data. This can be observed with precision in B.12c. Here, the instants at which the PIV images are captured are shown by a red cross.

Thus, through this process, the data is recast into the reference frame of the wing motion  $(X, t)$ : where  $t$  is the time elapsed since the crossing of the measurement plane and where  $X$  is the longitudinal distance between the measurement plane and the wing TE. In this way, precise timing information is obtained for each of the PIV snapshots. Furthermore, this synchronization process ensures a repeatable PIV snapshot between different runs of the same experiment. This is validated in the PIV images since the wing maintains a consistent position at the same cliché number for a given towing velocity.

Quantity Measured	Hardware	Frequency Range (Hz)
$X_{TE}(t)$	Sensors and E1433 card	50 to 500
$F_i(t)$	Force Probe and E1403 card	1000 to 5000
$\mathbf{v}(X = X_{PIV}, t)$	PIV Hardware	5 to 10

TABLE B.2: Timing synchronization for the experimental data : the three measurements to synchronize are that of the trailing edge position  $X_{TE}(t)$ , the aerodynamic forces  $F_i(t)$  and the velocity field  $\mathbf{v}(X = X_{PIV}, t)$

Quantity Measured	Data Acquisition Trigger	Time Reference Frame
$X_{TE}(t)$	Chariot movement on the rising edge of $TTL_{10}(t)$	Origin at $t_{PIV}$ based on $X_{TE}(t)$
$F_i(t)$	Falling edge of $TTL_{trig,1}$ emitted by the gate	Recast into the same time frame
$\mathbf{v}(X = X_{PIV}, t)$	Falling edge of $TTL_{trig,2}$ emitted by the gate	Recast into the same time frame

TABLE B.3: Timing synchronization for the experimental data : the three measurements to synchronize are that of the trailing edge position  $X_{TE}(t)$ , the aerodynamic forces  $F_i(t)$  and the velocity field  $\mathbf{v}(X = X_{PIV}, t)$

## Appendix C

# Analysis of the uncertainty of the PIV measurement

The uncertainties associated with our velocity measurements obtained through PIV are analyzed in this section. This uncertainty is influenced by three main components: uncertainty in particle displacement estimation, timing, and image magnification. We quantify each source of uncertainty individually and then assess the overall uncertainty. In this study, we follow guidelines outlined by Raffel *et al.* [81] and Sciacitano [91].

We begin with the fundamental equation used to estimate the velocity magnitude  $v$  from the particle displacement  $d_m$  provided by PIV:

$$v = \frac{d_m}{dt} = \frac{d_{px}}{Mdt} \quad (\text{C.1})$$

Here,  $dt$  represents the time between successive frames, and  $d_{px}$  denotes the displacement in pixels. It's evident that  $d_m = d_{px}/M$ , with  $M$  being the magnification factor that represents the spatial dimension per pixel. By treating  $d_{px}$ ,  $dt$ , and  $M$  as independent variables, we can estimate the uncertainty in  $v$  using a Taylor series propagation method [91]:

$$\left(\frac{U_v}{v}\right)^2 = \left(\frac{U_{d_{px}}}{d_{px}}\right)^2 + \left(\frac{U_{dt}}{dt}\right)^2 + \left(\frac{U_M}{M}\right)^2 \quad (\text{C.2})$$

Where  $\frac{U_v}{v}$  is the uncertainty on the velocity measurements relative to the measured value. Furthermore,  $\frac{U_v}{v}$  relates to the uncertainty on the measurement realized by one camera only. Indeed, the stereoscopic arrangement of our measurement installation has an effect on the random uncertainty of out-of-plane measurements ( $v_x$ ) and on that of in-plane measurements ( $v_y, v_z$ ). This was shown by Prasad [79], who demonstrated that

$$\frac{U_{v_y}}{v_y} = \frac{U_{v_z}}{v_z} = \frac{U_v}{\sqrt{2}v} ; \quad \frac{U_{v_x}}{v_x} = \frac{\tan(\theta) U_v}{\sqrt{2} v} \quad (\text{C.3})$$

Where  $\theta$  is the semi-angle between the two cameras. On the experiments of this work where  $\theta = 45^\circ$ ,  $\tan(\theta) = 1$ , and on those where  $\theta = 37^\circ$ ,  $\tan(\theta) \approx 0.75$ . The factor  $\sqrt{2}$  stems from the fact that both cameras contribute equally to the final measurement result. Having defined the basis for our quantification of measurement uncertainty, the next step is to determine the contribution of each term in eq.C.2.

## Assessment of timing uncertainty

The uncertainty related to timing, denoted as  $U_{dt}$ , is addressed first. In our experimental setup, camera activation is synchronized with laser pulses using specialized hardware which is a Portable Timing Unit from LAVISION. The time interval  $dt$  between frames ranges from 1 to 10 milliseconds, which is small compared to the time scale of the vortex flow discussed in section 3.2.2.3. As a result, truncation errors in equation C.1 are negligible. The uncertainty  $U_{dt}$  in the inter-frame time is determined by the equipment manufacturer and is typically around  $U_{dt} = 1$  nanosecond.

## Assessment of uncertainty in magnification

Next, we consider the uncertainty associated with image magnification, denoted as  $U_M$ . This is linked to the calibration procedure performed before conducting experiments. It's important to note that due to the camera's angle relative to the measurement plane, the magnification factor is not constant but varies across the image. For computing  $\frac{U_M}{M}$ , we use the mean magnification value  $M$  from our PIV setup. Detailed guidelines for assessing  $U_M$  are provided in reference [15]. Uncertainty  $U_M$  arises from several sources :

- Uncertainty on the locations of dots on the calibration target,
- Errors in calculating calibration coefficients, which correct for perspective deformations caused by camera positioning, lens distortion, optical aberrations and refraction when light transitions from water to the tank window to the prisms medium to air.
- Misalignment between the calibration plane and the laser plane (measurement plane).

Possible errors due to misalignment between the measurement and camera planes are accounted for in the numerical image dewarping process (see appendix B). Assuming these variables to be uncorrelated, we can express the uncertainty in magnification  $U_M$  in terms of individual components:

$$\left(\frac{U_M}{M}\right)^2 = \left(\frac{U_s}{s}\right)^2 + \left(\frac{U_m}{m}\right)^2 + \left(\frac{U_l}{l}\right)^2 \quad (\text{C.4})$$

Here,  $s$ ,  $c$ , and  $l$  represent the uncertainty in dot positions, image dewarping, and alignment between the laser and the calibration target, respectively.

The dots in the calibration target are printed in and are spaced by  $s = 20 \text{ mm}$  (see Fig. B.8 for a photo of the calibration target). The printer's uncertainty is 0.1% of the instructed spacing, resulting in an estimated  $\frac{U_s}{s} = 0.001$ .

Error in the image dewarping procedure is provided by the calibration software. The mean squared error  $U_m$  between dewarped dot positions and grid positions is provided at the end of the dewarping procedure. A representative value from multiple calibrations during the experimental campaign is  $U_m = 2.1 \text{ px}$ . The spacing  $s$  on the dewarped image covers approximately  $m = s/M \sim 98.5$  pixels on average, leading to  $\frac{U_m}{m} = \frac{MU_m}{s}$ .

Uncertainty due to misalignment between the laser sheet and the calibration target is assessed. During a calibration, we adjust the alignment of the laser plane using the PIV software as shown in appendix B. After careful alignment, an offset

$l_t = 0.3mm$  is estimated relative to the middle of the target which is  $3mm$  in thickness. The alignment error  $\frac{U_l}{l}$  is proportional to  $\arctan(l_t/L_t)$ , where  $L_t = 500mm$  is the width of the calibrated image plane.

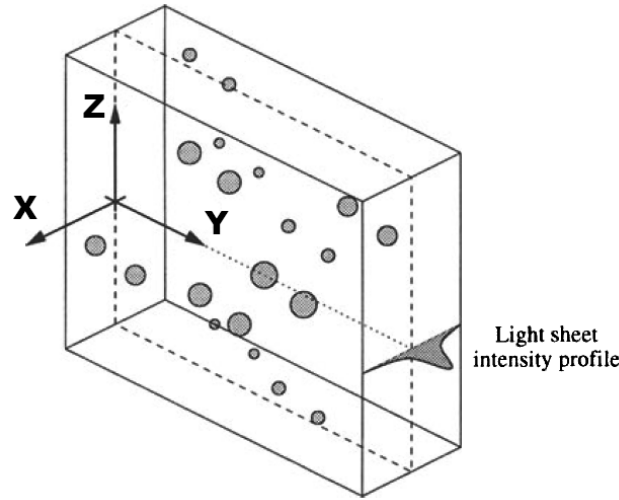


FIGURE C.1: From [81] : Schematics of the generation of artificial particle images : three-dimensional volume containing a light sheet and particles. Note that contrary to the picture, in our simulations the particle size is uniform.

## Analysis of the uncertainty in particle displacement using numerical simulations

The random errors in particle displacement, denoted as  $U_{d_{px}}$ , are estimated. These errors originate from both PIV software precision and image quality, influenced by factors such as particle image density, particle diameter, image noise, displacement amplitude, and velocity gradients[61]. Our investigation does not cover typical PIV software aspects like outlier detection due to the specific algorithm used in the FOLKI software. During our experimental campaign, we enhance correlation computation by optimizing the interrogation window size and applying pre-processing steps like background removal. However, in this assessment of  $U_{d_{px}}$ , we exclude the effects of interrogation window size and background removal.

To evaluate  $U_{d_{px}}$ , we opt to study the remaining parameters through numerical particle images input into our PIV software. We simulate a group of particles whose coordinates evolve within a 3D domain measuring  $2b_0 \times 1.5b_0 \times 6mm$ , as depicted in Fig. C.1. Two snapshots of this domain are taken, separated by  $dt = 5ms$ . The particle positions between  $t$  and  $t + dt$  follow a Lamb-Oseen vortex profile with center  $(y_c, z_c)$ . We denote  $d_{\perp}^{LO}(y, z)$  the field of in-plane particle displacement magnitude defined by this Lamb-Oseen vortex. Additionally, each particle's illumination is determined by its  $x$  coordinate, simulating a light sheet of thickness  $dz$  at  $x = 0$ . The illumination function  $I(x)$  follows a normal distribution with mean 0 and standard deviation  $\sigma = dz/6$ . Therefore half of the laser thickness is covered by  $3\sigma$ . This simulation accounts for particle overlap but not out-of-focus effects. Real images are affected by background noise in the camera sensor, but in our simulations no noise is added so we do not consider this effect. This approach allows us to control seeding density ( $N = P/m^2$ , where  $P$  is particle count) and particle diameter ( $\odot$ ) on

the images to assess their impact on displacement error. The vortex characteristics  $(\Gamma, R_d)$  in the simulation are chosen to result in particle displacements ( $d_{\perp}$ ) ranging from 0 to 10 pixels between two snapshots, resembling our experimental setup (see Fig. 3.12). The snapshots have dimensions of  $2160 \times 2560$  pixels, matching our camera snapshots. The representative magnification factor  $M = 2.03 \times 10^{-4} \text{ m}/\text{px}$  corresponds to the average magnification in our experiments. It is worth mentioning that, in a comparable investigation, Raffel [81] adopted a Monte-Carlo technique involving 1000 simulations for each parameter set, providing a complete statistical analysis of the effect of individual parameters on PIV uncertainty. In contrast, our study is limited to a single simulation per parameter set, a limitation primarily attributed to time constraints. Consequently, we interpret the outcomes of this study as an estimation of the magnitude of  $U_{d_{\text{px}}}$ . Nevertheless this approach is sufficient for our purpose of estimating the influence of the measurement parameters on the uncertainty in the context of this experiment.

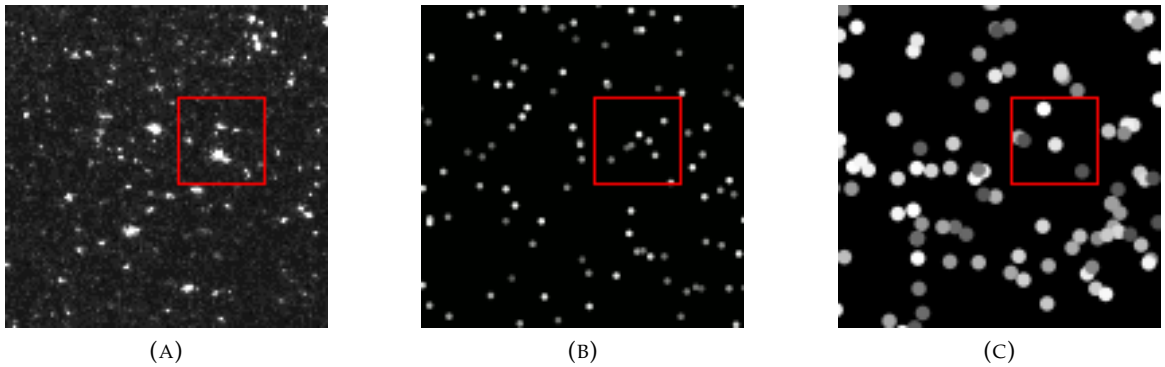


FIGURE C.2: Windows of dimension  $120 \times 120 \text{ px}$  extracted from images of particles **A)** during an experiment, **B)** simulated with  $\varnothing = 2 \text{ px}$  and  $N = 2.3 \times 10^5 \text{ P}/\text{m}^2$ , **C)** simulated with  $\varnothing = 6 \text{ px}$  and  $N = 2.3 \times 10^5 \text{ P}/\text{m}^2$ . An interrogation window of  $32 \times 32 \text{ px}$  is represented by a red square.

To illustrate our methodology, we compare two simulated images with a real image in Fig. C.2. Fig. C.2a is taken from a snapshot during our experimental campaign. The red square indicates a  $32 \times 32$ -pixel window, corresponding to the interrogation window size in this study. Information from this and other real snapshots helps estimate the parameters  $N$  and  $\varnothing$  that we set in our simulations. Particle counts in windows like Fig. C.2a range from 95 to 135, yielding  $N^{\text{exp}} \in [1.6 \times 10^5, 2.3 \times 10^5] \text{ P}/\text{m}^2$ . From this information, we set  $N^{\text{exp}} = 2.3 \times 10^5 \text{ P}/\text{m}^2$  as a representative value from our experiments. Additionally, particle diameters in the images vary from  $\varnothing \sim 2 \text{ px}$  to  $\varnothing \sim 6 \text{ px}$ . Simulations with  $\varnothing = 2 \text{ px}$  and  $\varnothing = 6 \text{ px}$  are shown in Fig. C.2b and C.2c, respectively. While improvements could involve diverse particle sizes and image noise, these images suffice for our objectives. They closely resemble real PIV images in terms of particle count per interrogation window and the dynamic range.

The next step is to obtain a quantification of the error that exists between the simulated displacement field  $d_{\perp}^{\text{LO}}(y, z)$  and the one obtained from the PIV software  $d_{\perp}^{\text{PIV}}(y, z)$ . A velocity field  $v_{\perp}^{\text{PIV}}(y, z)$  is extracted from the simulated particle images using the same software as the one used for our experiments. Thus,  $v_{\perp}^{\text{PIV}}(y, z)$  is defined over a discrete grid of size  $n_y, n_z$  so that  $(y, z) = (y_i, z_j)$  where  $i = 1, 2, \dots, n_y$  and  $j = 1, 2, \dots, n_z$ . The analysis parameters, like grid resolution and interrogation

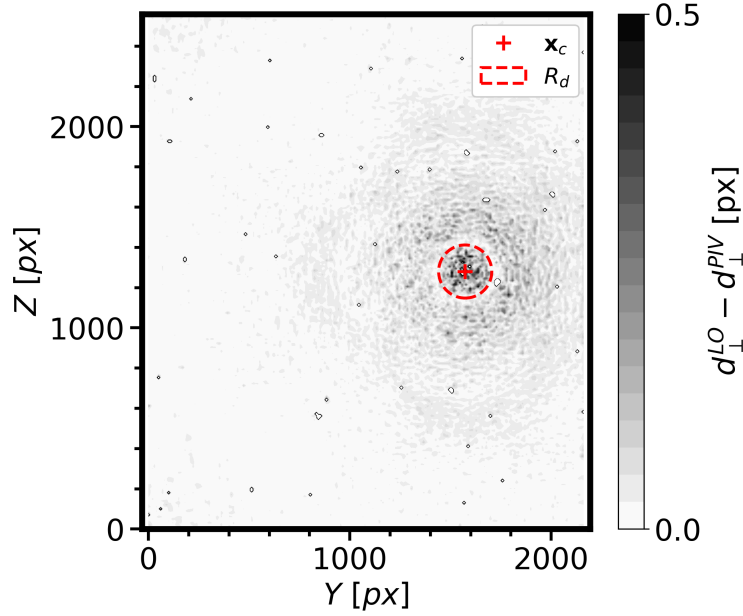


FIGURE C.3: Magnitude of the error in PIV displacement estimation,  $E_{\perp}(y, z)$ , over a simulated particles snapshot ( $N = N^{exp}, \varnothing = \varnothing^{exp}$ ). The vortex position and radius are shown by a red cross and dashed line, respectively.

window size are kept the same to those of the experiments. The velocity field is transformed into a displacement field following

$$d_{\perp}^{PIV}(y, z) = v_{\perp}^{PIV}(y, z) * dt \quad (C.5)$$

Next, we define  $E$  the error between the simulated field and the extracted field :

$$E_{\perp}(y, z) = d_{\perp}^{LO}(y, z) - d_{\perp}^{PIV}(y, z) \quad (C.6)$$

The field  $E_{\perp}(y, z)$  obtained for a simulation where  $N = N^{exp}$  and  $\varnothing = 4.5 px$  is shown in Fig. C.3. On the following we set  $\varnothing^{exp} = 4.5 px$  since this is an averaged value of the range of sizes observed in our experiments. In the figure, the vortex core is shown by a red dashed line. Errors in the displacement estimation are concentrated in regions where velocity gradients are significant, i.e. around the vortex core. However, small regions where errors reach peak values of  $> 0.5 px$  are randomly located on the field (these are shown in the figure as outlined white spots). Upon comparison with the PIV images we find that these are regions where almost no particles are present.

Now, we quantify the global error following two methodologies. The first consists in computing the root mean squared error in all of the gridpoints  $(y_i, z_j)$  following :

$$RMS_{2D}(E_{\perp}) = \left[ \frac{1}{n_y} \frac{1}{n_z} \sum_{i=1}^{n_y} \sum_{j=1}^{n_z} E_{\perp}(y_i, z_j)^2 \right]^{1/2} \quad (C.7)$$

We trace  $RMS_{2D}$  as a function of the seeding density  $N$  and as a function of particle size  $\varnothing$  in Fig.C.4a and b respectively. In Fig.C.4a, particle size is kept constant at  $\varnothing = \varnothing^{exp}$ . In Fig.C.4b, seeding density is kept constant at  $N = N^{exp}$ . First, we note that the seeding density in our experiments is close to the critical value for which the

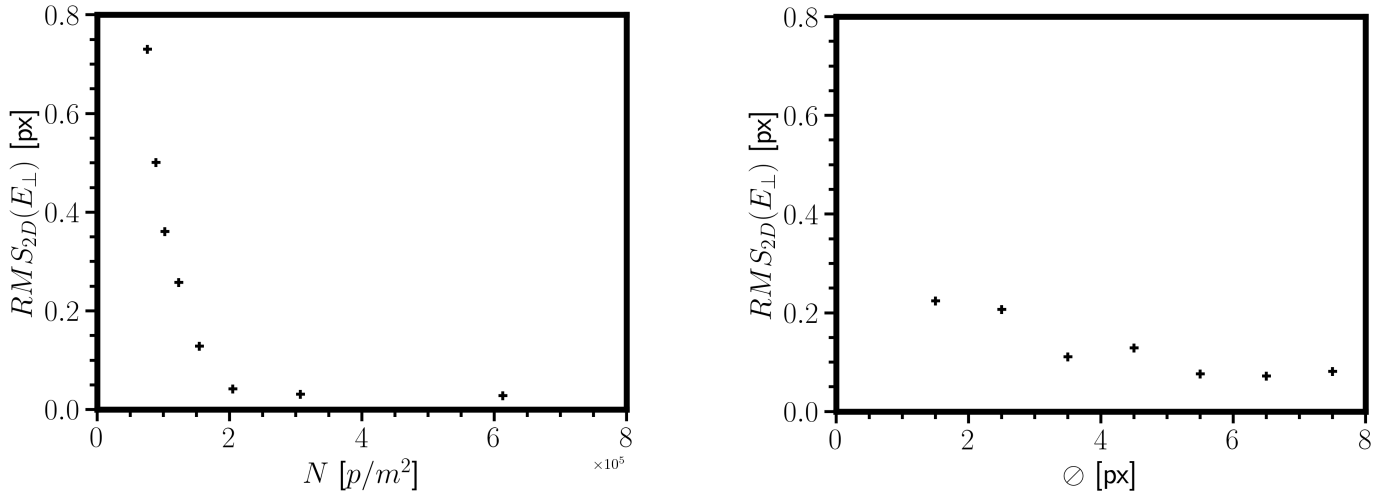


FIGURE C.4: Global root mean squared error  $RMS_{2D}(E_{\perp})$  as a function of **a)** seeding density  $N$  when  $\varnothing = \varnothing^{exp}$  and **b)** particle size  $\varnothing$  when  $N = N^{exp}$ .

density has little effect on the PIV error. Indeed, the simulations show that  $RMS_{2D}$  converges to  $0.04 \text{ px}$  for  $N \geq 2 \times 10^5 \text{ P/m}^2$ . If seeding density is reduced by a factor of 2 ( $N \sim 1 \times 10^5 \text{ P/m}^2$ ),  $RMS_{2D}$  grows to  $0.36 \text{ px}$  which is larger by a factor of 9. This is because the interrogation windows may contain few to no particles when  $N$  is low. Second, we observe that PIV error evolves significantly in the range of particle size of our experiments. Indeed,  $RMS_{2D} \sim 0.2$  for  $\varnothing = 2 \text{ px}$ , and  $RMS_{2D} \sim 0.1$  for  $\varnothing = 6 \text{ px}$ . The significant error at small particle sizes could be a consequence of "peak-locking" effect. These preliminary analysis provides a range for the particle displacement error  $U_{d_{px}}$  in the order of 0.1 to 0.2 px for our experiments.

We improve upon this result by assessing  $RMS$  as a function of the simulated displacement magnitude  $d_{\perp}^{LO}$ , computing, for a given value  $d'$  :

$$RMS_d(E_{\perp}, d') = \begin{cases} \left[ \frac{1}{n_y} \frac{1}{n_z} \sum_{i=1}^{n_y} \sum_{j=1}^{n_z} E_{\perp}(y_i, z_j)^2 \right]^{1/2} & , \text{if } d_{\perp}^{LO}(y_i, z_j) = d' \\ 0 & , \text{otherwise} \end{cases} \quad (\text{C.8})$$

It is seen that the error is a function of the displacement magnitude, with maxima at both  $d_{\perp}^{LO} \sim 0 \text{ px}$  and  $d_{\perp}^{LO} \sim 7 \text{ px}$ , and a minima at  $d_{\perp}^{LO} \sim 1.5 \text{ px}$ . We trace the evolution of  $RMS_d$  as a function of  $d_{\perp}^{LO}$  for different particle densities  $N$  in Fig.C.5. The effect of seeding density is seen in the magnitude of  $RMS_d$  at a given value of  $d_{\perp}^{LO}$  but it does not affect the distribution of  $RMSE(d)$ . For  $N = N^{exp}$ , a maximum error of  $RMS_d \sim 0.2 \text{ px}$  is obtained with low particle displacements  $d_{\perp}^{LO} < 1 \text{ px}$ .

Then, we trace the evolution of  $RMS_d$  as a function of  $d_{\perp}^{LO}$  for different particle sizes  $\varnothing$  in Fig.C.6. The effect of particle diameter on  $RMS_d$  seems negligible in the range of  $d_{\perp}^{LO}$  and  $\varnothing$  studied, except for small displacements  $1 \leq d_{\perp}^{LO} \leq 2$ . In this particular region, a larger error is estimated when  $\varnothing \sim 1.5 \text{ px}$ . However, in this region, the maximum magnitude of  $RMS_d$  is in the order of  $0.02 \text{ px}$ , which is negligible with respect to error estimated on  $d_{\perp}^{LO} \leq 1$  and on  $d_{\perp}^{LO} \geq 2$ .

Based on these findings, we deduce that, given the expected seeding density and sizes in our actual images ( $N \in [1.6 \times 10^5, 2.3 \times 10^5] \text{ P/m}^2$  and  $\varnothing \in [2, 6] \text{ px}$ ), we can estimate  $U_{d_{px}} = f(d_{px})$  by utilizing the results obtained for the simulations where

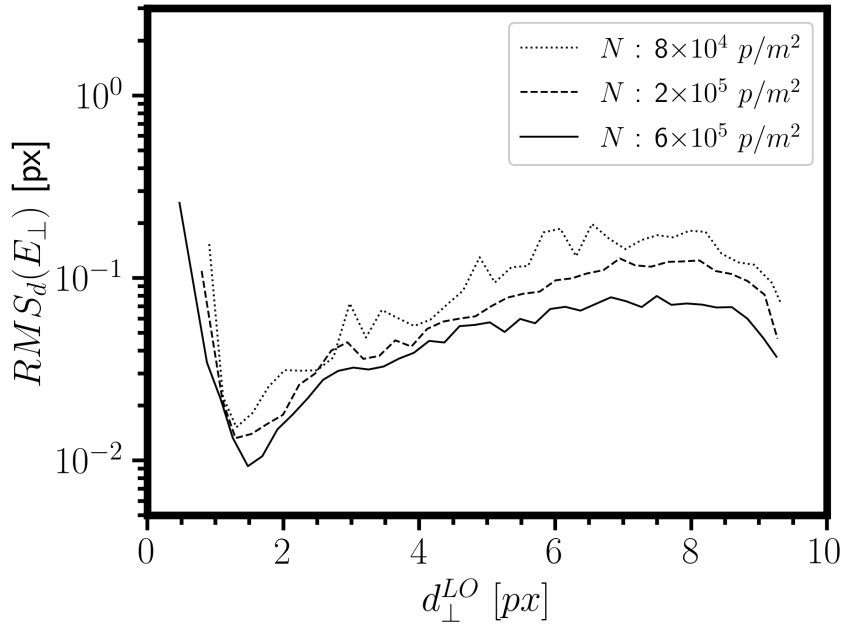


FIGURE C.5: Root mean squared error on the PIV measurements as a function of particle displacement magnitude  $d_{\perp}^{LO}$  and of seeding density  $N$ . Here,  $\varnothing = \varnothing^{exp}$

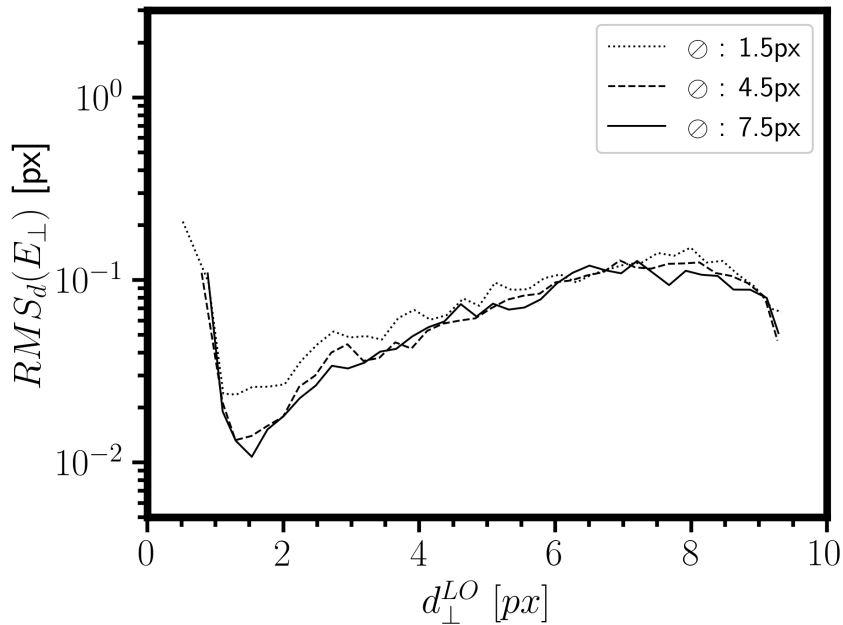


FIGURE C.6: Root mean squared error on the PIV measurements as a function of particle displacement magnitude  $d_{\perp}^{LO}$  and of particle diameter  $\varnothing$ . Here,  $N = N^{exp}$

$(\varnothing^{exp}, N^{exp})$ . Indeed, we can consider that, for a given  $d_{px}$ , the variation of  $U_{d_{px}}$  with respect to the parameters  $N$  and  $\varnothing$  is small. This leads to the relationship:

$$U_{d_{px}}(d_{px}) = RMS_d(N^{exp}, \varnothing^{exp}, d_{px}) \quad (C.9)$$

Now, we incorporate these results into eq. C.2. We plot  $|U_v/v|$  as a function of the estimated displacement  $d$  in Fig. C.7a. The magnitude of  $|U_v/v|$  is in the order of 3%

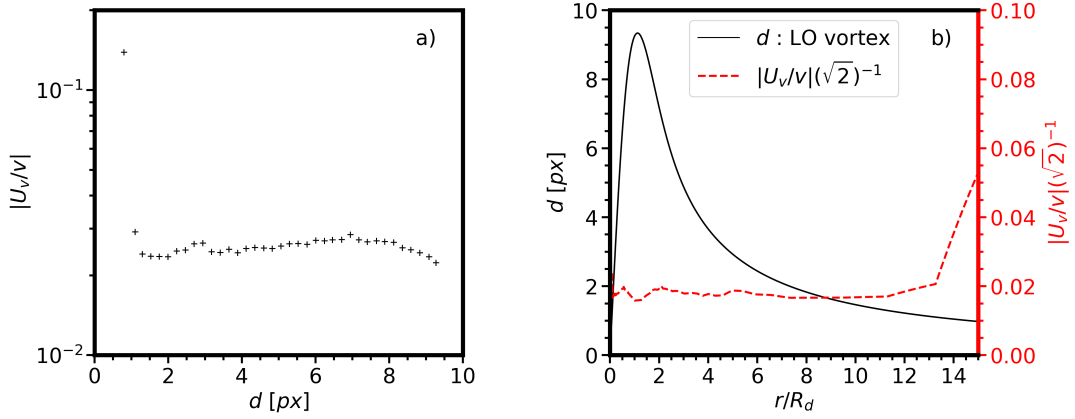


FIGURE C.7: Evolution of measurement uncertainty : **a)** uncertainty on the estimation of velocities on an artificial particle image  $|\frac{U_v}{v}|$  as a function of displacement magnitude  $d$  and **b)** stereoscopic uncertainty  $|\frac{U_v}{v}|(\sqrt{2})^{-1}$  over a Lamb-Oseen vortex for which particle pixel displacements range in  $d \in [0, 10]$  px

for most values of  $d$ , with the exception of very small displacements ( $d \sim 0$  px) where  $|U_v/v| \sim 15\%$ . Then we compute  $|U_v/v|(d)$  where  $d$  follows a typical vortex profile (see Fig. C.7b). We restrain our study to  $r/R_d \leq 15$  which is a conservative measure of the maximum radius at which we analyze velocity measurements in the experiments of this work. The stereoscopic aspect of our experiments is accounted for on the in-plane displacements with the factor  $(\sqrt{2})^{-1}$  following eq. C.3. Axial displacements would also yield an uncertainty of  $\frac{\tan(\theta)|U_v/v|(d)}{\sqrt{2}} = \frac{|U_v/v|(d)}{\sqrt{2}}$  since for most experiments  $\theta = 45^\circ$ . It becomes evident that, for most of the vortex, the displacement magnitude is big enough so that uncertainty is in the order of  $3/\sqrt{2} \approx 2.1\%$ . Far from the vortex, this uncertainty reaches a magnitude of 5% of  $v$ . Furthermore, we showed in sec. 3.2.2.3 that the inter-frame time  $dt$  is set on each experiment so that the particle displacement magnitude lies in the same range of  $[0, 10]$  px for every vortex flow, independently of the towing conditions. We deduce that, for the ensemble of our vortex velocity measurements, the PIV measurement uncertainty can be approximated to be around 2.1% in the region where the induced velocity field of the vortex is significant (this region can be estimated by  $r/R_d \leq 13$  in Fig. C.7b) and in the order of 5% in the rest of the flow where velocity is very weak ( $d < 1$  px).

In summary, our investigation focused on studying various sources of random errors in measurements obtained from our PIV setup. Negligible contributions from timing errors were observed, while magnification errors were found to be significant, given the complex dewarping and laser alignment procedures. To quantify displacement error uncertainty, we generated artificial particle images via numerical simulations and quantified displacement estimation errors that are related to the use of PIV software. The results indicated that velocity measurement uncertainty amounts to approximately 2.1% of the measured velocity magnitude, a level deemed adequate for our purposes. Nonetheless, the effect of certain factors remained unexplored in this study, primarily due to time constraints. A more comprehensive study of measurement uncertainty would require investigating the impact of the following aspects: inclusion of out-of-plane velocities resulting from the vortex or streamwise flow in the simulated particle images (this is particularly important in our work due to axial flow in the vortex core); closer examination of uncertainty in regions with significative velocity gradients, notably the core area; adjusting the simulation

settings for varying particle size, out-of-focus effects, and camera sensor noise to be more comparable with actual images; accounting for laser light diffusion through water by introducing a spanwise luminosity gradient in the artificial particle images; and a more rigorous statistical analysis of displacement errors, such as employing a Monte Carlo-like approach involving an extensive number of simulations for each parameter set.



## Appendix D

# Method for computing the average and standard deviation of combined sub-populations

In this appendix we provide a detailed description of the method we employ to combine the average value and standard deviation of given multiple sub-populations in order to estimate the average value and standard deviation of the global population.

Let two different populations be

$$x = (x_1, x_2, \dots, x_n) \quad (\text{D.1})$$

$$y = (y_1, y_2, \dots, y_m) \quad (\text{D.2})$$

$$(\text{D.3})$$

and the joint population be

$$z = (x_1, \dots, x_n, y_1, \dots, y_m) \quad (\text{D.4})$$

The average of population  $x$  is noted

$$\bar{x} = \frac{1}{n} \sum_{i=1}^n x_i \quad (\text{D.5})$$

and the biased estimator of the standard deviation of population  $x$  is noted

$$s_x = \sqrt{\frac{1}{n} \sum_{i=1}^n (x_i - \bar{x})^2} \quad (\text{D.6})$$

note that  $s_x^2$  is the variance of  $x$ . The mean value of the global population  $\bar{z}$  can also be expressed in terms of the means of the sub-populations  $\bar{x}$  and  $\bar{y}$ :

$$\bar{z} = \frac{\sum_{i=1}^n x_i + \sum_{i=1}^m y_i}{n + m} = \frac{n\bar{x} + m\bar{y}}{n + m} \quad (\text{D.7})$$

Regarding the variance of the global population, we note

$$s_z^2 = \frac{\sum_{i=1}^n (x_i - \bar{z})^2 + \sum_{j=1}^m (y_j - \bar{z})^2}{n + m} \quad (\text{D.8})$$

we can express  $s_z^2$  as a function of the known variances  $s_x^2$ ,  $s_y^2$  and means  $\bar{x}$ ,  $\bar{y}$  and  $\bar{z}$  by decomposing the sums of squares as follows :

$$(x_i - \bar{z})^2 = (x_i - \bar{x} + \bar{x} - \bar{z})^2 = (x_i - \bar{x})^2 + 2(x_i - \bar{x})(\bar{x} - \bar{z}) + (\bar{x} - \bar{z})^2 \quad (\text{D.9})$$

and then

$$\sum_{i=1}^n (x_i - \bar{z})^2 = ns_x^2 + 2(\bar{x} - \bar{z}) \sum_{i=1}^n (x_i - \bar{x}) + n(\bar{x} - \bar{z})^2 \quad (\text{D.10})$$

The term in the middle vanishes since  $\sum_{i=1}^n (x_i - \bar{x}) = n\bar{x} - n\bar{x}$ . Finally, the expression for  $s_z^2$  is

$$s_z^2 = \frac{ns_x^2 + n(\bar{x} - \bar{z})^2 + ms_y^2 + m(\bar{y} - \bar{z})^2}{n + m} \quad (\text{D.11})$$

# Bibliography

- [1] Advisory Group for Aerospace Research and Development. *The characterization and modification of wakes from lifting vehicles in fluids*. AGARD, 1996. ISBN: 9283600347.
- [2] J. D. Anderson. *Fundamentals of Aerodynamics (6th edition)*. 3. 2011, p. 1128. ISBN: 9780071289085.
- [3] S. Arendt, D. Fritts, and Ø. Andreassen. “The initial value problem for Kelvin vortex waves”. In: *Journal of Fluid Mechanics* 344 (1997), pp. 181–212. ISSN: 0022-1120. DOI: [10.1017/S0022112097005958](https://doi.org/10.1017/S0022112097005958).
- [4] G. K. Batchelor. *An Introduction to Fluid Dynamics*. Cambridge University Press, 1967. ISBN: 9780511800955. DOI: [10.1017/CB09780511800955](https://doi.org/10.1017/CB09780511800955).
- [5] G. K. Batchelor. “Axial flow in trailing line vortices”. In: *Journal of Fluid Mechanics* 20.4 (1964), pp. 645–658.
- [6] A. Betz. “Behaviour of Vortex Systems”. In: XII.3 (1932), pp. 164–174. DOI: [10.1002/zamm.19320120307](https://doi.org/10.1002/zamm.19320120307).
- [7] A. Betz. *Screw propellers with Minimum Energy Loss*. Tech. rep. Göttingen Reports, 1919.
- [8] C. Breitsamter. “Wake vortex characteristics of transport aircraft”. In: *Progress in Aerospace Sciences* 47.2 (2011), pp. 89–134. ISSN: 03760421. DOI: [10.1016/j.paerosci.2010.09.002](https://doi.org/10.1016/j.paerosci.2010.09.002).
- [9] V. Brion and L. Jacquin. “Measurements of a turbulent vortex pair using time resolved PIV”. In: *6th AIAA Theoretical Fluid Mechanics Conference*. June. 2011, pp. 1–15. DOI: [10.2514/6.2011-3892](https://doi.org/10.2514/6.2011-3892).
- [10] V. Brion, D. Sipp, and L. Jacquin. “Optimal amplification of the Crow instability”. In: *Physics of Fluids* 19.11 (2007). ISSN: 10706631. DOI: [10.1063/1.2793146](https://doi.org/10.1063/1.2793146).
- [11] R. L. Bristol, J. M. Ortega, P. S. Marcus, and Ö Savaş. “On cooperative instabilities of parallel vortex pairs”. In: *Journal of Fluid Mechanics* (2004). ISSN: 00221120. DOI: [10.1017/S0022112004001016](https://doi.org/10.1017/S0022112004001016).
- [12] R. L. Bristol, J. M. Ortega, and Ö Savaş. “Experimental study of corotating wake-vortex merger at Reynolds numbers of order 10<sup>5</sup>”. In: *AIAA Journal* 41.4 (2003), pp. 741–744. ISSN: 00011452. DOI: [10.2514/2.2006](https://doi.org/10.2514/2.2006).
- [13] C. Brossard, J.-C. Monnier, P. Barricau, F. Vandernoot, Y. Le Sant, F. Champagnat, and G. Le Besnerais. “Principles and applications of particle image velocimetry”. In: *Onera AerospaceLab Journal* 1 (2009), pp. 1–11.
- [14] D. C. Burnham. “How to Use Wake Vortex Measurements to Set Separation Standards”. In: *Proceedings of the Aircraft Wake Vortices Conference*. 1991.

- [15] A A Campagnole dos Santos, M Childs, T D Nguyen, and Y Hassan. "Convergence study and Uncertainty quantification of average and statistical PIV measurements in a matched refractive index 5x5 rod bundle with mixing vane spacer grid". In: *Experimental Thermal and Fluid Science* 102.215–31 (2018).
- [16] F. Champagnat, A. Plyer, G. Le Besnerais, B. Leclaire, S. Davoust, and Y. Le Sant. "Fast and accurate PIV computation using highly parallel iterative correlation maximization". In: *Experiments in Fluids* 50.4 (2011), pp. 1169–1182. ISSN: 07234864. DOI: [10.1007/s00348-011-1054-x](https://doi.org/10.1007/s00348-011-1054-x).
- [17] A. L. Chen, J. D. Jacob, and Ö Savaş. *Dynamics of corotating vortex pairs in the wakes of flapped airfoils*. Vol. 382. 1999, pp. 155–193. ISBN: 0022112098003. DOI: [10.1017/S0022112098003814](https://doi.org/10.1017/S0022112098003814).
- [18] P. M. Condit and P. W. Tracy. "Results of the Boeing Company Wake Turbulence Test Program". In: *Aircraft Wake Turbulence and Its Detection*. Boston, MA: Springer US, 1971, pp. 473–508. ISBN: 2013206534. DOI: [10.1007/978-1-4684-8346-8\\_25](https://doi.org/10.1007/978-1-4684-8346-8_25).
- [19] J. D. Crouch. "Airplane trailing vortices and their control". In: *Comptes Rendus de Physique* 6.4-5 SPEC. ISS. (2005), pp. 487–499. ISSN: 16310705. DOI: [10.1016/j.crhy.2005.05.006](https://doi.org/10.1016/j.crhy.2005.05.006).
- [20] J. D. Crouch. "Instability and transient growth for two trailing-vortex pairs". In: *35th Aerospace Sciences Meeting and Exhibit* 350 (1997), pp. 311–330. DOI: [10.2514/6.1997-62](https://doi.org/10.2514/6.1997-62).
- [21] J. D. Crouch, G. Miller, and P. Spalart. "Active-Control System for Breakup of Airplane Trailing Vortices". In: 39.12 (2001).
- [22] S.C. Crow. "Stability Theory for a Pair of Trailing Vortices". In: *AIAA Journal* 8.12 (1970), pp. 2172–2179. DOI: <https://doi.org/10.2514/3.6083>.
- [23] C. Dalton and X. Wang. "The vortex roll-up problem using Lamb vortices for the elliptically loaded wing". In: *Computers and Fluids* 18.1 (1990), pp. 139–150. ISSN: 00457930. DOI: [10.1016/0045-7930\(90\)90006-J](https://doi.org/10.1016/0045-7930(90)90006-J).
- [24] I. Delbende, J. M. Chomaz, and P. Huerre. "Absolute/convective instabilities in the Batchelor vortex: a numerical study of the linear impulse response". In: *Journal of Fluid Mechanics* 355 (1998), pp. 229–254.
- [25] M. Dghim, M. Ferchichi, and H. Fellouah. "Mid-wake wing tip vortex dynamics with active flow control". In: *Experimental Thermal and Fluid Science* 98 (2018), pp. 38–55. DOI: [10.1016/j.expthermflusci.2018.05.011](https://doi.org/10.1016/j.expthermflusci.2018.05.011).
- [26] C. P. Donaldson and A. J. Bilanin. "Vortex Wakes of Conventional Aircraft." In: *Advisory Group for Aerospace Research and Development*. 204. 1975.
- [27] D. G. Dritschel. "The stability and energetics of corotating uniform vortices". In: *Journal of Fluid Mechanics* 157 (1985), pp. 95–134. ISSN: 14697645. DOI: [10.1017/S0022112085002324](https://doi.org/10.1017/S0022112085002324).
- [28] A. M. Edstrand, Y. Sun, P. J. Schmid, K. Taira, and L. N. Cattafesta. "Active attenuation of a trailing vortex inspired by a parabolized stability analysis". In: *Journal of Fluid Mechanics* 855 (2018), pp. 1–12. ISSN: 14697645. DOI: [10.1017/jfm.2018.701](https://doi.org/10.1017/jfm.2018.701). arXiv: [1806.07327](https://arxiv.org/abs/1806.07327).
- [29] D. Fabre. *Instabilités et instationnarités dans les tourbillons applications aux sillages d'avions*. 1st ed. Chatillon: ONERA, 2002.

- [30] D. Fabre and L. Jacquin. “Stability of a four-vortex aircraft wake model”. In: *Physics of Fluids* 12.10 (2000), pp. 2438–2443. ISSN: 10706631. DOI: [10.1063/1.1289397](https://doi.org/10.1063/1.1289397).
- [31] D. Fabre and L. Jacquin. “Viscous instabilities in trailing vortices at large swirl numbers”. In: *Journal of Fluid Mechanics* 500.500 (2004), pp. 239–262. ISSN: 00221120. DOI: [10.1017/S0022112003007353](https://doi.org/10.1017/S0022112003007353).
- [32] D. Fabre, L. Jacquin, and A. Loof. “Optimal perturbations in a four-vortex aircraft wake in counter-rotating configuration”. In: *Journal of Fluid Mechanics* 451 (2002), pp. 319–328. ISSN: 0022-1120. DOI: [10.1017/s0022112001006954](https://doi.org/10.1017/s0022112001006954).
- [33] D. Fabre, D. Sipp, and L. Jacquin. “Kelvin waves and the singular modes of the Lamb-Oseen vortex”. In: *Journal of Fluid Mechanics* 551 (2006), pp. 235–274. ISSN: 14697645. DOI: [10.1017/S0022112005008463](https://doi.org/10.1017/S0022112005008463).
- [34] T. Gerz, F. Holzäpfel, and D. Darracq. “Commercial aircraft wake vortices”. In: *Progress in Aerospace Sciences* 38.3 (2002), pp. 181–208. ISSN: 03760421. DOI: [10.1016/S0376-0421\(02\)00004-0](https://doi.org/10.1016/S0376-0421(02)00004-0).
- [35] H. Glauert. *The Elements of Aerofoil and Airscrew Theory*. Cambridge University Press, 1926.
- [36] L. Graftieaux, M. Michard, and N. Grosjean. “Combining PIV, POD and vortex identification algorithms for the study of unsteady turbulent swirling flows”. In: *Measurement Science and Technology* 12.9 (2001), pp. 1422–1429. ISSN: 09570233. DOI: [10.1088/0957-0233/12/9/307](https://doi.org/10.1088/0957-0233/12/9/307).
- [37] J. N. Hallock and D. C. Burnham. “Decay characteristics of wake vortices from jet transport aircraft”. In: *35th Aerospace Sciences Meeting and Exhibit*. 1997. DOI: [10.2514/6.1997-60](https://doi.org/10.2514/6.1997-60).
- [38] J. N. Hallock and F. Holzäpfel. *A review of recent wake vortex research for increasing airport capacity*. 2018. DOI: [10.1016/j.paerosci.2018.03.003](https://doi.org/10.1016/j.paerosci.2018.03.003).
- [39] H. Helmholtz. “Über Integrale der hydrodynamischen Gleichungen, welche den Wirbelbewegungen entsprechen.” In: *Journal für die reine und angewandte Mathematik (Crelles Journal)* 1858.55 (1858), pp. 25–55. ISSN: 0075-4102. DOI: [10.1515/crll.1858.55.25](https://doi.org/10.1515/crll.1858.55.25). URL: <https://www.degruyter.com/document/doi/10.1515/crll.1858.55.25/html>.
- [40] H.W.M. Hoeijmakers. “Vortex Wakes in Aerodynamics”. In: *The Characterisation and Modification of Wakes from Lifting Vehicles in Fluids*. 1996.
- [41] K. Hutter, Y. Wang, and I. P. Chubarenko. *Phenomenological Coefficients of Waker*. September 2015. 2011, pp. 389–418. ISBN: 9783642151781. DOI: [10.1007/978-3-642-15178-1\\_10](https://doi.org/10.1007/978-3-642-15178-1_10).
- [42] International Civil Aviation Organization (ICAO). *Air Traffic Services Planning Manual*. Tech. rep. 1984.
- [43] L. Jacquin, D. Fabre, P. Geffroy, and E. Coustols. “The properties of a transport aircraft wake in the extended near field - An experimental study”. In: *39th Aerospace Sciences Meeting and Exhibit*. Reston, Virginia: American Institute of Aeronautics and Astronautics, 2001. DOI: [10.2514/6.2001-1038](https://doi.org/10.2514/6.2001-1038). URL: <https://arc.aiaa.org/doi/10.2514/6.2001-1038>.
- [44] L. Jacquin, D. Fabre, D. Sipp, and E. Coustols. “Unsteadiness, instability and turbulence in trailing vortices”. In: *Comptes Rendus Physique* 6.4-5 SPEC. ISS. (2005), pp. 399–414. ISSN: 16310705. DOI: [10.1016/j.crhy.2005.05.007](https://doi.org/10.1016/j.crhy.2005.05.007).

- [45] L. Jacquin and C. Pantano. "On the persistence of trailing vortices". In: *Journal of Fluid Mechanics* 471 (2002), pp. 159–168. ISSN: 00221120. DOI: [10.1017/S0022112002002161](https://doi.org/10.1017/S0022112002002161).
- [46] J. Jimenez. "Stability of a pair of co-rotating vortices". In: *The Physics of Fluids* 18.11 (1975), pp. 1580–1581. ISSN: 0031-9171. DOI: [10.1063/1.861056](https://doi.org/10.1063/1.861056). URL: <https://pubs.aip.org/pfl/article/18/11/1580/437222/Stability-of-a-pair-of-co-rotating-vortices>.
- [47] H. Kaden. "Aufwicklung einer unstabilen unstetigkeitsflache." In: *Ing. Arch.* 2 (1931), p. 140.
- [48] R. D. Keane, R. J. Adrian, and Y. Zhang. "Super-resolution particle imaging velocimetry". In: *Measurement Science and Technology* 6.6 (1995), pp. 754–768. ISSN: 0957-0233. DOI: [10.1088/0957-0233/6/6/013](https://doi.org/10.1088/0957-0233/6/6/013). URL: <https://iopscience.iop.org/article/10.1088/0957-0233/6/6/013>.
- [49] F. Klein. "Über die Bildung von Wirbeln in reibungslosen Flüssigkeiten". In: *Z. Math. Phys* 59 (1910), pp. 259–262.
- [50] R. Krasny. "Computation of vortex sheet roll-up in the Trefftz plane". In: *Journal of Fluid Mechanics* 184 (1987), pp. 123–155. ISSN: 14697645. DOI: [10.1017/S0022112087002830](https://doi.org/10.1017/S0022112087002830).
- [51] H. Lamb. *Hydrodynamics*. 6th ed. Cambridge University Press, 1932. ISBN: 9780521458689.
- [52] F. Laporte and T. Leweke. "Elliptic instability of counter-rotating vortices: Experiment and direct numerical simulation". In: *AIAA Journal* 40.12 (2002), pp. 2483–2494. ISSN: 00011452. DOI: [10.2514/2.1592](https://doi.org/10.2514/2.1592).
- [53] G. Le Besnerais and F. Champagnat. "Dense optical flow by iterative local window registration". In: *Proceedings - International Conference on Image Processing, ICIP*. 2005. ISBN: 0780391349. DOI: [10.1109/ICIP.2005.1529706](https://doi.org/10.1109/ICIP.2005.1529706).
- [54] S. Le Dizès and A. Verga. "Viscous interactions of two co-rotating vortices before merging". In: *Journal of Fluid Mechanics* 467 (2002), pp. 389–410. ISSN: 0022-1120. DOI: [10.1017/S0022112002001532](https://doi.org/10.1017/S0022112002001532). URL: [https://www.cambridge.org/core/product/identifier/S0022112002001532/type/journal\\_article](https://www.cambridge.org/core/product/identifier/S0022112002001532/type/journal_article).
- [55] B. Leclaire, B. Jaubert, F. Champagnat, G. Le Besnerais, and Y. Le Sant. "FOLKI-3C : a Simple , Fast and Direct Algorithm for Stereo PIV". In: *8TH International symposium on particle image velocimetry 3* (2009), pp. 2–5.
- [56] M. Lessen and F. Paillet. "The stability of a trailing line vortex. Part 2. Viscous theory". In: *Journal of Fluid Mechanics* 65.4 (1974), pp. 769–779. ISSN: 14697645. DOI: [10.1017/S0022112074001649](https://doi.org/10.1017/S0022112074001649).
- [57] T. Leweke, S. Le Dizès, and C. H. K. Williamson. "Dynamics and Instabilities of Vortex Pairs". In: *Annual Review of Fluid Mechanics* 48.1 (2016), pp. 507–541. ISSN: 0066-4189. DOI: [10.1146/annurev-fluid-122414-034558](https://doi.org/10.1146/annurev-fluid-122414-034558).
- [58] T. Leweke and C. H.K. Williamson. "Experiments on long-wavelength instability and reconnection of a vortex pair". In: *Physics of Fluids* 23.2 (2011). ISSN: 10706631. DOI: [10.1063/1.3531720](https://doi.org/10.1063/1.3531720).
- [59] H. T. Liu. "Effects of ambient turbulence on the decay of a trailing vortex wake". In: *Journal of Aircraft* 29.2 (1992), pp. 255–263. ISSN: 00218669. DOI: [10.2514/3.46153](https://doi.org/10.2514/3.46153).

- [60] E. W. Mayer and K. G. Powell. "Viscous and inviscid instabilities of a trailing vortex". In: *Journal of Fluid Mechanics* 245 (1992), pp. 91–114. ISSN: 14697645. DOI: [10.1017/S0022112092000363](https://doi.org/10.1017/S0022112092000363).
- [61] P. Meunier. "Etude expérimentale de deux tourbillons corotatifs". PhD thesis. Université de Provence Aix-Marseille I, 2001.
- [62] P. Meunier, S. Le Dizès, and T. Leweke. "Physics of vortex merging". In: *Comptes Rendus Physique* 6.4-5 SPEC. ISS. (2005), pp. 431–450. ISSN: 16310705. DOI: [10.1016/j.crhy.2005.06.003](https://doi.org/10.1016/j.crhy.2005.06.003).
- [63] A. Mille. *Etude analytique et numérique des instabilités coopératives des tourbillons de sillage*. Tech. rep. Lille: ONERA - Internal Report, 2021.
- [64] F. Moens. *Lois de charge pour les essais au bassin de traction*. Tech. rep. Meudon: ONERA - Internal Report, 2018.
- [65] H. Moet, F. Laforte, and T. Poinso. "Wave propagation in vortices and vortex bursting". In: *Physics of Fluids* 17.5 (2005), pp. 1–15. ISSN: 10706631. DOI: [10.1063/1.1896937](https://doi.org/10.1063/1.1896937).
- [66] D. W. Moore. "A numerical study of the roll-up of a finite vortex sheet". In: *Journal of Fluid Mechanics* 63.2 (1974), pp. 225–235.
- [67] D. W. Moore and P. G. Saffman. "Axial flow in laminar trailing vortices". In: *Proceedings of the Royal Society of London. A. Mathematical and Physical Sciences* 333.1595 (1973), pp. 491–508. ISSN: 2053-9169. DOI: [10.1098/rspa.1973.0075](https://doi.org/10.1098/rspa.1973.0075).
- [68] D. W. Moore and P. G. Saffman. "The motion of a vortex filament with axial flow". In: *Philosophical Transactions of the Royal Society of London. Series A, Mathematical and Physical Sciences* 272.1226 (1972), pp. 403–429. ISSN: 0080-4614. DOI: [10.1098/rsta.1972.0055](https://doi.org/10.1098/rsta.1972.0055).
- [69] S. E. Morris and C. H. K. Williamson. "Impingement of a counter-rotating vortex pair on a wavy wall". In: *Journal of Fluid Mechanics* (2020), pp. 1–31. ISSN: 14697645. DOI: [10.1017/jfm.2020.263](https://doi.org/10.1017/jfm.2020.263).
- [70] Navrose, V. Brion, and L. Jacquin. "Transient growth in the near wake region of the flow past a finite span wing". In: *Journal of Fluid Mechanics* 866 (2019), pp. 399–430. ISSN: 14697645. DOI: [10.1017/jfm.2019.110](https://doi.org/10.1017/jfm.2019.110).
- [71] Navrose, H. Johnson, V. Brion, L. Jacquin, and J. C. Robinet. "Optimal perturbation for two-dimensional vortex systems : route to non-axisymmetric state". In: *Journal of Fluid Mechanics* 855 (2018), pp. 922–952.
- [72] C. Olendraru, A. Sellier, M. Rossi, and P. Huerre. "Inviscid instability of the Batchelor vortex: Absolute-convective transition and spatial branches". In: *Physics of Fluids* 11.7 (1999), pp. 1805–1820. ISSN: 10706631. DOI: [10.1063/1.870045](https://doi.org/10.1063/1.870045).
- [73] J. M. Ortega. "Stability characteristics of counter-rotating vortex pairs in the wakes of triangular-flapped airfoils". PhD thesis. University of California, Berkeley, 2001.
- [74] J. M. Ortega, R. L. Bristol, and Ö Savaş. "Experimental study of the instability of unequal-strength counter-rotating vortex pairs". In: *Journal of Fluid Mechanics* 474.474 (2003), pp. 35–84. ISSN: 00221120. DOI: [10.1017/S0022112002002446](https://doi.org/10.1017/S0022112002002446).
- [75] J. M. Ortega and Ö Savaş. "Rapidly Growing Instability Mode in Trailing Multiple-Vortex Wakes". In: *AIAA Journal* 39.4 (2001), pp. 750–754. ISSN: 0001-1452. DOI: [10.2514/2.1375](https://doi.org/10.2514/2.1375). URL: <https://arc.aiaa.org/doi/10.2514/2.1375>.

- [76] N. Pérenne, J. M. Foucaut, and J. Savatier. "Study of the Accuracy of Different Stereoscopic Reconstruction Algorithms". In: *Particle Image Velocimetry: Recent Improvements*. Ed. by M. Stanislas, J. Westerweel, and J. Kompenhans. Berlin, Heidelberg: Springer Berlin Heidelberg, 2004, pp. 375–389.
- [77] W. F. Phillips. "Lifting-Line Analysis for Twisted Wings and Washout-Optimized Wings". In: *Journal of Aircraft* 41.1 (2004), pp. 128–136. ISSN: 15333868. DOI: [10.2514/1.262](https://doi.org/10.2514/1.262).
- [78] L. Prandtl. *Applications of modern hydrodynamics to aeronautics*. Tech. rep. NACA Report No 116, 1921.
- [79] A K Prasad. "Stereoscopic particle image velocimetry". In: *Experiments in Fluids* 29.103-16 (2000).
- [80] M. Raffel, C. E. Willert, S. T. Wereley, J. Kompenhans, S. Willert, S. T. Wereley, and J. Kompenhans. *Particle Image Velocimetry: A Practical Guide*. Springer Berlin Heidelberg, 2007. ISBN: 9783540723073. DOI: [10.1097/JT0.0b013e3182370e69](https://doi.org/10.1097/JT0.0b013e3182370e69). arXiv: [arXiv:1011.1669v3](https://arxiv.org/abs/1011.1669v3).
- [81] M. Raffel, E. C. Willert, and J. Kompenhans. *Particle Image Velocimetry, A Practical Guide*. Springer Berlin Heidelberg, 1998. ISBN: 978-3-662-03637-2. DOI: [10.1007/978-3-662-03637-2](https://doi.org/10.1007/978-3-662-03637-2).
- [82] S. C. Rennich and S. K. Lele. "Method for Accelerating the Destruction of Aircraft Wake Vortices". In: *Journal of Aircraft* 36.2 (1999), pp. 398–404. ISSN: 0021-8669. DOI: [10.2514/2.2444](https://doi.org/10.2514/2.2444). URL: <https://arc.aiaa.org/doi/10.2514/2.2444>.
- [83] J. Rom. *High Angle of attack aerodynamics*. Springer verlag, 1992. ISBN: 9781461276869.
- [84] F. Rooseleer and V. Treve. *ReCaT-eu european Wake Turbulence Categorisation and Separation minima on approach and departure*. Tech. rep. EUROCONTROL Headquarters, Brussels., 2018.
- [85] V. J. Rossow. "Convective merging of vortex cores in liftgenerated wakes". In: *Journal of Aircraft* 14.3 (1977), pp. 283–290. ISSN: 00218669. DOI: [10.2514/3.58772](https://doi.org/10.2514/3.58772).
- [86] V. J. Rossow. "Extended-Betz methods for roll-up of vortex sheets". In: *Journal of Aircraft* 34.5 (1997), pp. 592–599. ISSN: 00218669. DOI: [10.2514/2.2234](https://doi.org/10.2514/2.2234).
- [87] V. J. Rossow. "Lift-generated vortex wakes of subsonic transport aircraft". In: *Progress in Aerospace Sciences* (1999). ISSN: 03760421. DOI: [10.1016/S0376-0421\(99\)00006-8](https://doi.org/10.1016/S0376-0421(99)00006-8).
- [88] V. J. Rossow. "Measurements in vortex wakes shed by conventional and modified subsonic aircraft". In: *Advisory Group for Aerospace Research and Development*. 1996.
- [89] C. Roy, T. Leweke, M. C. Thompson, and K. Hourigan. "Experiments on the elliptic instability in vortex pairs with axial core flow". In: *Journal of Fluid Mechanics* 677 (2011), pp. 383–416. ISSN: 14697645. DOI: [10.1017/jfm.2011.91](https://doi.org/10.1017/jfm.2011.91).
- [90] P. G. Saffman. *Vortex Dynamics*. Cambridge University Press, 1992. ISBN: 978-0-521-42058-7. DOI: [10.1017/CB09780511624063](https://doi.org/10.1017/CB09780511624063).
- [91] A. Sciacchitano. "Uncertainty quantification in particle image velocimetry". In: *Measurement Science and Technology* 30.9 (2019). ISSN: 13616501. DOI: [10.1088/1361-6501/ab1db8](https://doi.org/10.1088/1361-6501/ab1db8).

- [92] D. Sipp and L. Jacquin. "Widnall instabilities in vortex pairs". In: *Physics of Fluids* 15.7 (2003), pp. 1861–1874. ISSN: 10706631. DOI: [10.1063/1.1575752](https://doi.org/10.1063/1.1575752).
- [93] P. R. Spalart. "Airplane trailing vortices". In: *Annual Review of Fluid Mechanics* 30 (1998), pp. 107–138. ISSN: 00664189. DOI: [10.1146/annurev.fluid.30.1.107](https://doi.org/10.1146/annurev.fluid.30.1.107).
- [94] J. R. Spreiter and A. H. Sacks. "The Rolling Up of the Trailing Vortex Sheet and Its Effect on the Downwash Behind Wings". In: *Journal of the Aeronautical Sciences* 18.1 (1951), pp. 21–32. DOI: [10.2514/8.1830](https://doi.org/10.2514/8.1830).
- [95] M. Stanislas, K. Okamoto, and C.J. Kähler. "Main results of the third international PIV Challenge." In: *Exp Fluids* 45.45 (2008), 27–71. DOI: <https://doi.org/10.1007/s00348-008-0462-z>.
- [96] E. Stumpf. "Study of Four-Vortex Aircraft Wakes and Layout of Corresponding Aircraft Configurations". In: *Journal of Aircraft* 42.3 (2005), pp. 722–730. ISSN: 0021-8669. DOI: [10.2514/1.7806](https://doi.org/10.2514/1.7806). URL: <https://arc.aiaa.org/doi/10.2514/1.7806>.
- [97] W. Thomson. "XXIV. Vibrations of a columnar vortex". In: *The London, Edinburgh, and Dublin Philosophical Magazine and Journal of Science* 10.61 (1880), pp. 155–168. ISSN: 1941-5982. DOI: [10.1080/14786448008626912](https://doi.org/10.1080/14786448008626912). URL: <https://www.tandfonline.com/doi/full/10.1080/14786448008626912>.
- [98] C. Y. Tsai and S. E. Widnall. "The stability of short waves on a straight vortex filament in a weak externally imposed strain field". In: *Journal of Fluid Mechanics* 73.4 (1976), pp. 721–733. ISSN: 14697645. DOI: [10.1017/S0022112076001584](https://doi.org/10.1017/S0022112076001584).
- [99] J. Weiss. "A tutorial on the proper orthogonal decomposition". In: *AIAA Aviation 2019 Forum* June (2019), pp. 1–21. DOI: [10.2514/6.2019-3333](https://doi.org/10.2514/6.2019-3333).
- [100] F. L. Westwater. *The rolling up of a surface of discontinuity behind an aerofoil of finite span*. Tech. rep. ARC/R & M-1692, 1935.
- [101] S. E. Widnall, D. B. Bliss, and C. Yin Tsai. "The instability of short waves on a vortex ring". In: *Journal of Fluid Mechanics* 66.1 (1974), pp. 35–47.
- [102] S. E. Widnall, D. B. Bliss, and A. Zalay. "Theoretical and Experimental Study of the Stability of a Vortex Pair". In: *Aircraft Wake Turbulence and Its Detection* 1. 1971, pp. 305–338.



**TITRE EN FRANÇAIS : Impact du chargement alaire sur les propriétés et la dynamique des tourbillons de sillage, une analyse en bassin hydrodynamique**

**RÉSUMÉ EN FRANÇAIS :** L'impact des modifications dans la géométrie d'une aile sur la dynamique des tourbillons marginaux est étudié à l'aide d'expériences en bassin hydrodynamique. L'objectif est de comprendre si la dangerosité des tourbillons marginaux peut être réduite grâce à une conception intelligente des ailes. L'aile de référence est rectangulaire, l'effet des variations de la charge alaire est ensuite examiné, notamment à travers les cas d'une configuration hypersustentée, des perturbations du bord de fuite et des ailes générant plusieurs tourbillons. Des mesures Stereo PIV suivent le développement du sillage tourbillonnaire depuis la phase de formation jusqu'à 300 envergures en aval. Le nombre de Reynolds moyen basé sur la corde est de  $Re_c = 10^5$ .

Les propriétés des tourbillons sont analysées pour en dégager une interprétation physique. Les modifications du bord de fuite entraînent des tourbillons marginaux élargis tout en maintenant une circulation constante. Les configurations hypersustentées, générant des paires de tourbillons co-rotatifs, présentent un phénomène de fusion puis un effet diffusif sur le coeur du tourbillon fusionné par rapport à la configuration de référence. Ici, une augmentation de la circulation de jusqu'à 20% est observée en raison de la proximité des tourbillons. En revanche, les configurations avec des tourbillons contra-rotatifs montrent un processus de diffusion visqueuse, réduisant la circulation du tourbillon marginal.

Dans l'ensemble, ce travail démontre que la charge alaire a un impact significatif sur la position spécifique, la force et la taille des tourbillons dans le sillage.

**TITRE EN ANGLAIS : Impact of wing loading on the properties and dynamics of trailing vortices, a water towing tank analysis**

**RÉSUMÉ EN ANGLAIS :** The impact that span-wise shape modifications on a wing have on the dynamics of trailing vortices is studied using towing tank experiments. The focus is on understanding if wake hazard can be reduced through intelligent wing design. The baseline wing is rectangular, variations in wing-loading configurations are then examined, including high-lift loading, trailing edge disturbances and wings that generate multiple vortices. Stereo PIV measurements track vortex wake development from the roll-up stage up to 300 spans downstream. The mean chord-based Reynolds number is  $Re_c = 10^5$ .

The essential properties of the vortices are presented and analyzed to provide physical meaning. Trailing edge shape modifications result in enlarged trailing vortices with consistent circulation. High-lift wing-load configurations, generating co-rotating vortex pairs, show a fusion phenomenon and a subsequent diffusive effect on the fused vortex core compared to the baseline. An increase in circulation, up to 20%, is observed due to closer vortex proximity. Conversely, configurations with counter-rotating vortices exhibit a viscous diffusion process, reducing the circulation of the wing-tip vortex.

Overall, the present work shows that wing loading has an important impact on the specific position, strength and size of vortices in the wake.

**MOTS-CLEFS : Charge aérodynamique - Tourbillons de sillage - Stabilité des tourbillons**

